

# Non–Equilibrium Molecular Dynamics Study of an Amphiphilic Model System

Dissertation  
zur Erlangung der Grades  
“Doktor der Naturwissenschaften”  
am Fachbereich Physik  
der Johannes Gutenberg-Universität  
in Mainz

**Thomas Soddemann**  
geboren in Bad Driburg

Mainz, 2000

Tag der mündlichen Prüfung: 25. Januar 2001

# Summary

This PhD thesis is concerned with the investigation of the behavior of complex fluids especially in static out of equilibrium states. For this purpose a simple model is introduced which is then used in molecular dynamics simulations.

Since the influence of shear flows on structure formation in complex fluids is the main interest of this work, a novel shear algorithm and the thermostat of the DPD simulation method have been parallelized and implemented into an existing simulation program. The change of the thermostat is necessary since the default one is proved to fail under shear flow conditions. The treatment of the periodic boundary condition by the program is completely redesigned in order to fit the requirements of the new thermostat.

Important equilibrium properties of simple fluids and dimers are investigated within the scope of the simulation model. Among them is the order–disorder transition (ODT) from the isotropic to the lamellar phase.

The influence of shear flows at constant strain rate on the lamellar phase near the ODT is investigated. The results are later compared with two analytic theories. Shear on a lamellar phase with layers parallel to the shear plane leads to a flow alignment of the director. It is shown that this alignment causes an effective shrinkage of the layers. Above a critical strain rate undulation of the lamellae can be observed as predicted by the analytical theory. A similar behavior can be observed in smectic systems which are dilated along the director. It turned out that the type of bifurcation towards the formation of undulation is different in comparison to the case of applied shear.

Similar to observations in experiments of complex fluids a second phase transition, the transition from a parallel orientation of the layers to a perpendicular alignment, can be identified. The shear stress is observed to be lower in the perpendicular aligned phase than in the parallel one at same strain rates. It is known that such a behavior leads under certain conditions to the occurrence of shear bands. Under high strain rates shear bands are found to occur in form of a coexistence of perpendicular aligned lamellae and an isotropic phase. The ordered bands can crystallize and will then move as plugs. These bands exhibit various defect structures which are very similar to those which have been found in diblock copolymer experiments.

This work succeeds in accounting for many aspects of complex fluids with a remarkable simple model. This leads to the conclusion that influences on structure formation under shear seem to be caused by interaction of shear with the superstructure itself rather than with local properties of the different molecules.



# Kurzfassung

Diese Doktorarbeit beschäftigt sich mit der Untersuchung des Verhaltens von komplexen Fluiden speziell im statischen Nichtgleichgewicht. Dazu wird ein allgemeines Modell dieser entworfen, welches dann im Rahmen von Molekulardynamik Simulationen verwendet wird. Da insbesondere der Einfluss von Scherflüssen auf die Strukturbildung von komplexen Fluiden untersucht werden soll, wird zu diesem Zweck ein neuartiger Scheralgorithmus und der Thermostat der DPD Simulationsmethode parallelisiert und in ein bestehendes Simulationsprogramm eingebaut. Die Einführung eines neuen Thermostaten ist notwendig, da der übliche unter Scherflussbedingungen versagt, wie gezeigt wird.

Zunächst werden wichtige Gleichgewichtseigenschaften von einfachen Flüssigkeiten und Dimerschmelzen im Rahmen des Modells untersucht. Hierbei wird u.a. die Lage des Ordnungs-Unordnungsübergangs von der isotropen zur lamellaren Phase der Dimere bestimmt.

Der Einfluss von Scherflüssen mit konstanter Scherrate auf diese lamellare Phase wird nun untersucht. Die Ergebnisse werden mit zwei analytischen Theorien verglichen. Die Scherung einer lamellaren Phase, deren Schichten in der Scherebene liegen, ruft eine Neuausrichtung des Direktors in Flussrichtung hervor. Es kann gezeigt werden, dass diese Ausrichtung als Funktion der Scherrate eine effektive Verminderung der Schichtdicke zur Folge hat. Oberhalb eines Schwellwertes in der Scherrate zeigt das lamellare System Ondulationen, wie von dem analytischen Modell vorhergesagt. Ein vergleichbares Verhalten wird auch in einem lamellaren System gefunden, an dem in Richtung des Direktors gezogen wird. Allerdings wird festgestellt, dass die Art der Bifurkation zu dem System, das Ondulationen zeigt, unter Scherfluss und einfachem Ziehen verschieden ist.

Unter Scherung wird ein Phasenübergang von einem System mit paralleler Ausrichtung zu einem senkrecht orientiertem System gefunden. Dabei wird festgestellt, dass die Scherspannung in senkrechter Orientierung niedriger als in der parallelen ist. Es ist bekannt, dass dies unter bestimmten Bedingungen zum Auftreten von Scherbändern führen kann. Unter hohen Scherraten werden dann auch das Auftauchen von Scherbändern und Scherkristallisation mit dem Vorliegen einer Koexistenz von senkrecht orientierten Lamellen und isotroper Phase beobachtet. Ähnlich den Ergebnissen von Experimenten werden in den orientierten Bändern verschiedene Defekte gefunden.

Es ist gelungen mit einem einfachen Modell viele Aspekte des Verhalten von komplexen Fluiden wiederzugeben. Dies lässt den Schluss zu, dass Einflüsse auf die Strukturbildung unter Scherung Phänomene sind, die nur bedingt von den lokalen Eigenschaften der Moleküle abhängen.



# Contents

<b>Prologue</b>	<b>3</b>
<b>1. Complex Fluids under Shear</b>	<b>9</b>
1.1. Diblock Copolymers under Shear . . . . .	9
1.1.1. Experimental Observations . . . . .	9
1.2. Multi Lamellar Vesicles . . . . .	13
1.3. Experimental Setups and Methods . . . . .	16
<b>2. Theoretical Approaches</b>	<b>19</b>
2.1. Introduction to the Theory of Smectic A Liquid Crystals . . . . .	20
2.1.1. Elastic Properties . . . . .	20
2.1.2. Fluctuations . . . . .	23
2.2. Shearing of a Layered System . . . . .	24
2.2.1. Analytic Description . . . . .	24
2.3. Viscoelastic Response to Shear Flow . . . . .	29
2.4. Diblock Copolymer Description . . . . .	33
2.4.1. The Description of Diblock Copolymers . . . . .	35
2.4.2. Diblock Copolymers under Shear . . . . .	36
2.4.3. A Limitation of the Theory . . . . .	48
<b>3. The Simulation Methods</b>	<b>51</b>
3.1. Molecular Dynamics . . . . .	51
3.1.1. The Integrator . . . . .	52
3.1.2. Coupling to a Heat Bath . . . . .	54
3.2. Constant Pressure Molecular Dynamics . . . . .	56
3.2.1. The Virial Equation . . . . .	56

3.2.2.	Pressure and Molecular Systems . . . . .	57
3.2.3.	Constant-Pressure Molecular Dynamics . . . . .	59
3.2.4.	Anisotropic Rescaling of the Box Shape . . . . .	63
3.2.5.	Choice of the Parameters . . . . .	64
3.3.	The Shearing Algorithm . . . . .	65
3.3.1.	Lees-Edwards Boundary Conditions . . . . .	66
3.3.2.	Physical Details of the FMP Algorithm . . . . .	68
3.3.3.	Implementary Details . . . . .	69
3.4.	Dissipative Particle Dynamics . . . . .	71
3.4.1.	The DPD Thermostat . . . . .	72
3.4.2.	Implementary Details . . . . .	74
3.5.	A Comparison between the DPD and Langevin Thermostatting Methods . . . . .	75
<b>4.</b>	<b>The Simulation Model</b>	<b>77</b>
4.1.	Development of the Model . . . . .	77
4.1.1.	Interactions . . . . .	77
4.1.2.	Computational details . . . . .	80
4.2.	Simulation Results . . . . .	82
4.2.1.	Identical Monomers . . . . .	82
4.2.2.	Binary Mixture . . . . .	85
4.2.3.	Dimeric Systems . . . . .	86
4.3.	Conclusions . . . . .	91
<b>5.</b>	<b>Shear, flow alignment, and undulation instability</b>	<b>93</b>
5.1.	Introduction . . . . .	93
5.2.	Shear Flow Simulations . . . . .	94
5.2.1.	Director Splay Modulus - Layer Bending Modulus . . . . .	94
5.2.2.	Flow Alignment . . . . .	96
5.2.3.	Onset of undulation . . . . .	100
5.2.4.	Stretch Dilation of layers . . . . .	105
5.2.5.	Stress vs. strain rate . . . . .	106
5.3.	The mechanism of undulations . . . . .	108
5.3.1.	Questions and suggestions . . . . .	108



5.3.2. The system . . . . .	110
5.3.3. Investigation of the undulation mechanism . . . . .	110
5.4. The Phase Transitions . . . . .	112
5.4.1. The Parallel to Perpendicular Transition . . . . .	113
5.5. Conclusion and Outlook . . . . .	114
<b>6. Shear bands</b>	<b>117</b>
6.1. What are shear bands? . . . . .	117
6.2. Systems under Investigation . . . . .	119
6.3. Shear Bands in Simulations . . . . .	120
6.4. Defects and Defect Structures . . . . .	128
6.5. Conclusion . . . . .	130
<b>Conclusion</b>	<b>131</b>
<b>A. List of Abbreviations and Symbols</b>	<b>137</b>



*The road goes ever on and on  
Down from the door where it began.  
Now far ahead the road has gone,  
And I must follow if I can,*

*Bilbo Baggins [Tol54]*



# Prologue

## Experiment – Theory – Simulation

On the way of understanding nature experiments are often a first step, their theoretical explanation the second. But not less often theories based on some model of the nature are validated by experiments.

Since the power of computers has likewise exploded, simulation become more and more important. Their relevance is twofold. They have the possibility to test and verify theories and serve in this role as a kind of experiment themselves. On the other hand they are able to make predictions about the outcome of experiments. This is, e.g., used in the chemical industry where computers predict the result of chemical reactions or the behavior chemically modified substances and molecular modeling helps to find and design new drugs.

Quite often a triangle as displayed in figure P.1 is drawn, where experiment, theory and sim-

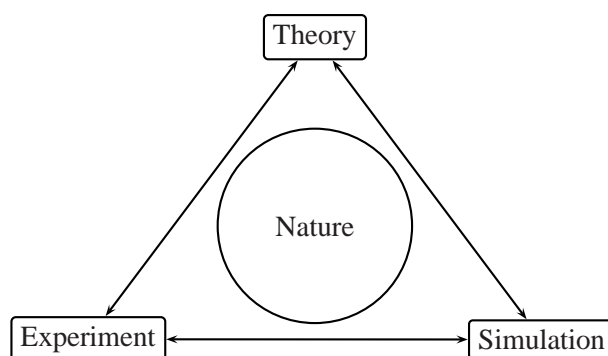


**Figure P.1.:** Theory, experiment, and simulation help to the unravel of the mystery nature. The edges serve as bilateral connections.

ulation act together in order to obtain a suitable picture of the nature. Edges are the pathways of bilateral communication, e.g. in form of verification of one endpoint's statements.

Simulations are carried out on different length scales reaching from the modeling of single atoms up to stellar systems. In the present work the simulation model substances such as

9 9 9  
 8 8 8  
 7 7 7  
 6 6 6  
 5 5 5  
 4 4 4  
 3 3 3  
 2 2 2  
 1 1 1  
 0 0 0

soaps, liquid crystals and special kind of polymers, diblock copolymers. Even those complex fluid exhibit a broad range of important length scales. Equivalent to the edges of the triangle the results will be compared with theory and experiment.

### Soaps – Diblock Copolymers – Liquid Crystals

A *polymer* is a molecule which is made of usually many chemical identical subgroups, the *monomers*. In the following only polymers will be considered where each monomer is bonded to at least one neighbor and maximum two. Such kind of polymers are also called *linear polymers*.

*Diblock copolymers* (DBCP) are special polymers where two different *homopolymers* (polymers which incorporate only one type of monomers) have been chemically glued together. Figure P.2 shows a model copolymer made of A (white) and B (blue) monomer blocks. Below a certain temperature those two block are physically incompatible and try to separate

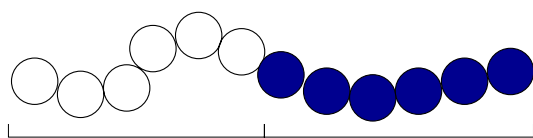


**Figure P.2.:** Schematic representation of a symmetric diblock copolymer. Monomers belonging to block A are white, the ones belonging to the B block are blue.

from each other. Since the block are chemically linked they cannot move far apart from each other, these phase separations is named microphase separation. Dependent on the relative length of each block in comparison to the total length of the DBCP various patterns evolve on length scales much larger than the polymer size. Figure P.3 shows sketches of typical micro-structures which can be found below the mentioned temperature, the *order–disorder transition* (ODT) temperature  $T_{ODT}$ . Figure P.4 shows monomers of the broadly used poly-

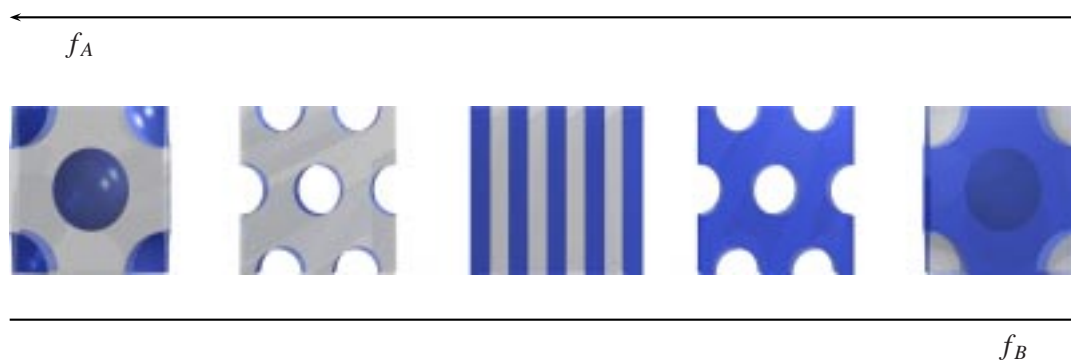


**Figure P.3.:** Typical equilibrium nanostructures of diblock copolymers with increasing fraction of monomers of type B (blue),  $f_B$ . Phases from left to right: Micellar, hexagonal, lamellar, inverted hexagonal, inverted micellar.

mers. Their range of technical applications reaches from food containers (PS) over packing foils (PE) to hitech fibers like Polartech (PP,PEP).

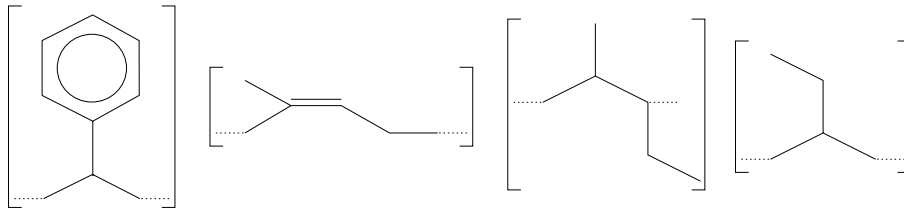


**Figure P.4:** The basic “ingredients” of the diblock copolymers polystyrene–polyisoprene (PS-PI) and polyethylene–polyethylpropylene (PEE-PEP). From left to right: the monomers of polystyrene, polyisoprene, polyethylene, and polyethylpropylene.

Soaps are quite similar to diblock copolymers at least in one aspect, they have two unlike parts which are chemically linked. They are very different in one other aspect: They are usually much smaller (shorter) than an ordinary polymer. Those molecules have a *hydrophilic*, water loving head and a *lipophilic*, oil friendly tail and hence they are often referred to as *amphiphiles*, loving both. Systems incorporating such amphiphiles are called *lyotropic*. Lyotropic systems exhibit a large variety of ordered phases, among them the lamellar phase. Their phase behavior is mainly influenced by the concentration of surfactant molecules. Since these are most often charged, altering the salt concentration does affect the phase behavior as well. Figure P.5 shows a sodium dodecyl sulfate molecule which is quite popular in shear experiments on lyotropic systems. Since it is a charged molecule the salt concentration in many

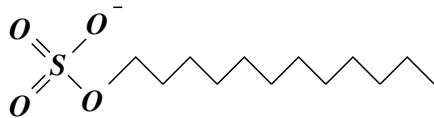


**Figure P.5:** Sodium dodecyl sulfate (SDS), a popular ingredient of lyotropic systems investigated under shear

experiments is quite high in order to screen the electrostatic interaction (See next chapter, section Onions).

A lamellar phase can also be found in liquid crystal (LC) systems. In the language of LC theory and experiment, this lamellar phase is denoted by the term *smectic* (from ancient Greek, soap). LC molecules have unlike amphiphiles no pronounced head or tail. It is more correct to see them as small rods. Below a certain temperature those rods keep their molecular axis in average pointing into the same single direction. This phase is called *nematic* and the vectorlike magnitude which points along this preferred direction is named *director*. The smectic phase lies at even lower temperature and due to the fact that those phases are reached by the variation of temperature those systems are denoted by the term *thermotropic*. The nematic and the smectic phase are sketched in figure P.6.

All three kinds of molecules, which are in common named *complex fluids*, show ordered phases but their range of order is seldom of macroscopic length scales, but nevertheless much larger in comparison to the molecular size. Flow fields now lead to microstructural changes and rearrangements which enhance or destroy long range order. Optical, permeability or electrical properties of complex fluids are influenced by the presence and orientation of ordered phases. As a cause of technical processing these fluids are often subjected to property

9 9 9  
8 8 8  
7 7 7  
6 6 6  
5 5 5  
4 4 4  
3 3 3  
2 2 2  
1 1 1  
0 0 0

9 9 9  
 8 8 8  
 7 7 7  
 6 6 6  
 5 5 5  
 4 4 4  
 3 3 3  
 2 2 2  
 1 1 1  
 0 0 0

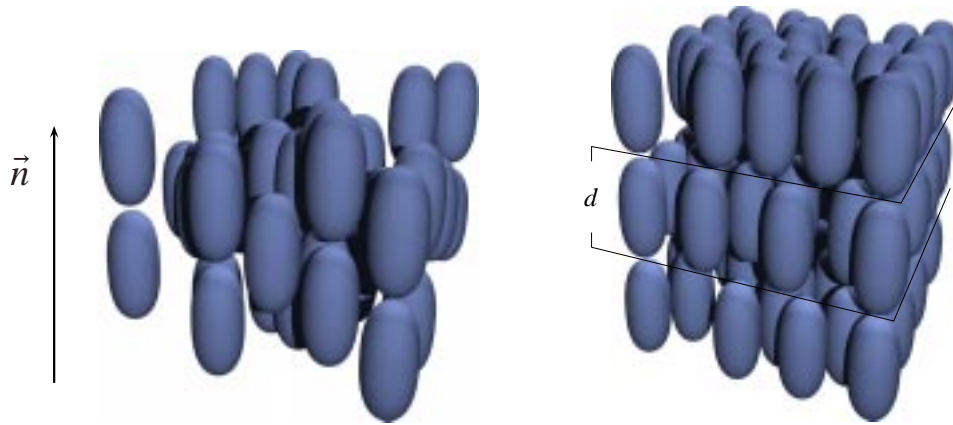


**Figure P.6.:** Sketches of the nematic and smectic phase. The nematic phase is shown on the left. The molecules are aligned into the same direction. The smectic phase, shown on the right, exhibits a layer structure in addition to a global alignment of the molecules.  $d$  denotes the layer thickness.

altering shear flows. Therefore a precise knowledge of their behavior under non-equilibrium conditions such as shear flows is of great interest. And since those systems are in a steady state out of equilibrium they are a good “toy” for researchers in fundamental physics.

Shear flow fields and their effect on a lamellar model system will be investigated by this work, simulation results will be compared to theory and experiment.

### Conventions

But first, in order to avoid confusion some conventions have to be made. In the notation of this work, shear fields,  $\vec{v}_0$ , are always parallel to the  $x$ -directions and their *velocity gradient* is parallel to the  $z$ -axis,  $\nabla v_0 \parallel \hat{z}$ . This leaves the  $y$ -direction unperturbed, which is also referred to as the *vorticity* direction,  $\nabla \times \vec{v}_0$ . Figure P.7 shows, the resulting coordinate system.

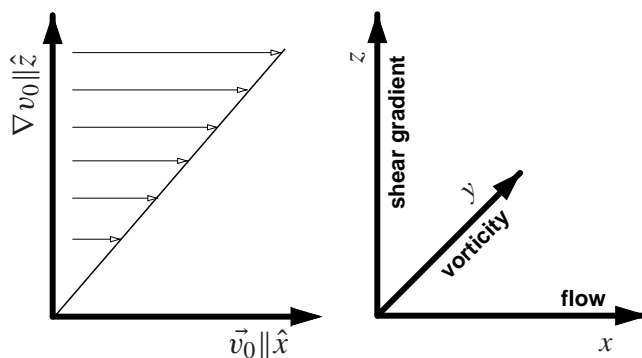


**Figure P.7.:** Coordinate system and shear flow. Shear flow in this work is always parallel to the  $x$ -axis. Its gradient direction is parallel to the  $z$ -axis and the vorticity direction to  $y$ .

All over this thesis, oriented lamellar structures will be mentioned. There are three basic



orientations, *parallel*, *perpendicular*, and *transverse*, which are defined as usual and depicted in figure P.8. A well ordered lamellar system is said to be perpendicular oriented if the layer

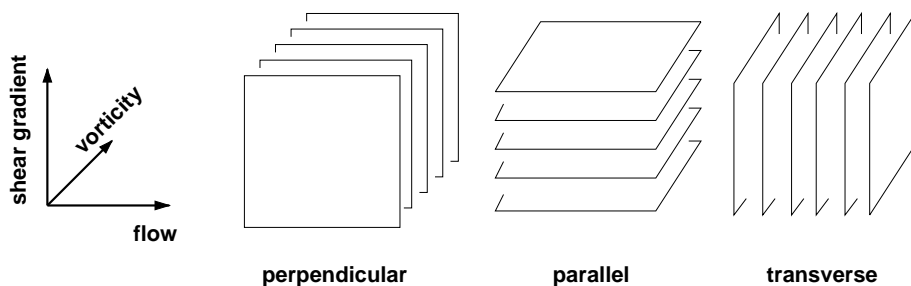


Figure P.8.: Perpendicular, parallel, and transverse orientation of lamellae.

normal points along the vorticity direction. A parallel orientation of the lamellae is defined by an orientation of the layers parallel to the flow–vorticity plane. The transverse orientation is given if the layer normal points along the flow direction.

It will turn out that at least the parallel and perpendicular orientation of the lamellae are favored under some certain conditions by complex fluids. The understanding of the pathways of alignment to each of those direction under different conditions of shear flow is believed to be the key to the understanding of shear alignment processes in general.

### Organization of the Thesis

This work is organized as follows. The first chapter reviews various experiments which have been conducted on diblock copolymers under shear. Many experimentalists suggested mechanisms based on their and others findings of how alignment of layers from arbitrary orientations to parallel or perpendicular may work. These mechanisms are briefly described since some of them might be observable in simulations as well. The formation of *onions* is certainly a very interesting research object. Nevertheless it is definitely one of the least understood. There is some considerable knowledge of how to find the onion phase but it still lacks an analytic treatment. At the end of the chapter some experimental setups are described.

A theoretical treatment of smectic liquid crystals under shear has been developed recently. A brief introduction into the theory of smectic liquid crystals is preceding the review of that analytical considerations. The equilibrium properties of diblock copolymers have been described analytically, too. One broadly applied theory has been extended to be able to handle shear flows. Since this has been the best accepted approach to the problem of DBCP under shear flow, its review has equally its place in chapter two. Both theories will be compared to simulation results later on.

The following chapter introduces the simulation methods to the reader. *Molecular dynamics* (MD) and the integration of the equations of motions in the different thermodynamical en-

9 9 9  
8 8 8  
7 7 7  
6 6 6  
5 5 5  
4 4 4  
3 3 3  
2 2 2  
1 1 1  
0 0 0

9 9 9  
8 8 8  
7 7 7  
6 6 6  
5 5 5  
4 4 4  
3 3 3  
2 2 2  
1 1 1  
0 0 0

sembles will be described. Most important in this chapter, the way how shear is applied to the model system within a simulation is discussed. A novel method of how to thermalize a system under flow conditions correctly will be derived from the so called *dissipative particle dynamics* (DPD) method which is germane to MD.

In the fourth chapter the model which will be used in the simulation, is introduced and tested. It will be shown that this model exhibits a broad range of possible applications apart from the current work, too.

The fifth chapter will be dedicated to simulation runs where shear is applied to lamellar model systems. A comparison with the findings to the two theories presented in the second chapter will be made. Especially the smectic liquid crystal description will turn out to match the results obtains from the simulations very well.

*Shear bands* are coexisting phases of different velocity gradient and hence a wonderful example of a nonlinear response to a shear field despite the laminar regime has not been left towards turbulent flows. This effect has been observed to be present under special conditions in complex fluids and it could be observed in form of plug flow in simulations, too. First findings and preliminary results which leaves plenty of space for further investigations, are discussed in this chapter.

This work is finished with a conclusion and outlook chapter where also further, future investigation are motivated.

# 1. Complex Fluids under Shear

## 1.1. Diblock Copolymers under Shear

The experiments on diblock copolymer melts reviewed in the following sections are all carried out under oscillatory shear. A sample is oscillatory deformed with a strain amplitude  $\gamma_0$  and a frequency  $\omega$ . Since all investigated copolymer species are below their glass transition the samples are heated in cone-to-plate and plate-to-plate rheometer geometries to temperatures around 100°C. The setups of those experiments are briefly described in the last section of this chapter. The theoretical treatment follows in the next chapter.

### 1.1.1. Experimental Observations

Koppi et al.[KTB<sup>+</sup>92] investigated the behavior of the order-disorder transition of a diblock copolymer melt under oscillatory shear. They used PEP-PEE which exhibits a significant difference in the entanglement lengths of its blocks (molecular weight of the used copolymer: 50 kg/mol). In binary fluid mixtures one observes a drop of the unmixing temperature with increasing shear stress, but they found an increase for  $T_{ODT}$  in their DBCP system instead, which is now known to be a normal feature of some complex fluids [KTB93, CK98a] (and references therein). All phase transitions they observed were isotropic to perpendicular transitions.

In some experiments the microstructural orientation was determined by ex-situ measurement methods after applying the shear field, while in others, more recent ones, by in-situ methods. They have the advantage to be able to follow the dynamics in the response to shear. But they are not for all cases applicable. The combination of both in-situ measurement like SAXS and SANS in flow and flow-gradient direction combined with ex-situ TEM and SAXS in vorticity direction seems to be most promising in recording the relevant data. E.g. Gupta et al. [GKC<sup>+</sup>96] showed that the lamellar alignment in a DBCP sample changed first from isotropic to perpendicular, and later to parallel, which underlines the importance of following intermediate states.

Defects may contribute to the degree of alignment of a lamellar phase and it is known that DBCP exhibit defects and imperfections. A DBCP-melt which is quenched below  $T_{ODT}$  shows ordered regions (grains), consisting of a limited but not necessary small number of layers, which are separated by discrete or continuous defects, such as lines, points, walls, and textures. Those defects are likely to persist, at least partly, under shear. Other factors like

9 9 9  
 8 8 8  
 7 7 7  
 6 6 6  
 5 5 5  
 4 4 4  
 3 3 3  
 2 2 2  
 1 1 1  
 0 0 0

undulations and imperfect alignment contribute to the degree of alignment, too.

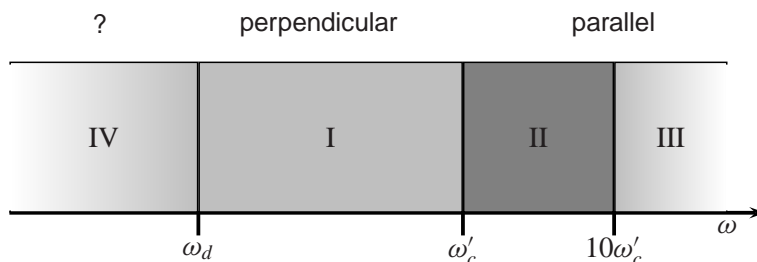


**Figure 1.1.:** Sketch of experimental finding of the phase behavior of DBCP under LAOS. The resulting long term alignment is depicted as both a function of the reduced order–disorder transition temperature and shear frequency.

Two *characteristic frequencies* have been proposed,  $\omega'_c$  and  $\omega_d$ . At frequencies above  $\omega'_c$  the viscoelasticity is dominated by the distortion of the chain conformations and below  $\omega_d$  the relaxation of the domains becomes significant. Between  $\omega'_c$  and  $\omega_d$  the distortion of the nanostructure dominates the viscoelastic response of the material [CK98a].

In experiments four regimes have been identified which are dominated by two different types of alignment. Those regimes are sketched in figure 1.1. Regime I describes the regime where the shear field couples to the nanostructure of the system. A perpendicular alignment of the lamellae is predominant. In Regime II ( $\omega'_c < \omega < 10 \omega'_c$ ) parallel orientation is found. On the way to this alignment perpendicular, parallel and all orientations in between can be seen. At frequencies higher than  $10 \omega'_c$  parallel alignment is induced, too, but the path leads through bimodal distributions rich in parallel and transverse orientations. At low frequencies ( $\omega < \omega_d$ ) in some systems parallel (such as PS–PI–type [CKS<sup>+</sup>97, PLWW95] except following a specific thermal treatment: prolonged annealing close to the BCPs' upper glass transition [ZW95, ZWY<sup>+</sup>96]) and in other perpendicular alignment (e.g. PEP–PEE–type) can be found [KTB93, KK94].

The strain amplitude is able to affect the rate and degree of alignment, and the especially the orientation of the alignment in the vicinity of the transitions between neighboring regimes. There are various hypothesis about the underlying mechanisms which lead to the observed behavior. In the following those proposed mechanisms and their relevance are briefly described.

When an unaligned and probably disordered DBCP sample is exposed to shear flow, two dynamic responses can be observed. One fast response which leads to a rough alignment of the layers and a slow response during which a fine tuning of the alignment takes place. For the region of the lowest frequencies, region IV, two mechanisms have been proposed, *grain rotation* and *irreversible rocking* [KK94]. In this region the shear flow couples to larger domains, the grains, as a whole. Therefore it is likely that those grains, which are misaligned to the selected direction, are able to respond with aligning to it with a rotation. The grains

are thought as rigid regions which rotate without any disturbance of the inner order. This mechanism is referred to as grain rotation.

Irreversible rocking describes a similar process of quick alignment of misaligned grains and is supposed to be the main process during the fast response to the shear excitation. An orientational dependence of the viscoelastic properties is thought to be the cause that oscillatory shear could produce a “wagging” or “rocking of the lamellar normal [KK94]. This motion may not be completely reversed over one cycle which leads to a new orientation during every cycle. A final steady state is reached if no rocking can take place any more or if the rocking becomes reversible. Irreversible rocking and the rotation of grains do not explain the dynamics and elimination of defects in the system, since focal conics, e.g., can only be destroyed by rupture of lamellae. Winey et al. have shown that shear flow–alignment leads to a reduction in the number of focal conics in a lamellar DBCP melt [WPLW93a].

Hence *defect migration* is another concept which certainly takes place in regime IV but is very likely to be found in the other regions, too. Since grains are misaligned, defects occur at the grain boundaries. During the alignment processes (especially grain rotation) the defects enclosing the grains migrate, build up little disordered regions, which then order and themselves align (either parallel or perpendicular).

In region I shear flow exerts the biggest effect on the nanostructure of the system. A (often re-) alignment to the perpendicular orientation takes place. First works explained this transition by the concept of *selective melting* of existing lamellae, which are broken apart by undulations, and a rebuilding of them in the perpendicular orientation [KTB<sup>+</sup>92]. This concept would result in a fast destruction of any orientation but perpendicular accompanied by an equally fast growing orientational order in that direction. At a later stage only a few barely misaligned layers remain which are then more slowly aligned. Further experiments on the kinetics of the orientation in this region showed that the dynamics is twofold [CKS<sup>+</sup>97]. First a fast process deletes all transverse orientation, but parallel and perpendicular orientations of the lamellae survive as well as all orientation in between. In a second slower process the perpendicular end alignment is reached. This can be described best by a *selective elimination* of transverse oriented grains and a *selective creation* of perpendicular aligned regions [GKC<sup>+</sup>96, GKKS96].

Region II and III are characterized by the distortion of the single chain conformation by the shear field. The pathways leading this regions are different. *Domain dissolution* is a concept which is valid in both cases. It describes the destruction of small unfavorable oriented regions which are then converted progressively into parallel layers. In order to account for the fact that different DBCP behave differently, Patel et al. introduced the concept of *viscoelastic contrast* [PLWW95]. In this region PS–PI are well aligned while PEP–PEE DBCP show no alignment at all. The difference between both substances is that PS–PI have very different local viscosities and are in the contrary to PEP–PEE not entangled. Region II is located near region one up to frequencies  $10 \omega'_c$ . After an initial fast process only parallel, perpendicular and layer–orientation in between have survived. In the following slow process the parallel orientation is favored and the all perpendicular orientation vanish. In the contrary at high shear frequencies in a fast response all layers except those which are parallel to transverse

9 9 9  
8 8 8  
7 7 7  
6 6 6  
5 5 5  
4 4 4  
3 3 3  
2 2 2  
1 1 1  
0 0 0

9 9 9  
 8 8 8  
 7 7 7  
 6 6 6  
 5 5 5  
 4 4 4  
 3 3 3  
 2 2 2  
 1 1 1  
 0 0 0

oriented are destroyed. In a further slow process a parallel alignment is established and the transverse orientation vanishes.

In the next chapter theoretical approaches are discussed, but already at this point should be clear that a complete theoretical understanding has not been reached. Actually it seems that there is a long road to go, since not all experimental observations can be interpreted consistently.

### Global Behavior in Experimental Results?

Assuming that in a certain regime, which has to be defined (and has first of all nothing to do with the previously mentioned four regime graph), large strain amplitudes and low shear frequencies have the same effect on a sheared sample as small strain amplitudes and high frequencies, the magnitude  $\dot{\gamma}_i = \gamma_0 \omega$  where the strain amplitude  $\gamma_0$  has been multiplied by the shear frequency  $\omega$ , will be interpreted as an effective strain rate. Further, a *reduced temperature*  $\tau$  can be defined in the following way

$$\tau \equiv \frac{T - T_{\text{ODT}}}{T_{\text{ODT}}} \quad (1.1)$$

where  $T_{\text{ODT}}$  is the equilibrium order–disorder transition temperature.

Revisiting the experimental data obtained in the experiments presented in [KTB<sup>+</sup>92, KTB93, KK94, GKKS95, GKC<sup>+</sup>96, GKKS96, CIK<sup>+</sup>97, WPLW93a, WPLW93b, LMTAW99] and plotting them with reduced temperature  $\tau$  and *effective strain rate*  $\dot{\gamma}_{\text{eff}} = \gamma_0 \omega$ , one should be able to distinguish between regions of disordered and of parallel and perpendicular aligned samples. This approach of collecting all the experimental data into a unique picture is different from the one used by Chen et al. [CK98b]. The result is shown in figure 1.2. Mainly three regions can be seen. The disordered region lies above a line of points which were taken from [KTB<sup>+</sup>92, KTB93] (white area in the plot). Koppi et al. investigated in those publications the behavior of the order–disorder transition as a function of shear frequency at a fixed strain amplitude. In those experiments a PEP-PEE melt with a molecular weight of 50 kg/mol was investigated. Their samples showed always a perpendicular orientation below the non–equilibrium ODT temperature. This region lies in the middle between the disordered and parallel ones, at least above an effective strain rate of  $\dot{\gamma}_e \geq 0.8$ . At lower strain rates parallel oriented samples were found by [WPLW93a, WPLW93b] which might be related to the method of preparation of those. Winey et al. used pressed samples which means that they are partly prealigned in the parallel orientation. Under weak shear this orientation might be metastable, although they see an increase in the alignment towards parallel. The parallel region is found at the lower values of the reduced temperature,  $\tau \leq -0.2$ .

Remarkably, data regardless of composition and molecular weight fit into the diagram. It seems that for this plot it does not matter whether the samples are composed of PEP-PEE or PS-PI or whether the molecular weight is 7 kg/mol or 50 kg/mol.

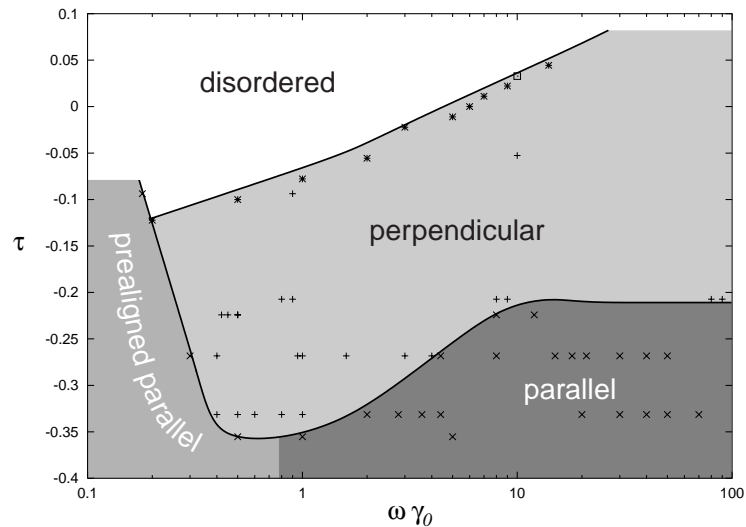


**Figure 1.2.:** Plot of various findings in shear experiments [KTB<sup>+</sup>92, KTB93, KK94, GKKS95, GKC<sup>+</sup>96, GKKS96, CIK<sup>+</sup>97, WPLW93a, WPLW93b, LMTAW99] via the reduced temperature  $\tau$  vs. the strain amplitude  $\gamma_0$  times the shear frequency  $\omega$ . Three different regimes can be distinguished, disordered and perpendicular and parallel orientation.

## 1.2. Multi Lamellar Vesicles

There are lamellar phases in other complex fluid than DBCP present as mentioned in the prologue and lyotropic systems belong to these. Diat and coworkers investigated the behavior of a quaternary mixture of water, sodium dodecyl sulfate (SDS), octanol, and sodium chloride.<sup>1</sup> Those systems were investigated under different compositions, temperatures, and strain rates.

Diat et al. showed that two lamellar phases in parallel orientation are stationary phases under shear flow. They are separated by a phase which turned out to be one of the most striking features of lyotropic system, the occurrence of a multi lamellar vesicle phase [DRN93b, DRN93a, DRN95]. These objects, also called *onions* and *spherulites*, are a closed compact assembly of mono disperse lamellar bilayers. This phase forms at intermediate strain rates and can exhibit a long range order due to a quasi-crystallization of the spherulite structure [DRN95]. Figure 1.3 shows a sketch of such an object. The size of the vesicles is dependent on the shear rate and may vary from a few microns to a tenth of a micron, as the applied shear rate increases [DRN95]. Bernheim-Grosswasser and coworkers recently managed to encapsulate an enzyme with a spherulite and to transport it through a cell membrane [BGUG<sup>+</sup>00].

There is a lack of theoretical description of the onion phase and the mechanism for the evolu-

<sup>1</sup>A typical composition is in weight 85.6% of water containing 20g/l of NaCl, 6.5% of SDS, and 7.9% of octanol.

9 9 9  
8 8 8  
7 7 7  
6 6 6  
5 5 5  
4 4 4  
3 3 3  
2 2 2  
1 1 1  
0 0 0

9 9 9  
 8 8 8  
 7 7 7  
 6 6 6  
 5 5 5  
 4 4 4  
 3 3 3  
 2 2 2  
 1 1 1  
 0 0 0

Regime	Mechanism	Short Description	Reference
I	selective melting	Selection of one direction of the others, melting of the non-aligned regions, and rebuilding in the selected alignment	[KTB <sup>+</sup> 92]
	selective creation	Isotropic regions order aligned to the selected direction.	[CIK <sup>+</sup> 97]
	selective elimination	Misaligned regions are destroyed by the shear flow. They are thought to recreate via selective creation.	[CIK <sup>+</sup> 97]
II	viscoelastic contrast	Accounting for the effect of very different viscosities of PS (near $T_g$ ) and PI (far above $T_g$ ), respectively different entanglement effects in PEP-PEE blocks.	[PLWW95]
II+III	domain dissolution	Dissolution of whole domains as an effect of shear flow. Occurs primarily in PEP-PEE systems where no ordering of any kind survives.	[WPLW93a, MW89]
	chain distortion	Distortion of and coupling to the local chain conformation by shear flow.	
IV	grain rotation	Rotation of grains in order to align to the selected direction. Grains rotate as rigid objects.	[MW89]
	irreversible rocking	A quick partial alignment of misaligned grains which continuously change their viscoelastic properties due to the new direction relative to the shear flow.	[KK94]
all	defect migration	Movement and elimination of defects	[KK94]

**Table 1.1.:** Overview on proposed mechanism for shear flow alignment of DBCP melts.

tion are still under debate, since there is no formalism describing the strong coupling between flow and structure in these complex fluids [DRN93a].

Panizza e.a. state that in complex fluid flow cannot be assumed uniform at all scale, since the characteristic lengths of these fluids are large [PCCR98]. That is the reason why a good analysis has to take into account the coupling between flow and details of the fluid. The relationship of viscoelastic properties to the micro structure of the fluid seems to be very important also in the present case.



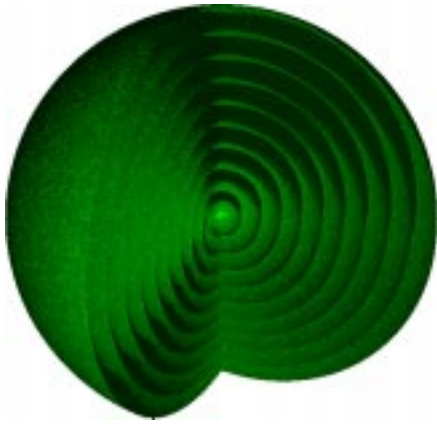


**Figure 1.3.:** Sketch of a multi lamellar vesicle. Sheets of bilayers are folded around a core. Their size can vary from a few microns to a tenth of a micron.

In their experiments they find four regime while shearing which are sketch in figure 1.4.

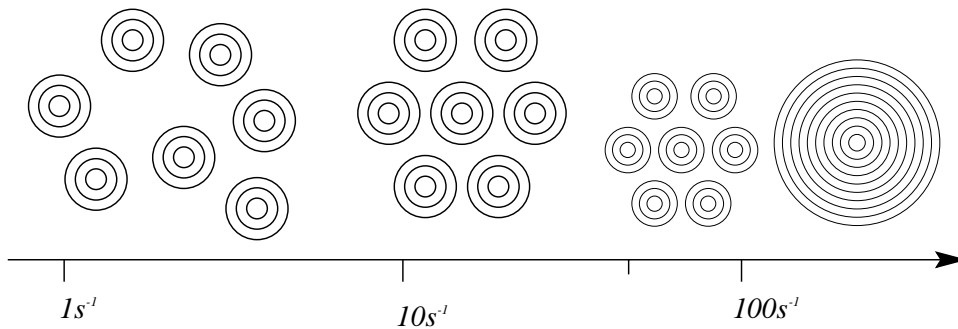


**Figure 1.4.:** Four regimes of occurrence of onions in a lyotropic system under shear (see text).

1. At low shear rates,  $\dot{\gamma} \approx 1s^{-1}$ , no characteristic patterns are found.
2. At shear rates  $\dot{\gamma} > 1s^{-1}$  onion with no long range order occur. For shear rates  $10s^{-1} < \dot{\gamma} < 50s^{-1}$  a so called layering transition (LT) can be found. The onions arrange in planes and exhibit a hexagonal ordering. The LT has no effect on the onion size which stays at 3-4  $\mu m$ .
3. At shear rates beyond the LT the size of the onions decreases slowly.
4. For a shear rate of  $\dot{\gamma} \approx 200s^{-1}$  a jump in the onion size can be found. The much bigger onions order.

Roux and coworkers stopped shearing but the pattern stayed the same. They could even enhance the pattern by applying low amplitude oscillatory shear to the sample. This behavior could be observed for different temperatures in the range from 20°C to 28°C. Stationary state have been studied, very little known about the transient behavior [PCCR98].

9 9 9  
8 8 8  
7 7 7  
6 6 6  
5 5 **5**  
4 4 4  
3 3 3  
2 2 2  
1 **1** 1  
0 0 0

9 9 9  
 8 8 8  
 7 7 7  
 6 6 6  
 5 5 5  
 4 4 4  
 3 3 3  
 2 2 2  
 1 1 1  
 0 0 0

Those findings are quite unexpected and not intuitive if the shear profile is really linear throughout the sample. There are no evidences why the onion size should grow or jump to a large size at such high shearing rates.

There are many other groups which investigate this specific subject by different means. Among them one has certainly to mention the Richtering group from Freiburg (now Kiel), Germany (e.g. [RJWP96, JJPW98, JJW98, ZLT<sup>+</sup>99]), the Hoffmann group in Bayreuth, Germany (e.g: [HU98, BGHM98]).

Unfortunately it seem not to be possible to investigate those structures with the simulation approach which will be introduced in chapter three. The size of even small onions is that big that millions of particles are needed just in order to build up a few. Hence this thesis concentrates on the problems arising from lamellar structure and their transitions to other orientations.

### 1.3. Experimental Setups and Methods

There are different possibilities to apply shear to a sample in an experiment. But all of these methods have all in common that the shear strain is acting on the surfaces of the sample and a momentum flow is imposed by that. It is assumed that the response is linear a laminar flow is present and hence a linear profile is the result of the shear stress<sup>2</sup>.

There are three different geometries which are mainly used and have already been mentioned in the previous sections. Those are the *plate-to-plate*, the *cone-to-plate* and the *Couette* geometries. In the following the way how shear is exerted to a sample is briefly outlined. Since many groups use home brew extensions of industrial rheometers, such as the ones by companies like Rheometrics (<http://www.rheometrics.com/>) or Bohlin (<http://www.bohlin.de/>), the reader may refer to papers and home-pages of the experimental groups for details.

Figure 1.5 shows the sketch of a Couette cell. Here, the sample fills the small gap between

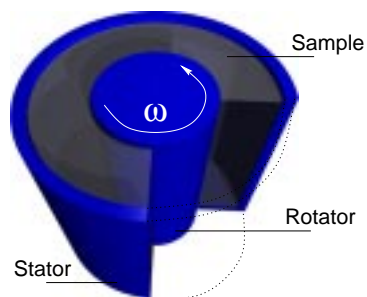


**Figure 1.5.:** Sketch of a Couette cell. A static cylindrical decanter (stator) contains an inner cylinder (rotator), which can be rotated with an angle velocity  $\omega$ . The space between the two cylinders is filled with the liquid sample and their gap is usually small. This geometry is usually used for constant strain rate experiments on lyotropic systems.

an outer static cylindrical container and an inner cylinder. This inner cylinder is pivoted and due to its rotation a shear profile can be induced to the system. The height of such a cell is about 50 mm, and the width of the gap lies in the range of 1 mm. The gap can be varied by exchanging the inner cylinder. In principle many kinds of shear field can be exposed

<sup>2</sup>This is not true in all cases as discussed in chapter 6.

to the sample but usually the strain rate or the shear stress is kept constant. Such cells are predominantly used for the investigation of low-viscosity liquids like lyotropic systems and diblock copolymer solutions in their laminar regime (in context with the work described earlier). Roux and coworkers find their onion structures using this kind of cells [DRN93a]. But also Taylor eddies can be found if the rotation of the inner cylinder is high enough [Sti89] and the turbulent regime is reached, which is beyond the scope of the present work.

In figure 1.6 a plate-to-plate and a cone-to-plate geometry have been sketched. In this

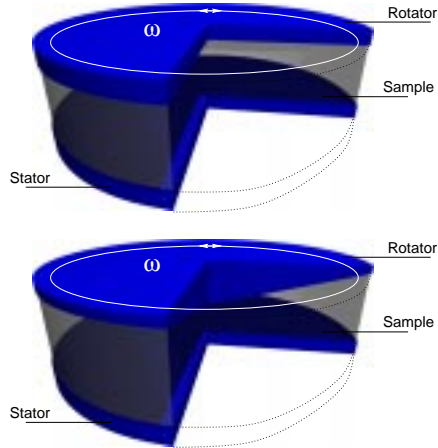


**Figure 1.6.:** Sketch of plate to plate (upper sketch) and cone to plate (lower sketch) geometries. Here bottom plate serves as the stator, the upper plate or the cone respectively, are movable and hence named rotator. The space between them is filled by the highly viscous sample and also their gap is quite small. Both geometries are usually used for the rheometrical investigation of diblock copolymers under oscillatory shear. The cone-to-plate geometry allows constant strain along its radius.

geometry the sample is located between two plates. The upper plate rotates (rotator) the lower one is static (stator). In the cone-to-plate geometry the cone is usually the rotator. Both geometries are used for rheometric investigation of high viscous substances such as diblock copolymer melts. They are usually investigated with oscillatory shear at large amplitudes (LAOS) or at low strains of constants strain rate. In oscillatory experiments, the strain is measured from the center to the outer rim of the plate and hence measured in percent. The gap is again only a few millimeters thick and the sample has to be pressed in order to fit. Since most samples are below their glass transition the plates are heatable.

Figure 1.3 shows a picture of a rheometer installed at the Institut Laue-Langevin.



**Figure 1.7.:** Experiment installed at the Institut Laue-Langevin. the stress controlled Bohlin CVO rheometer on the instrument D11. This allows to obtain SANS data from samples under various shear conditions: controlled shear stress or controlled shear rate, simple shear, oscillatory shear, and creep. The rheological data are obtained simultaneously. [ZLR99]

9 9 9  
8 8 8  
7 7 7  
6 6 6  
5 5 5  
4 4 4  
3 3 3  
2 2 2  
1 1 1  
0 0 0

9 9 9  
8 8 **8**  
7 7 7  
6 6 6  
5 5 5  
4 4 4  
3 3 3  
2 2 2  
1 **1** 1  
0 0 0

## 2. Theoretical Approaches

The last chapter was dedicated to the various findings in experiments where shear was applied to systems that exhibit a lamellar phase. Especially, in the case of diblock copolymer melts many mechanisms were suggested which may describe the reorientation and alignment scenarios found in those systems. But it is less obvious what happens during the transition from a lamellar state to the onion phase in lyotropic systems. Not even an elucidative suggestion for a possible understanding of that effect exists.

Most approaches to analytic explanations of the role of shear flow in lamellar systems therefore are limited to the case of diblock copolymers, especially diblock copolymer melts. A reason for this might be the availability of precise equilibrium descriptions, e.g., the approaches by Leibler [Lei80] and Fredrickson and Helfand [FH87]. Especially, the last one is of interest since it describes a diblock copolymer melt in the vicinity of the order–disorder transition where most experiments under shear are performed.

Another class of systems where a reorientation of the orientation of lamellae under shear is found are Smectic *A* liquid crystals (LC). Their equilibrium structure is usually described on the coarse grained level of the properties of their lamellae. The treatment of the micro-structural physics is neglected in favor of the behavior of its superstructure. In contrast to the statistical analysis of the DBCP case a hydrodynamic description is applied. For a complete treatment of the equilibrium properties of Smectic *A* LC the reader is referred to [dGP93, deG72].

All theoretical approaches to the problem of shear exerted on lamellar systems (or systems which are in the vicinity of a lamellar phase in equilibrium) face the difficulty in analyzing fluid mechanics and micro-structural mechanics simultaneously. In the following two approaches are presented in which the micro-structural dynamics are neglected. Both treat the fluid as a viscoelastic homogeneous medium. The disadvantage is that they fail to describe flow induced micro-structural changes and inhomogeneities that may modify material properties dramatically.

The chapter is organized as follows. First the theoretical description of Smectic *A* liquid crystals, especially the energy contribution of the layer structure to the Hamiltonian of the system is briefly reviewed. Then the ansatz by Auernhammer and coworkers which is based on the hydrodynamic description of the layered structure of Smectic *A* LC is described. This is followed by a short analysis of how shear in a complex fluid can be described by thermodynamic expressions. This is different to the hydrodynamic treatment, since here the shear is described by its action on the micro-structure rather than on the director field.

9 9 9  
 8 8 8  
 7 7 7  
 6 6 6  
 5 5 5  
 4 4 4  
 3 3 3  
 2 2 2  
 1 1 1  
 0 0 0

The response of the shear stress and strain is discussed and the shear moduli  $G'$  and  $G''$  are introduced. Finally, the predictions of Fredrickson, Cates, and Milner for the shear induced transition from the isotropic state to a lamellar phase are presented.

## 2.1. Introduction to the Theory of Smectic A Liquid Crystals

A brief introduction of the theory of nematic and smectic phases is given on which the theory of Auernhammer's et al. work is based. The intention of this section is certainly not to fully present the theory of smectic liquid crystals. The treatment here is restricted on the aspects that are needed to describe the proposed mechanisms. A complete treatment on the subject of smectic LC can be found elsewhere [dGP93].

### 2.1.1. Elastic Properties

The elasticity of a material is defined as the ratio between applied static stress and strain produced in that material. The dynamic response to the stress is determined by the viscosity. Elastic properties of liquid crystals (LC) are a characteristic feature, since stress results directly in orientational anisotropy of the material. Elastic constants in LC depend on two fundamental structural features: the anisotropy and the orientational order.

For sufficiently small forces the response of the system (deformation) is linear (Hooke's law). The force  $F$  per unit area is then related to the relative extension  $x/l$  ( $x$ : elongation,  $l$ : length of a slab of material):

$$\frac{F}{A} = k \frac{x}{l}. \quad (2.1)$$

The elastic energy is then given by

$$\mathfrak{E}_{\text{el.}} = \int F dx = \frac{1}{2} V k \gamma^2, \quad (2.2)$$

where  $\gamma = x/l$  denotes the strain. Figure 2.1 sketches the situation.

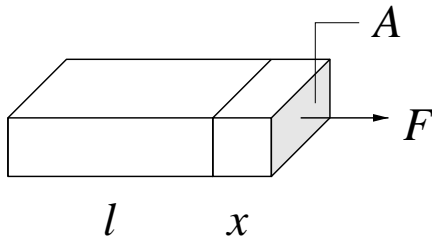


**Figure 2.1.:** Deformation of a slab of material. A force  $F$  is acting on an area  $A$  and elongates the material of length  $l$  by the factor  $x/l$ .

The new positions of the particles at  $\vec{r}^\alpha$  and  $\vec{r}^\beta$  under applied stress can be written as

$$(\vec{r}^\alpha)' = \vec{r}^\alpha + \vec{u} \quad (\vec{r}^\beta)' = \vec{r}^\beta + \vec{v}. \quad (2.3)$$

For small strain this can be rewritten as

$$v_i = u_i + \frac{du_j}{dr_i^\alpha} r_j^\beta, \quad (2.4)$$

where  $r_i^{\alpha\beta} = r_i^\alpha - r_i^\beta$  and the indices  $i$  and  $j$  denote the spatial components. Now a strain tensor can be defined as

$$\gamma_{ij} = \frac{du_j}{dr_i^{\alpha\beta}}. \quad (2.5)$$

The diagonal elements of this tensor measure the extensional strain along  $x$ ,  $y$  and  $z$ -axes, the off-diagonal elements are a measure of the shear strain.  $\gamma_{ij}$  can be splitted into its symmetric and its anti-symmetric part

$$\gamma_{ij} = \frac{1}{2} [(\gamma_{ij} + \gamma_{ji}) + (\gamma_{ij} - \gamma_{ji})]. \quad (2.6)$$

A totally anti-symmetric tensor refers to a pure rotation without any distortion. The symmetric part describes the changes in the relative position of the particles within a sample under strain. This part vanishes for nematics while in smectics and columnar phases the transitional order results in some non-zero components in the symmetric part of the strain tensor.

The applied stress to a body is given by the force per unit area. This force may contain components perpendicular and parallel to that area. Those are the normal stress (pressure) and the shear stress. For any direction there is one normal and two shear stress components. This set of forces can be described in terms of the stress tensor

$$\sigma_{ij} = \frac{n_i F_j}{A}, \quad (2.7)$$

where  $F_j$  denotes the force acting on an element of area  $A$  which is normal to  $n_i$ . The diagonal components are the pressure, the off-diagonal represent the shear stress. In equilibrium the normal forces on opposite faces must have equal absolute values and the torque must be zero.

The stress and the strain tensors which are both of second rank are related by a fourth rank tensor, the elasticity

$$\sigma_{ij} = v_{ij,kl} \gamma_{kl}. \quad (2.8)$$

The intrinsic symmetry of the stress and strain tensors reduce the number of components of the elasticity tensor to 36. This tensor is symmetric with respect of permutations of pairs of indices,  $v_{ij,kl} = v_{kl,ij}$ , which reduces the number of components further to 21. The comma in the tensor representation denotes this symmetry property. For small strains the elastic energy density can be written as

$$\mathfrak{F}_{\text{el.}} = \frac{1}{2} v_{ij,kl} \gamma_{ij} \gamma_{kl}. \quad (2.9)$$

For a homogeneous strain in the absence of any torque both,  $\sigma_{ij}$  as well as  $\gamma_{ij}$  are symmetric tensors having six independent components  $\sigma_\alpha = \sum_{\beta=1}^6 v_{\alpha\beta} \gamma_\beta$ .

9 9 9  
8 8 8  
7 7 7  
6 6 6  
5 5 5  
4 4 4  
3 3 3  
2 **2** 2  
1 1 **1**  
0 0 0

9 9 9  
 8 8 8  
 7 7 7  
 6 6 6  
 5 5 5  
 4 4 4  
 3 3 3  
 2 2 2  
 1 1 1  
 0 0 0

The angular displacement of a unit vector at position  $\vec{r}$  from its equilibrium orientation is given by

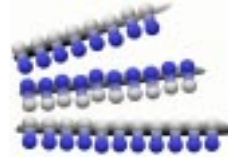
$$\begin{aligned} n'_i &= n_i + \frac{dn_i}{dr_j} r_j \\ &= n_i + \gamma_{ij} r_j. \end{aligned} \quad (2.10)$$

For simplicity  $\vec{n}$  is from now on considered to be parallel to the z-axis.  $\gamma_{iz}$  can then be neglected and the non-vanishing elements represent

director splay  $\hat{=}$  layer bend  $\gamma_{xx} = \frac{dn_x}{dx}$   $\gamma_{yy} = \frac{dn_y}{dy}$

director twist (not possible in smectic systems)  $\gamma_{xy} = \frac{dn_y}{dx}$   $\gamma_{yx} = \frac{dn_x}{dy}$

director bend  $\hat{=}$  layer splay  $\gamma_{zx} = \frac{dn_x}{dz}$   $\gamma_{zy} = \frac{dn_y}{dz}$



The elastic energy density is then

$$\mathfrak{F}_{\text{el.}} = \frac{1}{2} \sum_{i,j=1}^6 k_{ij} \gamma_i \gamma_j, \quad (2.11)$$

where the torsional elastic constants  $k_{11}$ ,  $k_{22}$ , and  $k_{33}$ , and the saddle splay  $k_{24}$  follow from the elasticity tensor to be the only remaining independent components. Terms containing  $k_{24}$  do not contribute to the free energy for configurations where the director is within a plane or parallel to it, which is true for Smectic A LCs. With eq. (2.11) and those assumptions the energy density is given by

$$\begin{aligned} \mathfrak{F}_{\text{el.,nematic}} &= \frac{1}{2} [k_{11}(\gamma_{xx} + \gamma_{yy})^2 + k_{22}(\gamma_{xy} - \gamma_{yx})^2 + k_{33}(\gamma_{zx} - \gamma_{xz})^2] \\ &= \frac{1}{2} [K_1(\nabla \cdot \vec{n})^2 + K_2(\vec{n} \cdot \nabla \times \vec{n})^2 + K_3(\vec{n} \times \nabla \times \vec{n})^2]. \end{aligned} \quad (2.12)$$

For Smectic A the only homogeneous strain supported is an extension or compression perpendicular to the layers. Bend and twist strains involve changes in the layer spacing which has a very high energy barrier. Those term are higher order contributions and are here neglected. Hence the energy density is

$$\mathfrak{F}_{\text{el.,smectic}} = \frac{1}{2} \left[ B \left( \frac{du_z}{dz} \right)^2 + K_1(\nabla \cdot \vec{n})^2 \right], \quad (2.13)$$

where  $u$  denotes the layer displacement. Note that the bending energy term is of the same order as the director splay term, since the director and the layer displacement are coupled by  $\hat{n} = -\nabla u$ .



### 2.1.2. Fluctuations

Neglecting static distortions (from interfaces or external fields) the conformation with the lowest free energy exhibits a director with one uniform orientation. The director is likely to fluctuate about its equilibrium value due to thermal excitations. These fluctuations are e.g. responsible for the turbidity of some LC at room temperature. Especially at transition points those fluctuations are big and hence some experimentalists call these points “clearing points” since the samples are clear at temperatures below these points.

The director’s orientational disorder can be formally represented by defining an order parameter

$$Q_{ij} = \frac{1}{2} 3 \langle n_i n_j - \delta_{ij} \rangle. \quad (2.14)$$

This expression is referred to as the nematic order parameter [dGP93].<sup>1</sup> Spatial variations of the director can be expressed in terms of Fourier components of the wave vector  $\vec{q}$

$$n_i(\vec{q}) = V^{-1} \int d^3 r n_i(\vec{r}) e^{i\vec{q}\cdot\vec{r}}. \quad (2.15)$$

Small distortions from a director axis  $z$  can be written in the Fourier components  $n_x(\vec{q})$  and  $n_y(\vec{q})$ . The normal modes of the excitation of wave length  $\lambda = 2\pi/q$  can be obtained by

$$\begin{pmatrix} n_1(\vec{q}_\perp) \\ n_2(\vec{q}_\perp) \end{pmatrix} = \frac{1}{q_\perp^2} \begin{pmatrix} q_x & q_y \\ -q_y & q_x \end{pmatrix} \begin{pmatrix} n_x \\ n_y \end{pmatrix}, \quad (2.16)$$

where  $\vec{q}_\perp$  denotes wave vectors perpendicular to the equilibrium director direction.  $q_x$  and  $q_y$  are its components in this contexts. The normal mode  $n_1(\vec{q}_\perp)$  refers to splay and bend deformations while the normal mode  $n_2(\vec{q}_\perp)$  accounts for twist bending. The latter one vanishes for Smectic A LCs. The free energy density can now be written in terms of the normal modes:

$$\mathfrak{F}_{\text{el.}} = \frac{1}{2} \sum_q \lambda_1 (n_1(\vec{q}_\perp))^2 + \lambda_2 (n_2(\vec{q}_\perp))^2, \quad (2.17)$$

where  $\lambda_1 = K_1 q_\perp^2 + K_3 q_\parallel^2$  and  $\lambda_2 = K_2 q_\perp^2 + K_3 q_\parallel^2$ . The fluctuations are assumed to be small. Therefore according to the equipartition theorem, the average contributions of each mode is supposed to be proportional to  $k_B T/2$

$$\langle (n_1(\vec{q}_\perp))^2 \rangle = \frac{k_B T}{V \lambda_1(q_\perp^2)} \quad \text{and} \quad \langle (n_2(\vec{q}_\perp))^2 \rangle = \frac{k_B T}{V \lambda_2(q_\perp^2)}. \quad (2.18)$$

Eq. (2.18) are valid for nematics, since they incorporate the elastic constants  $K_2$  and  $K_3$  which are neglectable for Smectic A. The left equation in (2.18) will be used to obtain  $K_1$  from a simulation (see chapter 5).

<sup>1</sup>A smectic order parameter can be defined, too. But since the simulations will deal with particles, which are unable to form a nematic phase and rather exhibit a lamellar, Smectic A phase, the nematic order parameters suffices to distinguish between isotropic and smectic order. The main advantage of the application of the nematic order parameter is, that it can be obtained with much less effort than the smectic one. (See next chapter.)

9 9 9  
 8 8 8  
 7 7 7  
 6 6 6  
 5 5 5  
 4 4 4  
 3 3 3  
 2 2 2  
 1 1 1  
 0 0 0

## 2.2. Shearing of a Layered System

There is a common characteristic all systems discussed in the first chapter regardless of chemical origin exhibit: a lamellar phase. Auernhammer et al. [ABP00] investigated the case where shear is applied to a system with lamellae parallel oriented to the shear plane. They introduced a simple model in order to explain the destabilization of the layers under shear flow which was observed e.g. by Wiesner and coworkers [ZW95, HDTU99]. This description is based on a derivation of the macroscopic hydrodynamic equation and an analysis of its linear stability. Auernhammer and coworkers show that parallel layers are unstable above a certain critical shear rate and exhibit undulations along the vorticity direction.

In the following the main ideas of Auernhammer et al. are presented. First the energetic contributions of layers and director tilt are discussed. The Gibbs relation and a set of balance equations serve as a starting point for the derivation of the description of shear flow alignment and its consequences.

The predictions of their theory are compared qualitatively and quantitatively to simulation results in a later chapter (5).

### 2.2.1. Analytic Description

First the energy contributions of a Smectic A LC are considered. The analytic theory makes the following assumptions

- All layered systems are isomorphic to Smectic A LC.
- Polymeric degrees of freedom are neglected.
- A possible coupling of thermal fluctuation of the layers to the shear flow is neglected.

These assumptions are in general not applicable to diblock copolymers, where fluctuations are likely to play an important role in the destabilization of layers. Figure 2.2 shows an idealized geometry of an shear experiment. Infinite layers of a mono-domain Smectic A LC of thickness  $d$  are shown. The upper plate at  $z = +d/2$  is moving with a velocity  $v_0/2$  while the lower plate at  $z = -d/2$  is moving in the opposite direction with  $-v_0/2$ . The resulting shear rate is hence  $\dot{\gamma} = v_0/d$  assuming a linear velocity profile. One can now define a layer normal denoted by  $\hat{p}$  and a director as in nematics denoted by  $\hat{n}$ . Layer normal and director are usually defined to be parallel [dGP93]. Auernhammer and coworkers drop this assumption and consider  $\hat{n}$  and  $\hat{p}$  as independent variables coupled elastically so that in equilibrium  $\hat{n} \parallel \hat{p}$ . The motivation for this view arises from the widely known coupling between shear flow and the direction of the nematic phase. Exposed to a shear flow a homeotropically aligned nematic LC feels a torque on the director. The response is described by the flow alignment parameter  $\lambda$ . At a given shear rate it determines whether the molecules show a tendency to simply tilt or whether they start to tumble. Auernhammer et al. assume that that torque is also present in a Smectic A LC and that it is balanced by the elastic coupling between  $\hat{n}$  and

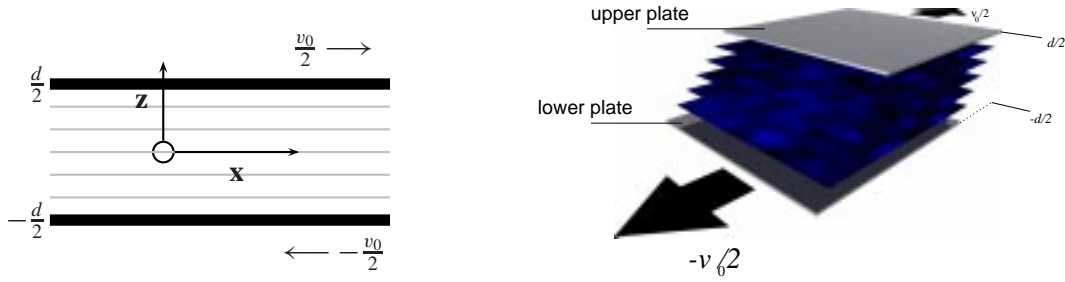


**Figure 2.2.:** Idealized geometry of a shear experiment. The thick lines denote the upper and lower plate at  $d/2$  and  $-d/2$  respectively. They are moving in opposite directions with a relative velocity of  $v_0$ . The  $x$ -axis points along the flow direction and the  $z$ -axis is direction of the velocity gradient.

$\hat{p}$ . That balance leads to a finite angle of the director and therefore to a component in flow direction which means that the director flow aligns. This flow alignment results in an effective dilatation of the layers. The system answers to the dilatation above a certain threshold with a development of undulations.

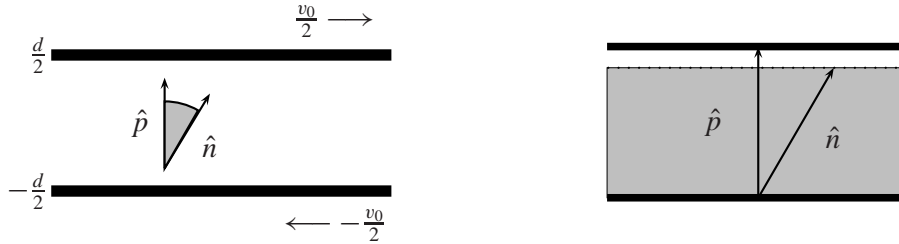


**Figure 2.3.:** A finite angle between the layer normal  $\hat{p}$  and the director  $\hat{n}$  leads to an effective reduction of the layer thickness.

Now the energy density is introduced which describes the system. The standard notation for the energy density is given by equation

$$\mathfrak{F}_{el.,nematic} = \frac{1}{2}K_1 (\nabla \cdot \hat{n})^2 + \frac{1}{2}K_2 [\hat{n} \cdot (\nabla \times \hat{n})]^2 + \frac{1}{2}K_3 [\hat{n} \times (\nabla \times \hat{n})]^2 \quad (2.12)$$

which represent splay, twist, and bend deformations, respectively, as shown in the previous section.

Besides  $\hat{n}$  and  $\hat{p}$  it is very convenient to introduce the variable  $u$  which describes the layer displacement in  $z$ -direction  $\hat{p} = \frac{\nabla(z-u)}{|\nabla(z-u)|}$ . The lowest order terms were in the previous section expressed by

$$\mathfrak{F}_{el.,smectic} = \frac{1}{2}K \left[ \left( \frac{\partial^2}{\partial x^2} + \frac{\partial^2}{\partial y^2} \right) u \right]^2 + \frac{1}{2}B_0 \left( \frac{\partial}{\partial z} u \right) \quad (2.13)$$

9 9 9  
 8 8 8  
 7 7 7  
 6 6 6  
 5 5 **5**  
 4 4 4  
 3 3 3  
 2 **2** 2  
 1 1 1  
 0 0 0

9 9 9  
 8 8 8  
 7 7 7  
 6 6 6  
 5 5 5  
 4 4 4  
 3 3 3  
 2 2 2  
 1 1 1  
 0 0 0

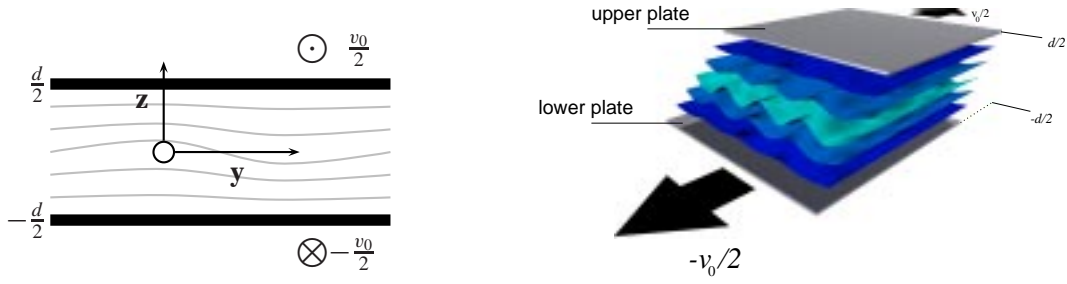


**Figure 2.4.:** Development of undulations in the vorticity direction. The undulation amplitude is largest in the bulk and vanishes towards the bounding plates. The wave vector is oriented along the vorticity direction. Note that the figure shows the  $y$ - $z$ -projection.

These terms describe the curvature and the dilatation of the layers. Rigid rotations of  $\hat{n}$  together with  $\hat{p}$  do not contribute to the energy density, relative rotation of  $\hat{n}$  versus  $\hat{p}$  might. Assuming a small angle between  $\hat{n}$  and  $\hat{p}$  Auernhammer et al. introduced the term

$$\frac{1}{2}B_1(\hat{n} \times \hat{p})^2 \quad (2.19)$$

This term is not hydrodynamic, since it does not vanish in the limit of small wave number excitations (i.e.  $q \rightarrow 0$ ). So it leads dynamically to a relaxation and not to diffusive behavior in the long wave length limit.

The following common simplifications have been made by Auernhammer and coworkers

- Bend deformation are higher order gradient corrections to dilatation. If the angle between  $\hat{n}$  and  $\hat{p}$  is small, bend is neglected
- In the hydrodynamics of smectics twist deformation are forbidden. Thus, for  $\hat{n}$  close to  $\hat{p}$ , any twist of  $\hat{n}$  has to be very small and is neglected.
- A curvature of the layers is very similar to a splay deformation of the director, so only the latter one is kept.

The derivation of the hydrodynamics equations usually involves two steps. First the Gibbs–Duhem relation is written down and the thermo-dynamical forces, which are defined via this relation, are expanded into the hydrodynamic variables. In a second step one expresses the currents (and quasi-currents) appearing in the conservation laws by the thermodynamic forces in order to close the system of hydrodynamic equations [PB96].

In the treatment of Auernhammer et al. the following Gibbs relation is used

$$d\epsilon = d\epsilon_0 + \Psi_i d(\nabla_i u) + h'_i dn_i + \Phi_{ij} d(\nabla_j n_i) \quad (2.20)$$

which includes the terms which arise due to nematic and smectic order.  $\vec{\Psi}$ ,  $\vec{h}'$  and  $\underline{\Phi}$  are the conjugate quantities to  $\nabla u$ ,  $\hat{n}$  and  $\nabla \hat{n}$ .

Quantities like mass or momentum can only be transported not created. Hence the balance equations can directly be written down. The mass conservation is given by

$$\frac{\partial}{\partial t}\rho + \nabla_i j_i = 0, \quad (2.21)$$

the momentum conservation by

$$\frac{\partial}{\partial t}g_i + \nabla_j(v_j g_j) + \nabla_j \sigma_{ij} = 0, \quad (2.22)$$

and the energy conservation by

$$\frac{\partial}{\partial t}\epsilon + \nabla_i[v_i(\epsilon + p)] + \nabla_i j_i^\epsilon = 0. \quad (2.23)$$

$\underline{\sigma}$  denote the stress tensor,  $\vec{j}^\epsilon$  the energy current and  $p$  the pressure.

Further, similar balance equations account for the broken symmetry in a Smectic A liquid crystal or the increase of entropy due to irreversible dynamics.

$$\frac{\partial}{\partial t}n_i + v_j \nabla_j n_i + Y_i = 0 \quad (2.24)$$

$$\frac{\partial}{\partial t}u + v_j \nabla_j u + Z = 0 \quad (2.25)$$

$$\frac{\partial}{\partial t}\sigma + \nabla_i(v_i \sigma) + \nabla_i j_i^\sigma = \frac{R}{T} \quad (2.26)$$

Here,  $\sigma$  denotes the entropy density,  $T$  is the temperature and  $\vec{j}^\sigma$ ,  $\vec{Y}$ , and  $Z$  are the (quasi-) currents associated with  $\sigma$ ,  $\hat{n}$ , and  $u$  respectively. The pressure is given via the Gibbs–Duhem relation

$$p = -\epsilon + \mu\rho + T\sigma + \vec{v}\vec{g} \quad (2.27)$$

where the chemical potential  $\mu$  is the conjugate quantity to the mass density  $\rho$ . The dissipation function is given as a positive definite quadratic form of the forces

$$R = \frac{1}{2}\gamma_1^{-1}h_i \delta_{ij}^\perp h_j + \frac{1}{2}v_{ijkl}\nabla_j v_i \nabla_l v_k + \frac{1}{2}\kappa_{ij}\nabla_i T \nabla_j T + \frac{1}{2}\lambda_p(\nabla_i \Psi_i)^2 \quad (2.28)$$

where  $\gamma_1$  is the rotational viscosity,  $v_{ijkl}$  the viscous stress tensor,  $\kappa_{ij}$  the thermal conductivity,  $\lambda_p$  the permeation coefficient,  $\delta_{ij}^\perp = \delta_{ij} - n_i n_j$  the transverse Kronecker symbol and  $h_i = \frac{\delta\epsilon}{\delta n_i} = h'_i - \nabla_j \Phi_{ij}$  is the variation of the energy density with respect to the director. The dissipation function  $R$  can be interpreted as the energy per unit time and volume dissipated into the microscopic degrees of freedom. Hence the term  $R/T$  is the entropy production term.

It is important to note that in the present model  $\hat{n}$  and  $\hat{p}$  are coupled via  $B_1$  and but are not necessarily parallel, especially if shear is applied. In that case, when  $\hat{n}$  and  $\hat{p}$  enclose a small angle as depicted in figure 2.3, the effective thickness of the layer reduces.

Following the standard procedure described in [PB96], Auernhammer et al. split the currents and quasi-currents in the balance equations in two parts, reversible and irreversible ones. From the Gibbs relation a set of macroscopic equations containing several phenomenological coefficients can now be derived.

The analysis of that set was done in two steps. First the flow field and the director were determined assuming that the layers are unchanged by the shear flow (i.e. stay parallel to the plates and keep their thickness). This assumption holds for weak shear flows. In a second step undulations of  $\hat{n}$  and  $\hat{p}$  with a wave vector parallel to the vorticity direction were investigated.

9 9 9  
8 8 8  
7 7 7  
6 6 6  
5 5 5  
4 4 4  
3 3 3  
2 2 2  
1 1 1  
0 0 0

9 9 9  
 8 8 8  
 7 7 7  
 6 6 6  
 5 5 5  
 4 4 4  
 3 3 3  
 2 2 2  
 1 1 1  
 0 0 0

## Shear Flow Alignment

Auernhammer and coworkers find the following behavior for the director under weak shear flow. For the limit of weak shear flow a linear velocity profile can be assumed,

$$\vec{v} = \dot{\gamma} z \hat{e}_x \quad (2.29)$$

which satisfies linear momentum conservation. The quasi-current  $\vec{Y}$  has to vanish, assuming a steady state and hence  $\hat{n}$  to be constant. This leads with the given velocity profile to a director tilt, given by [ABP00]

$$\left[ \frac{\lambda + 1}{2} - \lambda n_x^2 \right] \dot{\gamma} = \frac{B_1}{\gamma_1} n_x \sqrt{1 - n_x^2} + \frac{B_0}{\gamma_1} \left[ n_x (1 - \sqrt{1 - n_x^2}) \right]. \quad (2.30)$$

Taking into account only the linear terms which is justified in a situation where the angle between  $\hat{n}$  and  $\hat{p}$  is small, yields

$$n_x = \dot{\gamma} \frac{\gamma_1}{B_1} \frac{1 + \lambda}{2} \quad (2.31)$$

## Onset of Undulation

In Auernhammer's treatment the layer normal  $\hat{p}$  and the director need not necessarily to be parallel. As a consequence that if a small angle between  $\hat{p}$  and  $\hat{n}$  leads to a projection of the director in normal direction with a length less than unity. So the layer thickness cannot be constant, they shrink. Since the occupied volume is constant, space has to be filled. This could be done by insertion of a new layer if the shrinkage is large enough. The insertion process, however, has a huge energy barrier, since it relies on the formation and evolution of defect structures. For the given bounded system the layers start to undulate which costs much less energy [ABP00].

The critical values of the onset of undulation were derived by Auernhammer and coworkers. They assume in accordance following and Ben-Abrahams [OBA82] that undulation will be found in the vorticity direction since shear does not affect this direction directly. The derivatives in  $z$ -direction are replaced by

$$\frac{\partial}{\partial z} u \rightarrow \frac{\partial}{\partial z} u - \frac{1}{2} \left( \frac{\partial}{\partial y} \right)^2 \quad (2.32)$$

so that the apparent dilatation can be expressed by

$$\frac{\delta l}{l} \approx \frac{1}{2} \left( \frac{\partial}{\partial y} \right)^2 \quad (2.33)$$

where  $l$  is the layer thickness and  $\delta l$  is its increase according to the deviation of  $\hat{p}$  from its equilibrium value  $\hat{p}_0$ . In other words, the layer thickness  $l$  is dependent on the alignment

angle of the director. With increasing alignment angle the thickness  $l$  decreases from its equilibrium value  $l + \delta l$ . Speaking of a reduced  $l$  and its “increase”  $\delta l$  intends to point out the parallel to the theory of a Smectic  $A$  elongated along its director. The ansatz for the undulation has to incorporate the fact that they have to vanish at the plates confining the system. Auernhammer et al. use

$$u = A \cos\left(\frac{\pi}{d}z\right) \cos(q_y y) + \frac{1}{2}n_x^2 z, \quad (2.34)$$

with the amplitude of the undulations  $A$ . The behavior of the layer normal is hence given by

$$\hat{p} = q_y A \cos\left(\frac{\pi}{d}z\right) \sin(q_y y) \hat{e}_y + \hat{e}_z + \dots \quad (2.35)$$

Since the energy barrier is too high to form undulation at weak shear rates there is a finite onset of value. Auernhammer et al. determine this value and its critical parameters. The values for the critical strain rate  $\dot{\gamma}_c$ , the critical flow component of the director  $n_{x,c}$  and the wave vector  $q_{y,c}$  of the resulting wave in vorticity direction are given by

$$q_{y,c}^2 = \frac{\pi}{d} \sqrt{\frac{B_0}{K}} \quad (2.36)$$

$$n_{x,c}^2 = 4 \frac{B_0}{B_0 - 2B_1} \frac{\pi}{d} \sqrt{\frac{K}{B_0}} \quad (2.37)$$

$$\dot{\gamma}_c = \frac{4}{1 + \lambda} \frac{B_1}{\gamma_1} \sqrt{\frac{B_0}{B_0 - 2B_1} \frac{\pi}{d} \sqrt{\frac{K}{B_0}}} \quad (2.38)$$

### Limits of the Description

The above theory is able to describe the effect of shear flow on a parallel oriented sample of Smectic  $A$  LC. It predicts an undulation instability at higher strain rates. The main limit of this treatment is the inability to fully describe a transition from a parallel to a perpendicular orientation of the layers. Such a description has to include nonlinear effects and variations of the order parameter which are both neglected by Auernhammer et al.

The model includes elements of smectic as well as nematic descriptions. So by a suitable choice of the moduli  $B_0$  and  $B_1$  one can either obtain a nematic or a smectic theory. This does not imply that the transition from nematic to smectic order is described by this approach correctly and this was not intended.

## 2.3. Viscoelastic Response to Shear Flow

Again the case is considered, where shear is applied to a system in its liquid phase. It is assumed that the shear stress remains quite small and that the reaction by the system can be described by linear equations.

9 9 9  
 8 8 8  
 7 7 7  
 6 6 6  
 5 5 5  
 4 4 4  
 3 3 3  
 2 2 2  
 1 1 1  
 0 0 0

Viscoelastic properties of fluids are described by the relation between the stress tensor  $\sigma_{ij}$  and the velocity gradient tensor  $\nabla_i v_j$ . In a simple, incompressible fluid the following equation holds:

$$\sigma_{ij} = \eta(\nabla_i v_j(t) + \nabla_j v_i(t)) \quad (2.39)$$

where the proportional factor  $\eta$  is the shear viscosity. This expression is very similar to the simplified treatment of the stress strain relation 2.8. The single value viscosity represents an isotropic elasticity tensor. But it is not the same, since the gradient in the shear flow is equivalent with the rate of a strain deformation and not the strain itself. The strain rate is denoted by  $\dot{\gamma}$  in the following and related to the strain by the integral expression

$$\gamma(t) = \int_0^t dt' \dot{\gamma}(t') \quad (2.40)$$

in the case of a uni-directional velocity gradient.

In polymeric systems the stress-strain relation is usually much more complicated and in general not linear. Therefore the stress has to be expressed by a functional:

$$\sigma_{ij} = F_{ij}[\dot{\gamma}_{ij}] \quad \text{for } \dot{\gamma}_{ij}(t') \quad \text{with } t' < t \quad (2.41)$$

Assuming that the perturbation by the velocity gradient is small enough the relation between the stress and the velocity gradient is dominated by its linear terms and can be approximated by

$$\sigma_{ij} \approx \int_{-\infty}^t G(t-t')(\dot{\gamma}_{ij}(t) + \dot{\gamma}_{ji}(t)). \quad (2.42)$$

This equation includes only one material function  $G(t)$  which is called the shear relaxation modulus, whose Fourier transform is accessible in experiments.

For simplicity, as in the last sections, shear flows of the following form are considered

$$v_x(\vec{r}, t) = \dot{\gamma}(t)r_z \quad v_y, v_z = 0, \quad (2.43)$$

where  $\dot{\gamma}(t)$  denotes the time dependent shear rate.

Hence the shear stress can be written as a linear function in  $\dot{\gamma}(t)$  and equation (2.42) reduces to

$$\sigma_{xz}(t) = \int_{-\infty}^t dt' G(t-t')\dot{\gamma}(t'). \quad (2.44)$$

Assuming the above mentioned linear regime, there are three possibilities how to apply shear to a sample in an experiment which will be described now. In two of them the applied shear strain is controlled while in the other one the shear stress is kept constant.

### Stepwise strain

In the first scenario, which is considered here, shear is switched on in form of a step function at  $t_0$ . As the strain stays constant in the long time limit (no further deformation of the sample



takes place), the stress relaxes. Here the shear rate is not time dependent and reduces to a constant  $\dot{\gamma}(t) = \dot{\gamma} = \text{const}$ . This defines the steady shear viscosity  $\eta$ :

$$\eta = \frac{1}{\dot{\gamma}} \sigma_{xz}. \quad (2.45)$$

Shear is applied to the unsheared sample starting at time  $t = 0$ . That means that the shear strain performs a step from zero to its steady state value and is given by

$$\gamma(t) = \begin{cases} 0 & t < 0 \\ \gamma_0 & t \geq 0. \end{cases} \quad (2.46)$$

The response of the shear stress is only determined by the time behavior of the shear relaxation modulus,

$$\sigma_{xz}(t) = \gamma_0 G(t) \quad (2.47)$$

Hence the external force is applied for an infinite time starting at  $t = 0$  to the system. The situation is depicted in figure 2.5.

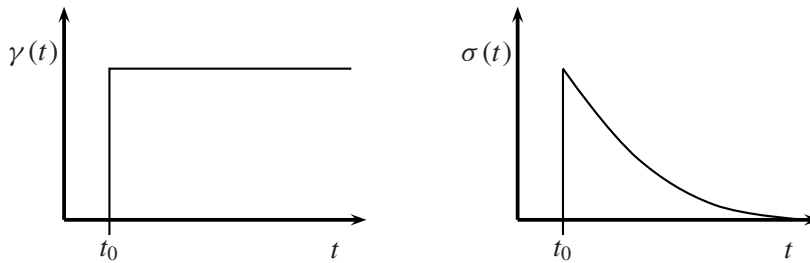


**Figure 2.5.:** Sketch of a stepwise shear applied to a sample. The strain step takes place at  $t = 0$ . The stress follows the excitation and relaxes afterwards.

### Oscillatory shear

The next possibility is to apply shear oscillatory in time. Here the sample is strained by an excitation of a certain frequency and amplitude. The stress answers with the same period but with a shifted phase. In an oscillatory shear experiment a sinoidal shear strain is applied to the sample leading to the followin shear rate

$$\dot{\gamma}(t) = \dot{\gamma}_0 \cos(\omega t) = \dot{\gamma}_0 \Re(e^{i\omega t}) \quad (2.48)$$

The response to this function is defined by the complex shear modulus  $G^*$

$$\sigma_{xz}(t) = \dot{\gamma}_0 \Re\left(\frac{G^*(\omega)}{i\omega} e^{i\omega t}\right) \quad (2.49)$$

It is convenient to measure the complex shear modulus  $G^*(\omega)$  in experiments, since this is a magnitude which varies with frequency for most polymers. Its real part  $G'(\omega)$  is named storage and its complex part  $G''(\omega)$  loss modulus. The situation is sketched in figure 2.6

9 9 9  
8 8 8  
7 7 7  
6 6 6  
5 5 5  
4 4 4  
3 **3** 3  
2 2 2  
1 1 **1**  
0 0 0

9 9 9  
8 8 8  
7 7 7  
6 6 6  
5 5 5  
4 4 4  
3 3 3  
2 2 2  
1 1 1  
0 0 0

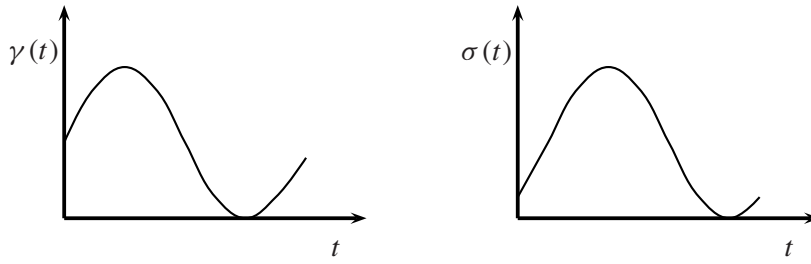


**Figure 2.6.:** Oscillatory shearing. The strain is applied with a given amplitude and frequency. The shear stress follows with a shift in phase.

### Constant stress – creep

As the last considered example, the strain rate is kept constant. This is equivalent to a constant stress exerted to the sample if it responds truly viscoelastic.<sup>2</sup> The strain itself grows then linearly in time (at least for longer times).

In a creep experiment things are a little bit different. The shear stress is given by

$$\sigma_0 = \int_0^t dt' G(t-t') \frac{d\gamma(t')}{dt'} \quad (2.50)$$

and is time independent. Here a constant shear field is applied from a time  $t = 0$  on. The shear strain grows monotonically in time

$$\gamma(t) = \sigma_0 \int_{-i\delta-\infty}^{i\delta+\infty} \frac{d\omega}{2\pi} \frac{e^{i\omega t}}{\omega G^*(\omega)} \quad (2.51)$$

while the strain rate  $\dot{\gamma}$ , the slope of shear strain, is constant in the long time behavior. The behavior of the system is determined by the complex shear relaxation modulus  $G^*(\omega)$

$$\begin{aligned} G^*(\omega) &= i\omega \int_0^\infty dt (1 - i\omega t + \dots) G(t) \\ &= i\omega g_0 + \omega^2 g_1 + \dots \end{aligned} \quad (2.52)$$

with

$$g_0 = \int_0^\infty dt G(t) \quad \text{and} \quad g_1 = \int_0^\infty dt G(t)t \quad (2.53)$$

So the shear strain can be rewritten as an approximation in  $g_1$  and  $g_0$

$$\gamma(t) = \sigma_0 \left( \frac{t}{g_0} + \frac{g_1}{g_0^2} \right) \quad (2.54)$$

<sup>2</sup>In experiment were a chemical reaction, e.g. a sol-gel transition, takes place which alters the viscoelastic properties a constant stress shear might result in a constant strain and zero strain rate in the long time limit. In such cases the dependence of the shear stress on the strain rate is no longer linear.

And the shear viscosity can be determined by

$$\eta_0 = \int_0^\infty dt G(t) = \lim_{\omega \rightarrow 0} \frac{G''(\omega)}{\omega} \quad (2.55)$$

The term  $g_1/g_0^2$  is called the steady state compliance and often denoted by  $J_e^0$ . It is obvious that it is given by

$$J_e^{(0)} = \int_0^\infty dt G(t)t / \left[ \int_0^\infty dt G(t) \right]^2 = \lim_{\omega \rightarrow 0} \frac{G'(\omega)}{G''(\omega)} \quad (2.56)$$

The situation is depicted in figure 2.7.

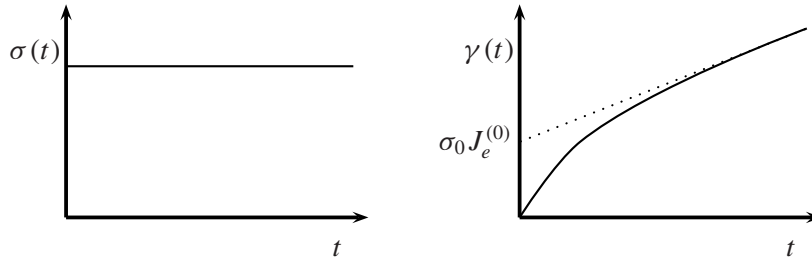


**Figure 2.7.:** Constant stress. In this experiment constant stress is applied to the sample. The strain grows linearly in the long time limit and hence the strain rate is constant.

### Remarks

The considerations in this section certainly hold for homo-polymeric liquids. For diblock copolymer melts especially below the order–disorder transition temperature those are not necessarily valid any more. Below this transition a micro-phase separation takes place which results in a broken symmetry of the system. Therefore the viscosity cannot be represented by a single value any more. Instead a viscosity tensor is needed as it was initially mentioned in the first section. Nevertheless in many oscillatory shear experiments, e.g. [CK98a], the loss and storage moduli are measured even in the ordered phase. Comparison of these moduli with measurements in the disordered phase (if available) give *hints* of where to find, e.g., orientational transitions.

In the following a brief introduction of Helfand and Fredricksons treatment of diblock copolymers is given, followed by Fredricksons treatment of those systems under shear.

## 2.4. Diblock Copolymer Description

Brazovskii suggested a model for the investigation of binary systems [Bra75]. This model was slightly generalized in order to be able to apply it to diblock copolymer melts [Lei80].

9 9 9  
8 8 8  
7 7 7  
6 6 6  
5 5 5  
4 4 4  
3 **3 3**  
2 2 2  
1 1 1  
0 0 0

9 9 9  
 8 8 8  
 7 7 7  
 6 6 6  
 5 5 5  
 4 4 **4**  
 3 **3** 3  
 2 2 2  
 1 1 1  
 0 0 0

The Hamiltonian is in the same universality class as the one for weakly anisotropic antiferromagnets, fluids near the Rayleigh–Bérnard instability, and liquid crystals near the nematic–smectic  $C$  transition (see [FH87] and references therein). All these system are characterized by having fluctuations in the vicinity of a shell of nonzero wave vectors. By the help of the modified Hamiltonian one is able to predict all micro-phase separated states seen experimentally. Nevertheless the model has some limitations in comparison to the experiment. E.g., it neglects polydispersity and assumes that the blocks have the same statistical segment length. The disadvantage for the comparison with the present simulations might be that it presumes a huge number of segments in each block,  $N_A \gg 1$  and  $N_B \gg 1$ .

Two variables describe completely the equilibrium thermodynamics in Leibler’s mean field theory. The product of the dimensionless Flory parameter and the chain length  $\chi N$  accounts for the enthalpic interaction between the different statistical segments of type A and B. The second variable is the composition  $f$ , the fraction of type A segments of all chains. In the case of a symmetric DBCP,  $f = 1/2$ . The mean field theory predicts a second order phase transition from the disordered to the lamellar phase for the case of a symmetric DBCP melt. Leibler’s theory proved to be inaccurate to describe especially this transition without further extension. Fredrickson and Helfand [FH87] enhanced his approach by the introduction of fluctuation corrections. They find among other things that the order–disorder transition for symmetric DBCP is of first order.

Based on the Brazovskii model Cates and Milner [CM89] investigated the role of steady shear flow on the isotropic to lamellar transition. This transition is of first order. In their work they showed the important role of shear flow in the suppression of fluctuations in compositions raising the transition temperature. Their theory is not capable of distinguishing between perpendicular and parallel alignment of the lamellae [Fre94]. They argued that a perpendicular orientation should be favored since the composition fluctuations with wave vectors in the vorticity direction are least affected by the shear flow.

With some physically motivated modifications Fredrickson was able to extend the Cates and Milner ansatz towards the distinction of both orientation regimes [Fre94]. The main idea was the incorporation of different viscosities of the blocks since in experiments copolymers like PS-PI have indeed very different bulk properties especially since in the experiments PS blocks are close to the glass temperature,  $T_g$ . In addition he accounts for the fact, that fluctuations about the mean composition pattern are correlated in orientation with the lamellar normal.

The generalized Brazovskii model for diblock copolymers is outlined in section 2.4.1. The main ideas of the extension to shear flow is presented in section 2.4.2.

### 2.4.1. The Description of Diblock Copolymers

For the description of the spontaneous micro-phase separation of a scalar order parameter, Brazvskii's Hamiltonian can be applied in its generalized form

$$\mathcal{H}[\psi] = \frac{1}{2} \int_q [\tau + (q - q_0)^2] \psi(\vec{q}) \psi(-\vec{q}) - \int_q h(q) \psi(-q) + \frac{1}{4!} \int_{q_1} \int_{q_2} \int_{q_3} \lambda(\{\vec{q}_i\}) \psi(\vec{q}_1) \psi(\vec{q}_2) \psi(\vec{q}_3) \psi(-\vec{q}_1 - \vec{q}_2 - \vec{q}_3) \quad (2.57)$$

where the abbreviations  $\int_q \equiv \int d^3q / (2\pi)^3$  and  $\{q_i\} \equiv \{q_1, q_2, q_3, -q_1 - q_2 - q_3\}$  have been used.

The generalization in comparison to the original formulation lies in the treatment of  $\lambda$  which is no longer a constant any more and depends on the wave vectors instead. A diblock copolymer melt can be described by the scalar order parameter  $\psi(\vec{r}, t) = \rho_A(\vec{r}, t) - f$  where  $\rho_A(\vec{r}, t)$  is the local volume fraction of type A monomers and  $f$  its volume average, since the melt is assumed to be incompressible and the densities of A and B monomers are hence not independent.  $\psi(\vec{r}, t)$  represents the local composition near  $\vec{r}$  at time  $t$ .<sup>3</sup>  $\psi(\vec{q}, t)$  is the Fourier transform of  $\psi(\vec{r}, t)$ . The conjugate field  $h(\vec{r}, t)$  is a contribution to states with non-zero values of  $\langle \psi(\vec{r}, t) \rangle$  and hence vanishes for symmetric BCP melts which are considered here.

Leibler et al. investigated the Hamiltonian using the random-phase approximation [Lei80]. They were able to show that the Hamiltonian covers the different morphologies known from experiments. Even in the vicinity of the order-disorder transition temperature the theoretical work of Fredrickson and Helfand [FH87] was in quantitative agreement with the micro-phase separation transition in experiments [BF90].

Now a few words to the details of the Hamiltonian. The quadratic term describes the selection of a wave number  $q_0$  for the condensation of the order parameter without preference of any condensation direction. The wave length  $2\pi/q_0$  accounts for the lowest free energy composition fluctuations.  $\tau$  is the reduced temperature in the mean field, which vanishes at the spinodal

$$\tau = \frac{T - T_c^{\text{MF}}}{T_c^{\text{MF}}}. \quad (2.58)$$

Due to symmetry considerations no terms of odd order can occur. So the next order is quartic and provides a stabilizing non-linearity. Mean field theory is not capable of describing the transition since fluctuations of the order parameter diverge as the hypothetical transition temperature  $\tau$  is reached,

$$\langle \psi^2(x) \rangle = \int_q [\tau + (q - q_0)^2]^{-1} \simeq \frac{q_0^2}{2\pi\sqrt{\tau}} \quad (2.59)$$

The assumption of independent Gaussian fluctuations of the condensing order parameter in the entire spherical shell of direction of the condensation leads to its divergence [MM93]. The

<sup>3</sup>In emulsions  $\psi$  represents the volume fraction of solvent "inside" and "outside" the bilayer

9 9 9  
 8 8 8  
 7 7 7  
 6 6 6  
 5 5 5  
 4 4 4  
 3 3 3  
 2 2 2  
 1 1 1  
 0 0 0

stabilizing quartic term is hence essential to describe the transition. Brazovskii showed that the system undergoes a fluctuation induced first order transition as the mean field transition temperature  $\tau$  is approached ( $\tau \rightarrow 0$ ) at a suppressed temperature [Bra75].

### Nematic or Smectic/Lamellar Phase?

Morse and Milner showed by the use of two complementary methods that there is no possibility of a nematic order in a system described by the Brazovskii model [MM93]. They investigated both, the isotropic to smectic transition where they considered the stability of the isotropic phase, and the low temperature smectic phase. In the first case they found a possibility for a transition from the isotropic to the nematic phase at temperatures below the isotropic–smectic transition. In the second case they were able to prove that the smectic phase is stable over the whole range of validity of the parameters in the Brazovskii model and no nematic phase can be found.

#### 2.4.2. Diblock Copolymers under Shear

Based on the description of diblock copolymer systems, which is given in the previous section, Fredrickson [Fre86, Fre94] and Cates and Milner [CM89] investigated the effect of shear flow in symmetric A-B DBCP melts. In the following the dynamics of such a melt is described by two coupled, fluctuating hydrodynamic equations.<sup>4</sup> The concentration field  $\psi(\vec{r}, t)$  is coupled to the continuum field  $\vec{u}(\vec{r}, t)$ , which describes the velocity of the melt.

Fluctuating hydrodynamic equations are similar to those of conventional hydrodynamics except for the fact that a certain stochastic noise term is added to them. This noise term is introduced to mimic the coupling of the hydrodynamic variables to a thermal bath. The noise statistics have to obey a certain fluctuation-dissipation theorem and a quantitative theory is obtained for describing spontaneous fluctuations in the hydrodynamic variables about equilibrium [Fre94].

#### Concentration Dynamics

The concentration equation for the field  $\psi(\vec{r}, t)$  is given by

$$\partial_t \psi = -\vec{u} \cdot \nabla \psi - \mu \frac{\delta \mathcal{H}}{\delta \psi} + \zeta \quad (2.60)$$

where  $\vec{r}$  is the position,  $\vec{u}$  the velocity field and  $\mu$  the Onsager coefficient.  $\zeta$  is a thermal white noise with the first and second momentum given by

$$\langle \zeta(\vec{r}, t) \rangle = 0 \quad \langle \zeta(\vec{r}, t) \zeta(\vec{r}', t') \rangle = 2\mu \delta(\vec{r} - \vec{r}') \delta(t - t') \quad (2.61)$$

<sup>4</sup>This approach can be generalized to any composition of DBCP by introducing the relative length of the A block  $f$

It has the form of a generalized convection-diffusion equation in  $\psi(\vec{r}, t)$  augmented by an appropriate Langevin-type noise source. The steady state distribution of the concentration fluctuations are given by the Boltzmann expression

$$P[\psi] \propto \exp(-\mathcal{H}[\psi]) \quad (2.62)$$

The coarse grained Hamiltonian  $\mathcal{H}$  is taken to be the standard one for the description of diblock-copolymer melts described in the previous section

$$\begin{aligned} \mathcal{H}[\psi] = & \frac{1}{2} \int_q [\tau + (q - q_0)^2] \psi(\vec{q}) \psi(-\vec{q}) \\ & + \frac{1}{4!} \int_{q_1} \int_{q_2} \int_{q_3} \lambda(\{\vec{q}_i\}) \psi(\vec{q}_1) \psi(\vec{q}_2) \psi(\vec{q}_3) \psi(-\vec{q}_1 - \vec{q}_2 - \vec{q}_3) \end{aligned} \quad (2.63)$$

$\tau$  denotes again the reduced temperature which vanishes at the mean field spinodal.  $q_0$  is a wave vector with wave length  $\frac{2\pi}{q_0}$ , which accounts for the lowest free energy composition fluctuation of a diblock copolymer melt. The Onsager coefficient  $\mu$  is for simplicity taken to be constant. In general  $\mu$  is a function of the wave vector  $\vec{q}$  the shear frequency  $\omega$  and possibly of the concentration field in strong inhomogeneous situations. So the theory is limited to the case of low frequency dynamics near the order-disorder transition ( $\omega \rightarrow 0$ ,  $q \rightarrow q_0$ ,  $\psi \rightarrow 0$ ).  $\psi$  is a conserved variable and eq. (2.60) is only appropriate in the case  $q \approx q_0 > 0$ .

### Approximative Hydrodynamics

Eq. (2.60) describes the dynamics of the concentration field  $\psi$ . The local velocity field  $u$  which incorporates the shear is only prescribed at the boundaries of the melt. Since it is locally correlated with  $\psi$ , the model must be completed by the prescription of this local correlation. This is done by a momentum balance equation.

The system is assumed to be locally incompressible and hence

$$\nabla \cdot \vec{u} = 0 \quad (2.64)$$

Assuming slow flows and high copolymer viscosities, the fluid inertia can be neglected, and the momentum balance equation takes the form

$$\nabla_j [\eta(\psi)(\nabla_j u_i + \nabla_i u_j)] - \nabla_i P - \psi \nabla_i \frac{\delta \mathcal{H}}{\delta \psi} = 0 \quad (2.65)$$

where  $\eta$  is the shear viscosity and  $P$  the pressure field. The first expression represents the viscous stress, the second the pressure, and the last the osmotic stress. The osmotic stress is formally the same as in the case of a binary fluid. It produces back-flows that support the lamellar spacing  $2\pi/q_0$ .

With the neglect of inertial terms and random stresses an adiabatic approximation is applied. This approximation implies that the velocity field relaxes instantaneously to a value

9 9 9  
8 8 8  
7 7 7  
6 6 6  
5 5 5  
4 4 4  
3 3 3  
2 2 2  
1 1 1  
0 0 0

9 9 9  
8 8 8  
7 7 7  
6 6 6  
5 5 5  
4 4 4  
3 3 3  
2 2 2  
1 1 1  
0 0 0

consistent with the local concentration field which is supported by the fact that viscosities in DBCP are high. Eq. (2.65) is hence suitable for slow flows, for high shear rates it has to be augmented by a term accounting for the finite relaxation time of the copolymers.

In the following only the first two terms of the Taylor expansion of the shear viscosity  $\eta$  in the concentration field,  $\psi$ , are considered:

$$\eta(\psi) = \eta_0 + \eta_1 \psi(\vec{r}, t) \quad (2.66)$$

The Onsager coefficient,  $\mu$ , is treated as a renormalized phenomenological parameter and the osmotic term in eq. (2.65) is omitted in order to keep the theory as simple as possible [Fre94].  $\eta_0$  is the shear viscosity of the homogeneous melt of mean composition  $f$ , and  $\eta_1$  denotes the first derivative in the composition field.

Omitting the osmotic term in eq. (2.65), Eqs. (2.65) and (2.64) are solved as an expansion to second order in  $(\eta_1/\eta_0)\psi$ , while the externally imposed shear stress is taken to be constant. It turned out to be convenient to separate the velocity field  $\vec{u}$  into two parts:

$$\vec{u}(\vec{r}) = \vec{u}_0(\vec{r}) + \vec{v}(\vec{r}) \quad (2.67)$$

The term  $\vec{v}$  represents the local deviations of  $\vec{u}$  from  $\vec{u}_0$ . The shear flow in zeroth order in  $\epsilon\psi \equiv \eta_1/\eta_0\psi$  is given by

$$\vec{u}_0 = \dot{\gamma} \hat{x} z \quad (2.68)$$

Now, a shear stress  $\sigma_{xz}$  is imposed externally. Then  $\dot{\gamma}$ , the shear rate of the homogeneous system, is given by

$$\dot{\gamma} = \sigma_{xz}/\eta_0 \quad (2.69)$$

Substituting the Fourier transform of  $v(\vec{r})$   $v(\vec{k}) = \int d\vec{r} \exp(i\vec{k}\vec{r})v(\vec{r})$  into eq. (2.65) leads to a nonlinear integral equation for  $v(\vec{k})$ . The pressure term can be eliminated by application of the transverse projection operator

$$T_{ij}(\hat{k}) = \delta_{ij} - \hat{k}_i \hat{k}_j \quad (2.70)$$

where  $\hat{k} = \vec{k}/|k|$  is a unit vector in the direction of  $\vec{k}$ .

The expansion of the resulting integral equation to second order in  $\epsilon\psi \equiv \eta_1/\eta_0\psi$  leads to

$$\begin{aligned} v_i(\vec{k}) = & -\frac{i\epsilon\dot{\gamma}}{k} \psi(\vec{k}) \left[ T_{ix}(\hat{k})\hat{k}_z + T_{iy}(\hat{k})\hat{k}_x \right] \\ & + \frac{i\epsilon^2\dot{\gamma}}{kV} \sum_q \psi(\vec{q})\psi(\vec{k}-\vec{q}) [f_i^{(1)} - f_i^{(2)}] \end{aligned} \quad (2.71)$$

with

$$f_i^{(1)} = (\hat{k} \cdot \hat{q}) T_{ij}(\hat{k}) \left[ T_{ix}(\hat{q})\hat{q}_z + T_{iy}(\hat{q})\hat{q}_x \right] \quad (2.72)$$

$$f_i^{(2)} = \left[ \hat{q}_i - \hat{k}_i (\hat{k} \cdot \hat{q}) \right] \left\{ [\hat{k}_x - \hat{q}_x (\hat{k} \cdot \hat{q})] q_z + [\hat{k}_z - \hat{q}_z (\hat{k} \cdot \hat{q})] q_x \right\} \quad (2.73)$$



The Einstein summation convention is applied over repeated indices.

Eq. (2.71) can now be used to obtain an expression for the Fourier transform of the local velocity gradient tensor  $E_{ij}(\vec{r}) = \nabla_j u_i$  in the melt:

$$\begin{aligned} E_{ij}(\vec{k}) &= \dot{\gamma} \delta_{ix} \delta_{jy} V \delta_{k,0} - i k_j v_i(\vec{k}) \\ &= \dot{\gamma} \delta_{ix} \delta_{jy} V \delta_{k,0} - \epsilon \dot{\gamma} \psi(\vec{k}) \hat{k}_j \left[ T_{ix}(\hat{k}) \hat{k}_z + T_{iy}(\hat{k}) \hat{k}_x \right] \\ &\quad + \epsilon^2 \dot{\gamma} \hat{k}_j \frac{1}{V} \sum_q \psi(\vec{q}) \psi(\vec{k} - \vec{q}) [f_x^{(1)} - f_x^{(2)}] \end{aligned} \quad (2.74)$$

In the following  $E_{ij}$  will be approximated by its volume average. Hence an effective shear rate  $\dot{\gamma}_e$  is introduced:

$$\dot{\gamma}_e = \frac{1}{V} \lim_{k \rightarrow 0} E_{xz}(k) = \dot{\gamma} \left( 1 + \frac{\epsilon^2}{V^2} \lim_{k \rightarrow 0} \sum_q \psi(\vec{q}) \psi(\vec{k} - \vec{q}) \hat{k}_z [f_x^{(1)} - f_x^{(2)}] \right), \quad (2.75)$$

where the identity  $\lim_{k \rightarrow 0} \psi(\vec{k}) = 0$  has been used. Within the current approximation the velocity field is now given by

$$\vec{u}(\vec{r}) = \dot{\gamma}_e \hat{x} y \quad (2.76)$$

$\dot{\gamma}_e$  is an average shear rate which differs from  $\dot{\gamma}$  if  $\epsilon$  and  $\psi$  are both non-zero.

$\dot{\gamma}_e$  and  $\vec{u}$  are both time dependent since the concentration field exhibits stochastic dynamics. Thus, as the concentration field evolves in time, the velocity field responds to it and this in turn influences the further evolution of the concentration field through the convective term in eq. (2.60). Fredrickson et al. treat  $\dot{\gamma}_e$  as a constant in the steady state and employ the preaveraged expression

$$\dot{\gamma}_e = \dot{\gamma} \left( 1 + \frac{\epsilon^2}{V^2} \lim_{k \rightarrow 0} \sum_q \langle \psi(\vec{q}) \psi(\vec{k} - \vec{q}) \rangle \hat{k}_z [f_x^{(1)} - f_x^{(2)}] \right) \quad (2.77)$$

according to the probability distribution functional of  $\psi$ ,  $P[\psi, t]$ .

The coupling between  $\psi$  and  $\vec{u}$  is produced by the gradients in the osmotic stress as well as by the assumption of a composition dependent shear viscosity.

### Fokker–Planck equation and cumulants

The Fokker Planck equation for (2.60) is given by

$$\partial_t P[\psi, t] = \int_k \frac{\delta}{\delta \psi(\vec{k})} \left[ \mu \left( \frac{\delta}{\delta \psi(-\vec{k})} + \frac{\delta \mathcal{H}}{\delta \psi(-\vec{k})} \right) - \dot{\gamma}_e k_x \frac{\delta}{\delta k_z} \psi(\vec{k}) \right] P[\psi, t] \quad (2.78)$$

[CM89, Fre94] This equation cannot be solved exactly because of the quartic term in  $\mathcal{H}[\psi]$  but a variety of techniques are available for an appropriate treatment [Ris89].

9 9 9  
8 8 8  
7 7 7  
6 6 6  
5 5 5  
4 4 4  
3 3 3  
2 2 2  
1 1 1  
0 0 0

9 9 9  
 8 8 8  
 7 7 7  
 6 6 6  
 5 5 5  
 4 4 4  
 3 3 3  
 2 2 2  
 1 1 1  
 0 0 0

Zwanzig introduced a scheme to solve the problem by developing a hierarchy of equations for the cumulant moments of  $P[\psi, t]$ . Equations of motion using  $\partial_t P[\psi, t]$  are then derived for the cumulants. The resulting equations for the first two cumulants, neglecting higher order terms which has been proved to be accurate in equilibrium studies of ODT [FH87, BF90] are given by [Fre94]

$$C(\vec{k}, t) = \langle \psi(\vec{k}, t) \rangle \quad (2.79)$$

$$S(\vec{k}, t) = V^{-1} \left[ \langle \psi(\vec{k}, t) \psi(-\vec{k}, t) \rangle - \langle \psi(\vec{k}, t) \rangle \langle \psi(-\vec{k}, t) \rangle \right] \quad (2.80)$$

The first cumulant (Eq. 2.79) describes the space time evolution of the average (lamellar) composition pattern. Leibler [Lei80] proved that this expression can be approximated near ODT by a single harmonic expression

$$C(\vec{k}, t) = a(t) V (\delta_{\vec{k}, q_0 \hat{n}} + \delta_{-\vec{k}, q_0 \hat{n}}) \quad (2.81)$$

where  $q_0$  is the wave number that characterizes the period of the sinusoidal pattern.  $\hat{n}$  is the unit normal to the lamellae and  $a(t)$  a time dependent amplitude. In general  $\hat{n}$  is free to point towards any direction. In the case of applied shear to the system Onuki et al. and Cates et al. [OK79, CM89] showed, that any lamellar structure with an  $n_x \neq 0$  is not stable and will be rotated and/or dilated. So only layers with  $\hat{n} = (0, n_z, n_z)$  are stable under shear.

The equation of motion for the first cumulant is given by

$$\begin{aligned} \partial_t a = \mu h - \mu \tau a - \frac{1}{2} \mu a^3 \lambda(-q_0 \hat{n}, q_0 \hat{n}, -q_0 \hat{n}, q_0 \hat{n}) \\ - \frac{1}{2} \mu a \int_q \lambda(-q_0 \hat{n}, q_0 \hat{n}, -\vec{q}, \vec{q}) S(\vec{q}, t) \end{aligned} \quad (2.82)$$

Fredrickson introduced here a chemical potential  $h$  which is the thermodynamical conjugate to the Fourier coefficient of  $\psi$  with wave vector  $q_0 \hat{n}$ . This is of use further below and ultimately  $h = 0$ .

The second cumulant describes the statistical evolution of fluctuations about the mean lamellar pattern. Its equation of motion is given by

$$\begin{aligned} \partial_t S(\vec{k}, t) = \dot{\gamma}_e k_x \frac{\partial}{\partial k_z} S(\vec{k}, t) + 2\mu - 2\mu \left( \tau + (k - q_0)^2 + \lambda(-\vec{k}, \vec{k}, -q_0 \hat{n}, q_0 \hat{n}) a^2 \right. \\ \left. + \frac{1}{2} \int_q \lambda(-\vec{k}, \vec{k}, -\vec{q}, \vec{q}) S(\vec{q}, t) \right) S(\vec{k}, t) \end{aligned} \quad (2.83)$$

By the help of the expressions for the equation of motion for the first two cumulants the right hand side of equation (2.77) for the effective shear rate can be evaluated. The result for the case of steady shear (no time dependence) is given by

$$\dot{\gamma}_e = \dot{\gamma} \left( 1 + 2a^2 \epsilon^2 n_z^2 + \epsilon^2 \int_q S(\vec{q}) [\hat{q}_x^2 n_z^2 + \hat{q}_z n_z (\hat{q} \cdot \hat{n}) (1 - 4\hat{q}_x^2)] \right). \quad (2.84)$$

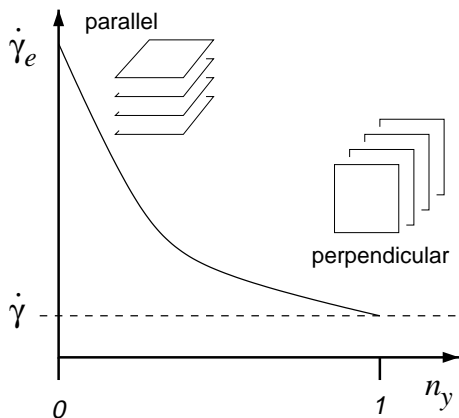


**Figure 2.8.:** Sketch of the functional behavior of the effective shear rate  $\dot{\gamma}_e$ .  $\dot{\gamma}_e$  assumes its largest value for a parallel orientation of the lamellae and reduces to the reference homogeneous system shear rate for perpendicular lamellae.

$\dot{\gamma}_e$  governs the fluctuation dynamics in the weakly ordered lamellar phase through  $S(\vec{k}, t)$  and it depends on the orientation of the lamellae relative to the shear plane.

Figure 2.8 sketches the case of a fixed shear stress  $\sigma_{xz}$ ,

- $\dot{\gamma}_e$  has its largest value for parallel lamellae, where  $\hat{n} = \hat{z}$  and
- $\dot{\gamma}_e$  reduces to the reference homogeneous system shear rate for perpendicular lamellae with  $\hat{n} = \hat{y}$ .

The physical interpretation of this fact is that strata with lower viscosity are permitted to respond to the fixed stress by floating at higher shear rate [Fre94, CM89]. This is a kind of multivalued stress strain relation on a microscopic scale. Figure 2.9 sketches this situation. The enhancement of  $\dot{\gamma}_e$  over  $\dot{\gamma}$  depends on the square of the magnitude of the viscosity

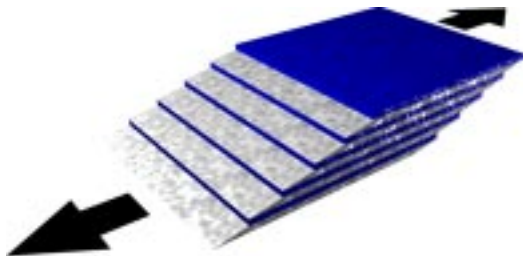


**Figure 2.9.:** Shear on layers with different viscosities. Layers with lower viscosity are permitted to respond to the fixed stress by floating at higher shear rate.

difference between the components,  $\epsilon$ , as well as on the amplitude of the composition pattern  $a$ :

$$\frac{\dot{\gamma}_e - \dot{\gamma}}{\dot{\gamma}} \propto \epsilon^2 a^2. \quad (2.85)$$

The quartic coefficient in eq. (2.84) has a very complicated dependence on the wave vectors  $\vec{k}$  and  $\vec{q}$  and the angle between them [Lei80]. But the fluctuations in  $S(\vec{k}, t)$  are dominant near

9 9 9  
8 8 8  
7 7 7  
6 6 6  
5 5 5  
4 4 4  
3 3 3  
2 2 2  
1 1 1  
0 0 0

9 9 9  
8 8 8  
7 7 7  
6 6 6  
5 5 5  
4 4 4  
3 3 3  
2 2 2  
1 1 1  
0 0 0

the critical shell  $|\vec{k}| = q_0$  which opens the possibility to restrict both,  $\vec{k}$  and  $\vec{q}$  to have magnitudes equal to  $q_0$ , i.e.  $\lambda(-\vec{k}, \vec{k}, -\vec{q}, \vec{q}) \simeq \lambda(-q_0\hat{k}, q_0\hat{k}, -q_0\hat{q}, q_0\hat{q})$ . The angular momentum dependence can be approximated by

$$\lambda(-\vec{k}, \vec{k}, -\vec{q}, \vec{q}) \simeq \lambda[1 - \beta(\hat{q} \cdot \hat{k})^2], \quad (2.86)$$

where  $\lambda$  and  $\beta$  are positive constants that can be determined by fitting these expression to Leibler's numerical calculations of  $\lambda(\{\vec{q}_i\})$  [MM93].

The fact that  $\beta > 0$  and the form of the coupling of  $a$  and  $S$  in equations (2.82) and (2.83) implies that fluctuations with a wave vector near the wave vector of the average pattern,  $q_0\hat{n}$ , are energetically preferred. Such an anisotropic fluctuation spectrum has been observed experimentally on oriented diblock copolymers by the means of neutron scattering [BF90]. In the following  $\lambda$  and  $\beta$  are treated as phenomenological parameters that could be obtained either by microscopic calculations or by fitting to experimental results. Additionally, the angular dependence of  $\lambda$  is weak so that  $\beta \ll 1$  [Lei80].

Hence the simplified equations of motions for the first two cumulants are

$$\partial_t a = \mu h - \mu \tau a - \frac{1}{2} \mu a^3 \lambda (1 - \beta) - \frac{1}{2} \mu \lambda a \int_q [1 - \beta(\hat{n} \cdot \hat{q})^2] S(\vec{q}, t), \quad (2.87)$$

$$\begin{aligned} \partial_t S(\vec{k}, t) &= \dot{\gamma}_e k_x \frac{\partial}{\partial k_z} S(\vec{k}, t) + 2\mu - 2\mu \left( \tau + (k - q_0)^2 + \lambda [1 - \beta(\hat{n} \cdot \hat{k})^2] a^2 \right. \\ &\quad \left. + \frac{1}{2} \lambda \int_q [1 - \beta(\hat{k} \cdot \hat{q})^2] S(\vec{q}, t) \right) S(\vec{k}, t). \end{aligned} \quad (2.88)$$

Now it is suitable to introduce some abbreviations and define derived quantities. Following Cates and Milner [CM89] the first quantity is the fluctuation integral which occurs in both equations of motion

$$\sigma(\hat{k}) \equiv \frac{1}{2} \int_q [1 - \beta(\hat{n} \cdot \hat{q})^2] S(\vec{q}). \quad (2.89)$$

The next expression accumulates the  $\vec{k}$ -dependent and independent terms

$$r - \hat{k} \cdot \mathbf{e} \cdot \hat{k} \equiv \tau + \lambda a^2 [1 - \beta(\hat{n} \cdot \hat{k})^2] + \sigma(\hat{k}). \quad (2.90)$$

$\mathbf{e}$  is a symmetric second rank tensor whose elements can be read of from the right hand side.  $r$  is defined as the sum of the  $\hat{k}$  independent terms:

$$r = \tau + \lambda a^2 + \frac{1}{2} \lambda \int_q S(\vec{q}) \quad (2.91)$$

The equations of motion (2.87) and (2.88) reduce at steady state to

$$h = a(r - \hat{n} \cdot \mathbf{e} \cdot \hat{n}) - \frac{1}{2} \lambda (1 - \beta) a^3, \quad (2.92)$$

$$[r - \hat{k} \cdot \mathbf{e} \cdot \hat{k} + (k - q_0)^2] S(\vec{k}) - \frac{\dot{\gamma}_e}{2\mu} k_x \frac{\partial}{\partial k_z} S(\vec{k}) = 1. \quad (2.93)$$

These equations combined with eq. (2.84) and the abbreviations provide a closed set of equations for the lamellar amplitude  $a$ , the inverse osmotic susceptibility  $r$ , the fluctuation anisotropy  $\mathbf{e}$ , and the fluctuation spectrum (scattering function)  $S(\vec{k})$  under conditions of steady shear flow. Onuki and Kawasaki [OK79] integrated eq. (2.88) by the method of characteristics, yielding

$$S(\vec{k}) = \mu \int_0^\infty \exp\left(-\mu \int_0^t ds \{r - \hat{k}(s) \cdot \mathbf{e} \cdot \hat{k}s + [k(s) - q_0]^2\}\right), \quad (2.94)$$

where  $\vec{k}(s)$  is a wave vector along the following path,

$$k_x(s) \equiv k_x \quad k_y(s) \equiv k_y \quad k_z(s) \equiv k_z + \frac{1}{2}\dot{\gamma}_e s k_x \quad (2.95)$$

### Equilibrium analysis

In equilibrium, i.e., for  $\dot{\gamma} = \dot{\gamma}_e = 0$ , the above treatment reveals similar results as obtained in an earlier work by Fredrickson and Helfand [FH87]. The difference to that work lies in the introduction of an angular dependence of  $\lambda(\{q_i\})$ , but nevertheless for values of  $\beta \ll 1$  both theories are in qualitative and quantitative agreement. It has been shown that the temperature of the order-disorder transition  $\tau_c$  is reduced in comparison to its mean field value due to fluctuations. This classifies the transition to be first order.

The equilibrium structure factor is obtained from eq. (2.93) by neglecting the convective term,

$$S_0(\vec{k}) = [r - \hat{k} \cdot \mathbf{e} \cdot \hat{k} + (k - q_0)^2]^{-1}. \quad (2.96)$$

$S_0(\vec{k})$  can now be substituted into eq. (2.90) and (2.92) which yields coupled algebraic equations for  $r$  and  $\mathbf{e}$ . For small  $r$  (near the equilibrium ODT) and to first order in  $\beta$  those integrals can be performed analytically,

$$e_{ij} = \beta(\lambda a^2 n_i n_j + \frac{1}{3}\alpha\lambda r^{-1/2}\delta_{ij}), \quad (2.97)$$

$$r = \tau + \lambda a^2 + \alpha\lambda r^{-1/2} + \frac{1}{6}\alpha\lambda r^{-3/2}e_{ii}, \quad (2.98)$$

where  $\alpha = q_0^2/(4\pi)$  and  $e_{ii}$  denotes the trace over  $\mathbf{e}$ . Eq. (2.97) directly indicates that  $\mathbf{e}$  is of the order of  $\beta$ . Hence terms incorporating  $\mathbf{e}$  can be neglected as well which leads to the equilibrium expression for the scattering and the susceptibility function [Fre94],

$$S_0(\vec{k}) = [r - (k - q_0)^2]^{-1} \quad (2.99)$$

$$r = \tau + \lambda a^2 + \alpha\lambda r^{-1/3}, \quad (2.100)$$

which are identical to that derived by Fredrickson and Helfand [FH87]. For the determination of  $\tau_r$ , the equilibrium transition temperature, the time dependent equation of state (2.82) can be written as a function of a thermodynamical potential (free energy)  $\Phi(a)$ ,

$$\partial_t a = \mu h - \frac{1}{2}\mu \frac{\partial}{\partial a} \Phi(a). \quad (2.101)$$

9 9 9  
8 8 8  
7 7 7  
6 6 6  
5 5 5  
4 4 4  
3 3 3  
2 2 2  
1 1 1  
0 0 0

9 9 9  
8 8 8  
7 7 7  
6 6 6  
5 5 5  
4 4 4  
3 3 3  
2 2 2  
1 1 1  
0 0 0

This equation can be solved and yield to first order in  $\beta$

$$\Phi(a) = \frac{1}{2\lambda}(r^2 - r_0^2) + \alpha \left(1 - \frac{1}{2}\beta\right) (r^{1/2} - r_0^{1/2}) - \frac{1}{4}\lambda(1 + \beta)a^4 + \frac{1}{2}\beta\tau\alpha(r^{-1/2} - r_0^{-1/2}) + \frac{1}{6}\beta\alpha^2\lambda(r^{-1} - r_0^{-1}), \quad (2.102)$$

where  $r$  is given by eq. (2.97) and eq. (2.98). For an implicit value of  $a$  one obtains the lamellar phase while for  $a = 0$  the corresponding disordered state is given. The ODT can be found by finding the value  $a = a_m$  where  $a_m$  is the value that minimizes  $\phi(a)$ . Fredrickson [Fre94] and Fredrickson and Helfand [FH87] find the transition temperature at

$$\tau_t = -2.0308(\alpha\lambda)^{2/3}, \quad (2.103)$$

with the amplitude

$$a_t = 1.4554\alpha^{1/3}\lambda^{-1/6}. \quad (2.104)$$

Since fluctuations are present, the ODT is suppressed to temperatures below the mean field ODT  $\tau_t = 0$  and the transition is of first order.

### Strong Shear Analysis

Now the behavior of the DBCP model under strong shear conditions is investigated. Strong shear means the asymptotic limit of high shear rates, where  $\dot{\gamma}_e \rightarrow \infty$ . In order to investigate the stability of the lamellar directions under that conditions one has to investigate the structure factor  $S(\vec{k})$  and the fluctuation integral  $\sigma(\hat{k})$ , which then makes the stability of the lamellar pattern in the high shear limit assessable.

First, an approximation for the steady state structure factor eq. (2.94) in this regime is given. This regime is characterized by  $S(\vec{k})$  being independent on  $e_{ij}$  and  $r$  for  $\dot{\gamma}_e \rightarrow \infty$  [CM89, Fre94]. Onuki and Kawasaki [OK79] find for the large  $\dot{\gamma}_e$  behavior of  $S(\vec{k})$  the expression

$$S(\vec{k}) \simeq c_0 \left( \frac{\mu\alpha^{1/2}}{\dot{\gamma}_e |k_x| |k_z|} \right)^{2/3} \quad (2.105)$$

with the constant  $c_0 = 1/3(48\pi)^{1/3}\Gamma(1/3) \approx 4.75304$ . This expression is valid for  $\dot{\gamma} \rightarrow \infty$  and for most  $\hat{k}$  except those one for a narrow region near  $\hat{k}_z = 0$  which proves to be of no consequence in the following [Fre94]. Cates and Milner give an expression that interpolates between the equilibrium structure factor eq. (2.96) and the one for the strong shear limit,

$$S(\vec{k}) \simeq \left( r - \hat{k} \cdot \mathbf{e} \cdot \hat{k} + (k - q_0)^2 + \frac{1}{c_0} \left( \frac{\dot{\gamma}_e |k_x| |k_z|}{\mu\alpha^{1/2}} \right)^{2/3} \right)^{-1}. \quad (2.106)$$

Next the fluctuation integral  $\sigma(\hat{k})$  is considered. For this purpose eq. (2.106) is inserted into eq. (2.89). This yields for large  $\dot{\gamma}_e$  in the leading order (in  $\dot{\gamma}_e$ ) [CM89]

$$\sigma(\hat{k}) = \frac{\sqrt{c_0}}{(2\pi)^{2/3}} (\alpha\lambda)^{2/3} \left( \frac{\dot{\gamma}_e^*}{\dot{\gamma}_e} \right)^{1/3} [I_1 - \beta(I_2\hat{k}_x^2 + I_3\hat{k}_y^2 + I_2\hat{k}_z^2)], \quad (2.107)$$

where a characteristic frequency  $\dot{\gamma}^* \equiv \lambda\mu\alpha^{1/2}$  has been introduced.  $I_1$ ,  $I_2$ , and  $I_3$  are constants given by

$$I_1 \equiv \frac{1}{4\pi} \int d\hat{q} |q_x|^{-1/3} |q_z|^{-1/3} \approx 2.18225, \quad (2.108)$$

$$I_2 \equiv \frac{1}{4\pi} \int d\hat{q} |q_x|^{5/3} |q_z|^{-1/3} \approx 0.219123, \quad (2.109)$$

$$I_3 \equiv \frac{1}{4\pi} \int d\hat{q} |q_x|^{-1/3} |q_y|^2 |q_z|^{-1/3} \approx 0.35249. \quad (2.110)$$

Now the stability of the disordered phase is investigated in the high shear limit. The amplitude of the lamellar pattern is in this phase identically zero,  $a = 0$ . Eq. (2.77) shows that the effective shear rate  $\dot{\gamma}_e$  approaches asymptotically the homogeneous shear rate  $\dot{\gamma}$  for  $\dot{\gamma}_e \rightarrow \infty$ . Eq. (2.96) tells that a divergence in  $S(\vec{k})$  can only occur for  $\hat{k}_x = 0$ . So the stability limit of the disordered phase is reached when fluctuations with wave vectors  $\vec{k}$  oriented in the  $y$ - $z$  plane with wave length  $2\pi/q_0$  occur. The spinodal corresponds to the condition  $r - \hat{k} \cdot \mathbf{e} \cdot \hat{k} = 0$ , so the reduced temperature can be evaluated by inserting eq. (2.107) into eq. (2.90):

$$\tau_S(\hat{k}) = -0.93774(\alpha\lambda)^{2/3} (D^*/D)^{1/3} [I_1 - \beta(I_3\hat{k}_y^2 + I_2\hat{k}_z^2)]. \quad (2.111)$$

Since  $I_2 < I_3$ , it follows that the first spinodal instability occurs for  $\hat{k}$  oriented along the  $y$ -direction, which means that the lamellae are oriented perpendicular to the shear flow [Fre94]. This prediction is in correspondence with the conjecture by Cates and Milner [CM89] that fluctuations near  $\hat{k}_z = 1$  should be unstable.

In order to describe the sequence of dynamical transitions that occur as a homogeneous DBCP melt is cooled while subjected to strong steady shear, an expression for the potential  $\Phi$  (eq. (2.102)) is required. Pattern with  $n_x = 0$  are stable under steady shear. The equation of motion (2.87) can hence be written in its potential form of (2.82) regardless of the shear rate,

$$\partial_t a = \mu h - \frac{1}{2}\mu \frac{\partial}{\partial a} \Phi(a) \quad (2.101)$$

In the equilibrium analysis this potential can be identified with a free energy. Now, under steady shear this is no longer correct, but it is nevertheless useful. The construction of eq. (2.101) allows that minima of  $\Phi$  with respect to  $a$  still correspond to permissible steady states of the sheared copolymer melt [Fre94], are taken on given a sufficient time. The equation of state (eq. (2.92) in approximation for high shear rates can be written in the form

$$h = -A(\vec{n})a + B(\vec{n})a^3, \quad (2.112)$$

where

$$A(\vec{n}) = \tau_S(\vec{n}) - \tau \quad (2.113)$$

$$B(\vec{n}) = \frac{1}{2}\lambda(1 - \beta) + \frac{2}{3}\epsilon^2 n_y^2 \tau_S(\vec{n}). \quad (2.114)$$

9 9 9  
8 8 8  
7 7 7  
6 6 6  
5 5 5  
4 4 4  
3 3 3  
2 2 2  
1 1 1  
0 0 0

9 9 9  
8 8 8  
7 7 7  
6 6 6  
5 5 5  
4 4 4  
3 3 3  
2 2 2  
1 1 1  
0 0 0

In these expressions the spinodal term  $\tau_S$  (eq. (2.111)) has been inserted and  $\dot{\gamma}_e$  was replaced by eq. (2.77). The fluctuation integral, which is subdominant at high shear rates, has been neglected [Fre94]. Now,  $\Phi$  can be constructed yielding

$$\Phi(\vec{n}) = \begin{cases} 0 & A(\vec{n}) < 0 \\ -A(\vec{n})^2/(2B(\vec{n})) & A(\vec{n}) \geq 0 \end{cases} \quad (2.115)$$

By aligning  $\vec{n}$  along the corresponding directions, parallel and perpendicular, expressions for  $\Phi_{\text{par}} = \Phi(\hat{z})$  and  $\Phi_{\text{per}} = \Phi(\hat{y})$  can be derived,

$$\Phi_{\text{par}} = -\frac{(\tau - \tau_{sz})^2}{\lambda(1 - \beta) + (4/3)\epsilon^2\tau_{sz}} \quad \text{for } (\tau - \tau_{sz}) \geq 0 \quad (2.116)$$

$$\Phi_{\text{per}} = -\frac{(\tau - \tau_{sy})^2}{\lambda(1 - \beta)} \quad \text{for } (\tau - \tau_{sy}) \geq 0 \quad (2.117)$$

where  $\tau_{sn} = \tau(\hat{n})$  is the reduced temperature of the corresponding direction given by eq. (2.111).

The full path of transitions is shown in fig. 2.10 by a sketch of the behavior of  $\Phi_{\text{par}}$  and  $\Phi_{\text{per}}$ . For temperatures which exceed  $\tau_{sy}$ , the melt is found to be disordered. When  $\tau$  is lowered to  $\tau_{sy}$  the ODT occurs and the system transforms into a lamellar phase with perpendicular alignment of its strata (light gray area). This phase transition is of first order for any given huge but finite value of  $\dot{\gamma}_e$ . In the limit of  $\dot{\gamma} \rightarrow \infty$  the transition is continuous. At a temperature of  $\tau_{sz}$  the stability limit of the parallel aligned phase is reached (dotted line). Since the denominator of  $\Phi_{\text{par}}$  is smaller than the one of  $\Phi_{\text{per}}$ , both functions intersect at a point denoted by  $\tau_p$ . Here the transition from perpendicular alignment to parallel (dark gray area) takes place. The transition temperature  $\tau_p$  can be evaluated from eqs. (2.116) and (2.117),

$$\tau_p = \frac{(\tau_{sy} - \tau_{sz})\lambda(1 - \beta) + (2/3)\tau_{sz}^2\epsilon^2}{(2/3)\tau_{sz}^2\epsilon^2}, \quad (2.118)$$

and it is straightforward to check that  $\tau_p \leq \tau_{sz}$  for any  $\epsilon$  and  $\dot{\gamma} \gg 1$  [Fre94]. For  $\dot{\gamma} \rightarrow \infty$  the transition temperature is dominated by the term  $-\beta\lambda/\epsilon^2$ . This means for the case of blocks with nearly equal viscosity,  $\epsilon \rightarrow 0$ , that the transition temperature drops to very low temperatures. In contrast the perpendicular to parallel transition raises near the parallel stability limit  $\tau_{sz}$  for rheological very different blocks.

### Weak Shear Analysis

Now as the equilibrium properties ( $\dot{\gamma}/\dot{\gamma}^* = 0$ ) and the behavior under high shear ( $\dot{\gamma}/\dot{\gamma}^* \gg 1$ ) are known, the intermediate, low shear regime is faced. Fredrickson et al. found that it suffices to solve equations to second order in  $\dot{\gamma}_e$  [Fre94].

The structure factor eq. (2.93) can be rewritten by the help of the equilibrium formulation eq. (2.96),

$$S(\vec{k}) = S_0(\vec{k}) + \left(\frac{\dot{\gamma}_e}{2\mu}\right) S_0(\vec{k}) k_x \frac{\partial}{\partial k_z} S(\vec{k}). \quad (2.119)$$



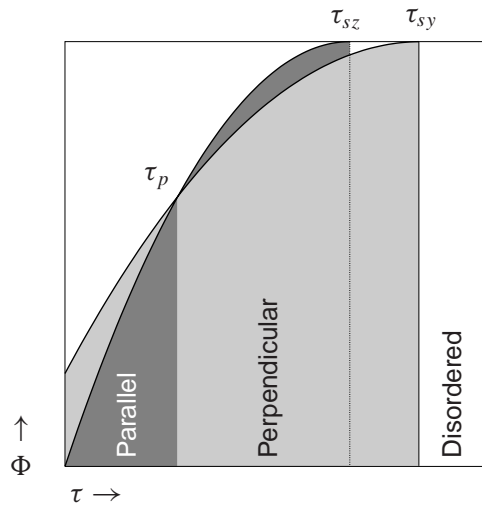


**Figure 2.10.:** Schematic sketch of the potential  $\Phi(\hat{n})$  as a function of the reduced temperature  $\tau$  in the high shear regime  $\dot{\gamma} \rightarrow \infty$ . The curve starting at  $\tau_{sy}$  depicts  $\Phi(\hat{k}_y)$ , the potential for perpendicular orientations. At temperatures above  $\tau_{sy}$  the system is disordered, below it shows perpendicular alignment. The curve starting at point  $\tau_{sz}$ , depicts  $\Phi(\hat{k}_z)$ , the potential for parallel orientation. Both curves  $\Phi(\hat{k}_z)$  and  $\Phi(\hat{k}_y)$  intersect at  $\tau_p$ . At this point the orientation changes from perpendicular at higher temperatures to parallel below. The vertical solid line separates the ordered and disordered states. It account for the stability limit of the perpendicular phase. At the dotted one the stability limit of the parallel state is reached.

Note that  $S_0(\vec{k})$  depends on  $r$  and  $\mathbf{e}$  which themselves contain term of orders of  $\dot{\gamma}_e$ . Iteration of eq. (2.119) and keeping the second order terms in  $\dot{\gamma}_e$  yield

$$S(\vec{k}) \approx S_0(\vec{k}) + \frac{\dot{\gamma}_e}{2\mu} S_0(\vec{k}) k_x \frac{\partial}{\partial k_z} S_0(\vec{k}) + \left(\frac{\dot{\gamma}_e}{2\mu}\right)^2 S_0(\vec{k}) k_x^2 \frac{\partial}{\partial k_z} \left( S_0(\vec{k}) \frac{\partial}{\partial k_z} S_0(\vec{k}) \right). \quad (2.120)$$

All the terms do not contribute to the fluctuation integral  $\sigma(\vec{k})$  can be omitted that:

$$S(\vec{k}) \simeq S_0(\vec{k}) + 2 \left(\frac{\dot{\gamma}_e}{2\mu}\right) S_0^3(\vec{k}) \hat{k}_x T_{zi}(\hat{k}) e_{ij} \hat{k}_j - \left(\frac{\dot{\gamma}_e}{2\mu}\right)^2 S_0^4(\vec{k}) k_x^2 \left\{ 2\hat{k}_z^2 + \left(2\beta\lambda \frac{q^2}{k^2}\right) \left[ r\hat{k}_z n_z (\hat{k} \cdot \vec{n}) - n_z^2 + (\hat{k} \cdot \vec{n})^2 - 4k_z^2 (\hat{k} \cdot \vec{n})^2 \right] \right\}, \quad (2.121)$$

where eq. (2.97) has been used to substitute  $e_{ij}$ . This expression retains all terms of first order in  $\beta$  and of  $\mathcal{O}(\dot{\gamma}_e^2)$ .

The evaluation of the fluctuation integral to the same orders in  $\beta$  and  $\dot{\gamma}_e^2$  can be undertaken using the following partitioning,

$$\sigma(\vec{k}) = \sigma_0(\vec{k}) + \left(\frac{\dot{\gamma}_e}{2\mu}\right) \sigma_1(\vec{k}) + \left(\frac{\dot{\gamma}_e}{2\mu}\right)^2 \sigma_2(\vec{k}) \quad (2.122)$$

9 9 9  
8 8 8  
7 7 7  
6 6 6  
5 5 5  
4 4 4  
3 3 3  
2 2 2  
1 1 1  
0 0 0

9 9 9  
 8 8 8  
 7 7 7  
 6 6 6  
 5 5 5  
 4 4 4  
 3 3 3  
 2 2 2  
 1 1 1  
 0 0 0

where  $\sigma_0(\vec{k})$  can be deduced from the equilibrium result eq. (2.97),

$$\sigma_0(\vec{k}) = \alpha\lambda r^{-1/2} \left[ 1 - \frac{1}{3}\beta \underbrace{\hat{k} \cdot \hat{k}}_{=1} \right] + \frac{1}{6}\alpha\lambda r^{-3/2} e_{ii} \quad (2.123)$$

Fredrickson et al. find that the first order term  $\sigma_1(\vec{k})$  vanishes identically [Fre94]. The derivation of second order term devours a considerable effort [Fre94] The expression completely valid for high molecular weight copolymers is given by

$$\begin{aligned} \sigma(\vec{k}) = & \alpha\lambda r^{-1/2} \left[ 1 - \frac{1}{3}\beta \hat{k} \hat{k} \right] + \frac{1}{6}\alpha\lambda r^{-3/2} e_{ii} - \left( \frac{\dot{\gamma}_e}{2\mu} \right)^2 \lambda \alpha^2 r^{-7/2} \frac{2\pi 5!!}{6!!} \left\{ \frac{1}{15} \right. \\ & \left. - \beta \left( \frac{1}{35}(k_x^2 + k_y^2) + \frac{1}{105}k_z^2 \right) + \frac{7\beta}{2r} \left[ \frac{1}{45}\alpha\lambda r^{-1/2} + \lambda a^2 \left( \frac{1}{35}n_y^2 + \frac{1}{105}n_z^2 \right) \right] \right\} \end{aligned} \quad (2.124)$$

This result can now be used to derive coupled equations for the inverse susceptibility  $r$  and the anisotropy factor  $\mathbf{e}$  in the weak shear limit. Fredrickson et al. [Fre94] find for the inverse susceptibility

$$\begin{aligned} r = & \tau + \lambda a^2 + a\lambda r^{-1/2} + \frac{1}{6}a\lambda r^{-3/2} e_{ii} - \left( \frac{\dot{\gamma}_e}{2\dot{\gamma}^*} \right)^2 \frac{(\lambda\alpha)^3}{r^{7/2}} \\ & \times \frac{2\pi 5!!}{6!!} \left\{ \frac{1}{15} + \frac{7}{2}\beta \left[ \frac{1}{45}\alpha\lambda r^{-3/2} + \frac{\lambda a^2}{r} \left( \frac{1}{35}n_z^2 + \frac{1}{105}n_y^2 \right) \right] \right\}. \end{aligned} \quad (2.125)$$

and for the anisotropy

$$e_{ij} = \beta(\lambda a^2 n_i n_j + \frac{1}{3}\alpha\lambda r^{-1/2} \delta_{ij}) - \left( \frac{\dot{\gamma}_e}{2\dot{\gamma}^*} \right)^2 \frac{2\pi 5!!}{6!!} \left( \frac{1}{35}(\delta_{ix}\delta_{jx} + \delta_{iz}\delta_{jz}) + \frac{1}{105}\delta_{iy}\delta_{jy} \right) \quad (2.126)$$

where again the characteristic shear rate  $\dot{\gamma}^* = \lambda\mu\alpha^{1/2}$  has been used. It is apparent from those equations that the fluctuation terms are smallest for the parallel orientation. That means that one has to expect parallel aligned lamellae at and below the ODT for weak shear.

### 2.4.3. A Limitation of the Theory

The coupling between the shear field and the concentration gradient is described in equation (2.61) by the term  $-\vec{u} \cdot \nabla \Psi$ . The shear field has the form  $\vec{u}_0 = \dot{\gamma} \hat{x} z$  (equation 2.68) and hence it does not exhibit any other components than one into  $x$ -direction. Parallel and perpendicular aligned layers have a concentration gradient direction perpendicular to the  $x$ -direction. This means that those orientations and any inbetween couple to the shear field only by fluctuations and are thus hardly influenced by shear in the scope of that theory.

So it is only possible for the theory to describe perpendicular and parallel oriented lamellae as a result of an alignment process from other orientations. A transition from parallel to perpendicular and vice versa can hardly be described satisfying. A second coupling of some orientation variable other than the concentration gradient seem to be necessary to fully describe the reordering.

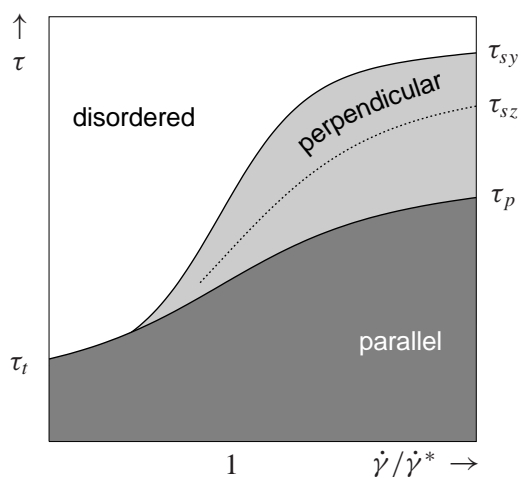


**Figure 2.11.:** Schematic phase diagram of the  $\tau$ - $\dot{\gamma}/\dot{\gamma}^*$ -plane. In the weak shear limit only a disorder-parallel transition is present at the transition temperature  $\tau_t(\dot{\gamma}/\dot{\gamma}^*)$  while in the strong shear limit an area of perpendicular orientation can be found below  $\tau_{sy}(\dot{\gamma}/\dot{\gamma}^*)$ . The dotted line at  $\tau_{sz}(\dot{\gamma}/\dot{\gamma}^*)$  represents the stability limit of the parallel oriented phase in the strong shear limit. In this regime a further transition from perpendicular to parallel can be found at  $\tau_p$ .

9 9 9

8 8 8

7 7 7

6 6 6

5 **5** 5

4 4 4

3 3 3

2 2 2

1 1 1

0 0 **0**

## 3. The Simulation Methods

### 3.1. Molecular Dynamics

*Molecular Dynamics* (MD) is a method of simulating equilibrium and transport properties of classical many particle systems. Classical in this sense means that all particles interact in the limits of classical mechanics. In a MD simulation Newton's equations of motion

$$m_i \frac{d^2}{dt^2} \vec{r}_i = \sum_{j, i \neq j} F_{ij} = -\nabla \sum_{j, i \neq j} U_{ij} \quad (3.1)$$

are solved for each single particle.  $m_i$  is mass of particle  $i$ . The potential  $U_{ij}$  denotes the sum of all two body interactions of particles  $i$  and  $j$ . Three and more body interactions are neglected here. Eq. (3.1) represents either  $3N$  second order linear differential equations (LDE) or  $6N$  first order, where  $N$  denotes the number of particles in the system. The set of first order LDE is given by

$$\frac{d}{dt} \vec{p}_i = \sum_{j, i \neq j} F_{ij} \quad (3.2)$$

$$\frac{d}{dt} \vec{r}_i = \vec{p}_i \quad (3.3)$$

That set is now solved (integrated) numerically. Numerical integration has to retain the essential physics of the system as time-reversibility and conservation of linear and angular momentum. Depending on the system ensemble, thermodynamic variables like kinetic energy or temperature have also to be kept constant. There is a huge variety of symplectic integrators which fulfill that task. They are very stable and allow are large time step. A convenient choice for an integrator is the famous velocity Verlet integrator in its lowest order scheme which is broadly applied [AT87].

This section now proceeds as follows. First the *velocity Verlet* integrator is introduced and the updating scheme for an constant energy ensemble is developed. Then it is shown how a standard MD simulation is coupled to a heat bath via the Langevin thermostat method to establish a constant temperature ensemble.

9 9 9  
 8 8 8  
 7 7 7  
 6 6 6  
 5 5 5  
 4 4 4  
 3 3 3  
 2 2 2  
 1 1 1  
 0 0 0

### 3.1.1. The Integrator

As stated above, an integrator is needed, which incorporates certain features as time-reversibility and momentum conservation. Among those features are:

- **speed**, which is a nice feature to have but not really important since most of the time is spent within the force calculation loop.
- **accuracy for large time steps**, which certainly is more important, since longer time steps mean fewer evaluations of the interactions. This often goes along with an increase in the memory need due to the storage of higher derivatives.
- **low memory need**, since the simulation of large system sizes is only possible if all available memory in the targeted machine can be used efficiently. This might reduce the maximum time step.
- **energy conservation** is definitely an important criterion. One might distinguish between two kinds of conservation, short time and long time. Sophisticated higher order schemes often have an excellent energy conservation for short times while they exhibit an undesirable long term drift. Verlet style algorithms show only a fairly good short time behavior but a little long term drift [FS96].
- **time reversibility** is an important feature likewise. True Hamiltonian dynamics leaves the magnitude of any volume element in phase space unchanged, but many numerical schemes, in particular those that are not time reversible, do not reproduce this area-preserving property [FS96]. Therefore time non-reversible algorithms are not energy conserving at least in the long term limit. Reversible algorithms will conserve the volume in phase space. This is compatible with long term energy conservation.

The Verlet integrator incorporates most of the above features.

- It is really fast but as mentioned this does not really matter.
- It requires as little memory as possible which allows in principle the simulation of large systems.
- It is not very accurate for large time step which requires more frequent updates of the interactions.
- It exhibits a little long term drift.
- It is time reversible and area conserving.

Although the Verlet algorithm does not conserve the total energy exactly, strong evidence indicates that it does conserve a pseudo-Hamiltonian approaching the true Hamiltonian in the limit of infinite short time-steps [FS96].

Tuckerman, Berne, and Martyna [TBM92] showed how to systematically derive an time reversible, area preserving MD algorithm from the Liouville formulation of classical mechanics. Such a derivation for the Verlet algorithm is reviewed in the following.

Considering a set of  $N$  particles with positions  $\vec{r}_i$ , mass  $m_i$  and momenta  $\vec{p}_i$  the Liouville Operator is given by

$$i\mathbf{L} = \sum_i \left( \frac{\vec{p}_i}{m_i} \frac{\partial}{\partial \vec{r}_i} + \vec{F}_i \frac{\partial}{\partial \vec{p}_i} \right) \quad (3.4)$$

The time development of an arbitrary observable  $A(t) = A(\{\vec{r}_i(t)\}, \{\vec{p}_i(t)\})$  can be expressed by

$$\frac{d}{dt} A = i\mathbf{L} A \quad (3.5)$$

$$\Leftrightarrow A(t) = e^{i\mathbf{L}t} A(0) \quad (3.6)$$

$\{\vec{r}_i(t)\}$  and  $\{\vec{p}_i(t)\}$  denote the dependency on the whole ensemble of particles. The right hand side of eq. (3.6) can in principle only be solved by the exact integration of the equations of motion. The operator  $\mathbf{L}$  itself incorporates a sum of non-commuting operators so a factorization of  $\mathbf{L}$  has to be done in an appropriate way. Using the Trotter identity one can split  $\mathbf{L}$  into

$$e^{i\mathbf{L}t} = \lim_{s \rightarrow \infty} \left( e^{i\mathbf{L}_p t/2} e^{i\mathbf{L}_r t} e^{i\mathbf{L}_p t/2} \right)^s \quad (3.7)$$

where  $\mathbf{L}_p$  denotes the momentum and  $\mathbf{L}_r$  the coordinate part of  $\mathbf{L}$ :

$$i\mathbf{L}_p = \sum_i F_i \frac{\partial}{\partial \vec{p}_i} \quad i\mathbf{L}_r = \sum_i \frac{\vec{p}_i}{m_i} \frac{\partial}{\partial \vec{r}_i} \quad (3.8)$$

For a small discrete time step  $\Delta t$  eq. (3.7) can be rewritten as

$$e^{i\mathbf{L}\Delta t} = e^{i\mathbf{L}_p \Delta t/2} e^{i\mathbf{L}_r \Delta t} e^{i\mathbf{L}_p \Delta t/2} + \mathcal{O}(\Delta t^4) \quad (3.9)$$

Applying  $e^{i\mathbf{L}_p t/2}$  to the observable  $A$  leads to

$$e^{i\mathbf{L}_p \Delta t/2} A \left( \begin{array}{c} \{\vec{r}_i(t)\} \\ \{\vec{p}_i(t)\} \end{array} \right) = A \left( \begin{array}{c} \{\vec{r}_i(t)\} \\ \{\vec{p}_i(t) + \vec{p}_i(t + \Delta t/2)\} \end{array} \right) \quad (3.10)$$

In the next step  $e^{i\mathbf{L}_r t/2}$  is applied to the above

$$e^{i\mathbf{L}_r \Delta t} A \left( \begin{array}{c} \{\vec{r}_i(t)\} \\ \{\vec{p}_i(t) + \vec{p}_i(t + \Delta t/2)\} \end{array} \right) = A \left( \begin{array}{c} \{\vec{r}_i(t) + \vec{r}_i(t + \Delta t)\} \\ \{\vec{p}_i(t) + \vec{p}_i(t + \Delta t/2)\} \end{array} \right), \quad (3.11)$$

and in the final step

$$\begin{aligned} e^{i\mathbf{L}_p \Delta t/2} A \left( \begin{array}{c} \{\vec{r}_i(t) + \vec{r}_i(t + \Delta t)\} \\ \{\vec{p}_i(t) + \vec{p}_i(t + \Delta t/2)\} \end{array} \right) \\ = A \left( \begin{array}{c} \{\vec{r}_i(t) + \vec{r}_i(t + \Delta t)\} \\ \{\vec{p}_i(t) + \vec{p}_i(t + \Delta t/2) + \vec{p}_i(t + \Delta t/2)\} \end{array} \right) \end{aligned} \quad (3.12)$$

9 9 9  
8 8 8  
7 7 7  
6 6 6  
5 **5** 5  
4 4 4  
3 3 **3**  
2 2 2  
1 1 1  
0 0 0

9 9 9  
8 8 8  
7 7 7  
6 6 6  
5 5 5  
4 4 4  
3 3 3  
2 2 2  
1 1 1  
0 0 0

From this factorization one can easily deduce an algorithm which is known as the *velocity Verlet* updating scheme:

$$\vec{r}_i(t + \Delta t) = \vec{r}_i + \Delta t \frac{\vec{p}_i(t)}{m_i} + \frac{(\Delta t)^2}{2m_i} \vec{F}_i(\{\vec{r}_j(t)\}) \quad (3.13)$$

$$\vec{p}_i(t + \Delta t) = \vec{p}_i(t) + \frac{1}{2} \Delta t \left[ \vec{F}_i(\{\vec{r}_j(t)\}) + \vec{F}_i(\{\vec{r}_j(t + \Delta t)\}) \right] \quad (3.14)$$

For the updating of the total momentum one finds

$$\begin{aligned} e^{i\mathbf{L}\Delta t} \sum_i \vec{p}_i(t) &= \sum_i \vec{p}_i(t + \Delta t) \\ &= \sum_i \vec{p}_i(t) + \frac{1}{2} \Delta t \sum_i \left[ \vec{F}_i(\{\vec{r}_j(t)\}) + \vec{F}_i(\{\vec{r}_j(t + \Delta t)\}) \right] \end{aligned} \quad (3.15)$$

And as forces always add up to zero if no external field is applied, the total momentum is exactly conserved.

### 3.1.2. Coupling to a Heat Bath

In a MD simulation the time average of a sufficiently long trajectory is related to a suitable statistical ensemble average. The above updating scheme represents the micro-canonical ensemble but in many cases it is more convenient to use constant temperature instead of constant energy simulation.

Constant temperature thermodynamically can be introduced by coupling a system to a heat bath. There are various method to modify the updating scheme and simulate in the canonical ensemble (see. [AT87, FS96]). The present work follows for the  $NVT$  ensemble the approach by Grest and Kremer [GK86]. In this approach instead of Newton's equation of motion, a set of Langevin equations is solved, which is given by

$$m_i \frac{d^2}{dt^2} \vec{r}_i = \vec{F}(\{\vec{r}_i\}) - \Gamma \vec{r}_i + \vec{\zeta}_i(t) \quad (3.16)$$

with  $\vec{\zeta}_i(t)$  being a  $\delta$ -correlated Gaussian noise source<sup>1</sup> and its first and second moments given by

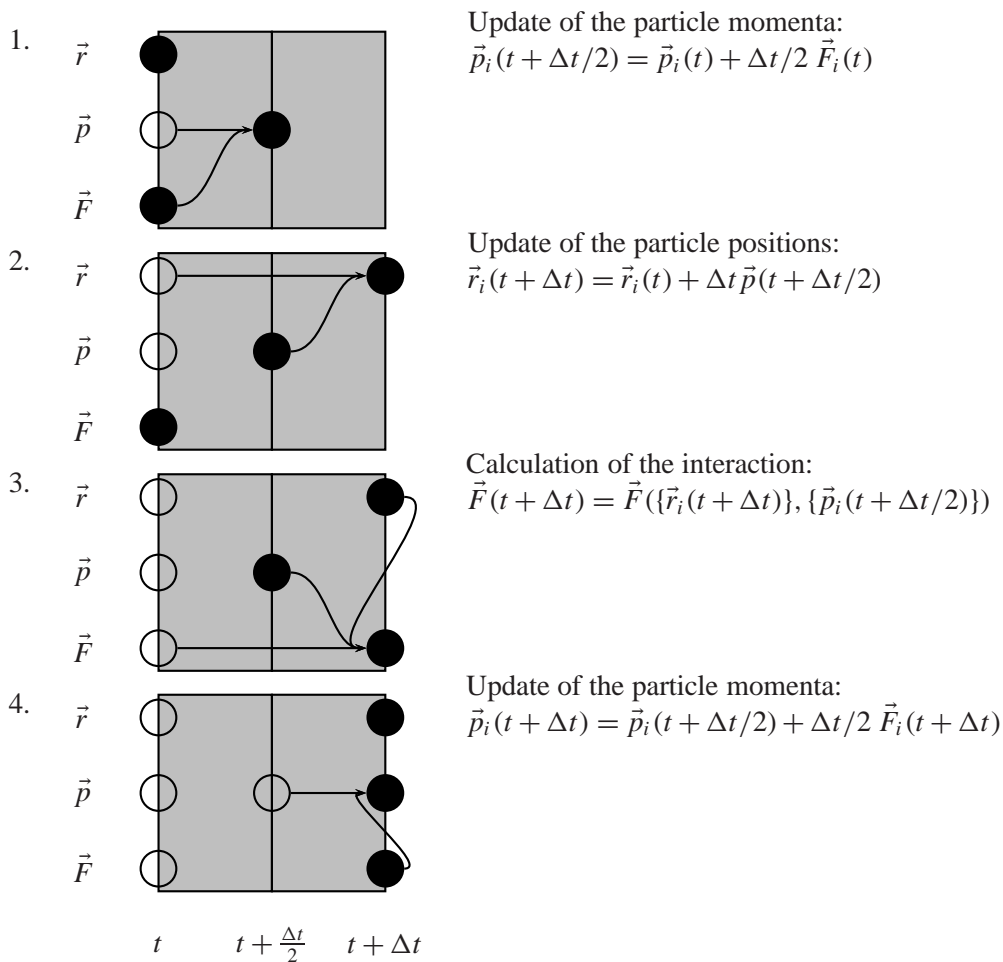
$$\langle \vec{\zeta}_i(t) \rangle = 0 \quad \text{and} \quad \langle \vec{\zeta}_i(t) \vec{\zeta}_i(t') \rangle = 6k_B T \Gamma \delta_{ij} \delta(t - t') \quad (3.17)$$

The balance between the friction force and the stochastic force is governed by the fluctuations-dissipation theorem.

The integration scheme for the evolution of a molecular system simulated with MD in the  $NVT$  ensemble is shown in box 3.1

<sup>1</sup>The noise is not really Gaussian since only the first two moments are given. For a real Gaussian noise higher moments equal zero. Nevertheless the term is commonly used in this context.



**Box 3.1** Velocity Verlet Updating scheme

9 9 9

8 8 8

7 7 7

6 6 6

5 **5 5**

4 4 4

3 3 3

2 2 2

1 1 1

0 0 0

9 9 9  
 8 8 8  
 7 7 7  
 6 6 6  
 5 5 5  
 4 4 4  
 3 3 3  
 2 2 2  
 1 1 1  
 0 0 0

## 3.2. Constant Pressure Molecular Dynamics

Sometimes it is more convenient to use the  $NpT$  ensemble rather than  $NVT$ . This is especially the case when one intends to explore e.g. the fluid–solid phase transition where under constant pressure conditions a jump in the density occurs. A two phase coexistence is hence avoided.

There have been several ways proposed to introduce constant pressure to MD. Quite often the Berendsen thermostat [BPv<sup>+</sup>84] is applied. But this thermostat has the disadvantage that the rescaling of the velocities leads to an iso-kinetic ensemble which does not reproduce the correct behavior at phase transition where large fluctuations are involved.

Another choice is the Anderson method [And80] which produces the correct  $NPH$  ensemble. This method and an extension by Kolb and Dünweg [KD99] which leads to the  $NpT$  ensemble, is presented below. But first the question is answered how to measure the pressure in a system with periodic boundary conditions.

### 3.2.1. The Virial Equation

Clausius virial function is defined as

$$\mathfrak{V}(\vec{r}^N) = \sum_i^N \vec{r}_i \cdot \vec{F}_i \quad (3.18)$$

where  $F_i$  is the total force acting on particle  $i$ . The ensemble average is given by

$$\begin{aligned} \langle \mathfrak{V} \rangle &= \lim_{\tau \rightarrow \infty} \frac{1}{\tau} \int_0^\tau dt \sum_i^N \vec{r}_i \cdot \vec{F}_i \\ &= -3Nk_B T \end{aligned} \quad (3.19)$$

Now the virial function can be separated into two parts: one  $\mathfrak{V}_{int}$ , arises from the forces between particles; the other,  $\mathfrak{V}_{ext}$ , originates from the external forces. Let the particles be confined in a cubic box of length  $L = V^{1/3}$ , the external forces are related in a simple way to the pressure exerted by the walls of area  $S = L^2$ . Their contribution to the virial function is  $\mathfrak{V}_{ext} = -3PSL = -3PV$ . So one can deduce from eq. (3.19)

$$\begin{aligned} PV &= Nk_B T + \frac{1}{3} \langle \mathfrak{V}_{int} \rangle \\ &= Nk_B T + \frac{1}{3} \left\langle \sum_i^N \vec{r}_i(t) \cdot F_N[\vec{r}_i^N(t)] \right\rangle \end{aligned} \quad (3.20)$$

And the well known *virial equation* is obtained

$$\frac{\beta P}{\rho} = 1 + \frac{\beta}{3N} \left\langle \sum_i^N \vec{r}_i(t) \cdot F_N[\vec{r}_i^N(t)] \right\rangle \quad (3.21)$$

where  $\rho$  denotes the number density and  $\beta$  the inverse temperature.

### 3.2.2. Pressure and Molecular Systems

To relate pressure to a molecular system one usually relies on the virial theorem from classical dynamics. The derivation of the virial theorem for a system of  $N$  atoms starts with the quantity

$$I = \frac{1}{2} \sum_i^N m \vec{r}_i \cdot \vec{r}_i \quad (3.22)$$

which is a measure of the shape of the object formed by the  $N$  atoms, the moment of inertia. The second derivative in time gives

$$\frac{d^2 I}{dt^2} = \sum_i^N m \dot{\vec{r}}_i^2 + \sum_i^N \ddot{\vec{r}}_i \cdot \vec{r}_i \quad (3.23)$$

Using Newton's second law on the right hand side and averaging over time gives

$$\left\langle \frac{d^2 I}{dt^2} \right\rangle = m \left\langle \sum_i^N \dot{\vec{r}}_i^2 \right\rangle + \left\langle \sum_i^N \vec{F}_i \cdot \vec{r}_i \right\rangle \quad (3.24)$$

Now in the usual development either external fields or container walls preserve the shape of the  $N$ -particle object (the shape measured by  $I$ ), if not at each instant, then at least on a time average. That means that the lhs equals zero and the force  $F_i$  on the rhs divides into internal and external terms.

Periodic boundary conditions (PBC) are applied to the simulation systems and there are neither walls nor external forces to preserve  $I$ , and the usual derivation of the virial theorem appears to be problematic. J.M. Haile [Hai92] gives an alternative derivation in which the pressure is interpreted as a momentum flux. His main idea is followed now.

#### Momentum Flux Based Derivation

A cubic region of space is considered, with side  $L$  and Volume  $V = L^3$  occupied by  $N$  particles. In molecular dynamics simulation this is the usual shape of the primary cell. The ensemble of particles is at equilibrium with zero total linear momentum. Now let us consider a virtual planar surface of area  $A = L^2$  inserted perpendicular to the x-Axis into the system (see fig. 3.1). The pressure can be defined as the force per unit area acting normal to the surface,

$$P_x = \frac{F_x}{A} = \frac{1}{A} \frac{d(mv_x)}{dt} \quad (3.25)$$

Thus the pressure can be interpreted as a momentum flux through a unit area of the surface in unit time. In general, this flux is composed of two parts, the momentum carried by the

9 9 9  
8 8 8  
7 7 7  
6 6 6  
5 5 5  
4 4 4  
3 3 3  
2 2 2  
1 1 1  
0 0 0

9 9 9  
8 8 8  
7 7 7  
6 6 6  
5 5 5  
4 4 4  
3 3 3  
2 2 2  
1 1 1  
0 0 0

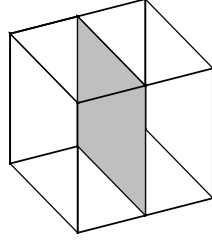


**Figure 3.1.:** Virtual surface inserted perpendicular to the x-axis into the cubic box.

particles  $P_m$  as they cross the surface area during  $dt$ , and the momentum transferred as a result of forces acting between particles that lie on different sides of the surface.

The momentum flux caused by movements of the particles can be described as follows.

$$\begin{aligned}\langle P_{mx} \rangle &\equiv \left\langle \int m v_x v_x \frac{N}{V} f(v_x, t) dv_x \right\rangle \\ &= \frac{Nm}{V} \langle \overline{v_x^2} \rangle\end{aligned}\quad (3.26)$$

Repeating the procedure for the y- and z- direction, as well, the total convective contribution to the pressure can be formed and the ideal-gas law thereby obtained,

$$\langle P_m \rangle = \frac{2N}{3V} [\langle E_{kx} \rangle + \langle E_{ky} \rangle + \langle E_{kz} \rangle] = \frac{2N}{3V} \langle E_k \rangle \quad (3.27)$$

Now the momentum flux is considered, caused by intermolecular forces. Let  $P_{fx}$  be the total force per unit area acting normal to the surface  $A$  where the forces are caused by particles on one side interacting with particles on the other one. The forces are pairwise additive and  $P_{fx}$  can then be written

$$P_{fx} = \frac{1}{A} \sum'_i \sum''_j F_{ij,x} \quad (3.28)$$

The first sum runs over all particles on the left side of the surface, the second over all particles, which are on the right side. Now an average over all possible location of the virtual surface is made. One obtains

$$\overline{P}_{fx} = \frac{1}{AL} \int_0^L \sum'_i \sum''_j F_{ij,x} dx \quad (3.29)$$

The integral can be approximated by a sum over all particles in the following way. Assuming the particles have been labeled sequentially from 1 to  $N$  as their x-position increases from zero to  $L$ , one can define  $x_{k,k+1} = x_{k+1} - x_k$ . Note, that only interactions of particles contribute to  $\overline{P}_{fx}$  which are on different side of the surface. So one can write

$$\overline{P}_{fx} = \frac{1}{V} \sum_{k=1}^{N-1} \sum_{i=1}^k \sum_{j=k+1}^N F_{ij,x} x_{k,k+1} \quad (3.30)$$

A rearrangement of the above sum leads to

$$\bar{P}_{fx} = \frac{1}{V} \sum_{i=1}^{N-1} \sum_{j=i+1}^N F_{ij,x} \underbrace{\sum_{k=i}^j x_{k,k+1}}_{x_{ij}} \quad (3.31)$$

$$= \frac{1}{V} \sum_{i=1}^{N-1} \sum_{j=i+1}^N F_{ij,x} x_{ij} \quad (3.32)$$

An average over time is taken, which leads to

$$\bar{P}_{fx} = \frac{1}{V} \left\langle \sum_{i=1}^{N-1} \sum_{j=i+1}^N F_{ij,x} x_{ij} \right\rangle \quad (3.33)$$

Repeating the procedure for the other axes leads to analogous expressions for  $\langle \bar{P}_{fy} \rangle$  and  $\langle \bar{P}_{fz} \rangle$ . Altogether one obtains

$$\langle P_f \rangle = \frac{1}{3V} \left\langle \sum_{i<j} \sum \vec{F}_{ij} \cdot \vec{r}_{ij} \right\rangle \quad (3.34)$$

which is the virial. Combining (3.27) and (3.34) gives the complete expression for the pressure,

$$P = \frac{2N}{3V} \langle E_k \rangle + \frac{1}{3V} \left\langle \sum_{i<j} \sum \vec{F}_{ij} \cdot \vec{r}_{ij} \right\rangle \quad (3.35)$$

where  $E_k$  is the kinetic energy per particle. The pressure can also be expressed in its tensor form which is sensible if it is not isotropic:

$$P_{\alpha\beta} = \frac{2N}{3V} \langle E_{k,\alpha\beta} \rangle + \frac{1}{3V} \left\langle \sum_{i<j} \sum \vec{F}_{ij,\alpha} \cdot \vec{r}_{ij,\beta} \right\rangle \quad (3.36)$$

where  $E_{k,\alpha\beta} = \sum_i m_i v_{i,\alpha} v_{i,\beta}$ .

### 3.2.3. Constant-Pressure Molecular Dynamics

Andersen [And80] suggested a method for performing MD in the isobaric-isoenthalpic (NPH) ensemble. He presented a scheme for introducing energy fluctuations into MD in order to fix the temperature  $T$  rather than the energy  $E$ . He showed that trajectory averages are equal to the canonical ( $NVT$ ) ensemble averages. He also suggested a way of introducing adiabatic volume fluctuations such that the pressure  $P$  and the enthalpy  $H$  instead of volume  $V$  and energy  $E$  are constant. This latter approach is followed now.

To simulate under constant pressure,  $P$ , the simulation box extension,  $\vec{L}$ , needs to be a variable. Following Anderson's implementation the dynamics of  $\vec{L}$  are specified by Hamiltonian

9 9 9  
8 8 8  
7 7 7  
6 6 6  
5 5 5  
4 4 4  
3 3 3  
2 2 2  
1 1 1  
0 0 0

9 9 9  
8 8 8  
7 7 7  
6 6 6  
5 5 5  
4 4 4  
3 3 3  
2 2 2  
1 1 1  
0 0 0

equations of motion. Therefore a canonical conjugate variable has to be introduced, the piston momentum and its artificial mass. This mass has no direct physical meaning but defines the time scale of the fluctuations. With this approach the box dynamics are subjected to the micro-canonical ensemble. Kolb and Dünweg [KD99] extended this approach. They coupled the box dynamics to a heat bath and so the temperature is retained for the box. By doing this the original Anderson's NPH method is converted into a  $NpT$  method.

### The Andersen Extended System

The method involves the coupling of the system to an external variable, the volume of the simulation box  $V$ . This coupling mimics the action of a piston on real systems. The piston has a 'mass'  $Q$  and is affiliated with a kinetic energy

$$E_{\text{kin}} = \frac{1}{2}Q \left( \frac{dV}{dt} \right)^2. \quad (3.37)$$

The potential energy is then given

$$E_{\text{pot}} = PV \quad (3.38)$$

where  $P$  is the specified pressure of the system.

The coordinates and momenta are related to the system via a dynamical scaling of space and time by an additional variable. Assuming a cubic box, this variable is its length  $L$ :

$$\vec{r}_i = L\vec{s}_i \quad (3.39)$$

For the velocities one obtains

$$\dot{\vec{r}}_i = L\dot{\vec{s}}_i + \dot{L}\vec{s}_i \quad (3.40)$$

The last term is omitted in order to permit independent fluctuations of  $L$  and  $\vec{s}_i$ . The Lagrange function of the system is given by

$$\mathcal{L} = \sum_i L^2 \frac{m_i}{2} \dot{\vec{s}}_i^2 - \sum_{i<j} U_{ij} + \frac{1}{2Q} \Pi_V^2 + PV, \quad (3.41)$$

where  $U_{ij}$  is the interaction potential of particles  $i$  and  $j$ . It is simple to derive the Hamiltonian of the system by a Legendre transformation

$$\mathcal{H} = \sum_i \frac{1}{2L^2 m_i} \vec{\pi}_i^2 + \sum_{i<j} U_{ij} + \frac{1}{2Q} \Pi_V^2 + PV \quad (3.42)$$

where

$$\Pi_V = \frac{\partial \mathcal{L}}{\partial \dot{V}} = Q\dot{V}, \quad \vec{\pi}_i = \frac{\partial \mathcal{L}}{\partial \dot{\vec{s}}_i} = m_i L^2 \dot{\vec{s}}_i, \quad (3.43)$$

are the conjugate momenta. The Hamilton equations of motions

$$\begin{aligned} \dot{\vec{s}}_i &= \frac{1}{L^2 m_i} \vec{\pi}_i & \dot{\vec{\pi}} &= L \vec{f}_i \\ \dot{V} &= \frac{1}{Q} \Pi_V & \dot{\Pi}_V &= \mathcal{P} - P \end{aligned} \quad (3.44)$$

where  $\vec{f}_i$  denotes the force acting on particle  $i$ , and  $\mathcal{P}$  is the ‘‘instantaneous’’ pressure given by

$$\mathcal{P} = \frac{L}{dV} \sum_{i < j} \vec{f}_{ij} \vec{s}_{ij} + \frac{1}{dL^2V} \sum_i \frac{1}{m_i} \vec{\pi}_i^2 \quad (3.45)$$

where  $\vec{f}_{ij}$  is the force between particle  $i$  and  $j$  and  $\vec{s}_{ij} = \vec{s}_i - \vec{s}_j$ .

Kolb and Dünweg [KD99] extended the equations of motion by a stochastic and a dissipative term

$$\dot{\vec{\pi}} = L \left( \vec{f}_i - \frac{\gamma_0}{Lm_i} \vec{\pi}_i + \sqrt{k_B T \gamma_i} \vec{\zeta}_i(t) \right) \quad (3.46)$$

$$\dot{\Pi}_V = \mathcal{P} - P - \frac{\gamma_v}{Q} \Pi_V + \sqrt{k_B T \gamma_V} \zeta_V(t) \quad (3.47)$$

where the first and second moments have been chosen

$$\begin{aligned} \langle \zeta_i^\alpha \rangle &= \langle \zeta_v \rangle = 0 \\ \langle \zeta_i^\alpha \zeta_j^\beta \rangle &= 2\delta_{ij} \delta_{\alpha\beta} \delta(t - t') \\ \langle \zeta_V(t) \zeta_V(t') \rangle &= 2\delta(t - t') \end{aligned} \quad (3.48)$$

and the cross correlation term

$$\langle \zeta_i^\alpha(t) \zeta_V(t') \rangle = 0 \quad (3.49)$$

It can easily be proven that this choice leads to the  $NpT$  ensemble by having a look at the resulting partition function.

Again the Liouville formalism is applied quite similar to the  $NVTMD$  case in order to develop a velocity Verlet type updating scheme. Since the motions of the box and the particles have to be considered independently the Liouville operator splits up in four parts:

$$i\mathbf{L}_1 = -\sum_i L \vec{f}_i \frac{\partial}{\partial \vec{\pi}_i} = -\sum_i \vec{f}_i \frac{\partial}{\partial \vec{p}_i} \quad (3.50)$$

$$i\mathbf{L}_2 = -(\mathcal{P} - P) \frac{\partial}{\partial \Pi_V} \quad (3.51)$$

$$i\mathbf{L}_3 = -\frac{\Pi_V}{Q} \frac{\partial}{\partial V} \quad (3.52)$$

$$i\mathbf{L}_4 = -\sum_i \frac{\vec{\pi}_i}{L^2 m_i} \frac{\partial}{\partial \vec{s}_i} = \sum_i \frac{\vec{p}_i}{m_i} \frac{\partial}{\partial \vec{r}_i} \quad (3.53)$$

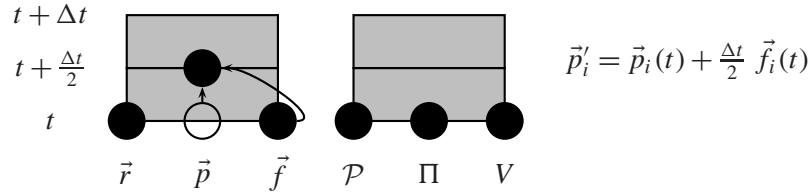
Since usually the conventional variables  $\vec{r}$  and  $\vec{p}$  are used it is convenient to replace  $\vec{s}_i$  and  $\vec{\pi}_i$  according  $\vec{r}_i = L\vec{s}_i$  and  $\vec{p}_i = L^{-1}\vec{\pi}_i$ . The instantaneous pressure is then given by the normal expression equation (3.35).

Updating scheme is given as follows.

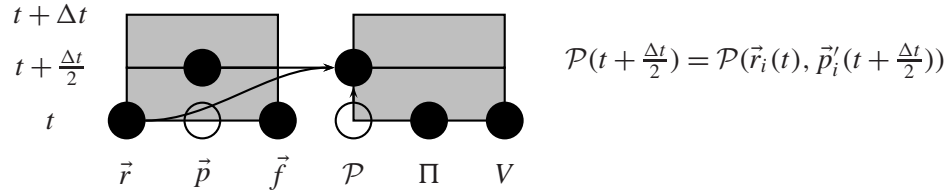
9 9 9  
8 8 8  
7 7 7  
6 6 6  
5 5 5  
4 4 4  
3 3 3  
2 2 2  
1 1 1  
0 0 0

9 9 9  
 8 8 8  
 7 7 7  
 6 **6** 6  
 5 5 5  
 4 4 4  
 3 3 3  
 2 2 **2**  
 1 1 1  
 0 0 0

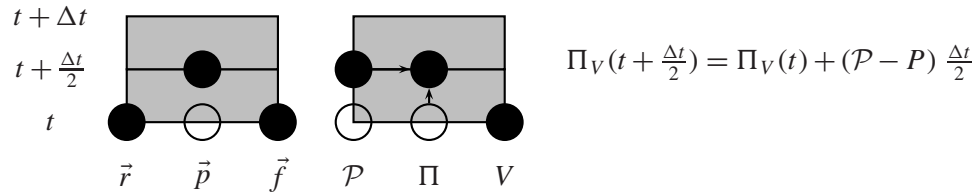
1. Update of the particle momenta:



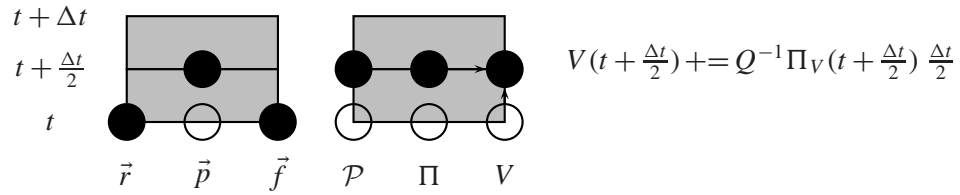
2. Calculation of the internal pressure:



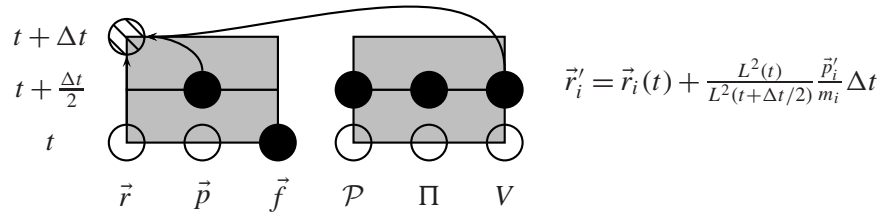
3. Update of the piston momentum:



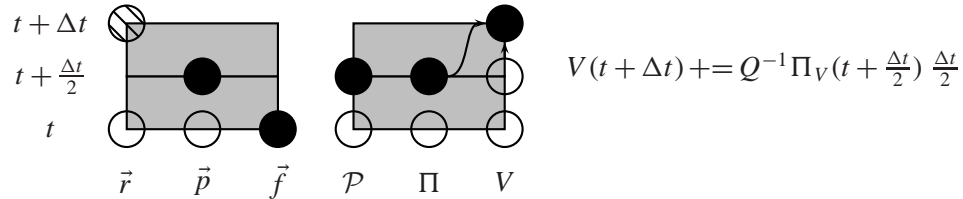
4. Adjustment of the box volume:



5. Update of the particle positions:

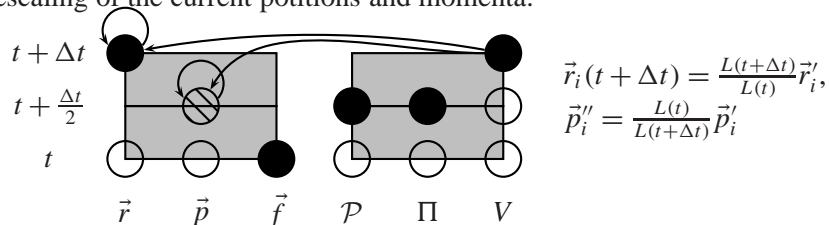


6. Adjustment of the box volume:

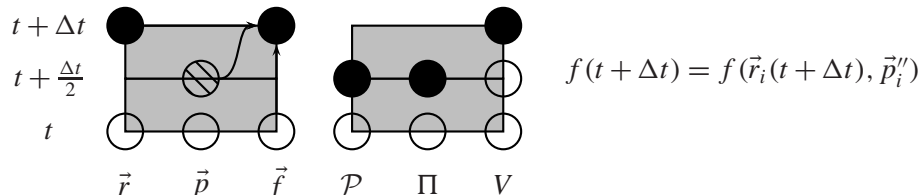




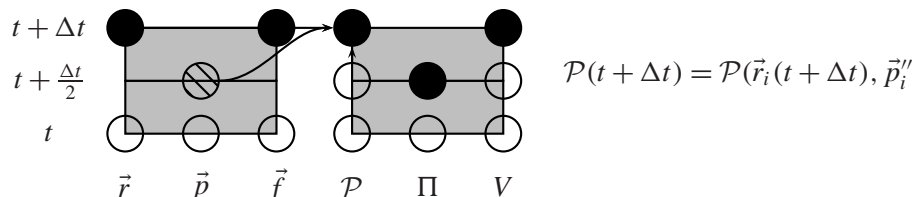
7. Rescaling of the current positions and momenta:



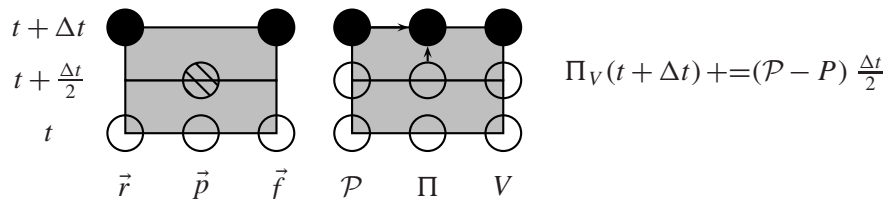
8. Calculation of the new forces:



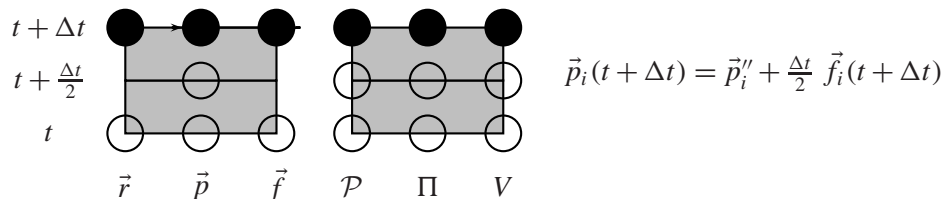
9. Calculation of the internal pressure:



10. Update of the piston momentum:



11. Update of the particle momenta



### 3.2.4. Anisotropic Rescaling of the Box Shape

The given algorithm rescales the box isotropically, and hence its edges conserve the relative dimensions:  $L_\alpha/L_\beta$  are constant for  $\alpha, \beta = \{x, y, z\}$ . In some cases it is favorable and maybe desirable that the box takes on another shape than the initial (e.g. cubic) one.

The problem one encounters is that the layers are often misaligned since the layer spacing is not commensurate with the box dimensions. In order to obtain a perfect aligned layered system, so that the layer normal is parallel to one of the normals to the box face, one usually

9 9 9  
8 8 8  
7 7 7  
6 6 6  
5 5 5  
4 4 4  
3 3 3  
2 2 2  
1 1 1  
0 0 0

9 9 9  
 8 8 8  
 7 7 7  
 6 6 6  
 5 5 5  
 4 4 4  
 3 3 3  
 2 2 2  
 1 1 1  
 0 0 0

has to measure the equilibrium distance of the layers, to set up a layered structure initially, and to equilibrate this system before performing further simulations. This work is concerned with complex fluids, so methods like the one suggested by Parinello and Rahman [PR80], which was developed for solids, is not applicable, since the box may become quite elongated in the absence of restoring forces. Even if the box-like shape of the box is not changed, it may take on quite extraordinary and unphysical shapes. Is there a physical method in order to avoid the system running into those states? Let us develop the equations of motions for a NpT algorithm, which allows the box to change its lengths  $L_x$ ,  $L_y$ , and  $L_z$  independently.

The Hamiltonian equations of motions (3.44) have two expressions which determine the box size,  $\dot{V} = Q^{-1}\Pi_V$  and  $\dot{\Pi}_V = \mathcal{P} - P$ . The instantaneous pressure can be written as the sum of the partial pressures  $\mathcal{P} = (p_x + p_y + p_z)$ , where  $p_\alpha$  are the diagonal components of the pressure tensor (3.36). The derivative of the volume in time has to be rewritten as the derivative of each box dimension

$$\begin{aligned}\dot{V} &= \frac{\partial}{\partial t}(L_x L_y L_z) \\ &= V \left( \frac{\dot{L}_x}{L_x} + \frac{\dot{L}_y}{L_y} + \frac{\dot{L}_z}{L_z} \right)\end{aligned}\quad (3.54)$$

Naturally each box dimension  $L_\alpha$  has its own conjugate momentum  $\Pi_\alpha$ . Assuming  $\Pi_V = \sum_\alpha \Pi_\alpha$ , the momenta are obtained by the comparison of the coefficients in the according Hamiltonian equation of motion

$$\Pi_\alpha = QV \frac{\dot{L}_\alpha}{L_\alpha}\quad (3.55)$$

Their derivative in time is then given by

$$\frac{\partial}{\partial t}\Pi_\alpha = p_\alpha - \frac{1}{3}P\quad (3.56)$$

This treatment allows an independent rescaling of the box dimensions while keeping the box-shape. This does not protect one from obtaining pan cake or elongated rectangular shapes during the course of the simulation. One possibility to avoid this is to stick to constant volume and allow the box to reshape according to it. In some simulations presented below one was only interested in keeping the pressure constant in one or two directions. This opens the opportunity to rescale only this particular direction according to the above rules.

### 3.2.5. Choice of the Parameters

In the harmonic approximation an atom vibrates in the mean field of its surrounding neighbors. Its frequency  $\omega_E$  is called the Einstein frequency. This frequency can be defined via the expansion of the velocity auto correlation function

$$\begin{aligned}\langle \vec{v}_i(t) \cdot \vec{v}_i(0) \rangle &= \langle v_i^2 \rangle - \frac{1}{2} \langle \dot{v}_i^2 \rangle \\ &= \langle v_i^2 \rangle (1 - \frac{1}{2} \omega_E^2 t^2 + \dots)\end{aligned}\quad (3.57)$$

and is given by

$$\omega_E^2 = \frac{1}{3m_i} \langle \nabla_{\vec{r}_i} U \rangle \quad (3.58)$$

where  $\nabla_{\vec{r}_i}$  accounts for the derivatives with respect to the particle positions and  $U$  is the pairwise additive interaction potential. This is exactly the frequency which governs the time-step applied to any MD simulation. A typical rule of thumb state  $\Delta t = (1/50)(2\pi/\omega_E)$ .

The piston oscillates within a constant temperature ensemble if a weak friction and random force is applied. The frequency  $\Omega_E$  of the piston can be estimated quite easily via the isothermic compressibility [KD99],

$$\kappa_T = -\frac{1}{V} \frac{\partial}{\partial p} V = \frac{1}{Vk_B T} (\langle V^2 \rangle - \langle V \rangle^2), \quad (3.59)$$

controls the relation between pressure fluctuations  $\delta\mathcal{P} = \mathcal{P} - p$  and volume fluctuations  $\delta V = V - \langle V \rangle$  via

$$\delta\mathcal{P} = -\frac{1}{\kappa_T V} \delta V \quad (3.60)$$

Using the Hamilton equations of motion (3.44) one obtains a second order differential equation,

$$\frac{d^2}{dt^2} \delta V = -\frac{1}{\kappa_T Q V} \delta V \quad (3.61)$$

which is the equation for a harmonic oscillator with the frequency,

$$\Omega_E^2 = \frac{1}{\kappa_T Q V} \quad (3.62)$$

On the one hand the mass of the piston has to be chosen large enough in order to keep  $\Omega_E \leq \omega_E$ , so that the box oscillation occur on time-scales lower than or equal to atomic oscillations. On the other hand the box should be able to adjust its volume fast enough. So  $\Omega_E$  must not be too small. Kolb and Dünweg suggested an optimum piston mass for the resonance condition  $\Omega_E = \omega_E$  [KD99]. The similar frequencies of the atoms and the box result in a efficient and fast energy transfer between them, and so quickly to a well equilibrated system. Often the piston mass  $Q$  is been chosen larger than that in order to separate the time scales of the box and the molecular system.

Note, that the piston mass scales with the inverse system size.

### 3.3. The Shearing Algorithm

There are several shearing algorithms. Certainly the most often used one is the SLLOD algorithm invented by Evans and Morriss [EM90]. This algorithm is based on the Lees and Edwards boundary conditions methods for applying shear to a system with periodic boundary conditions in equilibrium. The Lees and Edwards method has the main disadvantage that it has a lack of contact with response theory. Evans and Morriss improved this method

9 9 9  
8 8 8  
7 7 7  
6 **6** 6  
5 5 **5**  
4 4 4  
3 3 3  
2 2 2  
1 1 1  
0 0 0

9 9 9  
 8 8 8  
 7 7 7  
 6 6 6  
 5 5 5  
 4 4 4  
 3 3 3  
 2 2 2  
 1 1 1  
 0 0 0

by eliminating many disadvantages and especially that lack of contact with response theory. But from the programmers perspective one main disadvantage remains, the difficulty to apply Lees and Edwards boundary conditions to a parallel program which uses domain decomposition as its parallelization paradigm.

Müller-Plathe (FMP) introduced in 1999 a new algorithm based on momentum transport [MP99]. The idea to this algorithm originates from non-equilibrium molecular dynamics (NEMD) methods for obtaining thermal conductivities and Soret coefficients. Such an algorithm was extended and applied to the easy calculation of shear viscosities.

In the following first the Lees Edwards boundary conditions are briefly reviewed, then the original algorithm by FMP is introduced and the small changes applied to it are described.

### 3.3.1. Lees-Edwards Boundary Conditions

The Lees Edwards boundary conditions modify the periodic boundaries in such a way that the system responds with a planar Couette flow. Figure 3.2 gives an impression of how this algorithm works. The reader may consider the cell denoted as **E** as the basic simulation cell. All other cells are hence its periodic images. The lower left corner of cell **E** may define the origin of the system.

Now shear is applied to the system in the following way. The upper row of image cells **A** to **C** shown in the figure is moving at a constant velocity  $v_x = \dot{\gamma}L$  to the right, the lower row to the left accordingly. Particles moving out of the top of the simulation box have to reenter the box with a rescaled position and velocity at the bottom and vice versa. This movement of particles out of and into the simulation cell induces a linear shear profile which is stable in time. Particles within the simulation box have coordinates  $0 < \{x, y, z\} < L$ . Following the Evans and Morriss [EM90] the laboratory velocity of the particle is given by

$$\vec{v}_i = \vec{c}_i + \vec{u}(\vec{r}_i) \quad (3.63)$$

where  $\vec{c}_i$  denotes the thermal or peculiar velocity of particle  $i$  and  $\vec{u}(\vec{r}_i)$  the coordinate depending streaming velocity. In the situation of simple shear flow in x-direction with a gradient in y-direction the streaming velocity is given by  $\vec{u}(\vec{r}_i) = \gamma y_i \hat{x}$ . At  $t = 0$  the usual periodic replication is applied  $\vec{r}_i = (\vec{r}_i) \bmod L$ . The modulus  $\bmod L$  in this sense stands for the backfolding of the coordinates to the original simulation box with, e.g.

$$x_{\text{folded}} = x_{\text{unfolded}} - \text{anint}(x_{\text{unfolded}}/L) \quad (3.64)$$

for the x-coordinate. The particle  $\vec{r}_i$  has images  $\vec{r}'_i = \vec{r}_i + L \hat{y}$  and  $\vec{r}''_i = \vec{r}_i - L \hat{y}$  in y direction. At time  $t$  when the image cells have moved, their position has changed:

$$\vec{r}_i(t) = \vec{r}_i(0) + \int_0^t ds (\vec{c}_i + \gamma y_i \hat{x}) \quad (3.65)$$

$$\vec{r}'_i(t) = \vec{r}'_i(0) + \int_0^t ds (\vec{c}_i + \gamma y'_i \hat{x}) \quad (3.66)$$

$$\vec{r}''_i(t) = \vec{r}''_i(0) + \int_0^t ds (\vec{c}_i + \gamma y''_i \hat{x}) \quad (3.67)$$

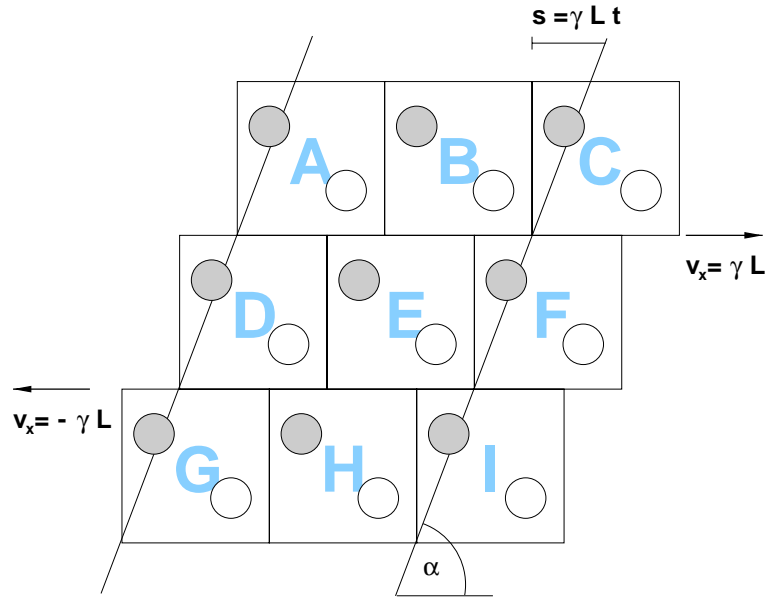


**Figure 3.2.:** Schematic view of Lees Edwards periodic boundary conditions for a planar Couette flow. **E** denotes the simulation cell surrounded by its periodic images **A** to **I**. As shear flow is applied, the images in the upper row are moving with a velocity  $v_x = \dot{\gamma}L$  while the lower is moving into the opposite direction.

By definition the thermal velocities are all equal. Replacing the primed parts by their unprimed equivalents one obtains

$$\vec{r}'_i(t) = \vec{r}_i(0) + L \hat{y} + \gamma L t \hat{x} \quad (3.68)$$

$$\vec{r}''_i(t) = \vec{r}_i(0) + L \hat{y} - \gamma L t \hat{x} \quad (3.69)$$

Now, if  $\vec{r}_i$  moves out of the bottom of the simulation box it is replaced by the image particle at  $\vec{r}'_i$ , if  $\vec{r}_i$  moves out of the top it is replaced by the image particle at  $\vec{r}''_i$ . In the modulus notation

$$\vec{r}_i^{\text{new}} = (\vec{r}'_i) \bmod L = (\vec{r}_i + \gamma L t \hat{x}) \bmod L \quad (3.70)$$

$$\vec{r}_i^{\text{new}} = (\vec{r}''_i) \bmod L = (\vec{r}_i - \gamma L t \hat{x}) \bmod L \quad (3.71)$$

The velocities have to be rescaled, too

$$v_i^{\text{new}} = d/dt r_i^{\text{new}} = \dot{\vec{r}}_i + \gamma L \hat{x} \quad \text{particle moving out of the bottom} \quad (3.72)$$

$$v_i^{\text{new}} = d/dt r_i^{\text{new}} = \dot{\vec{r}}_i - \gamma L \hat{x} \quad \text{particle moving out of the top} \quad (3.73)$$

There are certain difficulties in using this algorithm, since

- shear flow takes time to develop. The time is approximately the traversal time for a sound wave crossing the primitive cell.

9 9 9  
8 8 8  
7 7 7  
6 6 6  
5 5 5  
4 4 4  
3 3 3  
2 2 2  
1 1 1  
0 0 0

9 9 9  
 8 8 8  
 7 7 7  
 6 6 6  
 5 5 5  
 4 4 4  
 3 3 3  
 2 2 2  
 1 1 1  
 0 0 0

- it cannot be used to study time dependent flows.
- it lacks contact with response theory.
- it is very difficult to parallize under the domain decomposition paradigm.

The SLLOD fictitious force method introduced by Evans and Morris [EM90] solves some of these problems. It couples the shear flow to each molecules instead to rely on the modified boundary conditions. By doing this the impose a linear shear profile onto the system which is a disadvantage in the investigation of multivalued stress–strain relations.

Another achievement of the SLLOD method is the application of a suitable thermostating method in order to keep the NVT ensemble. In the following an alternative to the SLLOD algorithm by Müller–Plathe’s [MP99] is described.

### 3.3.2. Physical Details of the FMP Algorithm

As shown in the previous chapters, the shear viscosity is the elastic constant which couples a velocity gradient to a shear stress. For simplicity is is assumed that the velocity gradient tensor  $\nabla_i v_j$  has only one non–zero component  $\nabla_z v_x$ . Then the following momentum flux of momentum in  $z$ –direction,  $j_z(p_x)$  exists, which can be written as

$$j_z(p_x) = -\eta \nabla_z v_x \quad (3.74)$$

A flux like this can always be described as transport through an surface  $A$  perpendicular to its direction within a time interval  $t$ . Given a certain strain rate and therefore a known velocity gradient, the shear viscosity  $\eta$  can be determined, if the flux is known.

The momentum flux is imposed in Müller-Plathe’s algorithm in an unphysical way. The simulation box is subdivided into  $N$  slabs along the shear gradient direction  $z$  with a thickness  $\Delta d$ , as shown in figure 3.3. The middle slab<sup>2</sup> at position  $z = L_z/2$  and the bottom slab at

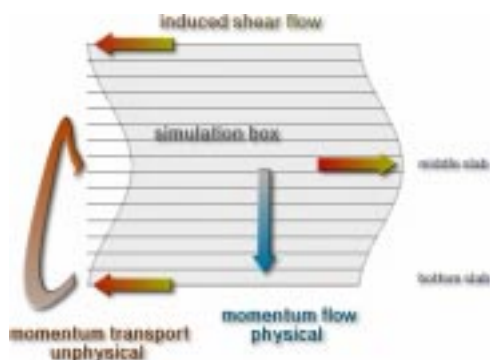


**Figure 3.3.:** Sketch of the shear algorithm. The simulation box is subdivided in  $z$ –direction into slabs of thickness  $d$ . The middle slab and the bottom slab are picked out (see text). The particles moving most against the preferred directions exchange their momenta. The system responds with a back-flow of the exchange momentum which imposes a shear profile.

position  $z = 0$  are picked out. Both slab get a preferred direction of flow, e.g. the middle

<sup>2</sup>It could be the top slab if some special kind of Lees–Edwards boundary conditions are applied.

slab the positive flow direction and the bottom slab the direction reverse to it. In Müller-Plathe's algorithm, one looks now for the particle in each slab, which is moving most against the preferred direction. Once they are found, their momentum components in flow direction are exchanged. Let now  $i$  be the particle in the middle slab, and  $j$  be the particle in the bottom slab. By doing that exchange, a momentum of  $\Delta p_x = p_{i,x} - p_{j,x}$  is transferred from the bottom slab to the middle slab. Those exchanges can take place periodically and the total transferred momentum is the sum of all momentum transfers  $P_z = \sum \Delta p_x$ . The response of the system to this non-equilibrium excitation is now a momentum flux into the opposite direction via a physical mechanism, the friction. In a steady state transport and flux are equal:

$$j_z(p_x) = \frac{P_z}{2L_y L_x t} \quad (3.75)$$

Note that the factor 2 arises because of the periodicity of the given system.

The momentum flux leads to a continuous velocity gradient in the fluid. The mean velocity of each slab is given by the average over the particles belonging to it

$$v_x(n) = \langle v_{x,i} | i \in \text{slab}(n) \rangle \quad (3.76)$$

If the momentum transport rate is not too high, the velocity profile is linear for a sheared fluid. In this case the error for the local strain rate can be easily obtained by linear regression. This error propagate into the measurement of the shear viscosity  $\eta$ . Note that the flux  $j_z(p_x)$  is exactly known. In case the velocity profile is non-linear the efficiency the momentum transfer is not uniform across the system. The system shows a velocity profile as sketched in Figure 3.4 (b).

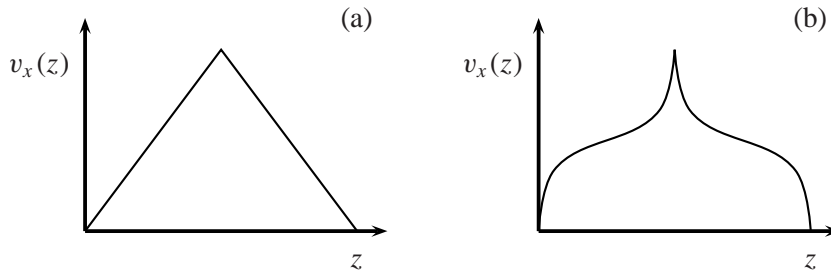


**Figure 3.4.:** Sketch of velocity profiles induced by the momentum transport and backflow in the system. (a) shows a normal linear profile, (b) a non-linear one (see text).

### 3.3.3. Implementary Details

The basic scheme works as follows:

1. Measuring of the mean velocity within the middle and the bottom slab. During this process the  $N$  particles moving most against the preferred direction are found and the moments and particles IDs are stored in a special array, which is finally sorted from lowest to highest value in the moment entry (or vice versa in the bottom slab).

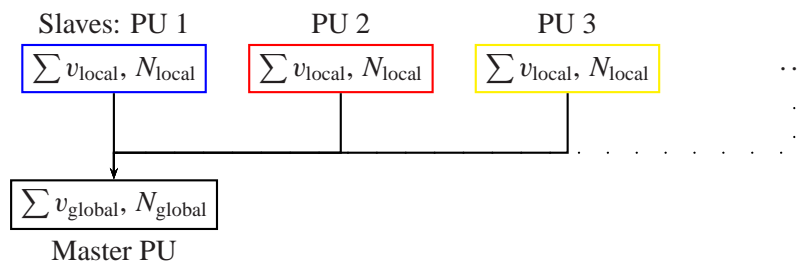
9 9 9  
8 8 8  
7 7 7  
6 6 6  
5 5 5  
4 4 4  
3 3 3  
2 2 2  
1 1 1  
0 0 0

9 9 9  
 8 8 8  
 7 7 7  
 6 6 6  
 5 5 5  
 4 4 4  
 3 3 3  
 2 2 2  
 1 1 1  
 0 0 0

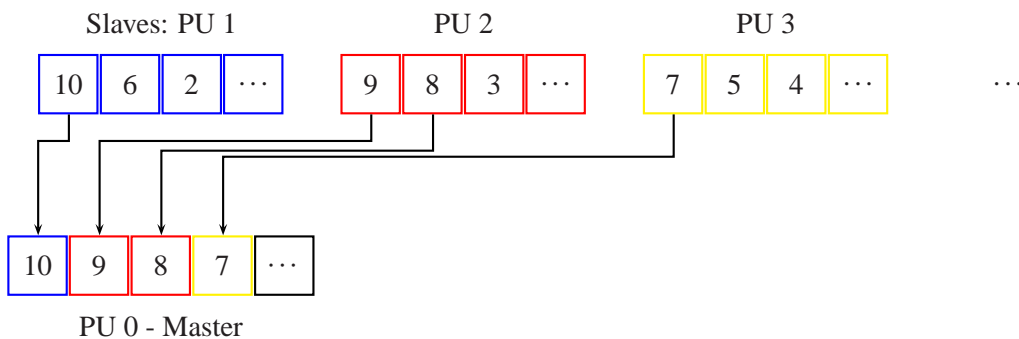
2. The number  $N_{\text{exchange}}$  of moments which have to be exchanged in order to maintain the target shear rate is calculated.
3. The moments of the  $N_{\text{exchange}}$  particles are exchanged.

The above works only for a single-processor environment. For a parallel execution communication between the processors sharing the same slab and the ones containing middle or bottom slab is necessary.

In the following the behavior of the processors dealing with the bottom slab is described. The processors containing the middle slab perform the action analog. The processing units (PU) sharing the bottom slab form a communication group. They have a master PU which handles communication with the master PU of the middle slab PUs. Each PU searches for its local slowest particles. During this procedure all momenta are summed up. This sum plus the number of local particles is reported to the master PU as depicted by the following sketch.

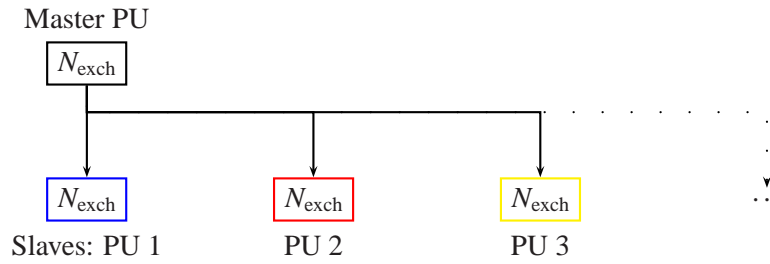


Now the master PU is able to calculate the mean slab velocity. This value is exchanged with the master PU of the middle slab. The PUs of the bottom slab now send their unpreferred momenta to the master PU which sort them and stored the origin of each momentum as well.

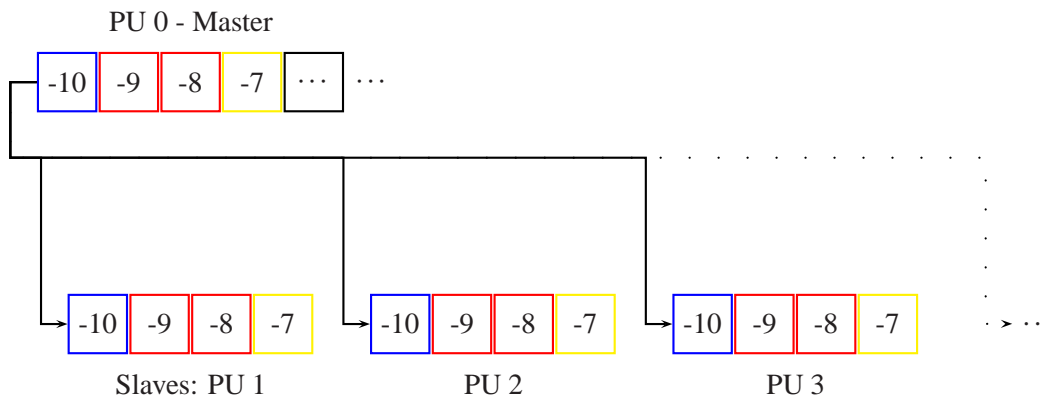




The master PU exchanges this sorted array with the master PU of the middle slab. Then it starts to calculate the number of momenta which have to be exchanged. This number is broadcasted to the communication group.



Now each member of the group receives the sorted array of exchange velocities and the origin information for the old array.



The PUs browse now through the array, look for the occurrence of their own index in the origin field and replace the velocity of the corresponding particle by the new one.

### 3.4. Dissipative Particle Dynamics

Dissipative particle dynamics (DPD) is a quite novel method for the simulation of complex fluid systems such as colloidal or polymeric suspension, immiscible mixtures etc. first introduced by Hoogerbrugge and Koelman [HK92, KH93]. The aim was to develop a method which is highly efficient for the simulations at time-scales where hydrodynamics plays a role but still keeps track of single fluid particles instead of solving continuum equations. DPD simulations deal with soft spheres whose motion is governed by certain collision rules. The

9 9 9  
8 8 8  
7 7 7  
6 6 6  
5 5 5  
4 4 4  
3 3 3  
2 2 2  
1 1 1  
0 0 0

9 9 9  
 8 8 8  
 7 7 7  
 6 6 6  
 5 5 5  
 4 4 4  
 3 3 3  
 2 2 2  
 1 1 1  
 0 0 0

introduction of bead-spring like interaction [SHM95] make the simulation of polymers possible, too.

DPD is essentially based on a molecular dynamics simulation in the NVE ensemble but the force between the particles has, in addition to a conservative part  $F^C$ , a dissipative part represented as a Brownian dash-pot, which enables the simulation of a NVT-like ensemble. That dash-pot damps out the relative approaching velocity and introduces a noise term that keeps the system at constant temperature. In terms of Hoogerbrugger et. al. [HK92, KH93] the damping part of the dash-pot is denoted by  $F^D$  and the stochastic part by  $F^R$ . Español and Warren [EW95] analyzed the relation between both parts. Groot and Warren discussed the physical meaning of that relation and elucidated the negative consequence of what happens if one does not follow the relation [GW97]. Since, the dash-pot acts on the relative approaching velocity, it conserves linear as well as angular momentum.

The construction of the momentum conservation make the thermostat interesting for application in non-equilibrium cases. The Langevin thermostat presented in section 3.1 is profile biased since it assumes that all particles are in equilibrium and are **not** subjected to any shear flow. The DPD-thermostat is by construction biased free. So it is perfectly suitable to be applied in a non-equilibrium molecular dynamics (NEMD) simulation.

In the following it is briefly describe how the basic DPD algorithm works and then how the thermostat is acquired for MD simulation method.

### 3.4.1. The DPD Thermostat

Considering again a set of interacting particles whose time evolution is governed by Newton's equation of motion

$$\frac{d}{dt}\vec{r}_i = \vec{v}_i \quad \frac{d}{dt}\vec{v}_i = \vec{f}_i \quad (3.77)$$

with forces acting pairwise

$$\vec{F}_i = \sum_{j \neq i} \left( \vec{F}_{ij}^C + \vec{F}_{ij}^D + \vec{F}_{ij}^R \right) \quad (3.78)$$

where  $\vec{F}^C$ ,  $\vec{F}^D$ , and  $\vec{F}^R$  denote the conservative, the dissipative, and the random force respectively. For convenience the mass of each particle is put equal to one. The conservative force in the DPD algorithm originates from a soft-core potential and is chosen as [Esp98]

$$\vec{F}_{ij}^C = \begin{cases} a_{ij}(1 - r_{ij}) \cdot \hat{r}_{ij} & r_{ij} < r_c \\ 0 & r_{ij} \geq r_c \end{cases} \quad (3.79)$$

where  $\hat{r}_{ij}$  denotes the unity vector of  $\vec{r}_{ij}$ .  $a_{ij}$  is the maximum repulsion for two particles  $i$  and  $j$ .

The dissipative or drag force in the formulation of Español and Warren [EW95] is given by

$$\vec{F}_{ij}^D = -\gamma w^D(r_{ij})(\hat{r}_{ij} \cdot \vec{w}_{ij})\hat{r}_{ij} \quad (3.80)$$

and the random force by

$$\vec{F}_{ij}^R = \sigma w^R(r_{ij})\theta_{ij}\hat{r}_{ij} \quad (3.81)$$

$w^D$  and  $w^R$  are  $r$ -dependent weight functions vanishing for  $r \geq r_c$ .  $\vec{v}_{ij} = \vec{v}_i - \vec{v}_j$  is the approaching velocity, and  $\theta_{ij}$  a randomly fluctuating variable with Gaussian statistics with its first and second moments

$$\langle \theta_{ij}(t) \rangle = 0 \quad \langle \theta_{ij}(t)\theta_{kl}(t') \rangle = (\delta_{ik}\delta_{jl} + \delta_{il}\delta_{jk})\delta(t - t') \quad (3.82)$$

$\vec{F}^D$  and  $\vec{F}^R$  act along the line of centers and conserve linear and angular momentum. There is an independent random function for each pair of particles. Español and Warren [EW95] showed how these quantities are related. The aim is to derive the Fokker-Planck equation that corresponds to the stochastic differential equations (SDEs) (3.77). The above requirement for the forces in general (Galilean invariance and transformation as a vector under rotations) and the linear dependence of  $\vec{F}^D$  in the momentum and the independence of  $\vec{F}^R$  on the same implies that the Fokker-Planck equation has a drift term linear in the variable and a diffusion term independent of the variable. The resulting Fokker Planck equation takes the form [EW95]

$$\frac{\partial}{\partial t}\rho(\{\vec{r}_i\}, \{\vec{p}_i\}; t) = (\mathbf{L}_C + \mathbf{L}_D)\rho(\{\vec{r}_i\}, \{\vec{p}_i\}; t) \quad (3.83)$$

where  $\rho(\{\vec{r}_i\}, \{\vec{p}_i\}; t)$  is the temporal evolution of the distribution function of the position and momenta of all particles, and with

$$\left. \begin{aligned} \mathbf{L}_C \rho(\{\vec{r}_i\}, \{\vec{p}_i\}; t) &= - \left[ \sum_i \frac{\vec{p}_i}{m} \frac{\partial}{\partial \vec{r}_i} + \sum_i \vec{F}_{ij}^C \frac{\partial}{\partial \vec{p}_i} \right] \rho(\{\vec{r}_i\}, \{\vec{p}_i\}; t) \\ \mathbf{L}_D \rho(\{\vec{r}_i\}, \{\vec{p}_i\}; t) &= \sum_{i,j \neq i} \hat{r}_{ij} \frac{\partial}{\partial \vec{p}_i} \left[ \gamma w_D(r_{ij})(\hat{r}_{ij} \cdot \vec{v}_{ij}) \right. \\ &\quad \left. + \frac{\sigma^2}{2} w_R^2(r_{ij}) \hat{r}_{ij} \left( \frac{\partial}{\partial \vec{p}_i} - \frac{\partial}{\partial \vec{p}_j} \right) \right] \rho(\{\vec{r}_i\}, \{\vec{p}_i\}; t) \end{aligned} \right\} \quad (3.84)$$

The relation between  $w^D$  and  $w^R$  quantities is given by [EW95]

$$w^D(r) = [w^R(r)]^2 \quad (3.85)$$

and that one of them can be chosen arbitrarily. Their usual choice is

$$w^D(r) = [w^R(r)]^2 = \begin{cases} (r_c - r)^2 & r < r_c \\ 0 & r \geq r_c \end{cases} \quad (3.86)$$

Groot and Warren [GW97] propose the following velocity Verlet updating scheme:

1.	$\vec{r}_i(t + \Delta t) = \vec{r}_i(t) + \Delta t \vec{v}_i(t) + 1/2(\Delta t)^2 \vec{f}_i(t)$	9 9 9
		8 8 8
2.	$\vec{v}_i(t + \lambda \Delta t) = \vec{v}_i(t) + \lambda \Delta t \vec{f}_i(t)$	7 7 7
		6 6 6
3.	$\vec{f}_i(t + \Delta t) = \vec{f}_i(\vec{r}_i(t + \Delta t), \vec{v}_i(t + \Delta t))$	5 5 5
		4 4 4
4.	$\vec{v}_i(t + \Delta t) = \vec{v}_i(t) + 1/2\Delta t (\vec{f}_i(t) + \vec{f}_i(t + \Delta t))$	4 4 4
		3 3 3
		2 2 2
		1 1 1
		0 0 0

9 9 9  
 8 8 8  
 7 7 7  
 6 6 6  
 5 5 5  
 4 4 4  
 3 3 3  
 2 2 2  
 1 1 1  
 0 0 0

where  $\lambda$  is a so called fudge factor. The actual velocity Verlet algorithm for conventional MD is represented with  $\lambda = 1/2$ . The DUD-forces (drag force) is velocity dependent which is not consistent with the formulation of the velocity Verlet algorithm. Therefore a prediction for the velocity, denoted by  $\tilde{v}$  is made in step 2. This prediction is corrected afterwards in step 4. Physical measurements of magnitudes only depending on the coordinates differences can be made after step 2 while velocity depending magnitudes like temperature are measured after step 4. The algorithm would be exact to  $\mathcal{O}(\Delta t^2)$  at  $\lambda = 1/2$  if there were no random or dissipative force. The order of the proposed algorithm becomes unclear [GW97]. A false prediction of the velocities would clearly lead to a wrong temperature.

Since in the following simulations the time-step is small due to the use of hard core potentials rather than soft potentials, commonly applied in DPD simulations, the uncertainty in  $\tilde{v}$  is negligible in the sense of the above discussion. Hence the conventional velocity Verlet updating scheme can be applied safely, as tests of the method will show (see below).

### NPT Ensemble and the DPD–Thermostat

The DPD method is developed to work in the NVT ensemble. Sometimes it is more suitable to switch to the NPT ensemble even in a non–equilibrium simulation. Therefore the NPT–ensemble method presented in section 3.2.3 was combined with the DPD thermostat.<sup>3</sup> The updating scheme is identical with that already presented except in one respect. The noise–friction term, which accounts for the standard Langevin thermo–stating, has been removed and a dissipative and random force have been added, in order to couple the particles to the DPD–thermostat.

#### 3.4.2. Implementary Details

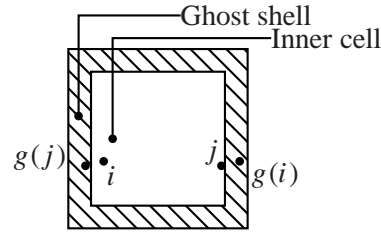
The implementation of the updating scheme is simple. More difficult is to account for the correct calculation of the random–pair forces in a parallel program. The original version of the program uses ghost–particle frames around the complete simulation cell.

The original version of the program [PK98] has a ghost shell or halo frame surrounding the whole particle cell which resides on a processing unit (PU). Particles in the shell, the so–called ghost particles, are the images of particles on neighboring PU which are in interaction distance with the local cell. This ghost shell is also used to establish periodic boundary conditions. As in normal MD all forces are only position depended ghost particles or short ghosts hold only the current positions of their originating particles but not velocities or forces. This concept is sketched in figure 3.5. Following Pütz and Kolb, the forces are for simplicity evaluated twice for each particle–ghost interaction. This was done in order to save the communication overhead created by necessary a necessary force broadcast if the evaluation would only occur once. Memory, which was certainly not the important argument, is saved, too.

---

<sup>3</sup>To the authors knowledge this is the first time that NPT–ensemble simulation with the DPD–method are carried out. It is also conceivable that a standard DPD simulation can be carried out in the NPT–ensemble.

**Figure 3.5.:** 2D simplification of the simulation cell with its surrounding ghost shell. Particles  $i$  and  $j$  are depicted together with their ghosts  $g(i)$  and  $g(j)$ .



In the case of DPD there is an additional communication need for the velocities, since the DPD–forces are velocity dependent. This increases the amount of data transferred. The double evaluation of forces makes it necessary to rethink the concept of applied ghost particles. A double evaluation means in the case of random forces two random number of the same interaction. This does not match with momentum conservation. The solution is a single sided ghost frame which covers all particle interaction exactly once. This decreases the amount of positions and velocities to be broadcasted. The disadvantages are that after the interaction loop all the forces of ghost particles have to be broadcasted back to their original particle and for the correct evaluation of observables depending on velocities it might be necessary to introduce a third communication step for the exchange of the new velocities after the final velocity update in the Verlet updating scheme. Figure 3.6 depicts the new case.

### 3.5. A Comparison between the DPD and Langevin Thermostatting Methods

In the previous sections it has been argued that the Langevin thermostat is not applicable for shear flow simulations in the  $NVT$  ensemble.

In the following a test simulation of a pure Lennard–Jones fluid system containing  $N = 2048$  particles is discussed, which shows an increase of the shear–viscosity  $\eta$  as a function of the friction  $\zeta$ .

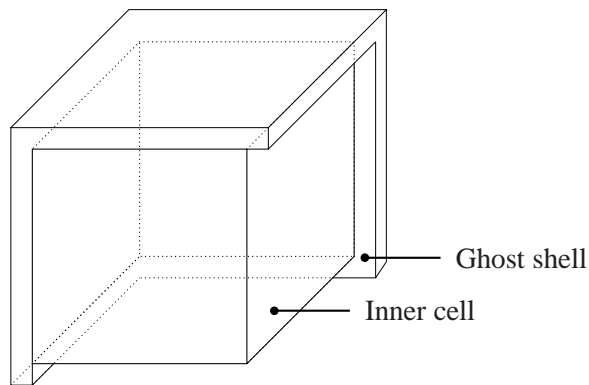
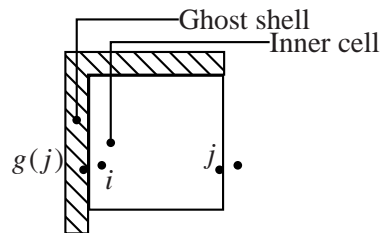
The simulation was carried out in the  $NVT$  ensemble using the FMP shear algorithm. The system has been equilibrated without shear for  $t = 2000^4$ . The friction has been varied in the interval  $0.01 \leq \zeta < 10$ . Then shear with a strain rate of  $\dot{\gamma} = 0.1$  has been switch on and simulation with the different values of the friction have been carried out using first the Langevin thermostat and in a second run the DPD thermostat. Figure 3.7 shows the simulation results. The  $\times$  symbols refer to the classical MD simulation using the Langevin thermostat. With increasing friction, the shear viscosity increases as well in this case. But a close coupling to the heat bath should not exhibit a direct effect on the shear viscosity in this non–equilibrium situation. The simulation with applying the DPD thermostat does not show such that behavior.

<sup>4</sup>Lennard Jones units will be used in this section.

9 9 9  
8 8 8  
7 **7** 7  
6 6 6  
5 5 **5**  
4 4 4  
3 3 3  
2 2 2  
1 1 1  
0 0 0

9 9 9  
 8 8 8  
 7 7 7  
 6 6 6  
 5 5 5  
 4 4 4  
 3 3 3  
 2 2 2  
 1 1 1  
 0 0 0

**Figure 3.6.:** Inner cell and its surrounding half-shell of ghosts particles in a 2D simplification (left). Below a 3D sketch of the ghost halo is shown as it is implemented in the parallel program.



This result is plotted with the  $+$ -symbols and does not show any influence in the observed range of friction.

The friction constants in the case of the Langevin thermostat and DPD thermostat cannot be directly compared, since their influence is by construction different. But nevertheless, the non-linear behavior in the Langevin case even for low values of the friction (values near  $\zeta = 1.0$ ) which are broadly applied in equilibrium situations sounds a note of caution.

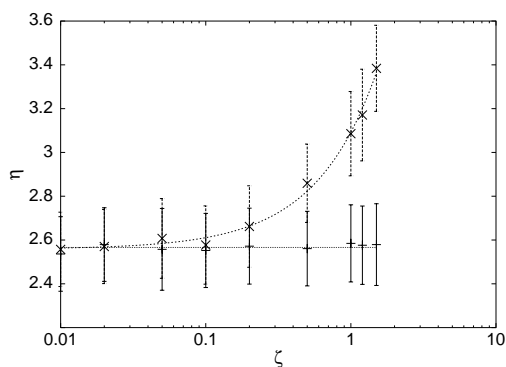


**Figure 3.7.:** Friction dependence of the shear viscosity. The shear viscosity,  $\eta$ , is plotted as a function of the friction constant,  $\zeta$ . The  $\times$ -Symbols refer to a classical MD simulation using the Langevin thermostating method, the  $+$ -Symbols denote the results of the same simulation, except that the DPD thermostat has been applied. The lines serve as a guide for the eye.

## 4. The Simulation Model

### 4.1. Development of the Model

#### 4.1.1. Interactions

The basic ingredients of the model are particles which interact through spherically symmetric potentials. These potentials should be continuous, in order to facilitate a standard Molecular Dynamics procedure like the Verlet algorithm [AT87], and short-ranged, in order to keep the number of force calculations at a minimum. A convenient choice for this is a Lennard–Jones (LJ) potential that is truncated at the minimum, and shifted:

$$U_{LJ} = \begin{cases} 4\epsilon \left[ \left(\frac{\sigma}{r}\right)^{12} - \left(\frac{\sigma}{r}\right)^6 + \frac{1}{4} \right] & r \leq 2^{1/6}\sigma \\ 0 & r \geq 2^{1/6}\sigma \end{cases} \quad (4.1)$$

This potential has found widespread applications for the simulation of bead–spring models for polymers [GK86, KG90]. Here,  $\epsilon$  sets the energy scale and  $\sigma$  the length scale. Henceforth Lennard–Jones units are used where  $\epsilon = \sigma = 1$ . The mass  $m$  of the particles is also set to unity, such that time is measured in units of  $\tau = (\sigma^2 m / \epsilon)^{1/2}$ . A typical dense system is characterized by a particle density of  $\rho = 0.85$ , and temperature  $k_B T = 1$ . This dense repulsive Lennard–Jones fluid will be the reference system from which the model will be constructed. The pair correlation function (PCF)  $g(r)$ , i. e. the normalized density–density correlation function, with  $g(r) \rightarrow 1$  for  $r \rightarrow \infty$ , is shown in Fig. 4.1 for this system (red graph, the reader may disregard the other graphs for a moment).

As a minimal model for amphiphilic molecules, only dimers of different species are considered.

From the polymer simulations it is known that it is computationally efficient to link the dimers via anharmonic FENE (“finitely extensible nonlinear elastic”) springs with spring constant  $k$  and maximum extension  $R_0$ :

$$U_{FENE} = \begin{cases} -\frac{1}{2}kR_0^2 \ln \left[ 1 - \left(\frac{r}{R_0}\right)^2 \right] & r < R_0 \\ \infty & r \geq R_0 \end{cases} . \quad (4.2)$$

While for the polymer simulations usually the values  $k = 30$  and  $R_0 = 1.5$  are applied [GK86], here a somewhat weaker attraction,  $k = 5$ ,  $R_0 = 2$ , is used. The reason is that it

9 9 9  
 8 8 8  
 7 7 7  
 6 6 6  
 5 5 5  
 4 4 4  
 3 3 3  
 2 2 2  
 1 1 1  
 0 0 0

is intended to adjust the typical bond length to the typical interparticle distance in the dense Lennard–Jones fluid, see below. By this match it is ensured that the model will also allow for an ensemble where the connectivity is not fixed, but the bonds are created and deleted between monomers. If the length scales would not fit, attempts of such processes would much too frequently be rejected.

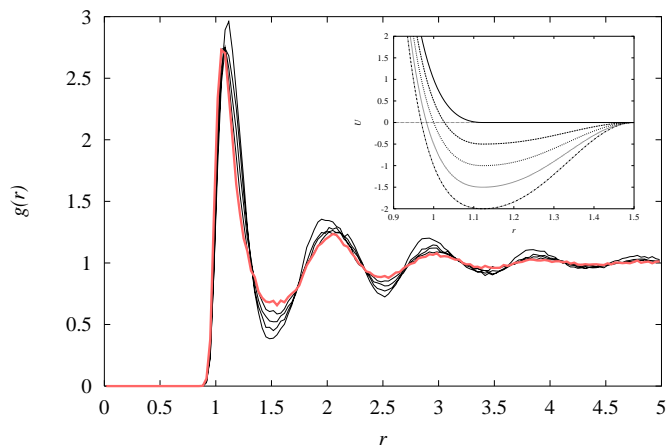


**Figure 4.1.:** Pair correlation functions. The red graph shows the pair correlation function of a pure Lennard–Jones fluid. The others refer to different values of the potential depth  $\phi = 0.0, 0.5, 1.0, 1.5, 2.0$  (see eq. (4.3)). The curve with the largest oscillations refers to  $\phi = 2.0$ . The inset shows the corresponding potentials.

Furthermore, the model needs to include different interactions between A and B particles, in order to distinguish them and drive the tendency towards phase separation. The simplest model has identical interactions for A–A and for B–B contacts, while an A–B contact is more repulsive, or less attractive, and thus unfavorable. Ideally, one would like to do this via repulsive potentials only, for example by increasing the pre-factor in Eq. 4.1 for A–B contacts, the advantage being twofold: Firstly, one would stick to a very short interaction range, and thus to few force calculations, and secondly the system would not exhibit a gas–liquid transition, which is not of interest per se, and would only introduce an unwanted complication into the system. Actually, this approach has been very successful to model the phase separation of polymer blends, and the micro-phase separation of block copolymers [GLKG96]. In that case, however, a very small difference in the interaction is already sufficient to drive the phase transition, as the polymerization strongly reduces the translational entropy, resulting in  $T_c \propto N$ , where  $T_c$  is the critical temperature, and  $N$  the degree of polymerization. Conversely, a low–molecular weight system would need a quite strong repulsion between A and B in order to access phase separation. Note that it is computationally more efficient to vary the interaction strength to drive the phase transition, rather than the temperature — the potentials are optimized such that the Molecular Dynamics, with its interplay between potential energy and kinetic energy, runs best for  $k_B T = 1$ . Tests have then shown that actually such a strong repulsion is needed that a very small time step is necessary, which again is inefficient.



For this reason, it has been resorted to the second choice, and included an attractive tail between the A–A pairs and the B–B pairs, while the A–B contacts are just subject to the purely repulsive Lennard–Jones potential.

For the choice of the attractive tail, the following considerations are important:

1. In the general spirit of a minimal model, the presence of several molecular length scales, which might lead to competition, frustration, etc., should be avoided. So the typical interparticle distance is chosen to be the same for A–A, B–B, and A–B bonds. In other words: The additional attractive tail should not substantially distort the pair correlation function  $g(r)$  of the original repulsive Lennard–Jones fluid, at least with respect to the positions of the maxima and minima. Guided by the same idea, we had already adjusted the parameters of the bond potential, Eq. 4.2.
2. The tail should be rather short–ranged, for reasons of efficiency.
3. In order to avoid instabilities in Molecular Dynamics simulations, the potential should be continuous, and have continuous first derivatives.

For these reasons, the potential should remain unchanged for  $0 < r < 2^{1/6}$ , while the attractive tail should reach from  $r = 2^{1/6}$  to the first minimum of  $g(r)$  (which occurs roughly at  $r = 1.5$ , as seen from Fig. 4.1), such that only the first neighbor shell is included in the interaction. Such a potential will then of course allow for a gas–liquid transition, and, even more importantly, favor crystallization into an fcc structure, since any frustration effects between length scales have been deliberately avoided. These issues will be considered in the next section in more detail. The tail should thus have zero derivative at  $r = 2^{1/6}$  and at  $r = 1.5$ , while it should have the values zero at  $r = 1.5$ , and  $-\phi$  at  $r = 2^{1/6}$ , where  $\phi$  is the depth of the attractive part, and is used by us as the independent parameter by which the system is driven into the ordered phase. Using a shifted cosine wave in  $r^2$ , one thus obtains

$$U_{LJcos} = \begin{cases} 4 \left[ \left( \frac{1}{r} \right)^{12} - \left( \frac{1}{r} \right)^6 + \frac{1}{4} \right] - \phi & r \leq 2^{1/6} \\ \frac{1}{2} \phi [\cos(\alpha r^2 + \beta) - 1] & 2^{1/6} \leq r \leq 1.5 \\ 0 & r \geq 1.5 \end{cases}, \quad (4.3)$$

where  $\alpha$  and  $\beta$  are determined as the solutions of the linear set of equations

$$2^{1/3} \alpha + \beta = \pi \quad (4.4)$$

$$2.25 \alpha + \beta = 2\pi, \quad (4.5)$$

i. e.  $\alpha = 3.1730728678$  and  $\beta = -0.85622864544$ .

As an alternative, a third–order polynomial in  $r^2$  was also considered,

$$U_p/\phi = A + r^2(B + r^2(C + r^2D)), \quad (4.6)$$

9 9 9  
8 8 8  
7 7 7  
6 6 6  
5 5 5  
4 4 4  
3 3 3  
2 2 2  
1 1 1  
0 0 0

9 9 9  
 8 8 8  
 7 7 7  
 6 6 6  
 5 5 5  
 4 4 4  
 3 3 3  
 2 2 2  
 1 1 1  
 0 0 0

where the same requirements yield  $A = 7.979574673$ ,  $B = -17.52538691$ ,  $C = 10.84948485$ ,  $D = -2.060727237$ . However, in benchmarks it was found that this potential is only a few percent faster than the cosine version, the reason being that the trigonometric functions are implemented as fast hardware instructions on the processors used (Compaq Alpha EV5, EV56, EV6, EV67, and Intel Pentium II and III). Therefore the original version was kept, Eq. 4.3. All results that follow will exclusively refer to this potential.

Figure 4.1 shows the resulting  $g(r)$  of a monomer fluid of  $N = 10000$  particles who are all subject to  $U_{LJcos}$ . While  $\phi = 0$  is the original repulsive Lennard–Jones fluid, the amplitude is systematically increasing with  $\phi$ . However, the position of the maxima and minima is nearly unchanged, as desired.  $\phi = 2.0$  is close to the fluid–solid transition (see below).

Figure 4.2 compares  $g(r)$  to the bond lengths which result from the FENE potential, Eq. 4.2, at a typical state point  $\phi = 1.5$ . It is seen that also these lengths match quite nicely.

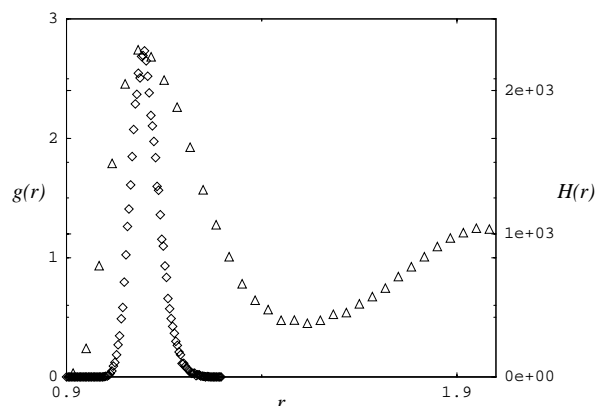


**Figure 4.2.:** Histogram of bond lengths for a system of dimers at  $\rho = 0.85$ ,  $\phi = 1.5$ , compared to the pair correlation function  $g(r)$  of a monatomic system at the same state point.

#### 4.1.2. Computational details

The simulation method applied is Molecular Dynamics (MD). Chapter 3 gives a short overview on MD. For stabilization purposes, a Langevin thermostat [DGK98] is used. The equations of motion are given by

$$m\ddot{\vec{r}}_i = -\vec{\nabla}_i U - \Gamma\dot{\vec{r}}_i + \vec{\zeta}_i(t), \quad (4.7)$$

where the friction coefficient  $\Gamma$  and the strength of the random noise  $\vec{W}_i(t)$  are related via the the fluctuation dissipation theorem:

$$\langle \vec{\zeta}_i(t) \cdot \vec{\zeta}_j(t') \rangle = 6k_B T \Gamma \delta_{ij} \delta(t - t'). \quad (4.8)$$

$U$  denotes the sum over all interactions of the bead  $i$ , and the temperature is always fixed at the value  $k_B T = 1.0$ . The equations of motion are integrated by using a velocity Verlet updating scheme [AT87]. The simulations were carried out in the constant volume (NVT)

as well as in the constant pressure (NPT) ensemble. For the NPT ensemble simulation a modified velocity Verlet algorithm was used, and the “box” degree of freedom coupled to a Langevin heat bath as well [KD99]. The time step used in the simulation was  $\Delta t = 0.01$ . The friction constant is set to the small value  $\Gamma = 0.5$ , thus ensuring that the dynamics is not too far away from the Hamiltonian limit. For a reasonable choice of parameters for the NPT ensemble, see Ref. [KD99]. The simulation box was always cubic with periodic boundary conditions. We used a highly optimized domain decomposition scheme in order to run the simulations in parallel on a Cray T3E [PK98].

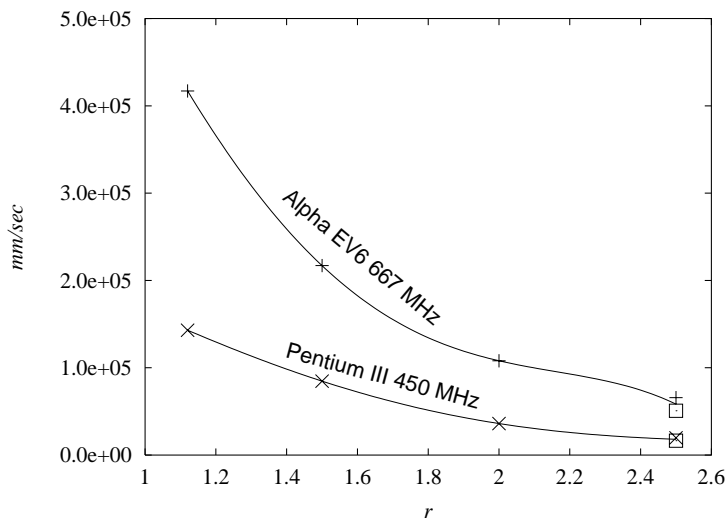


**Figure 4.3.:** Number of Molecular Dynamics steps per particle per CPU second on two different hardware platforms as indicated in the figure. Systems of pure monomers at density  $\rho = 0.85$  with different ranges of interaction  $r$  were studied: Purely repulsive LJ potential ( $r = 2^{1/6}$ ), attractive cosine potential for  $r = 1.5, 2.0, 2.5$ , and standard LJ potential cut off at  $r = 2.5$  (□ symbols). The cosine potential was run at strength  $\phi = 1.5$ ; the system size was always  $N = 1000$  particles.

Figure 4.3 shows that indeed the strategy of confining the interaction range to the first neighbor shell pays off in terms of computational efficiency: While the purely repulsive system is clearly by far the fastest, only a factor of two is lost in speed when increasing the interaction range to 1.5. If we would have used the “canonical” interaction range 2.5, then the loss would rather be a factor of eight.

The algorithm was augmented by a Monte Carlo (MC) procedure. In order to study the un-mixing of unlike monomers, a semi-grand-canonical ensemble was used where the total number of particles is fixed, while the fraction of A (or B) particles is allowed to fluctuate, such that the chemical potential difference  $\Delta\mu$  is being held fixed. For symmetry reasons, the un-mixing occurs at  $\Delta\mu = 0$ . The fluctuations in composition are then facilitated via stochastic “flips”, which can change an A particle to a B particle, or vice versa [GLKG96]. This was implemented via a simple single spin flip algorithm using the standard Metropolis [MRR<sup>+</sup>53] criterion.

9 9 9  
8 8 8  
7 7 7  
6 6 6  
5 5 5  
4 4 4  
3 3 3  
2 2 2  
1 1 1  
0 0 0

9 9 9  
 8 8 8  
 7 7 7  
 6 6 6  
 5 5 5  
 4 4 4  
 3 3 3  
 2 2 2  
 1 1 1  
 0 0 0

Furthermore, one might also think about the analogous procedure for dimers (an A-B dimer is “flipped” to a B-A dimer, or vice versa). Such a scheme would certainly somewhat speed up the equilibration when a lamellar structure is formed. However, this is far less important than for un-mixing: An un-mixing system without the MC procedure would exhibit a conserved order parameter and hence “hydrodynamic slowing down”, i. e. the necessity of transport over macroscopic distances. Conversely, in the case of the formation of a lamellar structure, the order parameter is not conserved, such that only local rearrangements are necessary. hence such dimer flips were not implemented, since they would have required substantial communication in the parallel program, whose data structure builds directly on that of Ref. [PK98], where the elementary units are the monomers, such that a dimer can be crossing processor boundaries.

## 4.2. Simulation Results

### 4.2.1. Identical Monomers

The simplest system to study consists only of monomers which are all identical. Figure 4.4 gives a rough sketch of the expected phase diagram in the  $(\phi, P)$ -plane,  $P$  denoting the pressure. Both a gas-liquid transition as well as a fluid-solid transition are expected, although the gas-liquid transition must not necessarily occur [Fre99]. Since the main interest

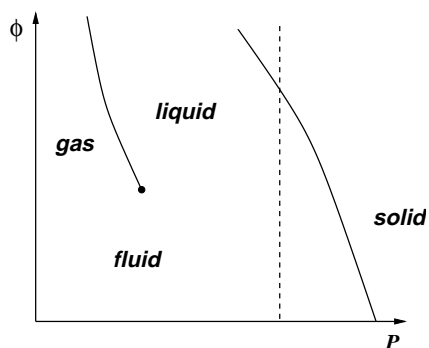


**Figure 4.4.:** Qualitative sketch of the expected phase diagram of a system of pure monomers in the  $\phi$ -pressure plane. The existence of the gas-liquid line was not proven numerically, but is strongly expected. All transition lines are of first order; the gas-liquid line ends in a critical point. Furthermore, the diagram shows the path along which the fluid-solid transition (dashed line) was studied.

lies in the investigation of the behavior at densities near the typical value  $\rho = 0.85$ , it has not been attempted to answer this question and map out the phase diagram as a whole. Instead  $\phi$  was varied at constant pressure  $P = 1.0$ . Test runs in the NVT ensemble had shown that this is a typical pressure for a dimer system at the typical high density near the order disorder transition (ODT), see below. The results indicate that along this chosen path only a fluid-solid transition occurs. This transition was located by obtaining a hysteresis loop of the density as a function of  $\phi$ . First a system of  $N = 500$  particles was run, started in its fluid phase. The potential depth  $\phi$  was increased systematically, until a jump in the density was observed, after which it was decreased again. The final configuration of the previous

run was always used as initial configuration for the next  $\phi$  value. In each run the system was first equilibrated and then an average of the data was taken over a limited run time of  $t = 2000$ . Figure 4.5 shows the resulting hysteresis loop; besides the  $N = 500$  data a system containing  $N = 10000$  particles was also studied (with the same observation time) near the transition, which was necessary to obtain good accuracy in the metastable states. It was

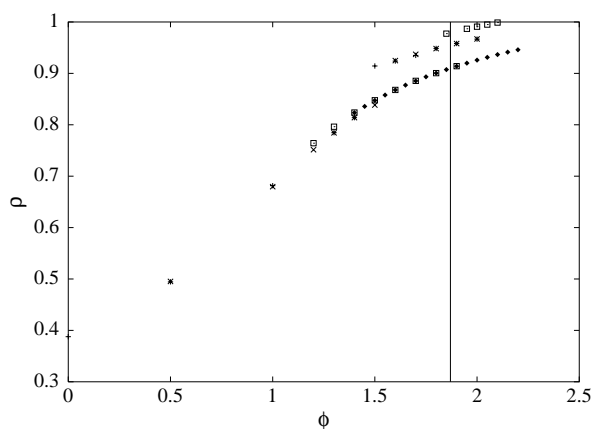


**Figure 4.5.:** Hysteresis loop of the density  $\rho$  as a function of the potential depth  $\phi$ , at constant pressure  $P = 1.0$ , for  $N = 500$  particles ( $\times$  and  $+$ ), and  $N = 10000$  ( $*$  and  $\square$ ). The vertical line marks the most likely transition value of  $\phi$ .

not attempted to locate the fluid–solid transition very accurately (this would have required thermodynamic integration or finite–size scaling [Dün96]), but it is quite clear that it occurs for  $1.8 < \phi < 2.2$ . Therefore, the simulations of the amphiphilic systems should clearly avoid such large  $\phi$  values.

The solid phase is further characterized by a strongly reduced diffusion. Figure 4.6 shows the mean square displacement (MSD) of a single particle as a function of time for different  $\phi$  values along the path it was studied. To this end an  $N = 500$  particle system was simulated in

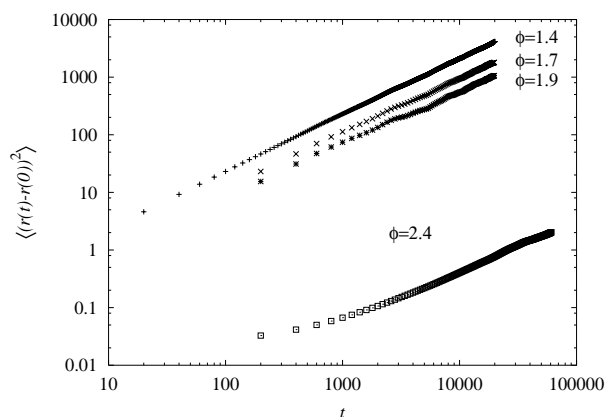


**Figure 4.6.:** Mean square displacement for different values of the potential depth  $\phi$ . The diffusion in the crystalline state is much slower than in the fluid state.

the NVT ensemble, starting off from the final configurations of the corresponding NPT run.

9 9 9  
8 8 8  
7 7 7  
6 6 6  
5 5 5  
4 4 4  
3 3 3  
2 2 2  
1 1 1  
0 0 0

9 9 9  
 8 8 8  
 7 7 7  
 6 6 6  
 5 5 5  
 4 4 4  
 3 3 3  
 2 2 2  
 1 1 1  
 0 0 0

The diffusion constant is extracted from the long-time behavior via the Einstein relation in  $d$  spatial dimensions (here  $d = 3$ )

$$D = \lim_{t \rightarrow \infty} \frac{1}{2dt} \langle (\vec{r}(t) - \vec{r}(0))^2 \rangle, \quad (4.9)$$

resulting in the values given in Table 4.1. Note that the mean square displacement has to be measured in the center-of-mass reference frame of the overall system, which diffuses as well. While diffusive behavior is observed without any problems in the fluid phase, it turns out that at the state point in the solid phase ( $\phi = 2.4$ ) the mobility is actually so small that the leaving of the local “cage” was not observed on the time scale of the simulation; hence there an upper bound for the diffusion constant can be given here.

$\phi$	1.4	1.5	1.7	1.9	2.4
$D$	$33.9 \cdot 10^{-3}$	$26.4 \cdot 10^{-3}$	$15.1 \cdot 10^{-3}$	$8.74 \cdot 10^{-3}$	$0.177 \cdot 10^{-3}$

**Table 4.1.:** Pure fluid system diffusion constants for different values of the potential depth  $\phi$ .

Details of the crystal structure are revealed by the static structure function  $S(q)$ , which is shown in figure 4.7 for  $\phi = 2.4$  in comparison to  $\phi = 1.4, 1.8, 2.0$  in the liquid state for an  $N = 10000$  system along the path studied. One clearly sees a much more pronounced

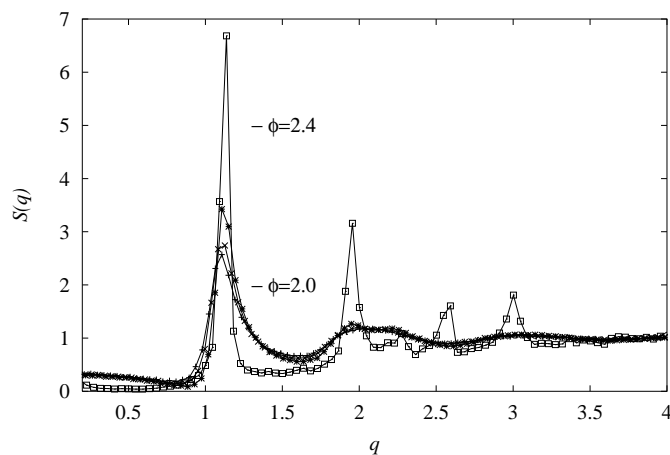


**Figure 4.7.:** Structure factor for systems with different values of the potential depth  $\phi = 1.4$  (+), 1.8 ( $\times$ ), 2.0 ( $*$ ) and 2.4 ( $\square$ ). Configurations with  $\phi \leq 2.0$  exhibit a fluid-like structure, while systems with higher values definitely show an crystal with fcc order.

structure with long-range order. The position of the peaks is compatible with an fcc crystal [Kit95]. Moreover, a determination of the number of nearest neighbors via integration over the first peak of  $g(r)$  yields the value 12, as expected for the fcc structure. Though the density data indicate that  $\phi = 2.0$  is still liquid, the empirical Hansen-Verlet criterion [HV69], which

states that crystallization occurs as soon as the first maximum of  $S(q)$  exceeds the value 2.8, would already assign this state point to the solid phase.

#### 4.2.2. Binary Mixture

For a system which contains rather two different species A and B, the phase behavior becomes more complicated, since at large values of  $\phi$  the two species will un-mix (macro-phase separation, MPS). The qualitative phase diagram which is expected is drawn in figure 4.8. The MPS was studied in the semi-grand-canonical ensemble for a system at fixed den-

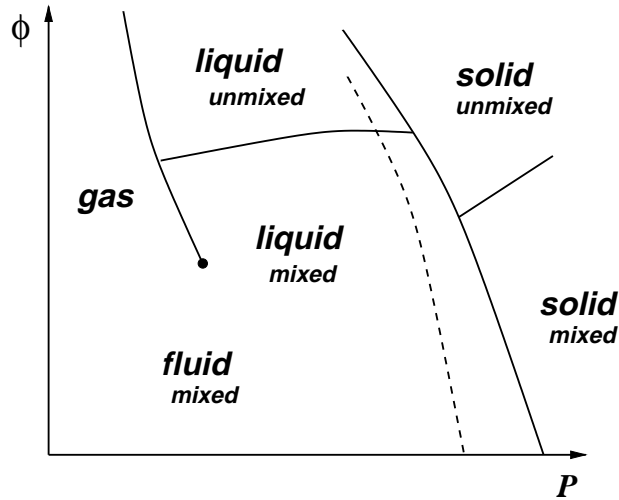


**Figure 4.8.:** Qualitative sketch of the expected phase diagram of a binary system of pure monomers in the  $\phi$ -pressure plane, for fixed composition. The diagram is partly speculative, since it was not checked if un-mixing also occurs for the gas phase. It is also not clear if the solid phase favors or disfavors un-mixing relative to the fluid phase. The transition line between the one-phase and the two-phase state is of first order, except for the case of composition 1/2, where, due to the symmetry of the model, the transition is of second order. The dashed line denotes the path along which the un-mixing transition (constant volume) was studied.

sity  $\rho = 0.85$  as a function of  $\phi$ . This situation is qualitatively depicted in figure 4.9. It is particularly important to know if the MPS occurs for smaller  $\phi$  than crystallization – otherwise no fluid phase in the unmixed state would exist, and it would be quite unlikely that a dimer system exhibits a fluid lamellar phase.

The order parameter is given by  $m = N_A - N_B$  and can vary from  $-N$  to  $+N$ . According to the usual theory of finite-size scaling [Dün96], the ratio of the second and first moments,  $\langle m^2 \rangle / \langle |m| \rangle^2$ , plotted as a function of  $\phi$  for different system sizes, should intersect at one point which is a very good estimate for  $\phi_c$ . Two different system sizes were studied, containing  $N = 2000$  and  $N = 4000$  particles. The moment's ratios are plotted in figure 4.10, from which  $\phi_c \approx 0.62$  can be estimated. One should expect that the ODT for a dimer system will occur at values  $\phi > \phi_c$ .

9 9 9  
8 8 8  
7 7 7  
6 6 6  
5 5 5  
4 4 4  
3 3 3  
2 2 2  
1 1 1  
0 0 0

9 9 9  
8 8 8  
7 7 7  
6 6 6  
5 5 5  
4 4 4  
3 3 3  
2 2 2  
1 1 1  
0 0 0

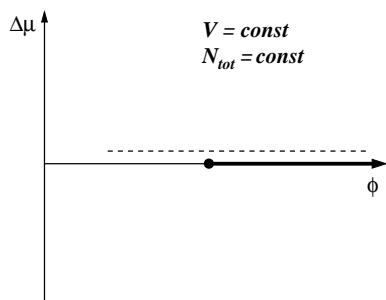


**Figure 4.9.:** Sketch of the un-mixing phase diagram in the plane  $(\phi, \Delta\mu)$ , where  $\Delta\mu$  is the chemical potential difference between species A and B. The first-order line occurs at  $\Delta\mu = 0$ , for reasons of A–B symmetry, and ends at an Ising-like critical point  $\phi_c$ .

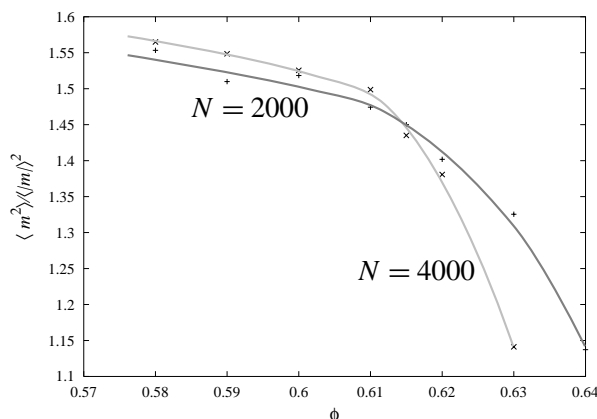


**Figure 4.10.:** Second moment – first moment ratio for a binary systems in the semi-grand-canonical ensemble at density  $\rho = 0.85$  as a function of  $\phi$ . The crosses denote a binary system containing  $N = 2000$ , and the stars one with  $N = 4000$  particles.

### 4.2.3. Dimeric Systems

A system of A–B dimers allows for three independent order parameters within the liquid phase. First of all, the molecules can orient along a spontaneously selected axis (the director), without distinguishing between A and B. If no additional ordering would occur, then such a phase would be nematic. Nematic ordering is measured via the symmetric and traceless Saupe tensor [dGP93] (refer to chapters 1 and 2):

$$Q_{ij} = \frac{3}{2} \left( \hat{r}_i \hat{r}_j - \frac{1}{3} \delta_{ij} \right), \quad (4.10)$$

where  $i$  and  $j$  are Cartesian indices,  $\delta_{ij}$  is the Kronecker symbol, and  $\hat{r}$  denotes a unit vector along the molecular axis. In the isotropic phase the volume average (or ensemble average) of  $Q_{ij}$  is identically zero, while in the uniaxial nematic phase  $Q_{ij}$  has the three eigenvalues  $(S, -S/2, -S/2)$ , where  $S > 0$  is the nematic order parameter, which at most can assume the value  $S = 1$  corresponding to the perfectly ordered state. In the simulation the volume average of  $Q_{ij}$  was measured, at any particular time, and the largest eigenvalue determined. The time average of these defines the numerical estimate for  $S$ .



Furthermore, there can be breaking of translational invariance and the formation of a smectic phase. In a Smectic A phase, the sheets are perpendicular to the director. This can be measured by studying the density–density correlation function (or the structure factor) along the director, which is “crystalline” with long–range order, and perpendicular to it, where the structure is fluid–like.

Finally, there can also be a rearrangement of the A–B molecules along the director axis  $\hat{n}$ : The vector from A to B can either point with identical probabilities in the direction  $+\hat{n}$  and  $-\hat{n}$  (disordered state), or prefer one particular direction (ordered state).

In the lamellar phase, all three types of ordering occur simultaneously, while the isotropic phase is disordered with respect to all order parameters. In principle, it would be possible that additional phases were stable, where only some, but not all, order parameters were nonzero. However, this is not expected for those parameters, and indeed not found in the simulations. The expected qualitative phase diagram is thus shown in figure 4.11, where also the path along which the order–disorder transition was studied at constant volume and constant number of dimers is shown.

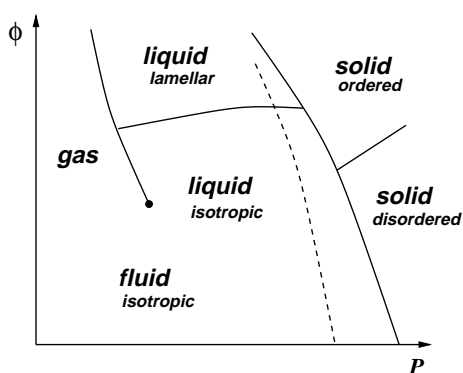


**Figure 4.11.:** Qualitative sketch of the expected phase diagram of a system of A–B dimers  $\phi$ –pressure plane. Again, the diagram is partly speculative. The dashed line denotes the path along which the order–disorder transition (constant volume) was studied. All transition lines are of first order.

It is clear that the ODT must be of first order, since already nematic ordering enforces first–order behavior, as is known from symmetry analysis and Landau–deGennes theory [dGP93]. There is thus a slight problem with studying the ODT in the constant–volume ensemble: Strictly spoken, one must expect that the isotropic and lamellar phases have different densities at coexistence, and therefore phase separation (i. e. un–mixing of the isotropic and the lamellar phase) must occur. However, it is expected that the density difference is so small that the phases will not un–mix unless the system is extremely large: For a small system, the free energy penalty of introducing an interface into the system will outweigh the bulk free energy gain obtained from phase separation. Indeed, it was checked, that both the coexisting phases, which we found via hysteresis loops for  $S$  (see below), have practically the same pressure at the same state points. This shows that the approach is consistent within the given numerical resolution. For high–accuracy studies however, this issue must be kept in mind. The constant–pressure ensemble was not used since it is computationally more expensive and less easy to handle.

9 9 9  
8 **8** 8  
7 7 **7**  
6 6 6  
5 5 5  
4 4 4  
3 3 3  
2 2 2  
1 1 1  
0 0 0

9 9 9  
 8 8 8  
 7 7 7  
 6 6 6  
 5 5 5  
 4 4 4  
 3 3 3  
 2 2 2  
 1 1 1  
 0 0 0

Another criticism against the constant-volume ensemble might arise from the potential incompatibility of the linear box size  $L$  with the smectic layer spacing  $d$ , i. e. the fact that  $L/d$  is usually not an integer when the system chooses its optimum value for  $d$ . However, the system has also the freedom to rotate the director with respect to the box. Considering, for simplicity, a two-dimensional system with tilt angle  $\alpha$  between the sheets and the box axis, it is clear that  $\tan \alpha$  must be some rational number  $p/q$  ( $p$  and  $q$  denoting the minimum integer values) in order to obtain a finite number of sheets, which is then just  $q$ . On the other hand,  $\cos \alpha = L/(dq)$  and thus  $d/L = \sqrt{p^2 + q^2}/q^2$ . For large  $L$  there will always be numbers  $p$  and  $q$  such that the condition is satisfied to a high degree of accuracy; hence the criticism is not valid. For figure 4.12, which shows a typical configuration deep in the lamellar phase, first the sheet thickness was measured and then the system size was adjusted in order to fit the sheets nicely. The number of dimers  $N = 48668$  at density  $\rho = 0.85$ , which will be con-

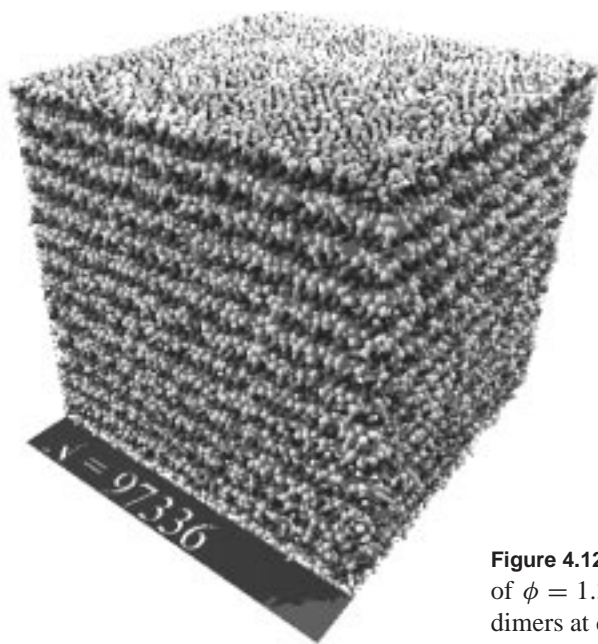


**Figure 4.12.:** Typical configuration for a potential depth of  $\phi = 1.3$ . The system is composed of 48668 A–B dimers at density  $\rho = 0.85$ .

sidered in what follows, results from such considerations. Figure 4.13 shows the hysteresis loop in  $S$  for this system (each state point was observed for 2000 LJ time units); the ODT is thus localized at roughly  $\phi = 1.2$ .

The important point is that the ODT occurs at a much smaller  $\phi$  value than that what was found previously for crystallization. Though the dimerization might favor crystallization compared to the monomeric system (it reduces the translational entropy), the effect is probably not that strong, and hence one must expect that the observed lamellar phase is indeed fluid, which is necessary for the model to be useful for real amphiphilic systems. Nevertheless, this was checked via

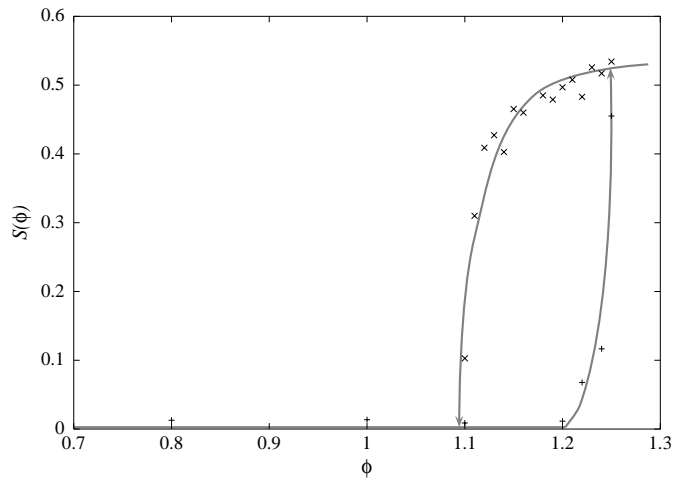


**Figure 4.13.:**  $S$  value as a function of the potential depth  $\phi$ . The plusses denote the way from  $\phi = 0$  to larger  $\phi$ , the crosses the reverse direction. The solid gray line serves as a guide for the eye

- the structure factor measured in the direction of the director, which is indeed a liquid-crystal-like (see Fig. 4.14), where  $q_0 = 3.36$  was found, and hence the layer spacing is

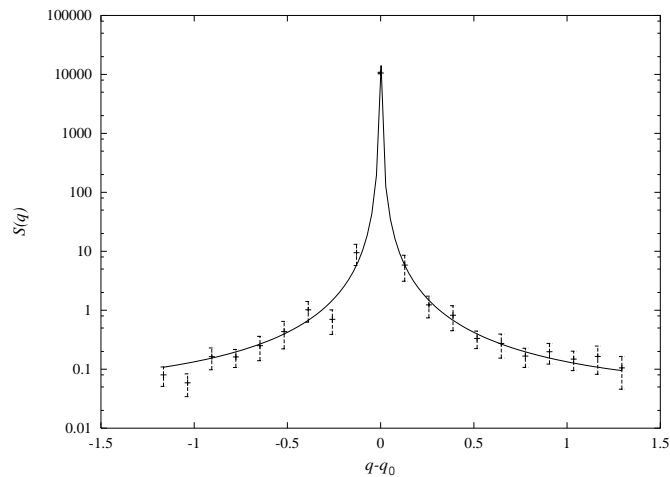


**Figure 4.14.:** Structure factor of a system of  $N = 48668$  dimers at  $\rho = 0.85$ ,  $\phi = 1.3$  in the direction of the director.  $q_0 = 3.36$ . In order to enhance the quality of the plot and reduce the error, the scattering vector was chosen to deviate with a tiny amount around the director direction  $z$ ,  $k_x \leq 0.01$  and  $k_y \leq 0.01$ .

here  $\lambda = 2\pi/q_0 = 3.73$ . Due to fluctuation of the layers, the structure function shows near  $q_0$  rather a power-law decay than a delta function peak. This effect is referred to as Landau–Peierls instability since the second moment of the layer displacement,  $\langle u^2 \rangle$ , diverges for infinite systems (see [dGP93, CL95]).

9 9 9  
8 8 8  
7 7 7  
6 6 6  
5 5 5  
4 4 4  
3 3 3  
2 2 2  
1 1 1  
0 0 0

9 9 9  
 8 8 8  
 7 7 7  
 6 6 6  
 5 5 5  
 4 4 4  
 3 3 3  
 2 2 2  
 1 1 1  
 0 0 0

- the structure factor in the directions perpendicular to the director, which clearly shows fluid structure (see Fig. 4.15), and

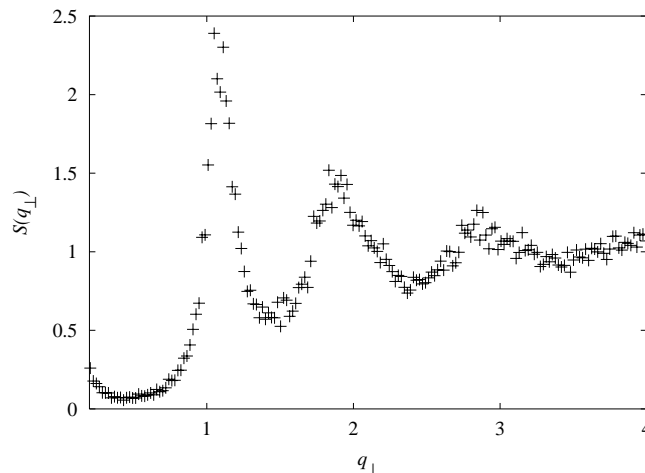


**Figure 4.15.:** Structure factor of a system of  $N = 48668$  dimers at  $\rho = 0.85$ ,  $\phi = 1.3$  in the directions perpendicular to the director.

- the diffusion behavior (see Fig.4.16): While the in-plane diffusion (measured via the

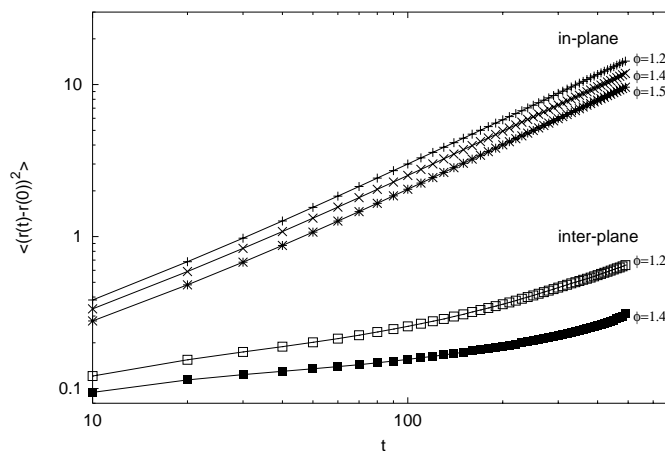


**Figure 4.16.:** Mean square displacements for different values of the potential depth  $\phi$ , inter-plane and in-plane in comparison.

mean square displacement in the directions perpendicular to the director) is nearly unhindered, with quite similar behavior as in the liquid phase of the monomers, the inter-plane diffusion is strongly reduced, similar to the behavior in the monomer crystal. The resulting diffusion constants are listed in Table 4.2.

$\phi$	1.2	1.4	1.5
$D_{\text{in-plane}}$	$14.5 \cdot 10^{-3}$	$11.9 \cdot 10^{-3}$	$9.72 \cdot 10^{-3}$
$D_{\text{inter-plane}}$	$1.3 \cdot 10^{-3}$	$0.6 \cdot 10^{-3}$	$0.6 \cdot 10^{-3}$

**Table 4.2.:** Diffusion constants for dimeric systems.  $D_{\text{in-plane}}$  denotes the two-dimensional diffusion constants within a layer in the lamellar phase.  $D_{\text{inter-plane}}$  represents the diffusion perpendicular to the layers.

### 4.3. Conclusions

A new simple continuum simulation model for the investigation of amphiphilic and copolymeric systems has been introduced. This model is capable of reproducing the essential physical characteristics in the targeted area of interest. All interactions are short ranged; therefore the number of interacting pairs is relatively small, resulting in good computational efficiency.

The structure of the monomeric fluid is hardly affected by the attractive tail compared to the purely repulsive Lennard–Jones fluid. The binary fluid of two disliking components phase separates; this occurs for roughly the same strength of interaction as the order–disorder transition of the dimeric liquid into the lamellar phase, where the dimers are made of both particle types. No indication for any other ordered fluid phase for the dimer system was found. Both from structural analysis and from the observation of fast two-dimensional diffusion, it was demonstrated that the lamellar phase is still fluid; crystallization occurs for stronger interactions. The diffusion constants of the pure fluid and the one within layers of dimers are within the same order of magnitude under same conditions.

With that choice of the short-ranged interaction potentials it is possible to simulate large system sizes much more efficiently than with other models like those of Refs. [GL98, LMTZ94]. Moreover, it is quite versatile in that it can be applied to a large variety of physical situations, avoiding lattice artifacts, while changes in the molecular architecture etc. are easy to implement.

9 **9** 9  
8 8 8  
7 7 7  
6 6 6  
5 5 5  
4 4 4  
3 3 3  
2 2 **2**  
1 1 1  
0 0 0

## 5. Shear, flow alignment, and undulation instability

### 5.1. Introduction

#### System under investigation

Several different systems will be used for the investigation of the effect of shear flow to the proposed model in the last chapter. One of the systems is the lamellar system containing 97336 particles as 48668 dimers which has been previously been shown (section 4.2.3).

The system has been quenched below ODT to a value of the potential depth  $\phi = 1.27$ . The lamellae are oriented parallel to the  $x$ - $y$  plane, hence the director is pointing parallel to the  $z$ -coordinate. Figure 5.1 shows the starting conformation for simulation runs in order to analyze the flow alignment behavior. Shear is applied with  $z$  as gradient direction and  $x$  as

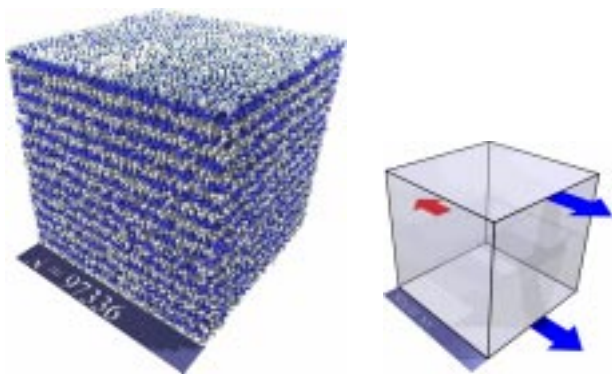


**Figure 5.1.:** Starting conformation containing 48668 dimers. The orientation of the lamellae is parallel to the  $x$ - $y$ -plane. The left picture shows a conformation snapshot. The right one sketches the direction of shear flow along the  $x$ -axis.

flow direction. The simulations were performed in both the NVT ensemble and the NpT ensemble. Using constant volume the particle density was  $\rho = 0.85$ . The simulation runs were performed at different strain rates over two decades  $\dot{\gamma} = [0.001, 0.1]$ . Flow alignment, orientational dependence as well as stress-strain-rate behavior were investigated. Another system containing  $N = 10000$  particles (5000 dimers) will be described later in section 5.3.2.

## This Chapter

The chapter is organized as follows. Since for the non-equilibrium theory by Auernhammer et al. [ABP00] some equilibrium properties are important it starts with a determination of the bending modulus for the simulation system in equilibrium. Then the weak shear limit is investigated. The flow alignment of the director in the linear response regime is observed. At higher strain rates the onset of undulation is analyzed. This is compared to smectic A conformations which are dilated in direction of the layer normal (at no shear). For the whole strain rate interval response in form of shear stress is analyzed. A possible mechanism for flow alignment and undulations on molecular level will be proposed, which seems to be supported by simulation results. It is discussed subsequently. At high strain rates the orientational change from parallel to perpendicular is investigated and compared to the analytic theory by Fredrickson et al. [Fre94]. A summary and outlook conclude the chapter.

## 5.2. Shear Flow Simulations

### 5.2.1. Director Splay Modulus - Layer Bending Modulus

The layer bending modulus  $K$  is an equilibrium parameter and accounts for the energy cost of the bending of a layer. It is very similar to the director splay modulus in nematics. As shown before, the splay term in the elastic energy of nematics is equal to the bending term in smectics (section 2.1), since the relation between the displacement of the smectic strata and the director is given by  $\hat{n} = -\nabla u$ .

In the analytic treatment by Auernhammer et al. [ABP00] the ratio of the bending and the compression modulus,  $K/B_0$ , occurs quite often. The next sections deals with comparison between simulation results and that theory, and hence if those moduli are known in advance, a consistency check could be made. As discussed below it is very difficult to determine the compression modulus since no layer description is available. But nevertheless it is possible to obtain the bending modulus  $K$ .

In a simulation on molecular level it is easier to identify the direction of the molecular axis' and hence the director,  $\hat{n}$ , as their ensemble average than to measure the fluctuation amplitude of the layers,  $u$ . So the equilibrium fluctuations of the director were used in order to obtain  $K$ .

The free energy cost of the layer bending as part of the elastic energy term equation 2.13 is given by

$$F_{\text{bend}} = \frac{1}{2} K \left[ \left( \frac{\partial}{\partial x} + \frac{\partial}{\partial y} \right) n \right]^2$$

With the help of the Fourier transform of this expression,  $F_{\text{bend}} = K q_{\perp}^2 n^2$ , the director's fluctuations can be investigated. Equation (2.17) relates the first normal mode with the layer



bending modulus by

$$\langle [n_1(\vec{q}_\perp)]^2 \rangle = \frac{k_B T}{V} \frac{1}{K_1 q_\perp^2}$$

For the simulation the fluctuations of the director can be directly analyzed from a set of equilibrium runs. In those runs the system was well oriented with layers within the  $x$ - $y$ -plane. Since the preferred axis of the director was hence chosen along the  $z$ -axis, the normal modes have to be expressed in terms of the director components perpendicular to its equilibrium orientation, the  $x$  and  $y$  components.

$$\langle [n_1(\vec{q}_\perp)]^2 \rangle = \frac{1}{V} \frac{1}{q_\perp^4} \left\langle \left[ \int d^3 r (q_x n_x(\vec{r}) + q_y n_y(\vec{r})) e^{i\vec{q}_\perp \vec{r}} \right]^2 \right\rangle \quad (5.1)$$

For the layer bending modulus one obtains

$$K \equiv y(q) = \frac{q_\perp^2 k_B T}{\langle \dots \rangle} \quad (5.2)$$

where  $\langle \dots \rangle$  stands for the right hand side of eq. (5.1). The above identity between  $K$  and the function  $y(q)$  only holds if the latter one is constant. A linear fit can now be applied to

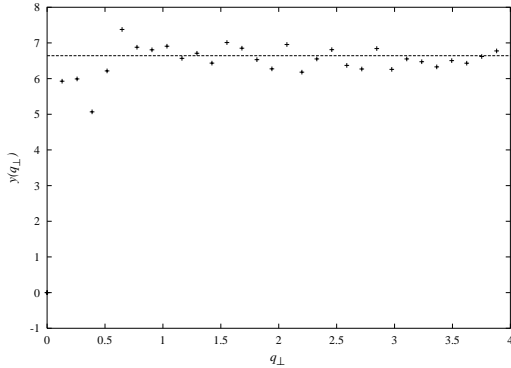


**Figure 5.2.:** Determination of the layer bending modulus  $K$ . The points are an average over 50 conformations. The line is a linear fit on the short wave length data  $q > 2.0$  producing  $K = 6.6$ .

the data, which consists of an average over  $y(q_\perp)$  of 50 conformations, in order to obtain the layer bending modulus  $K$ . For the investigated system the layer bending modulus was found to be  $K = 6.6$ .

There is an alternative method for the determination of  $K$  and  $B$  respectively. For single membranes and mono-layers the measurement of the fluctuation amplitude in  $z$ -direction is possible. Recently two similar methods have been suggested by Laradji et al. [LM00] and Goetz et al. [GGL99, GL98]

Laradji et al. investigated a mono-layer of model-DBCP in a mixture of A and B homopolymers. They introduced plaquettes into their simulation system whose  $x$ - $y$ -position was fixed on a grid. Those plaquettes were only able to move along the  $z$ -direction and their position was updated every time step depending on the  $z$ -position of the nearest A- and B-monomers. By doing this they were able to measure the height function  $u(x, y)$  and hence the bending modulus of their mono-layers.

9 9 9  
 8 8 8  
 7 7 7  
 6 6 6  
 5 5 5  
 4 4 4  
 3 3 3  
 2 2 2  
 1 1 1  
 0 0 0

Goetz et al. [GGL99] analyzed the density profile of their conformations and hence were able to determine middle sheet of their bilayer. By doing this they can record the necessary data for the analysis of the height function  $u(x, y)$ .

The result presented in this subsection is consistent with the results issued by Laradji et al. [LM00] and Goetz et al. [GGL99] as it lies the same order of magnitude of theirs. But the differences are obvious and a further comparison is not sensible, since this result is based on another model Hamiltonian and a smectic rather than a mono- or bi-layer system.

Unfortunately their methods are not applicable in the present case. A dimer melt below ODT exhibits more than one stratum and it is likely that within a short time the plaquettes would not refer to the same layer any more. In principle it is possible to record a density profile but the identification of specific layers is a difficult task. One has to apply methods like voronoi tessellation in order to obtain a correct representation. The existing roughness due to the shortness of the model molecules of the sheets makes that task no easier. The next and even more difficult problem is, to follow those layers in time, so that the fluctuations in  $u(x, y)$  are recordable.

In turn it is conceivable that the method applied here to obtain the value of the bending modulus does work for measurements in single layer systems as well. In that case the effort for the determination of the bending modulus is considerable lower.

### 5.2.2. Flow Alignment

The flow alignment of the director is the key effect in Auernhammers et al. treatment of Smectic A LCs under shear [ABP00]. It leads in their picture to an effective shrinkage of the layers which can under low energy cost only be balanced by undulations in order to keep the layer spacing constant. Auernhammer et al. find that undulations along the vorticity direction are possible above a certain threshold as discussed in chapter 2. In a simulation both the flow alignment of the director as well as the onset of undulations are be observable.

The flow alignment as a function of the strain rate was investigated in a simulation series with a system containing  $N_s = 48668$  dimers. A parallel oriented conformation of a system, which has been described in the introduction to this chapter, was exposed to shear flow. Starting with a strain rate of  $\dot{\gamma} = 0.001$  the system was successively exposed to higher and higher strain rates up to  $\dot{\gamma} = 0.1$ . The final conformation of each run serves as the initial one for the next simulation. Two step sizes were followed, a step size of  $\Delta\dot{\gamma} = 0.005$  with values belonging to path 1 ( $\times$  symbols) and a smaller step size of  $\Delta\dot{\gamma} = 0.002$  recorded as path 2 (+ symbols). In the scope of this section only the strain rate where a parallel orientation exists are of interest ( $\dot{\gamma} < 0.04$ ), larger strain rates will be discussed later.

Figure 5.3 displays the results in form of a graph where the flow–component of the director,  $n_x$ , is plotted versus the strain rate,  $\dot{\gamma}$ . At low values of the strain rate ( $\dot{\gamma} < 0.01$ ) the in–flow component of the director, grows linearly. This is the range where one can easy determine the ratio

$$R_1 = \frac{\gamma_1}{B_1} \frac{\lambda + 1}{2}, \quad (5.3)$$

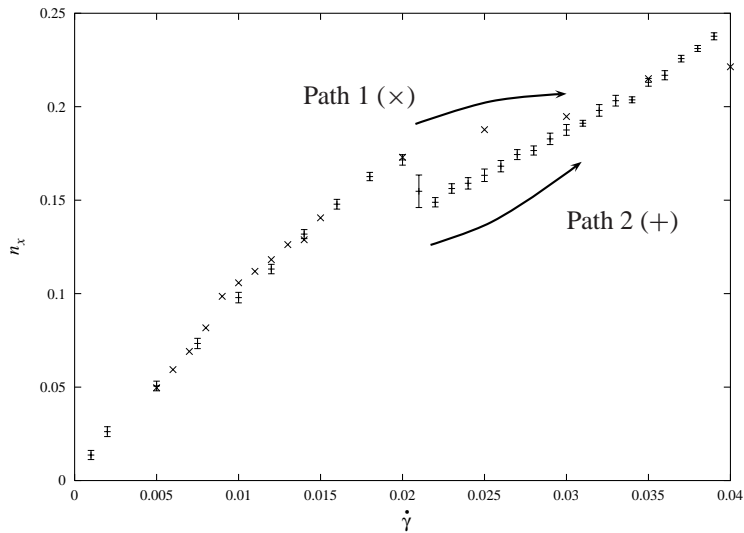


**Figure 5.3.:** Flow alignment of the director. The in flow component,  $x$ -component, of the director,  $n$ , is shown as a function of the strain rate,  $\dot{\gamma}$ . Path 1 and path 2 belong to different step sizes in the increase of the strain rate (see text). The error bars denote the standard deviation of an average over ten independent conformations.

since the flow alignment expression reduces to

$$n_x = R_1 \dot{\gamma}$$

From the simulation data a value of  $R_1 = 9.9 \pm 0.3$  is obtained. If the region for a fit is increased to  $\dot{\gamma} = 0.02$  the error in  $R_1$  increases and  $\chi^2$  is fairly large. That means that the measured values lie not very well on the assumed curve in that case. Figure 5.4 visualizes this observation. A grey highlighted area sketches the misfit of the initial result for higher strain rates.

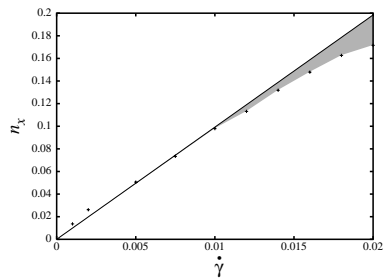


**Figure 5.4.:** The slope of the flow component of the director,  $n_x$  is linear only for very low values of the strain rate,  $\dot{\gamma}$ . This complicates the determination of the elastic constant ratio  $R_1$  (see text). The gray highlighted area sketches the disagreement of the fit of a straight line to the low strain rate data points.

The onset of undulation can be located at a strain rate of  $\dot{\gamma} = 0.02 \equiv \dot{\gamma}_c$ . Conformations below this value show apart from the flow alignment of the director no further observable response to the shear exerted on them. At values above  $\dot{\gamma}_c$ , undulations can be observed. There is a difference in the direction of undulations for the runs using a small and a larger pace of the strain rate increase. If one follows path 1, stepsize  $\Delta\dot{\gamma} = 0.005$ , undulations along the

9 9 9  
8 8 8  
7 7 7  
6 6 6  
5 5 5  
4 4 4  
3 3 3  
2 2 2  
1 1 1  
0 0 0

9 9 9  
 8 8 8  
 7 7 7  
 6 6 6  
 5 5 5  
 4 4 4  
 3 3 3  
 2 2 2  
 1 1 1  
 0 0 0

vorticity direction develop. This is sketched in figure 5.5, left illustration. Their amplitude grows with increasing strain rate. Their wave number is determined by the box length in that direction, due to the periodicity of the system. Hence can only be a multiple of it. The wave length is found to match the box extension. Without any obvious influence the flow component of the director grows further with increasing strain rate.

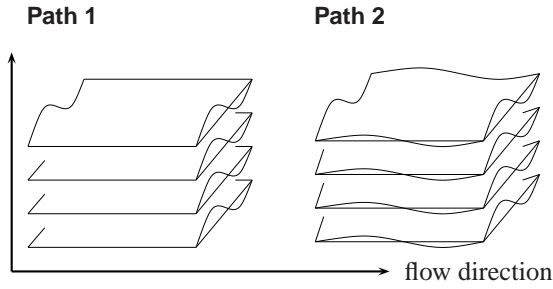


**Figure 5.5.:** Sketch of the different behavior of path 1 and 2. Conformations of path 2 show undulations along the flow direction for strain rates of  $0.02 < \dot{\gamma} < 0.03$ , conformations of path 1 do not.

Exactly this is not the case for the simulation runs following path 2.  $n_x$  drops just at the onset by a few percent and both pathways split. With a further increase of the strain rate  $n_x$  grows again. An investigation of the conformational 'appearance' reveals that conformation along path 2 show near but beyond the onset of undulation not only a wave vector parallel to the vorticity direction but also a wave vector in flow direction. Compare to figure 5.5, right illustration.

A wave vector parallel to the flow direction has not been considered by the analytic theory so far. Those undulations in  $x$ -direction get smaller and smaller with further increased strain rate and vanish again at  $\dot{\gamma} \approx 0.03$ . Near this strain rate both pathways rejoin. Figure 5.6 shows simulation snapshots of typical undulating conformations of path 1 and 2.

The analytic theory [ABP00] describes the dependence of the component of the director parallel to the flow direction by the following equation, which was introduced in chapter 2:

$$\left[ \frac{\lambda + 1}{2} - \lambda n_x^2 \right] \dot{\gamma} = \frac{B_1}{\gamma_1} n_x \sqrt{1 - n_x^2} + \frac{B_0}{\gamma_1} \left[ n_x (1 - \sqrt{1 - n_x^2}) \right] \quad (2.30)$$

Unfortunately this equation cannot be resolved in the way that the director's  $x$ -component is a function of the shear rate. Nevertheless the equation can be solved for the strain rate as a function of the directors  $x$ -component,  $\dot{\gamma}(n_x)$ , yielding

$$\dot{\gamma} = \left\{ \frac{B_1}{\gamma_1} n_x \sqrt{1 - n_x^2} + \frac{B_0}{\gamma_1} \left[ n_x (1 - \sqrt{1 - n_x^2}) \right] \right\} \left[ \frac{\lambda + 1}{2} - \lambda n_x^2 \right]^{-1} \quad (5.4)$$

Using  $R_1$  from above and introducing the following abbreviations:

$$A = \sqrt{\frac{\lambda \gamma_1}{B_1}}, \quad \tilde{B} = \frac{B_0}{B_1} - 1, \quad (5.5)$$

equation 5.4 can be rewritten as

$$v \equiv A \dot{\gamma} = \frac{u}{R_1 - u^2} + \frac{\tilde{B}}{2A^2} \frac{u^3}{R_1 - u^2}, \quad (5.6)$$

Path 1

Path 2

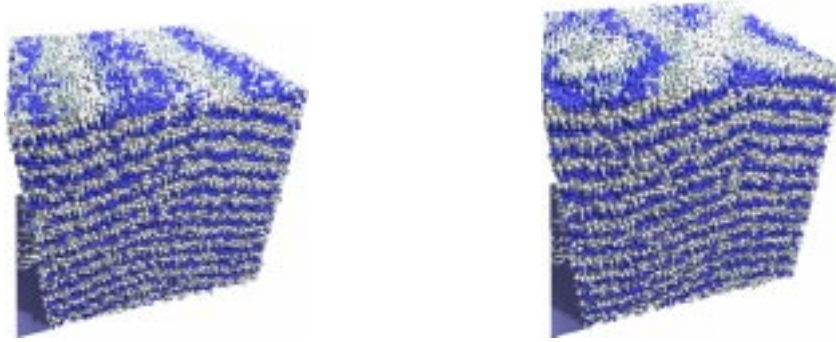


**Figure 5.6.:** Simulation snapshots of undulating conformations. The left one belongs to path 1 and shows a conformation at  $\dot{\gamma} = 0.025$  with no undulations in flow direction (which points along the partly hidden sign at the bottom). The right snapshot shows a conformation of path 2 right beyond the onset of undulation at  $\dot{\gamma} = 0.025$  where the amplitude of the excitation in flow direction is found to be largest.

where the transformation  $u = \sqrt{\lambda\gamma_1/B_1}n_x$  has been made.

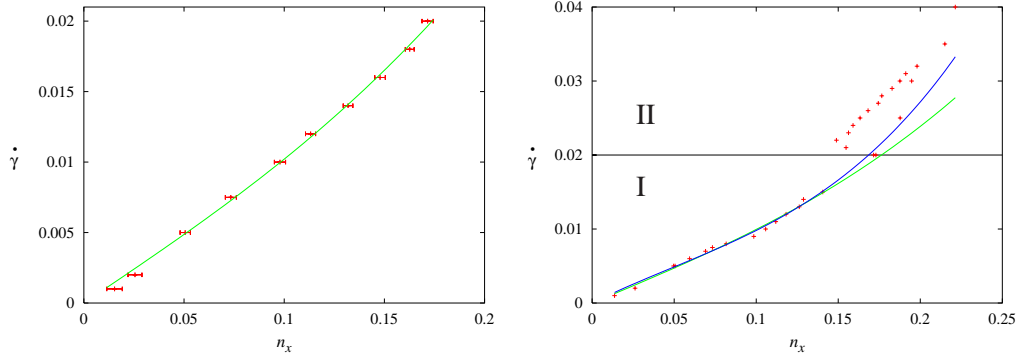
Equation 5.6 provides the means for a linear fit of  $\tilde{B}$  with additional parameters  $A$  and  $R_1$  which have to be guessed in advance. A guess for  $R_1$  is known from the previous analysis of the linear regime. The fit reveals for  $A = 1.6$  the best fit in  $\tilde{B} \approx 9$  but it does not depend that strong on the value of  $A$ . Therefore it is quite difficult to give a trustful estimate for the error in  $\tilde{B}$  which might be quite large. The resulting graph for the current fit is shown in figure 5.7 in the left plot, green line. The data set used for the fit was limited to the range below the onset of undulation at  $\dot{\gamma}_c = 0.02$  since the theoretical prediction is valid up to this strain rate. Above the onset, as it can be seen in the right graph of figure 5.7 (marked as region II), the function does not fit the data points. This is not very surprising since the theory has not been developed to be able to predict the flow alignment in that region. The blue line in the right graph shows a third order polynomial which has also been fitted to the data points in region I. It matches a little bit better to the path 1 data of region II, but there is no real theoretical basis for such a functional form.

Figure 5.7 shows a plot of the flow component of the director,  $n_x$ , as a function of the shear rate,  $\dot{\gamma}$ , and a fit of another third order polynomial. This time the fit was carried out over the whole range of data belonging to path 1 in region I and II. The fit renders the functional form of the data points until a strain rate of  $\dot{\gamma} = 0.03$ , where path 1 and path 2 rejoin, quite well. Nevertheless both, this and the previous fit of a third order polynomial, can only serve as an assumption for the analytical form of the flow alignment.

In the range of the validity of the theory (region I) the functional form equation (5.6) and hence eq. (5.4) fit the data very well, if one disregards the mentioned problem with the weak dependence of  $A$  on the fit for a moment. In the next section  $A$  will be determined from the

9 9 9  
8 8 8  
7 7 7  
6 6 6  
5 5 5  
4 4 4  
3 3 3  
2 2 2  
1 1 1  
0 0 0

9 9 9  
 8 8 8  
 7 7 7  
 6 6 6  
 5 5 5  
 4 4 4  
 3 3 3  
 2 2 2  
 1 1 1  
 0 0 0



**Figure 5.7.:** Both graph show the shear rate,  $\dot{\gamma}$ , plotted as a function of the flow component of the director,  $n_x$ . The lines in the plots are fits to the data points below the onset of undulation. The green line is the fit of equation (5.6) to that data range. The blue line in the right plot is a third order polynominal fitted to the same data range. It was left out in the left plot since it is in that range very similar to the fit of (5.6). The I and II in the right plot mark the regimes where no undulations of the parallel oriented sample can be found (I:  $\dot{\gamma} < 0.02$ ) and beyond the onset of undulation (II:  $\dot{\gamma} > 0.02$ ).

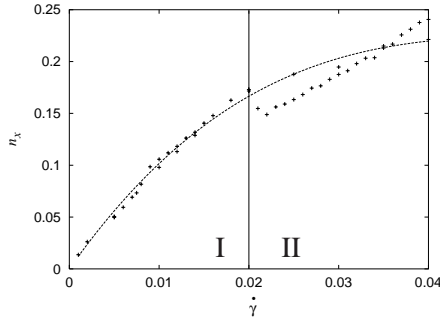


**Figure 5.8.:** In the right graph the date are plotted in the natural way,  $n_x$  as a function of  $\dot{\gamma}$ . The line is again a fit of a third order polynominal but this time fitted to the full data range belonging to path 1.

temporal behavior of the director to shear flow and a new fit will be made.

### 5.2.3. Onset of undulation

The onset of undulations is of specific interest for the analytic theory as it is governed by elastic constants and system dependent magnitudes. Compression and bending modulus,  $B_0$  and  $K$ , determine in combinations with the coupling of the director to the layer normal,  $B_1$ , this onset. Together with the rotational viscosity  $\gamma_1$ , as well as the flow alignment parameter,  $\lambda$ , in a linear approximation a set of critical values for the onset of undulations can be derived (see also eqs. 2.36-2.38).

$$\dot{\gamma}_c = \frac{B_1}{(1 + \lambda)\gamma_1} n_{x,c} \tag{2.38'}$$

relates the director's flow component to the critical shear rate at the onset of undulation.

The critical wave number eq. (2.36) is dependent on the thickness of the system, given by  $d$  in the analytic theory. In principle the simulation system has infinitely extended through the periodic boundary conditions. So there are no bounding plates here. In the analytic theory the distance  $d$  is assumed to be fairly large. The corresponding length of the simulation cell is  $L_z$ . But if the cell is not cubic, the maximum wave length is limited by  $L_y$ , since the undulations develop in the vorticity direction of the system beyond the onset. So equation (2.36) might be rewritten following the above considerations as

$$q_{y,c}^2 = \frac{\pi}{d} \sqrt{\frac{B_0}{K}} = \left( \frac{2\pi}{L_y} \right)^2. \quad (2.36')$$

Hence, the strain rate at the onset is given by

$$\dot{\gamma}_c = 4 \frac{B_1}{(1+\lambda)\gamma_1} \sqrt{\frac{B_0}{B_0 - 2B_1} \frac{4\pi^2}{L_y^2}} \propto \frac{1}{L_y}, \quad (5.7)$$

if the linear approximation holds. In any case the critical flow alignment of the director is then

$$n_{x,c} = 4\pi \sqrt{\frac{B_0}{B_0 - 2B_1} \frac{1}{L_y}}, \quad (5.8)$$

which is valid even for the non-linear regime. In principle the proportionality between  $\dot{\gamma}_c$  or  $n_{x,c}$  and the  $y$ -extension of the box is measurable, if that exists as predicted. Unfortunately, there have been no undulations observed in other configurations of smaller system size. For a system which exhibits undulations the extension in  $y$ -direction, the flow-component of the director has to double. For the  $N = 97336$  system  $n_{x,c} = 0.16$  is found, which would result in  $n'_{x,c} = 0.32$  for half the system size. Before those values can be reached, the parallel orientation of the layers is not stable any more. This indicates that for the investigation of the proportional behavior large system sizes (millions of particles) have to be considered. For the simulation of those system sizes an extensive amount of computing time has to be invested. Beside the intensive use of mega-computers other “problems” were found to be present in those systems which will be reported in the next chapter. Therefore this intention was abandoned.

In section 5.2.2 it was mentioned that two directions of undulations are observable. Since the theory has only considered a wave vector in  $y$ -direction, the flow direction cannot be analyzed. In the same section undulation were found to exist for a certain regime (regime II) starting a strain rate,  $\dot{\gamma} > \dot{\gamma}_c = 0.02$ . The value of  $\dot{\gamma}_c$  was found by visual inspection of the according conformational snapshots for the existence of undulations.

Figure 5.9 shows the nematic order parameter as a function of the strain rate for values of strain rates belonging to regime I and II ( $0 < \dot{\gamma} < 0.04$ ), the regimes where a parallel orientation of the lamellae is stable as discussed earlier. The order of the system in regime I seems to increase slightly towards the onset of undulation. If this effect is real, it is very weak and might occur due to growing energy barrier for the molecules to fluctuate in  $z$ -direction as the flow align with increasing strain rate. Directly beyond the onset of undulation the order within the system is increased by 7%. That increase is surprising since undulations are

9 9 9  
8 8 8  
7 7 7  
6 6 6  
5 5 5  
4 4 4  
3 3 3  
2 2 2  
**1 1 1**  
0 0 0

9 9 9  
 8 8 8  
 7 7 7  
 6 6 6  
 5 5 5  
 4 4 4  
 3 3 3  
 2 2 2  
 1 1 1  
 0 0 0

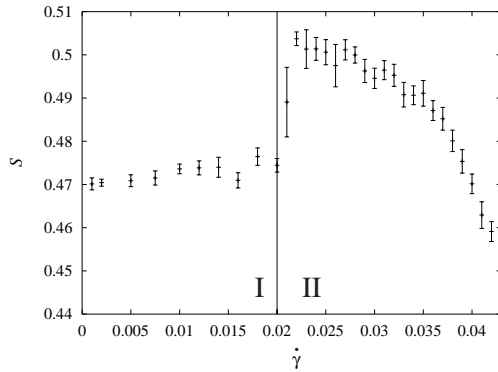


**Figure 5.9.:** Director alignment value  $S$  as a function of strain rate. Beyond the onset of undulation,  $\dot{\gamma} > \dot{\gamma}_c = 0.02$ , up to values of  $\dot{\gamma} = 0.03$  an increased order of the system in comparison with values below the onset can be observed.

present which should reduce the order. This might give insight into the way the layers undulate. Figure 5.10 shows two possibilities to achieve an undulating sheet, one with reduced total order, and one with increased. The lower sketch of figure 5.10 shows the possible layer

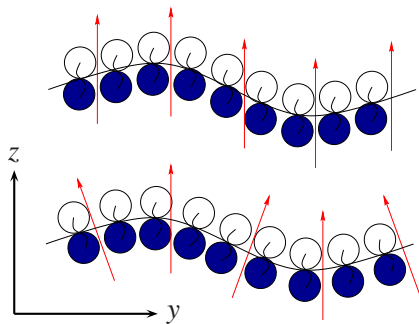


**Figure 5.10.:** Two possibilities for layers to undulate. The upper sketch shows an undulation where the single molecules do not follow the wave. They stay aligned as denoted by the red arrows. The order can be increased since fluctuations in direction of the wave are due to energy concerns less favorable. The lower sketch shows a similar situations, but the molecules follow the the wave so that their axis' projections into the shown plane are parallel to the wave normal. This reduces the order within the sheet.

bend as an effect of the undulation wave. The molecules are oriented along the normal of the wave, as shown in the sketch. This disturbs the overall alignment along the  $z$ -direction and leads to a lower value in the nematic order parameter,  $S$ , which is used as a measure of order within the system. In the upper sketch of 5.10 the molecules align along the undulation wave but their molecular axes and hence the director stays aligned in the  $z$ -direction. This effect does not diminish the nematic order parameter,  $S$ . Due to an increased number AB contacts the fluctuations of molecules could be slightly suppressed which would lead to a higher order in the system and would explain the jump in to higher values of  $S$  in the graph of figure 5.9. It is possible to obtain the information on how the layers undulate from the conformations directly. For that purpose the conformations were analyzed in slabs with extensions  $(L_x, \Delta L_y, L_z)$ , where  $\Delta L_y \simeq 2$ . The director of each slab was calculated and the resulting components in vorticity direction,  $n_y(y)$  are plotted in figure 5.11. The graph shows a clear undulation in this components. That means that the molecules are aligned the layer normal and do not stay parallel to the  $z$ -direction. Hence the lower picture of figure 5.10 sketches the situation correctly. Unfortunately that cannot explain the increase in order within the system at the onset.

In section 5.2.2 as well as above it was mentioned that not only undulation in vorticity direction but also undulation in flow direction occur which have not been investigated in Auern-



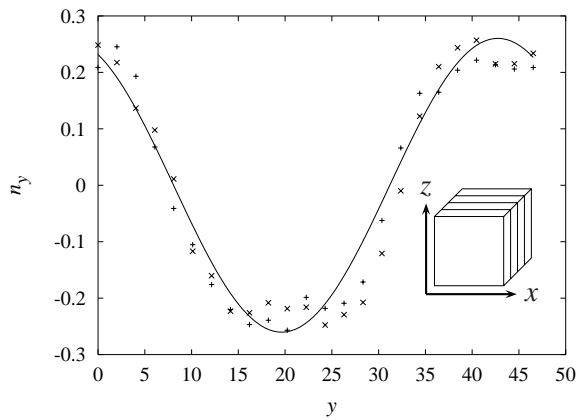


**Figure 5.11.:** Undulation of the vorticity component of the director,  $n_y$ . The graph shows  $n_y$  as a function of  $y$ . The values are obtained as averages over  $x$ - $z$ -slices as depicted in the inset. The clear undulation in  $n_y$  allows only the lower picture of figure 5.10 as an explanation of the way layers undulate. There are two sets of data depicted in the graph. The crosses,  $\times$ , denote a conformation at a point of time  $t = 0$ , the plusses,  $+$ , belong to a succeeding conformation after  $\Delta t = 900$ .

hammer's et al. approach, yet. Those undulations can be analyzed in a similar way as the undulations in vorticity direction but this time the conformation is sliced in  $x$ -direction as depicted in the inset of figure 5.12. Here undulations can be seen in the flow component of

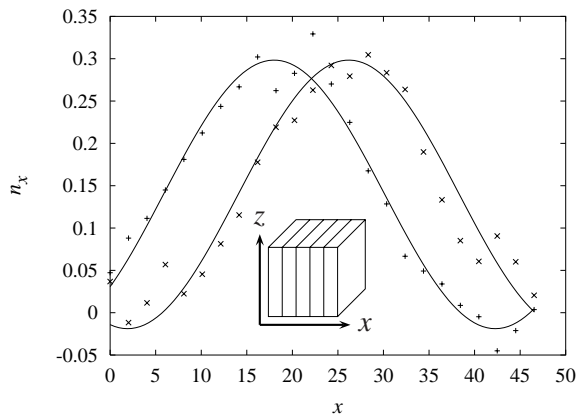


**Figure 5.12.:** Undulation of the flow component of the director,  $n_x$ . The graph shows  $n_x$  as a function of  $x$ , where its values have been obtained by averaging over  $y$ - $z$ -slices as sketched by the inset.

the director,  $n_x(x)$ . The average of this sinusoidal function equals the mean value  $n_x$  measured previously. Interestingly, the undulation wave is not stationary but it moves with the flow. The plusses (+) denote data obtained from a conformation at time  $t = 0$ . The crosses ( $\times$ ) belong to the same conformations evolved in time for  $\Delta t = 900$ . A shift in the position is visible from the graph of figure 5.12. Unfortunately only very few conformations of each run were written, so that the trajectory of the undulation wave and hence its traveling velocity is not available.

For the onset of undulation several scenarios are imaginable. Three of them are sketched in figure 5.13. Sketch (a) shows a linear increase of the amplitude beyond the onset, while (b) depicts a square root like increase. Both, (a) and (b), belong to forward bifurcating systems. (c) shows a different behavior and exhibit some kind of hysteresis, denoted by the arrows. Such behavior is called a backwards bifurcation.

9 9 9  
8 8 8  
7 7 7  
6 6 6  
5 5 5  
4 4 4  
3 3 3  
2 2 2  
1 1 1  
0 0 0

9 9 9  
 8 8 8  
 7 7 7  
 6 6 6  
 5 5 5  
 4 4 4  
 3 3 3  
 2 2 2  
 1 1 1  
 0 0 0

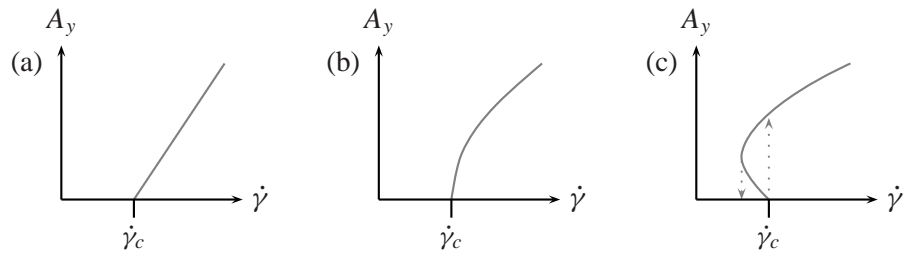


**Figure 5.13.:** Possible scenarios for a bifurcation. Each graph shows a sketch of the behavior of the amplitude of the director undulation in vorticity direction  $A_y$  as a function of the strain rate,  $\dot{\gamma}$ .

The present system is now analyzed in order to determine the type of bifurcation it shows. The undulation amplitude as a function of the strain rate can be evaluated from the data of  $n_x(x)$  and  $n_y(y)$ . Figure 5.14 shows the result. The data points denoted by the plusses (+)

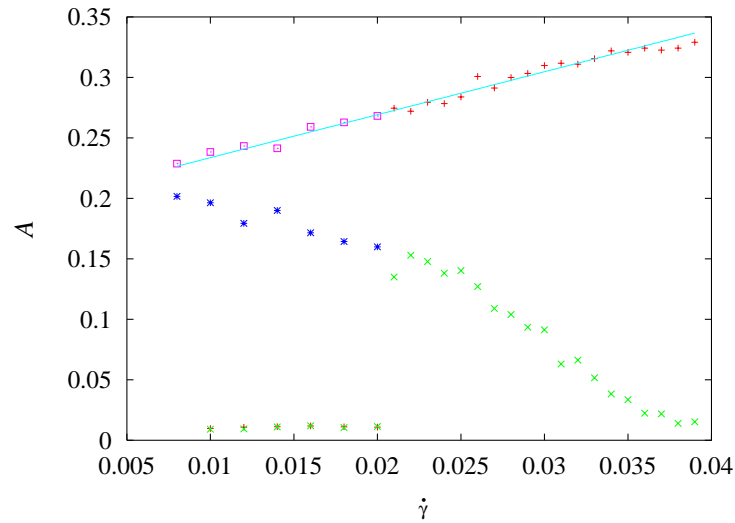


**Figure 5.14.:** Undulation amplitude as a function of strain rate  $\dot{\gamma}$ . The plusses (+) denote the amplitude of undulations with the wave vector parallel to the vorticity direction, the crosses ( $\times$ ) belong to the undulation amplitudes in flow direction. Each point represents an average of amplitudes originating from ten independent configurations. A clear onset of undulations can be observed at  $\dot{\gamma}_c = 0.02$ .

show the behavior of the amplitude of undulation wave in vorticity ( $y$ ) direction, the one denoted by the  $\times$ -symbols belong to the amplitude of the wave in flow ( $x$ ) direction. Each point represents an average of amplitude values originating from ten independent configurations. The sharp onset of undulations at  $\dot{\gamma}_c = 0.02$  suggests that the present system belongs to the group of backwards bifurcating ones. This suggestion is indeed true as simulation in the reverse direction reveal. The purple boxes ( $\square$ ) and blue asterisks ( $*$ ) are the result of these

simulation. The  $\square$ -symbols are the amplitudes of undulation in  $y$ -direction with decreasing strain rate, the  $*$ -symbols are that of the  $x$ -direction. Since those undulation amplitudes do not vanish, a backwards bifurcation is present.

This is in disagreement with the theories assumption. Auernhammer's and coworker's [ABP00] theory is based on a treatment of dilated systems which show a forward bifurcation.

In the next subsection the type of bifurcation for a dilated simulation system will be checked.

#### 5.2.4. Stretch Dilation of layers

Shear flow on a smectic system, the flow alignment of the director and the effective shrinkage of the layers can be seen as a dilatation of the whole system. A thermotropic Smectic A LC on which is cautiously dilated along its director direction shows an increased layer spacing, space which has to be filled. This is done by undulations as seen in experiments [ ] if a certain dilatation is exceeded. Auernhammer's et al. theory is partly based on the detailed analytical description [ ] of this experiment. From the work in [ABP00] an expression can be derived which connects the critical dilatation at the onset of undulation,  $\alpha_c$ , with the same elastic constants used before [SADK]:

$$\alpha_c = \left( \frac{2\pi}{L_y} \right)^2 \frac{K_1}{B} \frac{1}{1 + \frac{K_1(2\pi/L_y)^2}{B_1}} \quad (5.9)$$

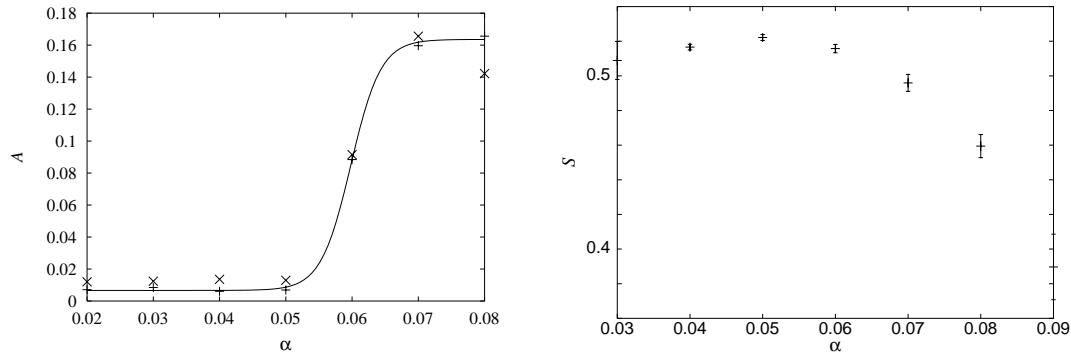
In the spirit of those experiments the initial conformation of the standard system with layers oriented parallel to the  $x$ - $y$ -plane was elongated along the  $z$ -direction. In a first simulation run the density of the system was decreased with the elongation (non-isochoric case). In a second run the density was conserved,  $L_x$  and  $L_z$  rescaled accordingly (isochoric case). Figure 5.15 display the results for the non-isochoric dilatation simulations. The onset of undulation can here be observed for a dilation slightly below  $\alpha = 6\%$ . The simulation covered only a few values of the dilation  $\alpha$ , just enough in order to check whether the system is forward bifurcating as found in the experimental system [RD77], or backwards like seen in the previous section. The increase of the amplitude just beyond the onset of undulation suggests that the system is indeed a forward bifurcating one, as it can be seen in the left graph of figure 5.15. There is obviously no sudden jump to high values of  $A$ . At higher values of  $\alpha$  ( $\alpha > 0.08$ ), a dissolution of layers takes place as indicated by the drop in the order parameter (right graph in figure 5.15. Figure 5.16 shows conformational snapshots of dilatation simulation with  $\alpha = 0.06$  (left image) and  $\alpha = 0.07$  (right image). From the waves and the knots on the top of the shown box, the amplitude could be estimated, if one considers the system as a set of oscillating membranes which are confined by the box. But the method to obtain the amplitude via the director of specific chosen slabs used in this chapter should be more exact.

Figure 5.17 shows the very similar results for the isochoric case.

In the contrary to the behavior under shearflow the order within the system starts to decrease at the onset of undulation in both cases. This indicates that the presence of shear flow must have some ordering effect itself, which has still has to be found.

9 9 9  
8 8 8  
7 7 7  
6 6 6  
5 5 5  
4 4 4  
3 3 3  
2 2 2  
1 1 1  
0 0 0

9 9 9  
 8 8 8  
 7 7 7  
 6 6 6  
 5 5 5  
 4 4 4  
 3 3 3  
 2 2 2  
 1 1 1  
 0 0 0



**Figure 5.15.:** Simple (non–isochoric) dilatation of a smectic model system. Left: The Amplitude of undulations in  $x$ - and  $y$ -direction as a function of the dilatation  $\alpha$ . Right: Strength of disorder in the system measured by the nematic order parameter  $S$  as a function of the dilatation  $\alpha$ . The lines serve as guides for the eye.

### 5.2.5. Stress vs. strain rate

The stress in shear flow - shear gradient plane,  $\sigma_{xz}$  was investigated as a function of the strain rate  $\dot{\gamma}$ . Figure 5.18 displays the results.

Three different regimes can be identified. Regime I is the regime of low strain rates,  $\dot{\gamma} < 0.02$ , where the parallel oriented samples show no undulations in any direction. For these strain rates the stress increases linearly. The transition area from regime I to regime II is located at  $0.02 \leq \dot{\gamma} < 0.025$ . Here the parallel oriented samples show undulations in both, flow and vorticity direction but the stress increases further on linearly. So the onset of undulation which lies at  $\dot{\gamma}_c = 0.02$  has been passed without having a visible influence on the stress behavior. For  $\dot{\gamma} > 0.025$  the stress increases not linear any more until it reaches its local maximum  $\sigma_{xz} = 0.55$  at a strain rate of  $\dot{\gamma} = 0.04$  which is the stability limit for the parallel orientation. In regime III no parallel orientation is found to be stable. Beyond the stability limit the stress drops to a much lower value,  $\sigma_{xz} = 0.41$  and the sample is now perpendicular oriented. With further increased strain rate the stress increases again but with a lower slope than for the parallel oriented conformations in regime I and II. The reverse path from high strain rates and a perpendicular orientated sample to lower strain rates was investigated, as well. The stress decreases with decreasing strain rate and rejoins the forward path at the origin.

The stress for the sheared sample in perpendicular orientation is lower than the stress in the parallel one within the range of coexistence of both orientations, regions I and II. That means that two strain rates are possible for each value of the stress. One strain rate for a parallel orientation and one for a perpendicular one. A sheared system with constant stress is hence able to respond with parallel and perpendicular bands within the system which are floating with different velocities and hence different strain rates. This is sketched in figure 5.19. The upper part of the system in that figure shows a parallel orientations for a suitable shear rate

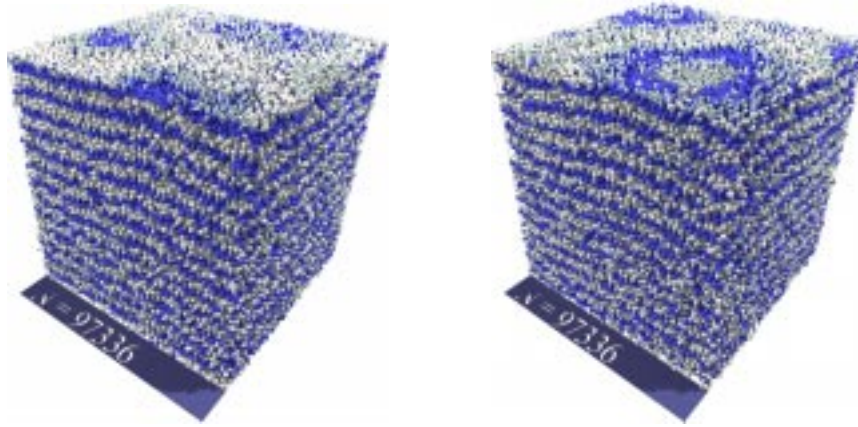


**Figure 5.16.:** Snapshots of conformations diluted with  $\alpha = 0.06$  (left image) and  $\alpha = 0.07$  (right image).

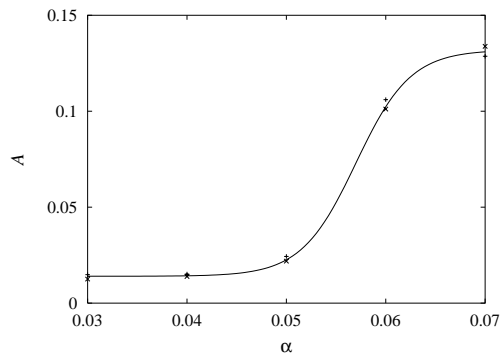


**Figure 5.17.:** Isochoric dilatation of a smectic model system. Again the undulation amplitude in  $x$ - and  $y$ - direction is shown as a function of the dilatation,  $\alpha$ . The onset of undulation seems to have not moved far compared to the non-isochoric case. The line serve as a guide for the eye.

$\dot{\gamma}_1$ . The lower part has a perpendicular orientation and an even higher strain rate  $\dot{\gamma}_2 > \dot{\gamma}_1$ , so that the stress is the same in both parts. The occurrence of such shear bands has been discussed by McLeish and Ball in [MB86]. There are several experiments where shear bands have been observed in systems which are different from the considered one [BC97]. If such a conformation as sketched in figure 5.19 exists and can be found in a simulation it might be interesting to look at the boundary between the parallel and perpendicular parts, too. This boundary will certainly be rich in defect structures.

A similar phase coexistence between an isotropic and a perpendicular oriented phase has been found in simulation and will be discussed in the next chapter.

9 9 9  
8 8 8  
7 7 7  
6 6 6  
5 5 5  
4 4 4  
3 3 3  
2 2 2  
1 1 1  
0 0 0

9 9 9  
 8 8 8  
 7 7 7  
 6 6 6  
 5 5 5  
 4 4 4  
 3 3 3  
 2 2 2  
 1 1 1  
 0 0 0

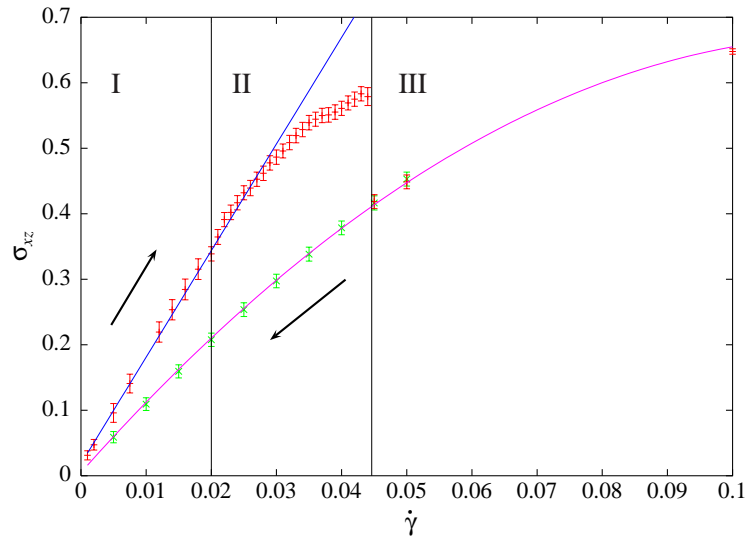


**Figure 5.18.:** The shear stress,  $\sigma_{xz}$ , as a function of the strain rate,  $\dot{\gamma}$ . The red pluses (+) denote the path along increasing values of the strain rate, the green crosses ( $\times$ ) the path in the opposite direction. The blue line in the plot emphasizes the linear response for lower strain rates ( $\dot{\gamma} < 0.03$ ). The purple line serves as a guide for the eye along the data points of a perpendicular orientation. In regime I and II a coexistence of perpendicular and parallel oriented conformation can be found. In the second one the parallel oriented conformation exhibit undulations but not in the first one. In regime III only a perpendicular orientation is found.

## 5.3. The mechanism of undulations

### 5.3.1. Questions and suggestions

Why can undulations develop in systems under shear? In the theoretical picture by Auernhammer et al. [ABP00] there is an effective shrinkage of the lamellae caused by the flow alignment of the director. This shrinkage can beyond some critical strain rate most easily be compensated by undulation. The previous simulations are able to support the theoretical picture and clearly show undulations.

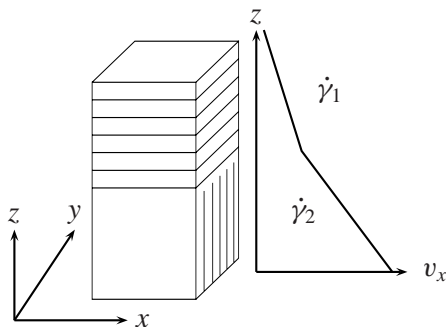


**Figure 5.19.:** Sketch of the coexistence of two different orientations under shear. The upper part of the sample shows a parallel orientation and an according strain rate  $\dot{\gamma}_1$ . The lower part exhibits a perpendicular orientation and a higher strain rate than the one in the upper part,  $\dot{\gamma}_2 > \dot{\gamma}_1$ . The stress in such a system is the same in the upper and the lower part.

But what happens on the molecular level? Since the director flow aligns, also the majority of the molecules have to flow align. But when they do so they feel their neighbors in flow direction because of geometrical constraints more stronger than without shear. Figure 5.20 sketches the situation. In equilibrium ((a) in the figure) the molecules are in average oriented

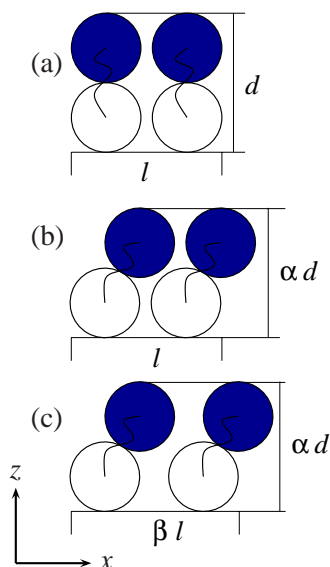


**Figure 5.20.:** Effect of shear flow on molecules. (a) shows a rough sketch of the ideal equilibrium situations where no shear is applied. The molecular axis' point along the layer normal. The layer possesses a length  $l$  into the flow direction and a width  $d$ . (b) Shear is exerted on the system, the molecules tilt and an effective shrinkage of the layer by  $\alpha < 1$  takes place. As the length of the layer  $l$  is kept constant the pressure component  $p_{xx}$  increases. A rearrangement of the layer is necessary to reach isotropic pressure conditions again, undulation may occur. (c) In a system which allows its extension into flow-direction to be rescaled, an extension of the layer in  $x$ -direction by a factor  $\beta > 1$  should be observable. No undulations should occur in this case.

along the normal of the lamellae. The corresponding equilibrium layer thickness is denoted by  $d$  and the equilibrium extension of the layer in  $x$ -direction, which will be the flow direction under shear is applied, is denoted by  $l$ . If now shear is applied to the system the molecules in average will flow align, which has been observed in the previous sections. This flow alignment leads to an effective shrinkage of the layer thickness by a factor  $\alpha < 1$ . Due to the tilt of molecules neighbors in flow direction are in closer contact than in equilibrium ((b) in the figure), especially for dimers the number of A–B contacts is increased. This results in a higher pressure component in flow direction,  $p_{xx}$ . In order to counterbalance the inhomogeneous stress distribution molecules have to be reordered, and the density of molecules in  $y$  direction is increased, which increases the pressure in that direction, too.  $p_{xx}$  and  $p_{yy}$  have now values above their equilibrium ones. In the case of long molecules  $p_{zz}$  is decreased due to the effective shrinkage of the layers. For short molecules this effect should be reduced due to the increase of number of A–B contacts which also leads to an additional pressure component in  $z$ -direction which is neglectable for long molecules. If the pressure imbalance between the  $x$ – $y$ -directions and the  $z$ -direction is large enough, the energy barrier which prohibits undulations of the stack of layers can be overcome and such evolve, preferable in the  $y$ -direction. This direction is favoured since

If the system is now able to extend its layers along the flow direction as needed in order keep  $p_{xx}$  near its equilibrium one, the tendency to show undulations should be suppressed ((c) in the figure). An additional balancing of the pressure in  $z$ -direction could make the delvelopment of undulation impossible. Even if only the pressure  $z$ -direction was kept constant, while in the other direction NVT ensemble rules are applied, undulations should be

9 9 9  
8 8 8  
7 7 7  
6 6 6  
5 5 5  
4 4 4  
3 3 3  
2 2 2  
1 1 1  
0 0 0

9 9 9  
 8 8 8  
 7 7 7  
 6 6 6  
 5 5 5  
 4 4 4  
 3 3 3  
 2 2 2  
 1 1 1  
 0 0 0

suppressed in favour of a realignment of the layers

### 5.3.2. The system

In order to test the assumption a system of  $N = 10000$  particles (5000 dimers) was investigated. The initial conformation was set up in a way that it contains 11 bilayers of dimers. These bilayers need a reasonable amount of space and so the box has to be cuboid with different lengths of the edges. (The  $N = 97336$  system which is cubic, supports 13 bilayers.) In order to allow undulations the box size was chosen to have a larger extension into  $y$ -direction than into the flow-direction. The box with are given by  $\vec{L} = (10.572666, 26.431664, 43.761238)$ .

So the initial system had already been set up in a layered structure and was quenched and equilibrated for a total time of  $t \approx 20000$ . The ensemble which was used in this simulation is a kind of mixture between a real  $NpT$  ensemble and a  $NVT$  one. The box is free to fluctuate in  $z$ -direction and its height was controlled by the pressure component  $\sigma_{zz}$  which was kept constant. In the other directions no rescaling was made so that the extensions of the box and hence its base were kept at the presetted values. This ensemble will be denoted as  $Np_zT$ . Figure 5.21 shows a conformational snapshot of such a run at  $t = 20000$ . The layer normal

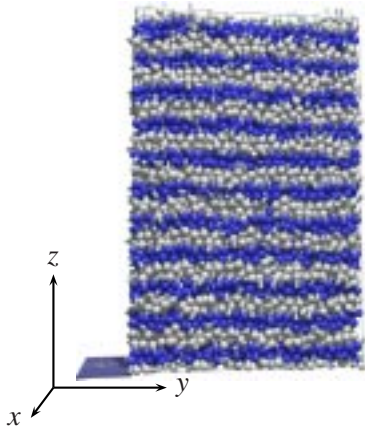


**Figure 5.21.:** The image shows a configuration snapshot taken at time  $t = 20000[LJ]$  during the equilibration. It was simulated under some kind of special  $NpT$  ensemble where the box was free to fluctuate in  $z$ -direction, but  $x$  and  $y$  direction were fixed (see text). It stays under the given pressure value of  $p_{zz} = 0.33$  constant.

points along the  $z$ -axis and hence the lamellae stay parallel to the  $x$ - $y$ -plane. The density of the system is with  $\rho = 0.82$  slightly lower than in the previous used  $N = 97336$  conformations ( $\rho = 0.85$ ).

### 5.3.3. Investigation of the undulation mechanism

The system described in the previous section was exposed to shear flow with different strain rates. During the simulation runs of a duration of  $t = 5000[LJ]$  each. In difference to the procedure in the case of the  $N = 97336$  system, section 5.2.2, for each run at a certain strain rate the same initial equilibrium conformation was used. The reason for that will become apparent later in this section. Following the argumentation of section 5.3.1 the director should



flowalign, the pressure in flow as well as in vorticity direction should increase. No undulations should show up by two reasons. On the one hand the freedom of the box to adjust its length in gradient-direction, in order to keep the according pressure component,  $p_{zz}$ , constant, on the other hand since the system might be too small following the consideration to equation (5.8).

If the picture in section 5.3.1 is correct, the  $z$ -extension of the box,  $L_z$ , should hardly be effected by the existence of shear flow and stay constant. This was tested for the strain rate  $\dot{\gamma} = 0.01$  and the results are collected in the graphs of figure 5.22. The graph shows the

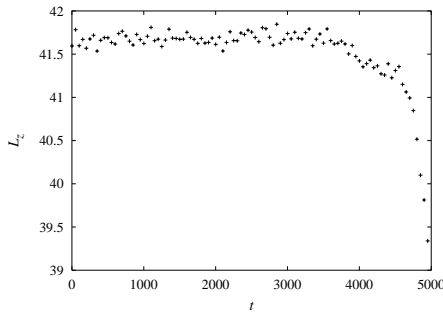


**Figure 5.22.:** Evolution of the height of the simulation box,  $L_z$ , in time in a shear simulation under strain rate  $\dot{\gamma} = 0.01$ . The height of the box decreases as defects enable the structure to reformat and build up tilted layers (see text).

time evolution of the variable box height during one simulation run. For a duration of nearly  $\Delta t = 4000$  the height stays constant. Then it drops until the end of the run. Figure 5.23 shows for this strain rate snapshots of the evolution of the simulation in time. Until nearly

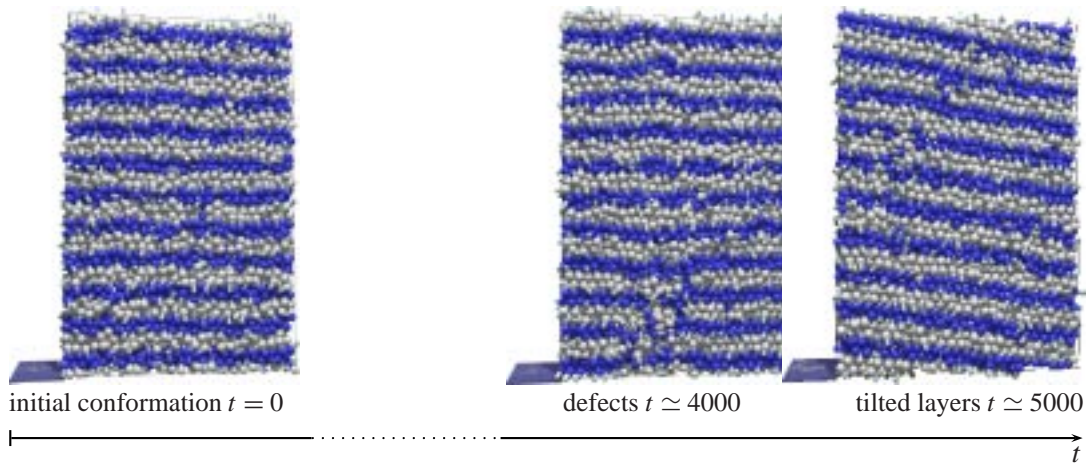


**Figure 5.23.:** The left image shows a snapshot the starting conformation for a simulation run under shear with a strain rate of  $\dot{\gamma} = 0.01$ . It stays under the given pressure value of  $p_{zz} = 0.33$  constant. Until  $t \simeq 4000$  a parallel orientation of the layers survives. Then defects develop which lead to a rearrangement of the layers within  $\Delta t = 1000$ . The right image shows the final conformation exhibiting tilted layers.

$t = 4000$  the system shows a perfect parallel aligned lamellar system. Then defects develop and allow the reorientation of layers. Until the end of the simulation run the lamellae have reoriented and reordered.

9 9 9  
 8 8 8  
 7 7 7  
 6 6 6  
 5 5 5  
 4 4 4  
 3 3 3  
 2 2 2  
**1 1 1**  
 0 0 0

9 9 9  
 8 8 8  
 7 7 7  
 6 6 6  
 5 5 5  
 4 4 4  
 3 3 3  
 2 2 2  
 1 1 1  
 0 0 0

This behavior is perfectly consistent with the proposed mechanism of section 5.3.1 and hence with the . The layers need more space in their plane and tilted layer provides this space. When more space is available their effective thickness is lower and in that special isobaric ensemble ( $Np_zT$ ), as argued previously, the  $z$ -extension of the box is reduced, which is aparent from the data. Until the layers start to reorient their effective thickness cannot be reduced. Hence, besides the shear flow alignment of the director, the system remains in a meta stable state which is later destroyed by the evolution of defects which finally results in the new order.

In a pure  $NVT$  ensemble simulation defects do not have this reordering effect on the superstructure, as seen before (section 5.2.2). In the contrary the may produce under certain circumstances two phase coexistences, known as shear bands, which are going to be discussed in the next chapter. The present simulations reveal undulations as the only method under shear flow to compensate the effective shrinkage of the layers if the bending energy can be overcome.

This holds also for pure  $NpT$  ensemble simulations which has been checked both with the present system and the system used in section 5.2.2.

## 5.4. The Phase Transitions

Cates and Milner [CM89] and Fredrickson [Fre94] investigated the effect of shear on the order-disorder transition of DBCPs. They showed that in their model an isotropic to perpendicular transition occurs for high shear rates if the block are not too different.

Figure 5.24 shows again the phase diagram predicted by Fredrickson et al. which has been described in chapter 2. It exhibits in for values of the reduced strain rate  $\dot{\gamma}/\dot{\gamma}^* > 1$  two phase transition, a disordered-perpendicular, and a perpendicular-parallel. The stability limit for the parallel orientation ends within the perpendicular regime. At temperatures below  $\tau_{sz}$  and above  $\tau_p$  a perpendicular orientation is stable and a parallel orientation at least meta-stable.

In the simulation runs it turned out that a parallel orientation of the lamellae is stable for a very long time. No parallel-perpendicular transition has been observed for low strain rates (strain rates below and slightly above the onset of undulation). But an intropic to perpendicular transition is observable. A perpendicular orientation is stable for all investigated strain rates where a single orientation was present. (Phase coexistence (shear bands) will be discussed in the next chapter.) If Fredrickson's theory is applictable to the present situations, the model covers a region in the predicted phase diagram, where parallel and perpendicular orientations are both stable and the perpendicular one is favoured. Such a region is indeed present in Fredrickson's phase diagram. In figure 5.24 it is marked with a black spot. The lower reduced temperatures where a parallel orientation alone is stable may not be reachable, since the fluid-solid transition seems to lie above it.

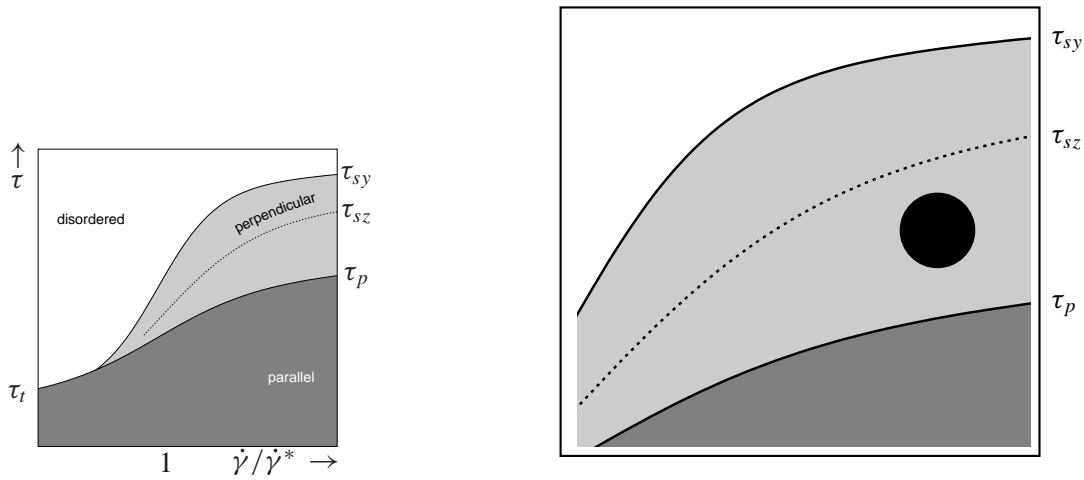


**Figure 5.24.:** The left sketch shows Fredrickson’s picture of the world in the reduced temperature – reduced strain rate diagram as seen in figure 2.11. The right sketch is a magnification of the the upper righth part of the previous one.  $\tau_{sy}$  and  $\tau_{sz}$  are the stability limits for the perpendicular orientation and the parallel respectively.  $\tau_p$  is the transition point for a perpendicular–parallel transition (see text). The black spot highlights the region where the present simulation model should live (see text).

#### 5.4.1. The Parallel to Perpendicular Transition

As seen in section 5.2.2 the parallel aligned orientation is stable for shear rates  $\dot{\gamma} < 0.4$  within the scope of the simulations. But the perpendicular orientation of the simulation conformations is more stable as seen in section 5.2.5 and there is no transition perpendicular–parallel which could be observed.

Experiments on diblock copolymers reveal both a perpendicular to parallel as well as a parallel to perpendicular transition, as mentioned in chapter 1. The analytic theory by Fredrickson et al. [Fre94] allows a parallel to perpendicular transition for DBCP system where both blocks have nearly the same viscosity, which is the case for the presented dimer–model.

The simulations to section 5.2.2 exhibit a transition from a parallel to a perpendicular orientation, too. It can be found at strain rates  $\dot{\gamma} > 0.04$ , where the parallel oriented phase starts to become instable. Figure 5.25 shows the decrease of the director in  $z$ -direction and its increase in  $y$ -direction with rising strain rate. The lines in the plot serve as a guide for the eye.

The  $z$ -component  $n_z$  of the director stay nearly constant until the transition is reach. It decreases rapidly to zero mean. The  $y$ -component  $n_y$  stays zero until the transition and jumps to high values beyond it. It does not reach its maximum value within the simulated time since some undulation in the shear gradient direction are present. The final conformation of strain rate  $\dot{\gamma} = .05$  was therefore simulated much longer and one can observe that the ondulation vanish and a steady state is reached. This undulation in  $z$ -direction can be observed in other investigated systems as well.

9 9 9  
8 8 8  
7 7 7  
6 6 6  
5 5 5  
4 4 4  
3 3 **3**  
2 2 2  
**1 1 1**  
0 0 0

9 9 9  
 8 8 8  
 7 7 7  
 6 6 6  
 5 5 5  
 4 4 4  
 3 3 3  
 2 2 2  
 1 1 1  
 0 0 0

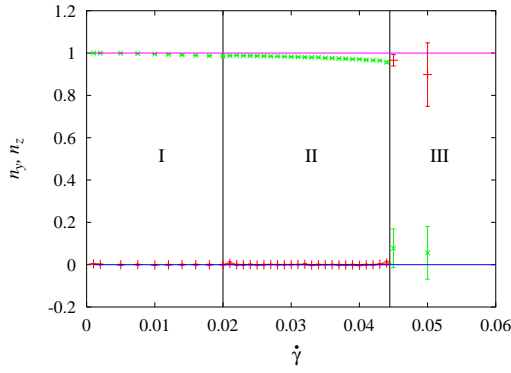


**Figure 5.25.:** Directors  $z$  and  $y$  component  $n_z$  and  $n_y$  as a function of the strain rate  $\dot{\gamma}$ . The lines serve as a guide for the eye. The regimes I and II are again the ones where a parallel orientation is (meta-) stable, in III only a perpendicular orientation can be found.

Figure 5.26 shows successive snapshots of conformation during their reorientation from parallel to perpendicular aligned layers at a strain rate  $\dot{\gamma} = 0.045$ . One can observe the evolution of defects in the layer structure. The layered structure fluctuates and the layers themselves rearrange in the perpendicular orientation without actually breaking up totally. The system shown here is the one investigated in the previous section. The strain rate was slowly increased to  $\dot{\gamma} = 0.04$  where the parallel orientation is still stable. Then the strain rate was set to  $\dot{\gamma} = 0.045$  and the transition could be observed. The rearrangement in the  $N = 97336$  particle system at the same strain rate looks very similar.

Comparing the snapshots of figure 5.26 with the proposed mechanisms in the first chapter one might speak of grain rotation with defect migration, as the mechanisms which drive the transition. The grain rotation mechanism was proposed for low frequencies and medium strain ( $\gamma_0 \approx 0.5$ ). In the simulation steady shear is applied and so the mechanism intuitively seems to be the one for the description of the transition. But much larger system sizes and defined grains are necessary to prove or disprove the picture rather than snapshots with a view to the time evolution within an arbitrary slice.

Back to the simulation, one can observe, if the strain rate is increased quite drastically, e.g., from  $\dot{\gamma} = 0.02$  to  $\dot{\gamma} = 0.05$  the intermediate configurations show no order. The lamellar structure is completely dissolved as it can be seen from measurements of the nematic order parameter and it takes quite long to build up a new perpendicular structure.

## 5.5. Conclusion and Outlook

The intention of this chapter was to test the two most promising theories which have been developed for the description of shear exerted on layered structures.

Steady shear was hence exerted to a model system within several simulation runs. A flow alignment of the director was found as predicted by Auernhammer et al. [ABP00]. In agreement with Auernhammer et al. [ABP00] the existence of an effective shrinkage of the layer thickness which in turn leads to undulations, has been found

The wave vectors of these undulations point in both, flow and vorticity direction, but the

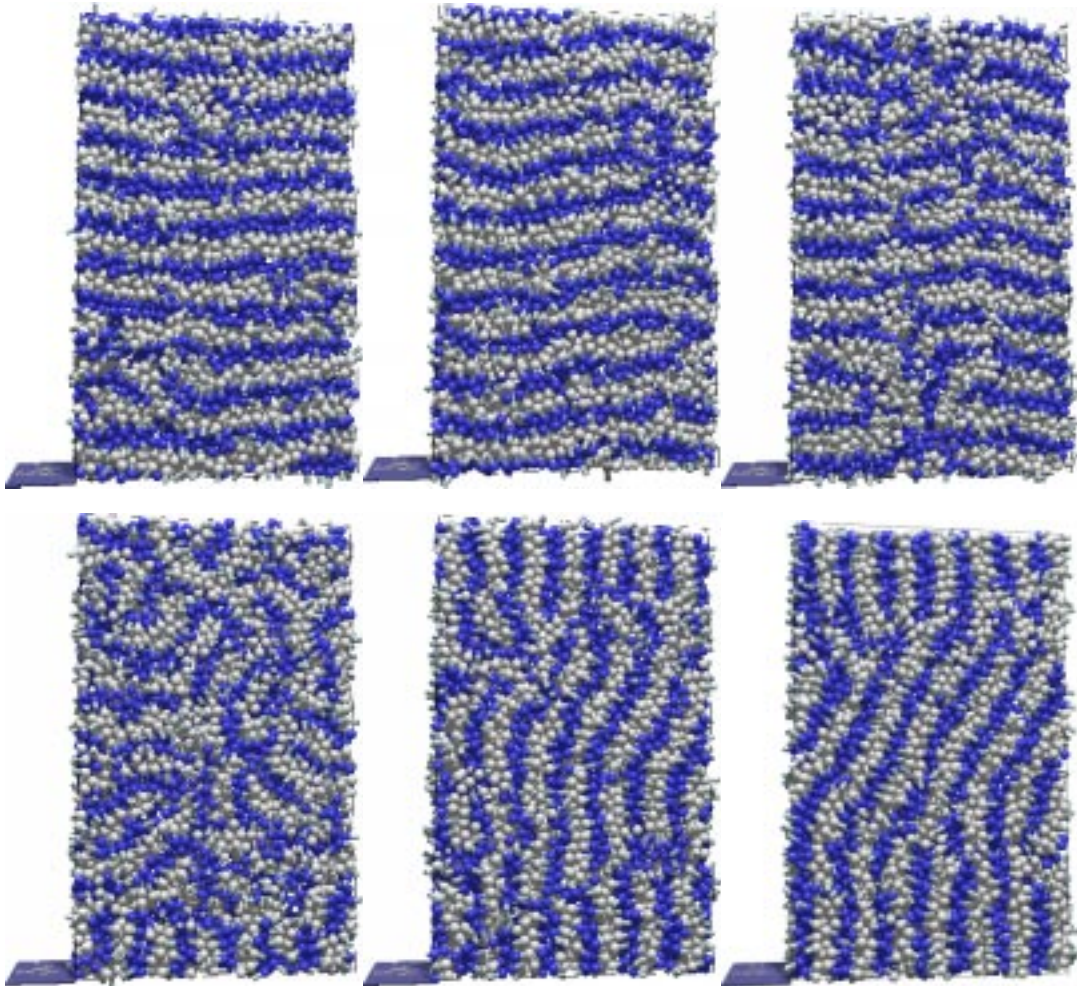


**Figure 5.26.:** Conformation snapshots of a transition from parallel to perpendicular orientation of the lamellae (left top to right bottom). The  $y$ - $z$ -plane of each conformation is shown. The initial conformation exhibits parallel oriented strata with undulation. During the transition defects evolve and smaller grains of different orientation can be observed. The final conformation is then perpendicular oriented. The elapsed time between two consecutive conformations is  $t = 1000$ .

9 9 9  
 8 8 8  
 7 7 7  
 6 6 6  
 5 5 **5**  
 4 4 4  
 3 3 3  
 2 2 2  
**1 1 1**  
 0 0 0

9 9 9  
 8 8 8  
 7 7 7  
 6 6 6  
 5 5 5  
 4 4 4  
 3 3 3  
 2 2 2  
 1 1 1  
 0 0 0

flow direction has not been checked for the occurrence of undulations by Auernhammer et al., before, and they have been seen for the first time in the presented simulations. It could be shown that the undulation wave in flow directions travels with time. Due to the low time resolution of the specific simulation runs in time, the trajectory has not been sampled. This might be interesting to have a look at it in future work. The behavior of the system below the onset of those matches the predictions by Auernhammer et al qualitatively. But it was found that the undulations are backwards bifurcating which makes it difficult to identify the onset as the predicted onset in Auernhammer's et al. theory. There a forward bifurcating system was assumed, since dilatation experiments, on whose description the theory is based, show this behavior. The model system exhibits a forward bifurcation for dilatations which is in coincidence with experiments and their description. An increase of the nematic order parameter at the onset of undulations in the case of shear was observed, but has not been understood, so far.

An analysis of the stress – strain rate behavior of the system reveals the possibility of coexisting orientations, so called shear bands, as discussed by McLeish and Ball in [MB86], and found in wormlike micelle systems by Britton and coworkers [BC97]. Indeed, a coexistence of isotropic and perpendicular aligned layers have been found and will be discussed in the next chapter.

A mechanism for the occurrence of undulation on molecular level has been proposed and successfully tested. But further more intense tests are necessary to support or disprove this mechanism ultimately.

Besides those considerations and simulations an efficient method for the determination of the bending modulus was found, which will certainly be applied to various systems which exhibit layer structures and where a director can be defined.

In chapter 2 Fredrickson et al.[Fre94, CM89] consideration about diblock copolymers were briefly reviewed. They state, that if both blocks in a diblock copolymer have the same bulk-viscosity, those copolymers should favour a perpendicular orientation when exposed to a shear flow. The dimeric systems in the simulations were designed to be symmetric in A- and B-block interactions. They have the same homopolymeric properties (A-fluid and B-fluid) and hence the same bulk viscosities. Those systems favour the perpendicular orientation and hence the theoretical prediction in this sense is fully supported. Note the fact that dimers are certainly not of the length which has been initially considered by the theory. In order to obtain a full view about the position of the present model in Fredrickson's phase diagram, it is necessary to introduce a possibility to alter the viscosities of the blocks which in principle can be done by the introduction of different interaction strengths  $\phi_{AA}$  and  $\phi_{BB}$ , of the AA and BB interactions.

In the first chapter several possible mechanisms for the reorientation and alignment of layered structures, developed by several experimentalists, were described. The proposed mechanism 'defect migration' is certainly present in the reorganisation process of layered structures under shear flow. It is likely that grain rotation mechanism has been observed as well. Certainly it is worth to identify grains during the realignment process and follow their behavior as time evolves. Since it is difficult to identify grains this task includes a considerable effort.

## 6. Shear bands

### 6.1. What are shear bands?

Shear banding is a phenomenon of coexisting regions of different strain rate. These regions, which are called *shear bands*, are separated by sharp interfaces. Usually such bands occur in systems of complex fluids under shear, whose dimensions are much larger than the molecular length. In those systems the super structure of the fluid interacts with the flow field and structural changes affect the viscosity of the fluid, which in turn modifies the flow field as seen in section 5.2.5.

Experimental examples for complex fluids with the ability to show shear bands range from lyotropic systems over entangled polymer melts to liquid crystals. Bagley et al. [BCW58] found a discontinuity in the flow curve of polyethylene (PE). Vinogradov et al. [Vin72, Vin73] investigated the flow behavior of polymers in cylindric tubes. They found a behavior which they called spurt effect. Figure 6.1 sketches this effect. The complex fluid (e.g. a PE

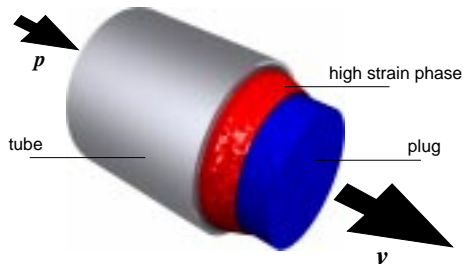


**Figure 6.1.:** Sketch of the spurt effect. A complex fluid is pressed through a tube under high pressure  $p$ . The Poiseuille flow regime is left and two phases coexist, a plug with no velocity gradient (blue) and a phase of high shear gradient (red).

melt) is pressed through a tube under high pressure. It leaves the Poiseuille flow regime and separates into two phases, a plug which exhibits no velocity gradient and a phase under high shear strain.

Shear bands have been found in various systems since then. E.g. in worm like micelles have been investigated by the Callaghan group [MC97, BC97, FC00]. They find a coexistence of an isotropic region with a well ordered one. Mair et al. [MC97] especially find that there may be not only a single interface but multiple interfaces. Liquid crystal systems have been investigated by Bonn et al. [BMG<sup>+</sup>98]. Their systems show inhomogeneities along both the flow as well as the vorticity direction.

Figure 6.2 sketches the situation of a non-monotonic stress strain rate relation, which is believed to be the reason for the occurrence of shear banding flows. For low strain rates the

9 9 9  
 8 8 8  
 7 7 7  
 6 6 6  
 5 5 5  
 4 4 4  
 3 3 3  
 2 2 2  
 1 1 1  
 0 0 0

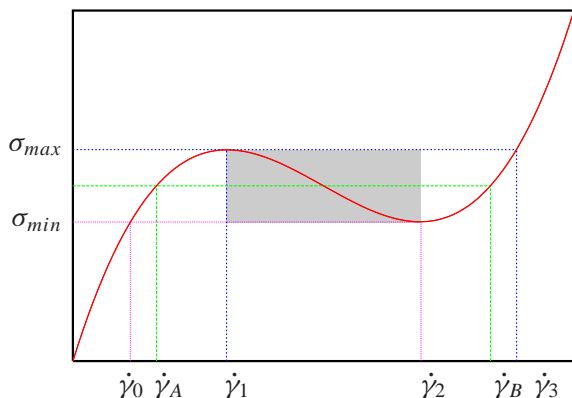


**Figure 6.2.:** Sketch of a non-monotonic stress strain rate relation. Shown is the stress,  $\sigma$ , as a function of the strain rate,  $\dot{\gamma}$ . The newtonian flow regime lies below a strain rate  $\dot{\gamma}_1$ , at which the stress takes on a local maximum. The region of decreasing stress,  $\dot{\gamma}_1 < \dot{\gamma} < \dot{\gamma}_2$ , is unstable. Systems with such strain rates separate into a high and low strain rate band under the same shear stress.  $\sigma(\dot{\gamma}_A) = \sigma(\dot{\gamma}_B)$  (see text).

stress is a monotonic increasing function and its maximum is reached at  $\dot{\gamma}_1$ . Beyond that point the stress decreases. In the polymer theory of Doi and Edwards, this behavior was interpreted as a complete alignment of the polymers to the exerted shear flow and  $\sigma(\dot{\gamma}_1)$  is there a global maximum [DE86]. But in experiments it has been observed that in some systems the stress increases again at a strain  $\dot{\gamma}_2$ . The regions of decreasing stress at strain rates  $\dot{\gamma}_1 < \dot{\gamma} < \dot{\gamma}_2$  was found to be unstable. The system separates into two different phases with different strain rates  $\dot{\gamma}_A$  and  $\dot{\gamma}_B$  but equal stress  $\sigma(\dot{\gamma}_A) = \sigma(\dot{\gamma}_B)$ . This behavior has been described for the case of entangled polymer melts by McLeish et al. [MB86], who have added a correction to the theory by Doi and Edwards [DE86].

But since then there has been significant amount of theoretical activity in this area. In the context of worm like micelles Spenley et al. considered shear banding as the result of multi-valued stress strain curve [SCM93, SYC96]. Homogeneous steady states are seen as unstable and the system separate into low and high shear rate phases.

Another class of work deals with fact that equilibrium phase transitions are shifted by the presence of shear. In this case the stress strain curve is effectively multivalued, and the high and low shear bands correspond to the coexisting equilibrium phases, which have different rheological constitutive behaviors [GF99, OL97]. This class will not be of relevance in this chapter.

Figure 6.1 shows a sketch of the spurt effect. Figure 6.3 sketches a similar situation for the case of a Couette or plate-to-plate like geometry. Here two phases under high shear are present (red areas) which kind of shield the plug from the moving plates. It turns out that

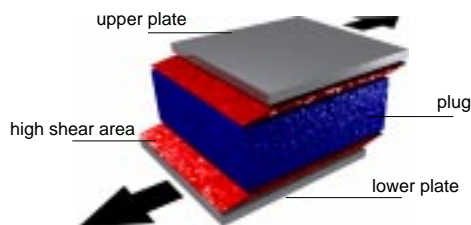


**Figure 6.3.:** Sketch of shear bands with plug flow. In a Couette cell or a plate-to-plate like geometry a complex fluid is sheared under high stress. Similar to the spurt effect (compare figure 6.1) a plug of material (blue) with no velocity gradient can be found in coexistence with two high sheared areas (red).

such a situation can be achieved within a simulation study. In section 5.2.5 it was argued that due to a non-monotonic behavior in the stress-strain rate curve a coexistence of parallel



and perpendicular aligned lamellae is possible. In a simulation study shear was applied to a large dimeric system ( $N \approx 2,000,000$ ) which was found to exhibit shear bands and plug flow under certain conditions. The occurrence and structure of those will be treated in the next sections.

## 6.2. Systems under Investigation

Two different system sizes have been investigated on the occurrence of shear bands. The *large* system contains nearly 2,000,000 particles ( $N = 1,990,656$ ) and the *medium* system is made up of  $N_S = 48668$  dimers. The aspect ratio of the large system is not equal one, since the initial intention was to investigate the  $y$ - $z$ -plane best for the occurrence of possible wave vectors in those directions. The ratio for the large system is 1 : 3 : 3. Figure 6.4 shows

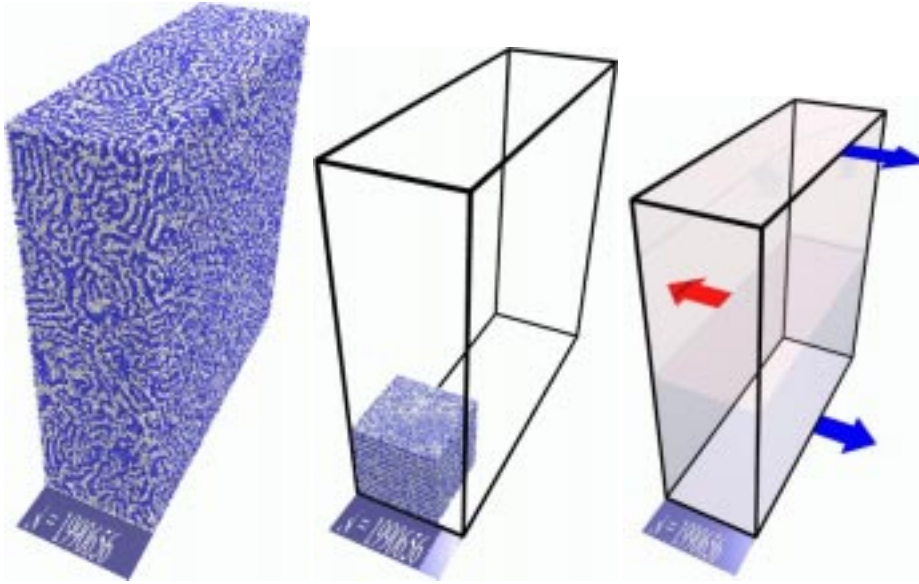


**Figure 6.4.:** Snapshot of the large system, size comparison with the medium system and directions of flow. On the left a “large” system containing  $N = 1,990,656$  particles is shown after a quench to  $\phi = 1.3$  and an equilibration for  $t = 2000$ .

The middle shows a simple size comparizon of the “medium” system containing  $N = 97336$  particles. It is embedded into the frame of the large system.

The right image shows the direction of shear flow in the large system. Again the sign at the bottom is parallel to the flow–direction ( $x$ ), the vertical is the  $z$ -axis.

at the left a conformation snapshot of the large system after a period of time,  $t = 2000$ , of equilibration. It shows a lamellar disordered structure which is certainly not in equilibrium. The middle image shows a size comparison between the large and the medium system. A conformation snapshot of a medium system is embedded into the frame of a large system. The right image shows the direction of shear for the large system. The flow–direction is again

9 9 9  
8 8 8  
7 7 7  
6 6 6  
5 5 5  
4 4 4  
3 3 3  
2 2 2  
1 1 1  
0 0 0

9 9 9  
 8 8 8  
 7 7 7  
 6 6 6  
 5 5 5  
 4 4 4  
 3 3 3  
 2 2 2  
 1 1 1  
 0 0 0

along the sign at the bottom of the image.

### 6.3. Shear Bands in Simulations

In first simulation runs the large system has been quenched from  $\phi = 0$  to  $\phi = 1.27$  and sheared at the same time with strain rates of  $\dot{\gamma} = 0.001$ ,  $\dot{\gamma} = 0.005$ , and  $\dot{\gamma} = 0.01$ .<sup>1</sup>

The systems at the two smaller strain rates behave as expected. They show the usual transition from the lamellar disordered state to a perpendicular orientation including defects and the velocity profile is linear. The situation is very different for the simulation with strain rate  $\dot{\gamma} = 0.01$ . The system shows in addition to the perpendicular alignment process of parts of the conformation an growing inhomogeneity in other parts. The velocity profile is not linear any more, it exhibits two different regions, regions of very low and quite high strain rate. Shear bands have occurred. Finally, one observes that there are two blocks moving with the same velocity,  $|v_x|$ , separated by small regions with a large velocity gradient. The results of the analysis of this final conformation are accumulated in figure 6.5.

The first graph of figure 6.5 shows the density profile of the conformation in shear gradient direction. The density is highest in the ordered phases ( $\rho \approx 0.9$ ) and very low in the middle of the disordered regions ( $\rho < 0.75$ ). This situation is reflected in the behavior of the order parameter,  $S(z)$ , which is plotted in the second graph,  $\times$ -Symbols. It takes on its maximum values in the regions of high density and shows nearly no order in the regions of low density. This leads to the preliminary conclusion, that the low density phase is completely disordered, as one directly assumes from a view to these regions in snapshot of the conformation. Having a look at the flow and gradient components of the director within the disordered regions, one observes here for the flow and for the shear gradient components,  $n_x$  and  $n_z$  non-zero values. The vorticity component of the director,  $n_y$ , completely follows the behavior of  $S(z)$ , high values in the ordered phase (of course, a perpendicular orientation is present), and low values in the disordered one. Which supports the conclusion, that the low density phases are not oriented. The bottom plot shows the non-linear velocity profile. It clearly reveals that two plugs are moving in opposite direction absorbed in the low density regions.

The situation turns out to be similar in many things but different in some other in the following situation. A large system is exposed to shear after it has been quenched to  $\phi = 1.27$  and equilibrated for some time,  $\Delta t = 1200$ , which leads to a lamellar disordered state. After further  $\Delta t \approx 5000$  the configuration shown in figure 6.6 was reached.

This final conformation of the simulation run was then analyzed in the same way as the previous one. The velocity profile  $v_x(z)$  shows regions of no shear gradient (for  $0 < z < 35$ ,  $60 < z < 95$ , and  $z > 180$ ) similar to figure but these regions are smaller. Hence the regions exhibiting a shear gradient are larger but the strain rate in this region is nearly the same as in the previous case. The density profile now shows a trough profile with a pronounced bottom. The high density regions can in comparison with the order parameter  $S(z)$  be identified as

<sup>1</sup>This simulation have been performed in the microcanonical ensemble, since the DPD-thermostat was available at that time. All others are performed under constant temperature with the DPD-thermostat.

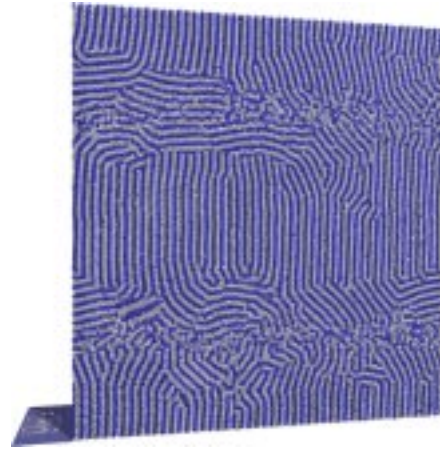
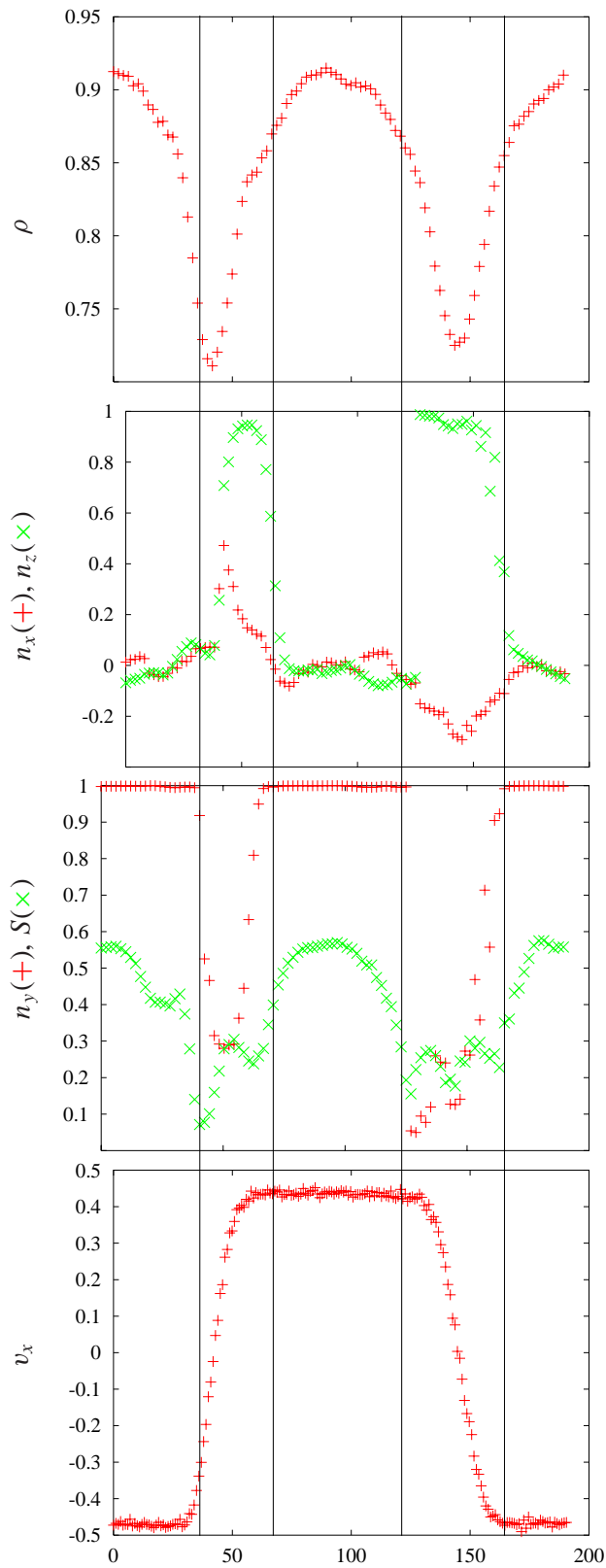


**Figure 6.5.:** Analysis of a conformation ( $N = 1,990,656$ ) snapshot. The local density, the director's components, the nematic order parameter, and the velocity in flow direction are plotted as a function of the system height,  $z$  (velocity gradient direction). The system which was simulated in the  $NVE$ -ensemble and exhibits shear bands in form of a perpendicular aligned smectic plug and a non-smectic phase at lower density with a high velocity gradient. All bands are not equal in width. The above snapshot images the molecular structure within the system. Obviously, the system contains many defect structures.

9 9 9  
 8 8 8  
 7 7 7  
 6 6 6  
 5 5 5  
 4 4 4  
 3 3 3  
 2 2 2  
 1 1 1  
 0 0 0

9 9 9  
 8 8 8  
 7 7 7  
 6 6 6  
 5 5 5  
 4 4 4  
 3 3 3  
 2 **2 2**  
 1 1 1  
 0 0 0

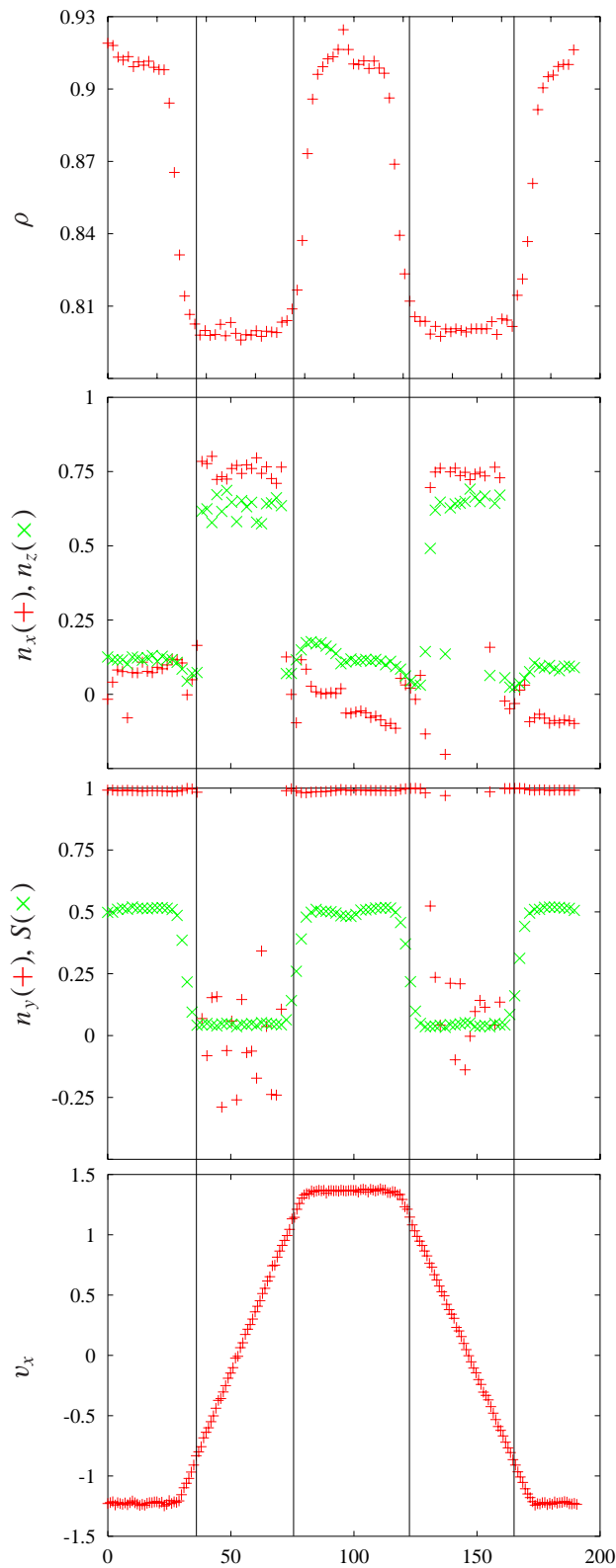


**Figure 6.6.:** Analysis of a conformation snapshot at  $\Delta t = 5380$  and strain rate  $\dot{\gamma} = 0.03$ . Graphs of different magnitudes as a function of the velocity gradient direction,  $z$ , are plotted on the left and above an image of the conformation snapshot is shown. The system clearly exhibits shear bands in form of a plug with no velocity gradient and a second phase with a high velocity gradient. The density in the smectic phases is higher than in the non-smectic ones. Surprisingly the director shows on average no  $y$ -component in the non-smectic regions, whereas the alignment of the smectic one is clearly perpendicular oriented.

smectic ordered regions, the low density regions show no layered structure. The direction of the smectic regions is again perpendicular, as seen from the behavior of the directors components in this regions. Surprisingly, the director shows no  $y$ -component in the non-smectic regions. If those regions were completely disordered, it should take on some value which reflects the main orientation of the molecules at this point of time. So a value around zero is surprising, since the values of  $n_y(z)$  have been quite low in the disordered region in the previous case, too. This could be an indication for an ordering of the molecules, which might reside on average in the flow–shear–gradient plane. Since the flow direction is involved, each molecule has either to tumble or to rotate around an axis along the vorticity direction. This will be investigated now.

### The Disordered Looking Phase

In order to test the above assumptions about a possible rotation or tumbling of the molecules, the time evolution of the motion of the molecules in the disordered phase has to be investigated. The magnitude  $\vec{m}(t)$ , defined as follows,

$$\vec{m}_1(t - t_0) \equiv \langle \vec{n}_i(t) \times \vec{n}_i(t_0) \rangle, \quad (6.1)$$

carries information about a possible tumbling or rotation of the molecular axes on average.  $\vec{n}_i(t)$  denotes the molecular axis of dimer  $i$  at time  $t$  and the brackets stand for the average over all molecules in the system followed by the average over all time slices of length  $t$ . For convenience,  $t_0 = 0$  in the following.  $m_1(t) \equiv |\vec{m}_1(t)|$  should be constant for long times if

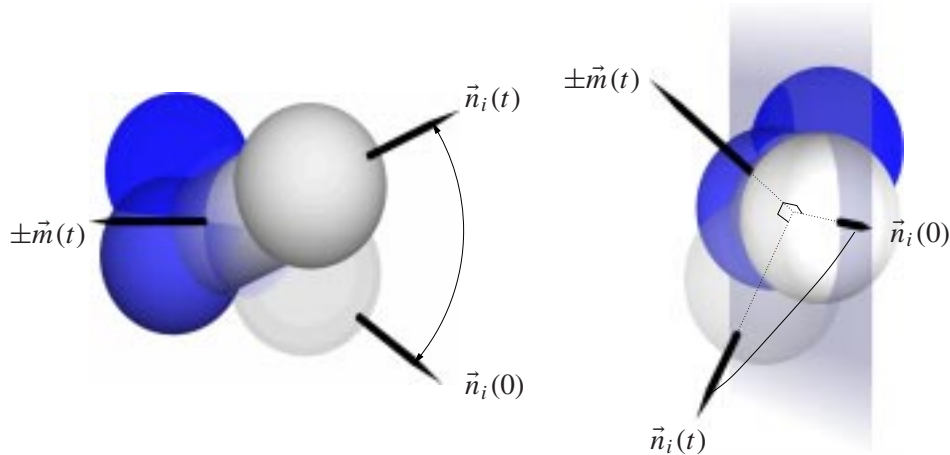


**Figure 6.7.:** Tumbling and rotation of a molecule. Left: The two different orientations of the molecular axes result in a vector  $\vec{m}(t) \equiv \vec{n}_i(t) \times \vec{n}_i(0)$ . A simple average over all  $\vec{m}(t)$  has only non-zero components if the molecules have some kind of order (see text).

Right: A molecule tumbles around its mean rotation plane (violet plane in the sketch). So the magnitude  $\vec{m}(t)$  is distributed around the rotation plane's normal and its variance can be measured. An out of plane rotation of many molecules around one main-plane is also possible and cannot be distinguished in the averaging process.

the molecules rotate uncorrelated. An uncorrelated rotation should occur since the molecules

9 9 9  
8 8 8  
7 7 7  
6 6 6  
5 5 5  
4 4 4  
3 3 3  
2 2 2  
1 1 1  
0 0 0

9 9 9  
 8 8 8  
 7 7 7  
 6 6 6  
 5 5 5  
 4 4 4  
 3 3 3  
 2 2 2  
 1 1 1  
 0 0 0

are likely to interact. A correlated rotation would result in an oscillatory functional behavior of  $m_1(t)$ . If  $m_1(t \rightarrow \infty)$  equals zero, it is still possible that the molecules tumble. This can then be detected by using the second moment,

$$(m_2)_i(t - t_0) \equiv \langle (\vec{n}_m(t) \times \vec{n}_m(t_0))_i \rangle^2. \quad (6.2)$$

For computational reasons<sup>2</sup> the medium system has been checked for the rotation of molecules in the disordered looking region. Also this system exhibits shear bands under high strain rates. In the contrary to the large systems it does not show plug flow but regions of different strain rate are present. Figure 6.8 shows velocity profile and  $S$ -value as a function of the shear gradient direction. In the low strain rate regions ( $0 < z < 8$ ,  $22 < z < 28$  and  $43 < z$ )

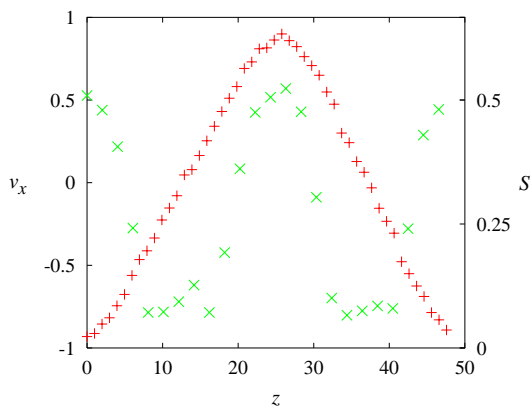


**Figure 6.8.:** Velocity profile and  $S$  value for a medium system under high shear strain. The non-linear velocity profile ( $\times$ -symbols) exhibits low strain rate regions for  $0 < z < 8$ ,  $22 < z < 28$  and  $43 < z$  and in those regions the smectic order is high. The other regions of high strain rate seem to be disordered.

high  $S$  values are present and perpendicular aligned lamellae can be found inspecting the components of the director (Those are not displayed, but the reader may convince himself by having a look at the conformation snapshot of figure 6.10). The high strain rate regions look disordered.

But before the magnitude  $\vec{m}_1$  is investigated, it should be worth having a closer look at the time evolution of the director's components in the disordered phase. Figure 6.9 shows graphs of the each director components,  $n_i$  ( $i = x, y, z$ ), as a function of the gradient directions for different points of time. Obviously, the  $n_i$  do not vary significantly, even for a long period of time. This behavior is normal for an ordered phase which does not change its orientation during the span of time, but it is remarkable that the behavior is the same for the disordered regions. The  $S$ -value is very low in this regions so the variation of the molecular axes to the direction of the director is large. But it still seems that there is some kind of order even if this effect is weak. This behavior will be analyzed further in combination with the following results.

Figure 6.10 displays the results of the proposed analysis towards a rotation or tumbling of at least some of the molecules. Again a plot of the order parameter  $S$  as a function of the shear

<sup>2</sup>A conformation of  $N = 1,990,656$  particles including positions and velocities has a size of roughly 50 MBytes. Writing this amount of data every few time steps to a disk consumes much time and space, transferring those data across the Internet costs many hours.

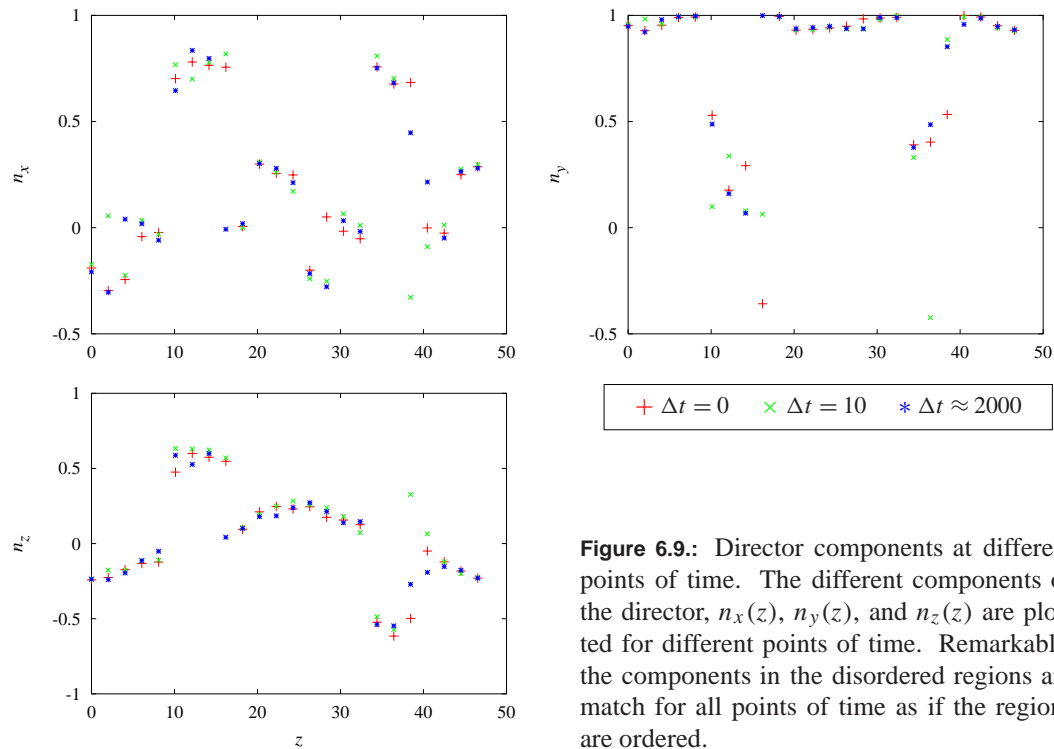


**Figure 6.9.:** Director components at different points of time. The different components of the director,  $n_x(z)$ ,  $n_y(z)$ , and  $n_z(z)$  are plotted for different points of time. Remarkable, the components in the disordered regions are match for all points of time as if the regions are ordered.

gradient direction is shown (upper left) in order to facilitate locating the disordered looking regions. The plot in the upper right shows the different components of  $\vec{m}(z)$ , obtained from consecutive pairs of conformations with  $\Delta t = 2$ . The green  $\times$ -symbols and the blue  $*$ -symbols denote the flow component  $m_x$  and the gradient component  $m_z$ . These average out to zero which means that there is no common rotation in any plane with layer normals parallel to  $\hat{x}$ ,  $\hat{z}$ , or any vector inbetween. The graph for  $m_y(z)$  shows values for from  $m_x$  and  $m_z$  in the high strain regions. In the lower left graph  $m_y(z)$  is plotted for different time differences ranging  $\Delta t = 0.1$  to  $\Delta t = 5$  (see legend).  $m_y$  is growing with increasing spans of time but its growth rate slows down. In order to see when a plateau was reached or an oscillation takes place, the system has to be observed for longer time spans. Figure 6.11 shows the maximum values of  $m_y$  as a function of the time span  $t$ .  $m_{y,\max}(t)$  grows with time until it reaches a maximum at  $t = 15$  and decreases again to zero for  $t = 100$ . There is obviously a correlation of particle movements for a limited amount of time ( $t = 15$ ) which decays afterwards and the particles move uncorrelated for long times. This excludes the possibility of a correlated rotation of molecules in the disordered phase. But it also excludes a steady rotation of all molecules. What remains is a tendency that molecules are preferred rotated by the shear field within the flow-shear-gradient plane.

Back to the values of the directors components in this phase. The  $x$ - and  $z$ -component are remarkable similar. So the director points along the shear field with angle of a 45 degree, and this does not change in time. The director is the eigenvector to the largest eigenvalue of the

9 9 9  
8 8 8  
7 7 7  
6 6 6  
5 5 5  
4 4 4  
3 3 3  
2 2 2  
1 1 1  
0 0 0

9 9 9  
8 8 8  
7 7 7  
6 6 6  
5 5 5  
4 4 4  
3 3 3  
2 2 2  
1 1 1  
0 0 0

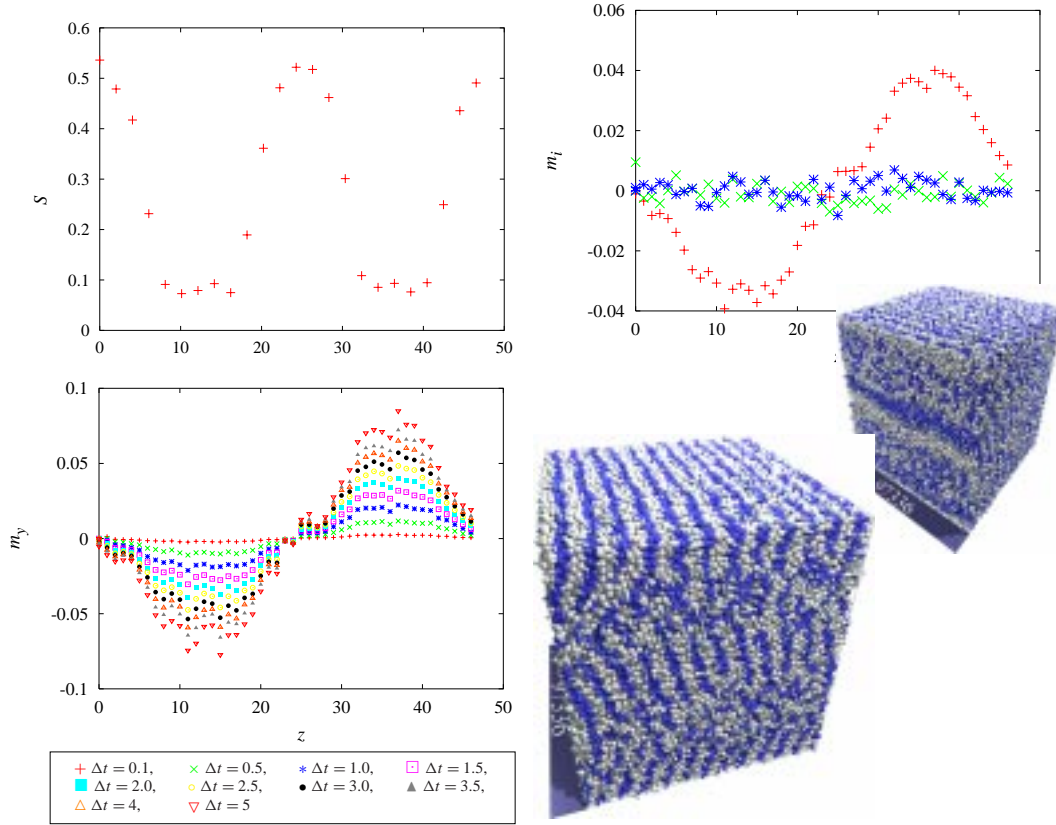


**Figure 6.10.:** Tumbling of dimers in the medium size system. The upper left graph shows again the  $S$ -value as a function of the shear gradient direction,  $z$ . The vorticity component of the magnitude  $\vec{m}$  is plotted as  $m_y(z)$  in the lower left graph for several time steps, as shown in the legend. The values for  $m_y$  increase in the regions of low  $S$ -values with time. For  $\Delta t = 2.0$  all components of  $\vec{m}(z)$  are plotted in the upper right graph. The flow and the shear gradient components,  $m_x$  ( $\times$ -Symbol) and  $m_z$  ( $*$ -Symbol) fluctuate around zero in all regions of the system. From a snapshot of the configuration on can distinguish ordered, high  $S$ -value, regions and low  $S$ -value regions which look disordered.

true<sup>3</sup> nematic order parameter  $\underline{Q}$ , which was defined by

$$Q_{ij} = \frac{3}{2} (\langle \hat{n}_i \hat{n}_j \rangle - \frac{1}{3} \delta_{ij}). \quad (4.10)$$

Now the molecular axes in equilibrium can be written as  $\hat{n} = (\cos \phi \sin \vartheta, \sin \phi \sin \vartheta, \cos \vartheta)$ . Due to the presence of the shear flow the  $x$ -coordinate has a constant shift,  $x' = x + \alpha z$ , and hence the molecular axes are given by

$$\hat{n}'_i = \begin{pmatrix} \cos \phi \sin \vartheta + \alpha \cos \vartheta \\ \sin \phi \sin \vartheta \\ \cos \vartheta \end{pmatrix}. \quad (6.3)$$

<sup>3</sup>see chapter 2



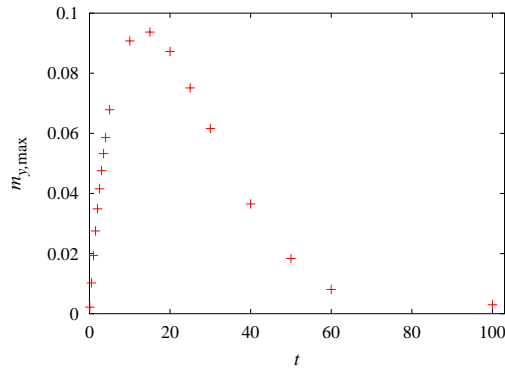


**Figure 6.11.:**  $m_y$  as a function of the time span. The maximum values of  $m_y$  grow with increasing time span until they reach a plateau.

Supposing that  $\hat{n}_i$  and  $\hat{n}_j$  are independent and uncorrelated (isotropic phase), in the above equation (eq. (4.10)) the average can be carried out separately:

$$\langle \hat{n}_i \hat{n}_j - \frac{1}{3} \delta_{ij} \rangle = \langle \hat{n}_i \rangle \langle \hat{n}_j \rangle - \frac{1}{3} \delta_{ij} \quad (6.4)$$

For a continuum one can easily now deduce the matrix

$$\underline{Q} = \begin{pmatrix} (\alpha/(2\pi))^2 & 0 & \alpha/(2\pi) \\ 0 & 0 & 0 \\ \alpha/(2\pi) & 0 & 1 \end{pmatrix} \quad (6.5)$$

The eigenvector to the largest eigenvalue points along  $(1, 0, 1)$ , the same direction which has been found for the director in the disordered looking phase.

Hence, the disordered looking phase is indeed disordered but it exhibits short time correlations, and the found director components are the same which one expects for shear flow conditions and an isotropic phase.

### Shear Crystallization

In the beginning of this section it was pointed out, that the medium system does not exhibit plug flow, but the large system, as seen in the previous section do. The evolution of plug flow in the large system simulated at  $\dot{\gamma} = 0.03$  is shown in figure 6.12.

The time evolution of the velocity profile is shown in the left graph, the evolution of the density profile is plotted in the right one. With the occurrence of plug flow, which can be identified by the occurrence of non-gradient regions, the density profile clearly shows troughs (for  $\Delta t > 2000$ ). The high density regions exhibit values of  $\rho > 0.9$  which should be beyond the equilibrium solid–fluid transition. The start to those high values can be observed in the two peaks at  $\Delta t = 1200$ . This implies that *shear crystallization* sets in, and the plugs are crystallized material, while the shear happens in the low density, fluid phase. This observation certainly has to be investigated in more detail.

9 9 9  
8 8 8  
7 7 7  
6 6 6  
5 5 5  
4 4 4  
3 3 3  
2 2 2  
1 1 1  
0 0 0

9 9 9  
 8 8 8  
 7 7 7  
 6 6 6  
 5 5 5  
 4 4 4  
 3 3 3  
 2 2 2  
 1 1 1  
 0 0 0

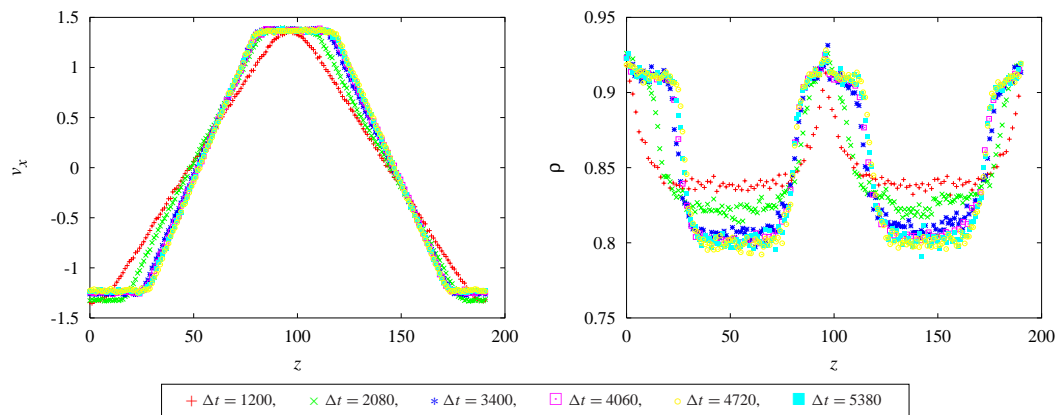


**Figure 6.12.:** The evolution of plug flow. The left graph shows the time evolution of the velocity profile  $v_x(z)$ . It evolves from a shear banded profile to a plug flow profile. The right graph shows the density profile as a function of the shear gradient direction. Troughs are developing as the velocity profile shows plug flow.

## 6.4. Defects and Defect Structures

Especially the large systems show various defect structures in their ordered regime. These defect structures might be similar to those which occur in real diblock-copolymer systems. On the snapshots of the conformation one can easily observe different tilt boundaries. Gido and Thomas [GT94] investigated those types of boundaries in lamellar diblock copolymer systems and distinguish between three morphologies: The *chevron* (denoted C), the *omega* (denoted  $\Omega$ ) and the *T-junction* type (denoted T). Figure 6.13 sketches these boundary morphologies. The chevron boundary, right sketch in the figure, is a continuous bend of the



**Figure 6.13.:** The three tilt boundaries found by Gido et al. [GT94], the chevron, the  $\Omega$ -type and the T-junction.

lamellae structure across the grain boundary. (Grains are regions of equal orientation of lamellae.) A variant of this chevron type is the omega tilt boundary which shows some kind of  $\Omega$  shaped bends directly at the grain boundary. These type of boundary is observed at higher tilt angles than the continuous bend. At the third type of boundary, the T-junction,

lamellae on the one side simply terminate. This allows the highest possible tilt angle.

At least two of those boundary structures are observable in the conformation snapshots as well, chevrons and T-junctions. Figure 6.14 shows magnifications of regions exhibiting interesting grain boundaries of a conformation snapshot. a) is a magnification of an upper left

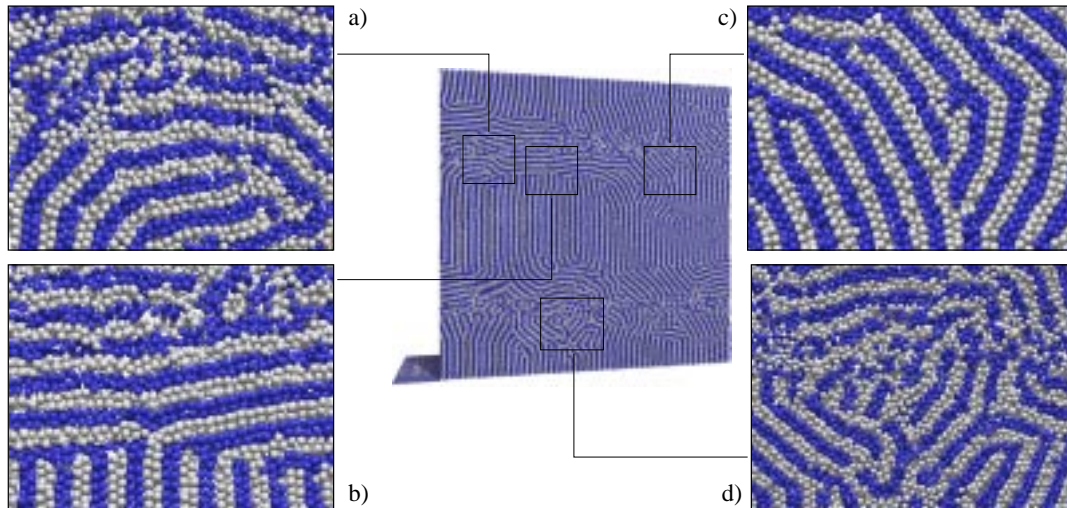


**Figure 6.14.:** Defects structures in the large system

part of the conformation snapshot, which is located near the disordered band structure. It shows clearly chevron structures in its middle right part. From the middle to the lower left three lamellae are tilting under a little higher angle than the previous describes chevrons. Some of those bend looks  $\Omega$  shaped but in direction from the lower middle to the upper left they break apart, as they approach the disordered shear band. b) shows a magnification of multiple T-junctions in its lower part. Vertical lamellae terminate at the grain boundary, horizontal continue. In c) apart from chevron like structures tilt boundaries can be found which are not mentioned by Guido and Thomas in [GT94]. They might be described as U-shapes and have been observed by Polis and Winey in [PW96] where kink band structures have been observed in a diblock copolymer melt under steady shear. Here a lamella terminates and is surrounded by others in a U-shape structure.

All of the mentioned structures are present in magnification d). In the lower right part a U-shape type boundary is followed by boundaries of  $\Omega$ -type.

There are certainly not only defect structures in form of tilt boundaries present in the systems. Focal conics, e.g., could occur as well, but they are at least not visible on the shown snapshots of figure 6.14 and the figure of the previous section 6.3 and 6.6.

9 9 9  
8 8 8  
7 7 7  
6 6 6  
5 5 5  
4 4 4  
3 3 3  
2 2 2  
**1 1 1**  
0 0 0

9 9 9  
 8 8 8  
 7 7 7  
 6 6 6  
 5 5 5  
 4 4 4  
 3 **3** 3  
 2 2 2  
 1 1 1  
 0 0 0

## 6.5. Conclusion

One of the intrinsic properties of the shear algorithm is, that it leaves it to the system to choose the best velocity profile. Usually this profile is linear as seen in the previous chapter, but under certain condition it is possible, that the system chooses a non-linear profile and shear bands occur.

Shear bands and plug flow have been observed in simulations as a coexistence of well ordered perpendicular aligned lamellae and an isotropic phase. This isotropic phase was found to exhibit a large shear gradient while the ordered region show only a weak or even no velocity change along the  $z$ -direction.

The behavior of the director in the isotropic phase raises the question if there might be some order hidden. The investigation of a newly introduced order parameter revealed a correlation of the molecular rotation lasting for some time. The molecules are found to exhibit a tendency to be preferably rotated by the shear field within the flow-shear-gradient plane. So the disordered phase is indeed isotropic but it reveals short time correlated movements of the molecules.

Another remarkable observation is that similar strain rates can be found in the disordered regions of the different investigated large systems under high strain rates, and the plugs showed hence different widths.

These plugs, again, have been found to be shear crystallized structures. The process of the crystallization could be observed, but the time resolution of the conformational snapshots was too low in order to see the starting of this process. Here more work is needed in order to make established statements about the mechanism.

The shear crystallized regions show defect structures as they can be observed by TEM images of diblock copolymer melts. In order to count and automatically classify defect structures in crystalline and fluid systems a program has been developed which is in principle able to identify a defect and follow the time evolution via a triangulation of the sheets. But the roughness of the layers in the fluid phase produces unfortunately detection errors. This could be compensated by using longer molecules which show a lower roughness of the interfaces and hence an enhanced layer coherence and reduced failure of defect detection.

# Conclusion

A novel simulation model for the investigation of complex fluids such as amphiphiles and diblock copolymers has been introduced. It is much more effective in molecular dynamics simulation than present models due to the limitation in the range of interaction. The equilibrium properties of this model have been tested in order to avoid complications such as an application in the unwanted neighborhood to a phase transition. It was shown that this model is well suited to investigate the intended problems.

A parallelized version of an existing shearing algorithm was developed and extended to support a steady strain rate. Especially this shearing algorithm has the advantage over commonly applied ones that it does not imply any velocity profile. Since most equilibrium thermostatting methods are not valid under non-equilibrium conditions, the DPD thermostat which incorporates the requirements of a non-equilibrium method has been parallelized and implemented, as well. The combination of both algorithms is a powerful tool for the investigation of non-equilibrium properties of the model system.

It has been shown that the theoretical work on smectic LC under shear flow by Auernhammer et al. [ABP00] is qualitatively in good agreement with the results found due to the computer simulations. There is even a quantitative agreement of theory and simulation in some parts. In others it has been shown that some assumptions in the theory turned out to be a little oversimplified. These findings will be taken into account for an extension of the theory (which is under development at the time these letters are written).

But most important, it could be confirmed that indeed undulations are the mechanism to compensate an effective dilatation for the case of a present shear flow as well as for a stretch deformation.

The comparison of simulation results with another theoretical approach by Fredrickson et al. [Fre94] has not revealed any disagreement, although the model does not meet the theory's assumptions in many points. But more intense work is certainly needed in order to complete such a comparison, which seems to be sensible on the basis of the obtained results.

For high strain rates shear bands, plug flow, and shear crystallization could be observed for the first time in a simulation. An isotropic band was found to ingest the most of the shear strain and an ordered phase moved as a plug. But since shear bands are best observable in large systems containing millions of particles, only a limited understanding of the ongoing processes were reached.

It is certainly a good idea to resume work especially on this field which is likely to lead to an enhanced understanding of these kind of problems which are present for nearly every

9 9 9  
 8 8 8  
 7 7 7  
 6 6 6  
 5 5 5  
 4 4 4  
 3 3 3  
 2 2 2  
 1 1 1  
 0 0 0

complex fluid.

The investigation of non-equilibrium of complex fluids by simulation requires due to the presence of many length scales large system sizes. Fortunately the parallelization of densed systems is simple and parallelized algorithms for shear and thermostating could be developed and implemented. But nevertheless the simulation of those system sized as the investigated need an considerable amount of computing time and data space. This has to be taking for further investigation.

### Outlook and Perspective

In the conclusion of the fifth chapter is has been suggested, that changing the symmetry in the interaction to different values of the potential depth for AA and BB interaction might lead to a prove or disprove of Fredrickson theory in relation to this model. A disprove in the for this model does not mean that this theory might not work for diblock copolymers in general, since the present model does not match all assumptions of the theory. So a small test simulation has been carried out with the small  $N = 10000$  particle system. The parameters for AA and BB interactions have been chosen to be  $\phi_{AA} = 1.0$ , which is lower than before, and  $\phi_{BB} = 1.5$  which is higher than before. So a viscoelastic contrast in the sense of Winey et al. has been introduced. That system has been set up in a parallel alignment of its lamellae and exposed to shear flow. The strain rate was increased in  $\Delta\dot{\gamma} = 0.005$  steps until  $\dot{\gamma} = 0.095$  has been reached. This strain rate is roughly double the rate of the parallel to perpendicular transition of the symmetric interaction system (section 5.4). But in this system incorporating the unsymmetry in the like particle interaction, the layers are still **parallel** aligned. Hence the parallel orientation of the lamellae is more stable than without a viscoelastic contrast. This is observation is in perfect agreement with experiments and theory.

But further work is needed now to find the precise location of the phase transition as a function of the viscosity difference of the particle types.

Though throughout this work only model dimer melts were considered, the introduced model is of course able to model other kinds of molecules as well. Binary and ternary system are thinkable including monomers of type A and B as solvent particles and more complicated types of amphiphiles. In the following simulation a microemulsion with a so-called bola surfactant of the structure ABBBBA was simulated. The system is a binary system of A-fluid and the surfactant with an concentration  $c_s = 0.4$ . The total system contains  $N = 27000$  particles. Figure E.1 shows a configuration snapshot of this system. The interaction parameters were chosen  $\phi_{\phi AA} = \phi_{BB} = 1.3$ .

These two points show that there are plenty of possibilities of further investigations in equilibrium as well as out-of-equilibrium on the basis of this model.

## Summary of the Important Points of the Work

- A novel model for the efficient simulation of amphiphilic system has been introduced.
- Nearly a full agreement with non-equilibrium liquid crystal theory could be seen. Undulations are the mechanism to compensate an effective dilatation for the case of a present shear flow as well as for a stretch deformation.
- No disagreement with non-equilibrium diblock copolymer theory has been found.
- The occurrence of shear bands has been observed in simulations for the first time.

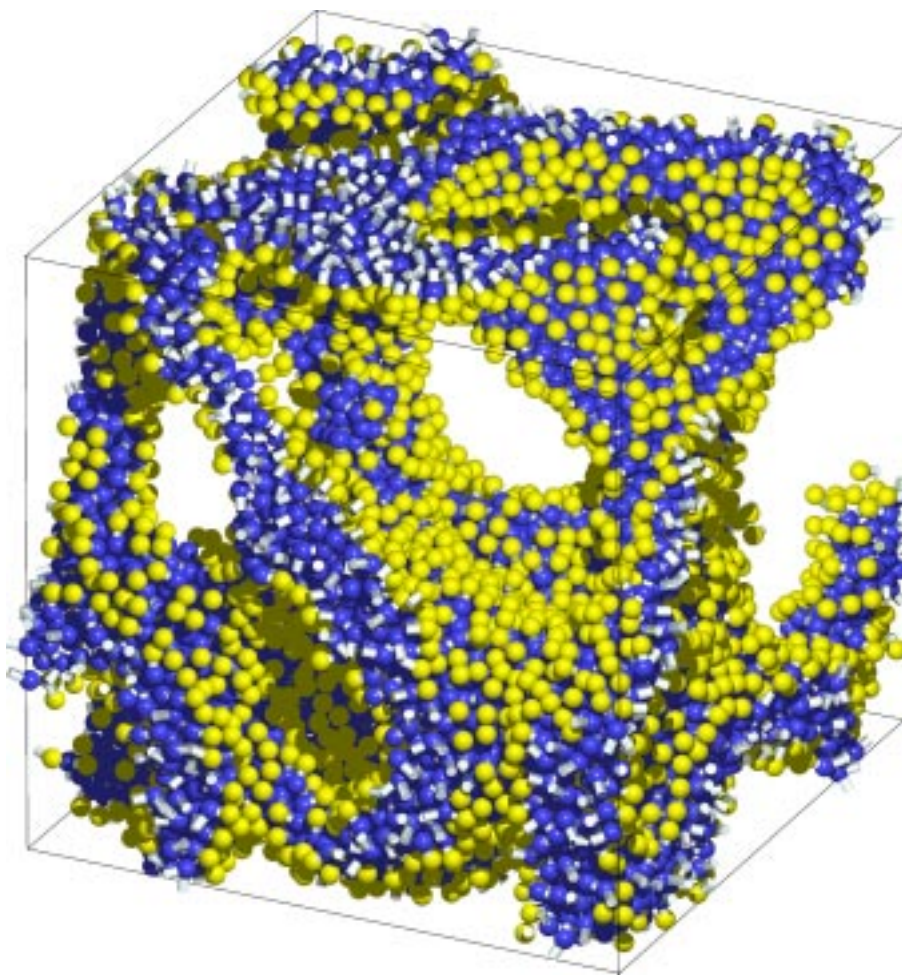


**Figure E.1.:** Snapshot of a bola surfactant system. The system is binary and contains type A–fluid monomers (not shown) and ABBBA-type bola surfactants of concentration  $c_s = 0.4$ . The cubic system contains  $N = 27000$  particles and was simulated with  $\phi_{AA} = \phi_{BB} = 1.3$ . (A particles yellow, B particles blue)

9 9 9  
8 8 8  
7 7 7  
6 6 6  
5 5 5  
4 4 4  
3 **3 3**  
2 2 2  
**1 1 1**  
0 0 0





*Pursuing it with eager feet, Until it joins some  
large way Where many paths and errands meet  
And whither then? I cannot say  
Bilbo Baggins [Tol54]*



# A. List of Abbreviations and Symbols

Table A.1.: Abbreviations and Symbols

A,B	types of monomers
BCP	block copolymer
DBCP	diblock copolymer
DPD	dissipative particle dynamics
FMP	Florian Müller Plathe
LAOS	large amplitude oscillatory shear
LC	liquid crystal
LDE	linear differential equation
MD	molecular dynamics
NEMD	non-equilibrium molecular dynamics
ODT	order disorder transition
PBC	periodic boundary conditions
PE	polyethylene
PEE	polyethylene
PEP	polyethylpropylene
PI	polyisoprene
PS	polystyrol
SAXS	small angle x-ray scattering
SANS	small angle neutron scattering
TEM	transmission electron microscope
<hr/>	
$A$	area
$B_0$	layer compression modulus
$B_1$	coupling between director and layer normal
$\gamma_{ij}$	strain tensor
$\dot{\gamma}$	strain rate, shear rate
$\dot{\gamma}_i$	intrinsic strain rate
$\dot{\gamma}_e$	effective strain rate

$\dot{\gamma}^*$	reduced strain rate
$d$	layer thickness
$\eta$	shear viscosity
$\vec{F}$	force
$\mathfrak{F}_{\text{el.}}$	elastic free energy
$G^*$	complex shear modulus
$G'$	storage modulus
$G''$	loss modulus
$\mathcal{H}$	Hamiltonian
$K$	layer bending modulus
$k$	spring constant
$K_1$	director splay modulus
$K_2$	director twist modulus
$K_3$	director bending modulus
$k_i$	scattering vector
$L_i$	simulation box extension
$\mathbf{L}$	Liouville operator
$\mathcal{L}$	Langrangian
$m_i$	mass of particle $i$
$n_i$	director
$\omega$	shear frequency
$P[\dots]$	distribution functional
$\mathcal{P}$	instantaneous pressure
$p$	pressure
$\vec{p}_i$	momentum of particle $i$
$\Pi$	conjugate momentum of the simulation box
$\vec{\pi}_i$	conjugate momentum of particle $i$
$\Psi$	concentration field
$Q$	box mass
$Q_{ij}$	nematic order parameter
$q_i$	scattering vector
$S(\vec{k})$	scattering function
$S$	degree of order
$s_i$	reduced coordinates
$\sigma_{ij}$	stress tensor
$\tau$	reduced temperature
$U_{ij}$	interaction potential between particle $i$ and $j$
$\vec{u}$	total velocity including fluctuations
$V$	volume

$\mathcal{V}$	virial
$\vec{v}_i$	velocity of particle $i$
$\vec{v}_0, \vec{u}_0$	shear fields
$\zeta$	friction constant



## Bibliography

- [ABP00] G. Auernhammer, H.R. Brand, and H. Pleiner, *The undulation instability in layered systems under shear flow a simple model*, Rheol. Acta **39** (2000), 215.
- [And80] H.C. Andersen, J.Chem.Phys. **72** (1980), 2384.
- [AT87] M.P. Allen and D.J. Tildesley, *Computer simulation of liquids*, Clarendon, Oxford, 1987.
- [BC97] M.M. Britton and P.T. Callaghan, *Two-phase shear band structures at uniform stress*, Phys. Rev. Lett. **78** (1997), no. 26, 4930–4933.
- [BCW58] E.B. Bagley, I.M. Cabot, and D.C. West, J. Appl. Phys. **29** (1958), 109.
- [BF90] F.S. Bates and G.H. Fredrickson, *Block copolymer thermodynamics: Theory and experiment*, Ann. Rev. Phys. Chem. **41** (1990), 525.
- [BGHM98] M. Bergmeier, M. Gradzielski, H. Hoffmann, and K. Mortensen, *Behavior of a charged vesicle system under the influence of a shear gradient: a microstructural study*, J. Phys. Chem. B **102** (1998), no. 16, 2837–2840.
- [BGUG<sup>+</sup>00] A. Bernheim-Grosswasser, S. Ugazio, F. Gauffre, O. Viratelle, P. Mahy, and D. Roux, *Spherulites: a new vesicular system with promising applications. an example: Enzyme microencapsulation*, J. Chem. Phys. **112** (2000), no. 7, 3424–3430.
- [BMG<sup>+</sup>98] D. Bonn, J. Meunier, O. Greffier, A. Al-kahwaji, and H. Kellay, *Bistability in non-newtonian flow: Rheology of lyotropic liquid crystals*, Phys. Rev. E **58** (1998), no. 2, 2115–2118.
- [BPv<sup>+</sup>84] H.J.C. Berendsen, J.P.M. Postma, W.F. van Gunsteren, A. DiNola, and J.R. Haak, *Molecular dynamics with coupling to an external bath*, J.Chem.Phys. **81** (1984), no. 8, 3684.
- [Bra75] S. Brazovskii, Sov. Phys. JETP **41** (1975), 85.
- [CIK<sup>+</sup>97] Z.R. Chen, A.M. Issaian, J.A. Kornfield, S.D. Smith, J.T. Grothaus, and M.M. Satkowski, *Dynamics of shear-induced alignment of a lamellar diblock: a rheo-optical, electron microscopy, and x-ray scattering study*, Macromolecules **30** (1997), no. 23, 7096–7114.

- [CK98a] Z.-R. Chen and J.A. Kornfield, *Flow-induced alignment of lamellar block copolymer melts*, *Polymer* **39** (1998), no. 19, 4679.
- [CK98b] Z.R. Chen and J.A. Kornfield, *Flow-induced alignment of lamellar block copolymer melts*, *Polymer* **39** (1998), no. 19, 4679–4699.
- [CKS<sup>+</sup>97] Z.R. Chen, J.A. Kornfield, S.D. Smith, J.T. Grothaus, and M.M. Satkowski, *Pathways to macroscale order in nanostructured block copolymers*, *Science* **277** (1997), no. 5330, 1248–1253.
- [CL95] P.M. Chaikin and T.C. Lubensky, *Principles of condensed matter physics*, Cambridge University Press, Cambridge, U.K., 1995.
- [CM89] M.E. Cates and S.T. Milner, *Role of shear in the isotropic-to-lamellar transition*, *Phys. Rev. Lett.* **62** (1989), no. 16, 1856.
- [DE86] M. Doi and S.F. Edwards, *The theory of polymer dynamics*, Clarendon, 1986.
- [deG72] P.G. deGennes, *Solid State Comm.* **10** (1972), 753–756.
- [DGK98] B. Dünweg, G. S. Grest, and K. Kremer, *Numerical methods for polymeric systems*, vol. 102, p. 159, Springer, Berlin, 1998.
- [dGP93] P. G. de Gennes and J. Prost, *The physics of liquid crystals*, Clarendon, Oxford, 1993.
- [DRN93a] O. Diat, D. Roux, and F. Nallet, *Effect of shear on a lyotropic lamellar phase*, *J. Phys. II* **3** (1993), no. 9, 1427–1452.
- [DRN93b] O. Diat, D. Roux, and F. Nallet, *Lamellar phase under shear SANS measurements*, *J. Phys. IV* **3** (1993), no. C8, 193–204.
- [DRN95] O. Diat, D. Roux, and F. Nallet, *Layering effect in a sheared lyotropic lamellar phase*, *Phys. Rev. E* **51** (1995), no. 4, 3296–3299.
- [Dün96] B. Dünweg, *Monte carlo and molecular dynamics of condensed matter systems*, p. 215, Societa Italiana Fisica, Bologna, 1996.
- [EM90] D.J. Evans and G.P. Morriss, *Statistical mechanics of nonequilibrium liquids*, Academic Press, London, 1990.
- [Esp98] Pep Español, *Fluid particle model*, *Phys. Rev. E* **57** (1998), 2930.
- [EW95] P. Español and P.B. Warren, *Statistical mechanics of dissipative particle dynamics*, *Europhys. Lett.* **30** (1995), 191.
- [FC00] E. Fischer and P.T. Callaghan, *Is a birefringence band a shear band?*, *Europhys. Lett.* **50** (2000), no. 6, 803–809.



- [FH87] G.H. Fredrickson and E. Helfand, *Fluctuation effects in the theory of microphase separation in block copolymers*, J. Chem. Phys. **87** (1987), 697.
- [Fre86] G.H. Fredrickson, *Nonequilibrium structure of the homogeneous phase of block copolymers under steady flow*, J.Chem.Phys. **85** (1986), no. 9, 5306.
- [Fre94] Glenn H. Fredrickson, *Steady shear alignment of block copolymers near the isotropic-lamellar transition*, J. Rheol. **38** (1994), no. 4, 1045.
- [Fre99] D. Frenkel, Physica A **263** (1999), 26.
- [FS96] D. Frenkel and B. Smit, *Understanding molecular simulation*, Academic Press, 1996.
- [GF99] J.L. Goveas and G.H. Fredrickson, *Curvature-driven shear banding in polymer melts*, J. Rheol. **43** (1999), no. 5, 1261–1277.
- [GGL99] R. Goetz, G. Gomper, and R. Lipowsky, *Mobility and elasticity of self-assembled membranes*, Phys. Rev. Lett. **82** (1999), no. 1, 221.
- [GK86] G. S. Grest and K. Kremer, Phys. Rev. A **33** (1986), 3628.
- [GKC<sup>+</sup>96] V.K. Gupta, R. Krishnamoorti, Z.R. Chen, J.A. Kornfield, S.D. Smith, M.M. Satkowski, and J.T. Grothaus, *Dynamics of shear alignment in a lamellar diblock copolymer:interplay of frequency, strain amplitude, and temperature*, Macromolecules **29** (1996), no. 3, 875–884.
- [GKKS95] V.K. Gupta, R. Krishnamoorti, J.A. Kornfield, and S.D. Smith, *Evolution of microstructure during shear alignment in apolystyrene–polyisoprene lamellar diblock copolymer*, Macromolecules **28** (1995), no. 13, 4464–4474.
- [GKKS96] V.K. Gupta, R. Krishnamoorti, J.A. Kornfield, and S.D. Smith, *Role of strain in controlling lamellar orientation during flowalignment of diblock copolymers*, Macromolecules **29** (1996), no. 4, 1359–1362.
- [GL98] R. Goetz and R. Lipowsky, J. Chem. Phys. **108** (1998), 7397.
- [GLKG96] G. S. Grest, M.-D. Lacasse, K. Kremer, and A M. Gupta, J. Chem. Phys. **105** (1996), 10583.
- [GT94] S.P. Gido and E.L. Thomas, *Lamellar diblock copolymer grain boundary morphology. 4. tilt boundaries*, Macromolecules **27** (1994), 6137.
- [GW97] R.D. Groot and P.B. Warren, *Dissipative particle dynamics: Bridging the gap between atomistic and mesoscopic simulation*, J. Chem. Phys. **107** (1997), no. 11, 4423.
- [Hai92] J.M. Haile, *Molecular dynamics simulation elementary methods*, John Wiley & Sons Inc., New York, 1992.

- [HDTU99] Heike Leist, Danile Maring, Thomas Thurn-Albrecht, and Ulrich Wiesner, *Double flip of orientation for a lamellar diblock copolymer under shear*, J.Chem.Phys. **110** (1999), no. 17, 8225.
- [HK92] P.J. Hoogerbrugge and J.M.V.A. Koelman, Europhys. Lett. **19** (1992), 155.
- [HU98] H. Hoffmann and W. Ulbricht, *Vesicle phases of surfactants and their behaviour in shear flow*, Tenside Surfactants Deterg. **35** (1998), no. 6, 421–438.
- [HV69] J.-P. Hansen and L. Verlet, Phys. Rev. **184** (1969), 151.
- [JJPW98] Jörg Berghausen, Johannes Zipfel, Peter Lindner, and Walter Richtering, *Shear-induced orientations in a lyotropic defective lamellar phase*, Europhysics Letters **43** (1998), no. 6, 683–689.
- [JJW98] J. Berghausen, J. Zipfel, and W. Richtering, *Shear-induced orientations in a lyotropic defective lamellar phase*, Europhysics Letters **43** (1998), no. 6, 683–689.
- [KD99] A. Kolb and B. Dünweg, J. Chem. Phys. **111** (1999), 4453.
- [KG90] K. Kremer and G. S. Grest, J. Chem. Phys. **92** (1990), 5057.
- [KH93] J.M.V.A. Koelman and P.J. Hoogerbrugge, Europhys. Lett. **21** (1993), 369.
- [Kit95] C. Kittel, *Introduction to solid state physics*, John Wiley & Sons, New York, 1995.
- [KK94] R.M. Kannan and J.A. Kornfield, *Evolution of microstructure and viscoelasticity during flow alignment of a lamellar diblock copolymer*, Macromolecules **27** (1994), 1177–1186.
- [KTB<sup>+</sup>92] K.A. Koppi, M. Tirrell, F.S. Bates, K. Almdal, and R.H. Colby, *Lamellae orientation in dynamically sheared diblock copolymer melts*, J.Phys. II France **2** (1992), 1941.
- [KTB93] K.A. Koppi, M. Tirrel, and F.S. Bates, *Shear-induced isotropic-to-lamellar transition*, Phys. Rev. Lett. **70** (1993), no. 10, 1449.
- [Lei80] L. Leibler, *Theory of microphase separation in block copolymers*, Macromolecules **13** (1980), 1602.
- [LM00] M. Laradji and O.G. Mouritsen, *Elastic properties of surfactant monolayers at liquid-liquid interfaces: A molecular dynamics study*, J.Chem.Phys. **112** (2000), no. 19, 8621.
- [LMTAW99] H. Leist, D. Maring, T. Thurn-Albrecht, and U. Wiesner, J. Chem. Phys. **110** (1999), 8225.

- [LMTZ94] M. Laradji, O. G. Mouritsen, S. Toxvaerd, and M. J. Zuckermann, *Phys. Rev. E* **50** (1994), 1243.
- [MB86] T.C.B. McLeish and R.C. Ball, *A molecular approach to the spurt effect in polymer melt flow*, *J. Pol. Science: B: Pol. Phys.* **24** (1986), 1735.
- [MC97] R.W. Mair and P.T. Callaghan, *Shear flow of wormlike micelles in pipe and cylindrical couette geometries as studied by nuclear magnetic resonance microscopy*, *J. Rheol.* **41** (1997), no. 4, 901–924.
- [MM93] D.C. Morse and S.T. Milner, *Absence of the nematic phase in symmetric diblock copolymers*, *Phys. Rev. E* **47** (1993), no. 3, 1119.
- [MP99] Florian Müller-Plathe, *Reversing the perturbation in nonequilibrium molecular dynamics: An easy way to calculate shear viscosities of fluids*, *Phys. Rev. E* **59** (1999), no. 5.
- [MRR<sup>+</sup>53] N. Metropolis, A. W. Rosenbluth, M. N. Rosenbluth, A. H. Teller, and E. Teller, *J. Chem. Phys.* **21** (1953), 335.
- [MW89] F.A. Morrison and H.H. Winter, *Macromolecules* **22** (1989), 3533.
- [OBA82] P. Oswald and S.I. Ben-Abraham, *Undulation instability under shear in smectic a liquid crystals*, *J. Phys. (France)* **43** (1982), 1193–1197.
- [OK79] A. Onuki and K. Kawasaki, *Non equilibrium steady state of critical fluids under shear flow: A renormalization group approach*, *Ann. Phys.* **121** (1979), 456.
- [OL97] P.D. Olmsted and C.-Y.D. Lu, *Coexistence and phase separation in sheared complex fluids*, *Phys. Rev. E* **56** (1997), no. 1, R55.
- [PB96] H. Pleiner and H.R. Brand, *Pattern formation in liquid crystals*, ch. Hydrodynamics and Electrohydrodynamics of Liquid Crystals, p. ??, Springer, N.Y., 1996.
- [PCCR98] P. Panizza, A. Colin, C. Coulon, and D. Roux, *A dynamic study of onion phases under shear flow: Size changes*, *Eur.Phys.J. B* **4** (1998), 65.
- [PK98] M. Pütz and A. Kolb, *Comp. Phys. Comm.* **113** (1998), 145.
- [PLWW95] S.S. Patel, R.G. Larson, K.I. Winey, and H. Watanabe, *Shear orientation and rheology of a lamellar polystyrene–polyisoprene block–copolymer*, *Macromolecules* **28** (1995), no. 12, 4313–4318.
- [PR80] Parinella and Rahman.
- [PW96] D.L. Polis and K.I. Winey, *Kink bands in a lamellar diblock copolymer induced by largeamplitude oscillatory shear*, *Macromolecules* **29** (1996), no. 25, 8180–8187.

- [RD77] R. Ribotta and G. Durand, *Mechanical properties of smectic-a liquid crystals under dilative or compressive stresses*, J.Phys. (France) **38** (1977).
- [Ris89] H. Risken, *The fokker-planck equation*, Springer, New York, 1989.
- [RJWP96] Richard Weigel, Jörg Lauger, Walter Richering, and Peter Lindner, *Anisotropic small angle light and neutron scattering from a lyotropic lamellar phase under shear*, J.Phys.II France **6** (1996), 529–542.
- [SADK] T. Soddemann, G. Auernhammer, B. Duenweg, and K. Kremer, *Shear-induced buckling of smectic a*, to be published.
- [SCM93] N.A. Spenley, M.E. Cates, and T.C.B. Mcleish, *Nonlinear rheology of worm-like micelles*, Phys. Rev. Lett. **71** (1993), no. 6, 939–942.
- [SHM95] A.G. Schlijper, P.J. Hoogerbrugge, and C.W. Manke, *Computer simulation of dilute polymer solutions with the dissipative particle dynamics method*, J. Rheol. **39** (1995), 567.
- [Sti89] K. Stierstadt, *Physik der materie*, 1 ed., VCH, Weinheim, 1989.
- [SYC96] N.A. Spenley, X.F. Yuan, and M.E. Cates, *Nonmonotonic constitutive laws and the formation of shear-banded flows*, J. Phys. II **6** (1996), no. 4, 551–571.
- [TBM92] M. Tuckerman, B.J. Berne, and G.J. Martyna, *Reversible multiple time scale molecular dynamics*, J.Chem.Phys. **97** (1992), 1990–2001.
- [Tol54] J.R.R. Tolkien, *The fellowship of the ring*, George Allen and Unwin Ltd., 1954.
- [Vin72] G.V. Vinogradov, J. Polym. Sci. **10** (1972), 1061.
- [Vin73] G.V. Vinogradov, Rheol. Act. **12** (1973), 273.
- [WPLW93a] K.I. Winey, S.S. Patel, R.G. Larson, and H. Watanabe, *Interdependence of shear deformations and block copolymer morphology*, Macromolecules **26** (1993), no. 10, 2542–2549.
- [WPLW93b] K.I. Winey, S.S. Patel, R.G. Larson, and H. Watanabe, *Morphology of a lamellar diblock copolymer aligned perpendicular to the sample plane transmission electron-microscopy and small-angle x-ray-scattering*, Macromolecules **26** (1993), no. 16, 4373–4375.
- [ZLR99] J. Zipfel, P. Lindner, and W. Richtering, Group’s homepage, 1999.
- [ZLT+99] J. Zipfel, P. Lindner, M. Tsianou, P. Alexandridis, and W. Richtering, *Shear-induced formation of multilamellar vesicles (“onions”) in block copolymers*, Langmuir **15** (1999), no. 8, 2599.

- [ZW95] Y. Zhang and U. Wiesner, *Symmetric diblock copolymers under large amplitude oscillatory shear flow: Entanglement effect*, *J.Chem.Phys.* **103** (1995), 4784.
- [ZWY<sup>+</sup>96] Y. Zhang, U. Wiesner, Y. Yang, T. Pakula, and H.W. Spiess, *Macromolecules* **29** (1996), 5427.



# List of Figures

P.1. Theory, experiment, and simulation help to the unravel of the mystery nature. The edges serve as bilateral connections. . . . .	3
P.2. Schematic representation of a symmetric diblock copolymer. Monomers belonging to block A are white, the ones belonging to the B block are blue. . . .	4
P.3. Typical equilibrium nanostructures of diblock copolymers. . . . .	4
P.4. Monomers of broadly applied polymers. . . . .	5
P.5. Sodium dedocyl sulfate . . . . .	5
P.6. Sketches of the nematic and smectic phase. . . . .	6
P.7. Coordinate system and shear flow. . . . .	6
P.8. Perpendicular, parallel, and transverse orientation of lamellae. . . . .	7
1.1. Sketch of experimental findings. . . . .	10
1.2. Plot of various findings in shear experiments. . . . .	13
1.3. Sketch of a multi lamellar vesicle . . . . .	15
1.4. Four regimes of occurrence of onions in a lyotropic system under shear. . . .	15
1.5. Sketch of a Couette cell. . . . .	16
1.6. Sketch of plate to plate and cone to plate geometries. . . . .	17
1.7. Picture of an experiment. . . . .	17
2.1. Deformation of a slab of material. . . . .	20
2.2. Idealized geometry of a shear experiment . . . . .	25
2.3. Angle between layer normal and director. . . . .	25
2.4. Unulations in vorticity direction . . . . .	26
2.5. Sketch of a stepwise shear applied to a sample. . . . .	31
2.6. Oscillatory shearing. . . . .	32
2.7. Constant stress. . . . .	33

2.8. Functional behavior of the effective strain rate . . . . .	41
2.9. Shear on layers with different viscosities. . . . .	41
2.10. Schematic sketch of the potentials. . . . .	47
2.11. Schematic phase diagram . . . . .	49
3.1. Virtual surface inserted perpendicular to the x-axis into the cubic box. . . . .	58
3.2. Schematic view of Lees Edwards periodic boundary conditions for a planar Couette flow. <b>E</b> denotes the simulation cell surrounded by its periodic images <b>A</b> to <b>I</b> . As shear flow is applied, the images in the upper row are moving with a velocity $v_x = \dot{\gamma}L$ while the lower is moving into the opposite direction. . . . .	67
3.3. Sketch of the shear algorithm . . . . .	68
3.4. Velocity profiles . . . . .	69
3.5. Ghost halo . . . . .	75
3.6. Ghost half shell . . . . .	76
3.7. Friction dependence of the shear viscosity. . . . .	76
4.1. Pair correlation functions. . . . .	78
4.2. Bond length distribution. . . . .	80
4.3. MD performance test. . . . .	81
4.4. Expected phase diagram . . . . .	82
4.5. Hysteresis loop. . . . .	83
4.6. Mean square displacement. . . . .	83
4.7. Structure factors. . . . .	84
4.8. Phase diagram of a binary system. . . . .	85
4.9. Un-mixing phase diagram . . . . .	86
4.10. Cumulant ratio. . . . .	86
4.11. Phase diagram for a dimer system. . . . .	87
4.12. Snapshot of a typical conformation. . . . .	88
4.13. Order parameter as a function of the potential depth. . . . .	89
4.14. Structure factor with scattering direction parallel to the director. . . . .	89
4.15. Structure factor with scattering direction perpendicular to the director. . . . .	90
4.16. Mean square displacement. . . . .	90
5.1. Snapshot of the initial conformation . . . . .	93



5.2. Determination of the layer bending modulus . . . . .	95
5.3. Flow alignment of the director. . . . .	97
5.4. The slope of the flow component of the director. . . . .	97
5.5. Sketch of undulations . . . . .	98
5.6. Simulation snapshots of undulating conformations. . . . .	99
5.7. Fit of the flow alignment theory. . . . .	100
5.8. Third order polynomial fit. . . . .	100
5.9. Flow alignment of the director. . . . .	102
5.10. Mechanism of undulating layers. . . . .	102
5.11. Undulation of the vorticity component of the director. . . . .	103
5.12. Undulation of the flow component of the director. . . . .	103
5.13. Possible scenarios for a bifurcation. . . . .	104
5.14. Undulation amplitude as a function of strain rate. . . . .	104
5.15. Non-isochoric stretch dilatation of a Smectic A . . . . .	106
5.16. Conformation snapshot. . . . .	107
5.17. Isochoric dilatation of a smectic model system. . . . .	107
5.18. Shear stress as a function of the strain rate. . . . .	108
5.19. Sketch of the coexistence of two different orientations under shear. . . . .	108
5.20. Effect of shear flow on molecules . . . . .	109
5.21. Configuration snapshots. . . . .	110
5.22. Time evolution of the box height. . . . .	111
5.23. Snapshot of an initial conformation. . . . .	111
5.24. Phase diagram of DBCP under shear in comparison with simulation. . . . .	113
5.25. Parallel to perpendicular transition. . . . .	114
5.26. Conformational snapshot series. . . . .	115
6.1. Sketch of the spurt effect. . . . .	117
6.2. Sketch of a non-monotonic stress strain rate relation. . . . .	118
6.3. Sketch of shear bands with plug flow. . . . .	118
6.4. Snapshot of the large system, size comparison with the medium system and directions of flow. . . . .	119
6.5. Analysis of conformation snapshot . . . . .	121
6.6. Analysis of conformation snapshot . . . . .	122

6.7. Tumbling and rotation of a molecule. . . . .	123
6.8. Velocity profile and S value for a system under high shear strain. . . . .	124
6.9. Director components at different points of time. The different components of the director, $n_x(z)$ , $n_y(z)$ , and $n_z(z)$ are plotted for different points of time. Remarkable, the components in the disordered regions are match for all points of time as if the regions are ordered. . . . .	125
6.10. Tumbling of dimers in the medium size system. . . . .	126
6.11. $m_y$ as a function of the time span. . . . .	127
6.12. The evolution of plug flow. . . . .	128
6.13. The three tilt boundaries found by Gido et al. [GT94], the chevron, the $\Omega$ -type and the T-junction. . . . .	128
6.14. Defects structures in the large system . . . . .	129
E.1. Snapshot of a bola surfactant system. . . . .	133

# Index

- algorithm
  - shear, 63
- amphiphiles, 5
  
- balance equation, 24
- bend, 22, 23
- bending energy, 22
- boundary condition
  - periodic, 55
  
- compression, 22
- Couette cell, see geometry
  
- defect
  - chevron, 126
  - omega, 126
  - t-junction, 126
- defects
  - focal conics, 11
- director, 5
- Dissipative particle dynamics, 69
- dissipative particle dynamics, 7
  
- elasticity, 20
- ensemble
  - $NpT$ , 52, 57
  - $NVT$ , 52
  - micro-canonical, 52
- equation of motion, 49
  
- fluid
  - complex, 5
- frequencies
  - characteristic, 10
  
- geometry
  - cone-to-plate, 16
  - Couette, 16
  - plate-to-plate, 16
  
- Gibbs relation, 24
  
- hydrophilic, 5
  
- LAOS, 17
- Liouville, 50
- lipophilic, 5
- liquid crystal, 5, 20
- lyotropic, 5
  
- mechanism
  - defect migration, 11
  - domain dissolution, 11
  - grain rotation, 10
  - irreversible rocking, 10
  - selective creation, 11
  - selective elimination, 11
  - selective melting, 11
  - viscoelastic contrast, 11
- mixture
  - quaternary, 13
- modulus
  - loss, 31
  - storage, 31
  - complex shear, 31
- molecular dynamics, 7, 49
  - non-equilibrium, 63
- monomer, 4
  
- nematic, 5, 20
- nematic order parameter, 23
  
- onion, 13
- order parameter
  - nematic, 123
  
- parallel, 6
- perpendicular, 6
- polymer, 4

diblock co-, 4  
homo, 4  
linear, 4

shear  
    crystallization, 125  
shear viscosity, 66  
shear bands, 8, **115**, 118  
shear rate, 24  
shear strain, 21  
shear stress, 66  
smectic, 5, 20  
soap, 4  
spherulite, see onion  
splay, 23  
    director, 22  
spurt effect, 115  
strain rate, 29  
    effective, 12  
strain tensor, 21  
stress tensor, 21, 29

temperature  
    reduced, 12

thermostat  
    Anderson, 54, 57  
    Anderson extended system, 54, **57**  
    Berendsen, 52  
    DPD, 69

thermotropic, 5

transition  
    order-disorder, 4

transverse, 6

twist, 22, 23

updating scheme, 51

velocity gradient, 6, 66  
velocity gradient tensor, 29  
velocity Verlet, 49, 50

vesicle  
    multilamellar, 13

virial  
    equation, 54  
    function, 54

theorem, 54  
vorticity, 6